Springer Remote Sensing/Photogrammetry

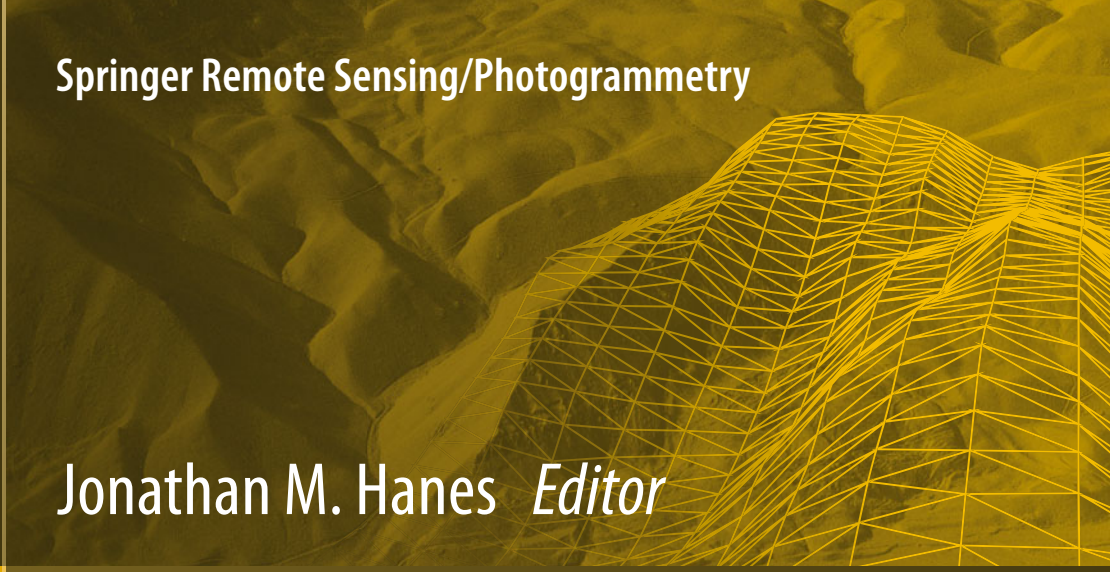

Jonathan M. Hanes *Editor*

Biophysical Applications of Satellite Remote Sensing

Springer

Springer Remote Sensing/Photogrammetry

For further volumes:
http://www.springer.com/series/10182

Jonathan M. Hanes
Editor

Biophysical Applications of Satellite Remote Sensing

Springer

Editor
Jonathan M. Hanes
Department of Geography
University of Wisconsin-Milwaukee
Milwaukee, WI
USA

ISSN 2198-0721 ISSN 2198-073X (electronic)
ISBN 978-3-642-25046-0 ISBN 978-3-642-25047-7 (eBook)
DOI 10.1007/978-3-642-25047-7
Springer Heidelberg New York Dordrecht London

Library of Congress Control Number: 2013956521

Printed on acid-free paper

Springer is part of Springer Science+Business Media (www.springer.com)

Foreword

I was pleased and honored when Jonathan M. Hanes asked me to write the foreword for this book. As a researcher who studies the interactions of plant life cycle events (phenology) with land surface and atmospheric processes, including the impacts of changing climates on the timing of these seasonal transitions, I have long appreciated the unique and developing role that satellite-derived measures play in biophysical research efforts. Simply stated, there is currently no other means to gather diverse large-scale vegetation information systematically across the Earth's surface, without employing remote sensing.

One of the most important developments in recent years has been the growing realization that integration of diverse perspectives and paradigms from many traditional fields will be essential to address the complex challenges posed by the expected worldwide impacts of global climate change on ecosystems. Increasingly, individual researchers must broadly cross-train, and research teams need quick access to diverse multidisciplinary techniques, in order to conduct cutting-edge global change research studies. The expert authors assembled for this book have collectively done an excellent job in their chapters of comprehensively addressing the major techniques used to measure and analyze land and ocean vegetation activity and biophysical processes at global scales. Such information will prove to be an invaluable part of advancing future global change and large-scale ecological research. Thus, I will look forward to adding this volume to my personal technical reference library, and expect to consult it often in the years ahead. I presume that many of my colleagues will want to do the same.

June 2013 Mark D. Schwartz

Preface

The utility of measurements of reflected and emitted radiation from the Earth system captured by space-borne sensors on satellites has been realized in numerous scientific disciplines in recent decades. This form of data collection (called satellite remote sensing) has enjoyed wide application in efforts to study the Earth system because space-borne sensors can monitor the planet consistently and at spatial scales not accessible by other methods of observation (Kerr and Ostrovsky 2003). In addition, the occurrence of significant environmental change has brought the tools of satellite remote sensing to the forefront of research on the physical characteristics and processes of Earth's biosphere (Myneni et al. 1997; Nemani et al. 2003; Pettorelli et al. 2005). With an eye toward assessing global environmental change, scientists have harnessed the capabilities of satellite remote sensing to derive various metrics of the biophysical characteristics of terrestrial and oceanic ecosystems.

The purpose of this edited volume is to highlight selected *Biophysical Applications of Satellite Remote Sensing* in terrestrial and oceanic ecosystems for the benefit of scientists, educators, and students. While the applications presented in this volume are distinct because they focus on particular biophysical characteristics of terrestrial and oceanic ecosystems, they all relate, in some form, to ecosystem productivity. As a collection of diverse metrics unified by the common theme of productivity, this volume provides the reader with a sampling of tools that can be used to better understand Earth's living systems. Within each chapter, the reader will find a discussion of the theoretical basis for the biophysical application, methods of validation, research findings, and future research directions. Chapters 1–6 focus on applications of satellite remote sensing to the study of terrestrial ecosystems, while Chaps. 7 and 8 concentrate on oceanic ecosystems.

Jonathan M. Hanes

References

Kerr JT, Ostrovsky M (2003) From space to species: ecological applications for sremote sensing. Trends Ecol Evol 18:299–305

Myneni RB, Keeling CD, Tucker CJ, Asrar G, Nemani RR (1997) Increased plant growth in the northern high latitudes from 1981 to 1991. Nature 386:698–702. doi:10.1038/386698a0

Nemani RR, Keeling CD, Hashimoto H, Jolly WM, Piper SC, Tucker CJ, Myneni RB, Running SW (2003) Climate-driven increases in global terrestrial net primary production from 1982 to 1999. Science 300:1560–1563

Pettorelli N, Vik JO, Mysterud A, Gaillard J-M, Tucker CJ, Stenseth NC (2005) Using the satellite-derived NDVI to assess ecological responses to environmental change. Trends Ecol Evol 20:503–510

Acknowledgments

I want to begin my acknowledgments by thanking Springer for their willingness to publish this edited volume. In particular, I would like to thank Johanna Schwarz and Carlo Schneider for their work on this project and their seemingly endless patience.

With regard to the content of this volume, I want to express my gratitude to all of the contributing authors who devoted extensive time and effort to the writing of their chapters. I also thank all of the reviewers who improved the quality of this work through their careful analysis and comments.

On a professional note, I want to thank Northern Michigan University and their Department of Earth, Environmental, and Geographical Sciences for providing reassigned time to work on this edited volume while I was a faculty member. Special thanks go to Dr. Susy Ziegler, who supported my work as department chair during my time in the department. On a personal note, I want to thank my wife and children for their loving support and the Lord for the ability to engage in this work.

Contents

Contributors

Frederic Baret INRA-EMMAH, Avignon, France

Michael J. Behrenfeld Department of Botany and Plant Pathology, Oregon State University, Corvallis, OR 97330-2902, USA

Jian Bi Department of Earth and Environment, Boston University, Boston, MA, USA

Mark Broich University of Technology Sydney, Ultimo, Australia

Janet Campbell Institute for the Study of Earth, Oceans, and Space, University of New Hampshire, Durham, NH, USA

Jinwei Dong Department of Microbiology and Plant Biology, Center for Spatial Analysis, University of Oklahoma, Norman, OK, USA

Sangram Ganguly NASA Ames Research Center/Bay Area Environmental Research Institute, Moffett Field, CA, USA

Jonathan M. Hanes Department of Geography, University of Wisconsin-Milwaukee, Milwaukee, WI, USA

Hirofumi Hashimoto Department of Science and Environmental Policy, NASA Ames Research Center/California State University at Monterey Bay, Moffett Field, CA, USA

Chuanmin Hu College of Marine Science, University of South Florida, St. Petersburg, FL, USA

Alfredo Huete University of Technology Sydney, Ultimo, Australia

Cui Jin Department of Microbiology and Plant Biology, Center for Spatial Analysis, University of Oklahoma, Norman, OK, USA

Liang Liang Department of Geography, University of Kentucky, Lexington, KY, USA

Cristina Milesi Department of Science and Environmental Policy, California State University at Monterey Bay/NASA Ames Research Center, Moffett Field, CA, USA

Tomoaki Miura University of Hawaii, Honolulu, USA

Jeffrey T. Morisette North Central Climate Science Center, U.S. Geological Survey, Fort Collins, CO, USA

Ranga B. Myneni Department of Earth and Environment, Boston University, Boston, MA, USA

Ramakrishna R. Nemani NASA Advanced Supercomputing Division, Moffett Field, CA, USA

Wenge Ni-meister Department of Geography, Hunter College, City University of New York, New York, NY, USA

Piyachat Ratana University of Technology Sydney, Ultimo, Australia

Arindam Samanta Atmospheric and Environmental Research Inc., Lexington, MA, USA

Kumaresh Singh Risk Management Solutions, Newark, CA, USA

Aleixandre Verger INRA-EMMAH, Avignon, France

Marie Weiss INRA-EMMAH, Avignon, France

Toby K. Westberry Department of Botany and Plant Pathology, Oregon State University, Corvallis, OR 97330-2902, USA

Jingfeng Xiao Earth Systems Research Center, Institute for the Study of Earth, Oceans, and Space, Durham, NH, USA

Xiangming Xiao Department of Microbiology and Plant Biology, Center for Spatial Analysis, University of Oklahoma, Norman, OK, USA

Hiroki Yoshioka Aichi Prefectural University, Nagakute, Japan

Gong Zhang NASA Ames Research Center/Bay Area Environmental Research Institute, Moffett Field, CA, USA

Xiaoyang Zhang Earth System Science Interdisciplinary Center, University of Maryland, College Park, MD, USA; NOAA/NESDIS/STAR, College Park, MD, USA

Chapter 1
Indices of Vegetation Activity

Alfredo Huete, Tomoaki Miura, Hiroki Yoshioka, Piyachat Ratana and Mark Broich

Abstract In this chapter we explain satellite-based vegetation indices (VIs) as dynamic spectral measures of vegetation activity. VIs are among the most widely used satellite products in monitoring ecosystems and agriculture, resource management, and estimations of many biophysical canopy properties. A theoretical basis for their formulation is presented and we describe how VIs are processed and composited from satellite imagery. Recent trends in their validation and quality assessment using in situ tower measurements are also discussed. Finally, a cross section of major findings involving the use of satellite VIs in ecological and climate science is presented and we conclude with research challenges and environmental issues that will drive future uses of satellite VIs.

1.1 Introduction

Vegetation indices (VIs) are spectral measures of the green foliage, and in some cases, moisture status of a canopy. They are seamless and highly robust satellite measurements computed the same across all pixels in time and space. Due in part to their simplicity and transparency, they are among the most widely used satellite products, providing key measurements in productivity, phenology, climate, hydrology, biogeochemical and biodiversity studies. They have become indispensable tools across an array of ecological, agricultural, and natural resource management applications.

A. Huete (✉) · P. Ratana · M. Broich
University of Technology Sydney, NSW, Australia
e-mail: Alfredo.Huete@uts.edu.au

T. Miura
University of Hawaii, Honolulu, HI, USA

H. Yoshioka
Aichi Prefectural University, Aichi, Japan

J. M. Hanes (ed.), *Biophysical Applications of Satellite Remote Sensing*,
Springer Remote Sensing/Photogrammetry, DOI: 10.1007/978-3-642-25047-7_1,

VIs generally have the scientific requirement of contrasting an absorbing leaf spectral feature with a non-absorbing one in a globally robust manner to capture essential plant biophysical phenomena with adequate fidelity. Most VIs will combine a chlorophyll-absorbing spectral band in the Red with a non-absorbing band in the near-infrared (NIR) to depict canopy greenness, or area-averaged canopy photosynthetic activity. Vegetation water indices, on the other hand, may combine a water absorbing leaf spectral feature in the shortwave infrared (SWIR) with the NIR to provide measures of canopy moisture content (Ceccato et al. 2002a, b; Gao 1996).

As a greenness measure, VIs encapsulate leaf- and whole-canopy optical properties expressed through several biophysical quantities related to foliage amount and structure (vegetation fraction, leaf angles, and leaf area) and physiological (pigments, water) status of a canopy. VIs have been widely used as proxies in the assessment of canopy biophysical/biochemical variables, including leaf area index (LAI), fraction of absorbed photosynthetically-active radiation (f_{APAR}), chlorophyll content, green vegetation fraction (F_{veg}), biomass, and canopy biophysical processes (Sellers 1985; Field et al. 1995; Gitelson et al. 2003; Glenn et al. 2008). Several comprehensive reviews on the use of VIs to assess ecological properties are found in Kerr and Ostrovsky (2003), Pettorelli et al. (2005), and Huete and Glenn (2011).

1.2 Theoretical Description of Vegetation Indices

The theoretical basis for vegetation indices is derived from an examination of leaf, soil, woody, and senesced plant spectral reflectance signatures (Fig. 1.1). The reflected energy from a green leaf is very low in the visible portion of the spectrum due to high absorption of photosynthetically active radiation (PAR) by leaf pigments, primarily in the Blue (470 nm) and Red (670 nm), whereas nearly all of the NIR radiation is scattered (reflected and transmitted) in a manner dependent on leaf type, morphology, and cellular structure. The resulting contrast between Red and NIR reflectances is a sensitive measure of variations in leaf physiology and structure, with maximum contrast occurring in healthy, structurally-developed leaves and minimal contrast in stressed and senesced leaves. At the canopy level, maximum NIR-Red contrasts occur in densely foliated canopies containing vigorous leaves, with lower contrasts found in stressed and open canopies, and the least contrasts occur in defoliated or sparse canopies.

1.2.1 Index Formulations

There are a variety of ways in which two or more spectral bands may be combined to quantify the NIR-Red contrast as a measure of canopy greenness or moisture. This has resulted in a multitude of VI formulas and variants that include two-band

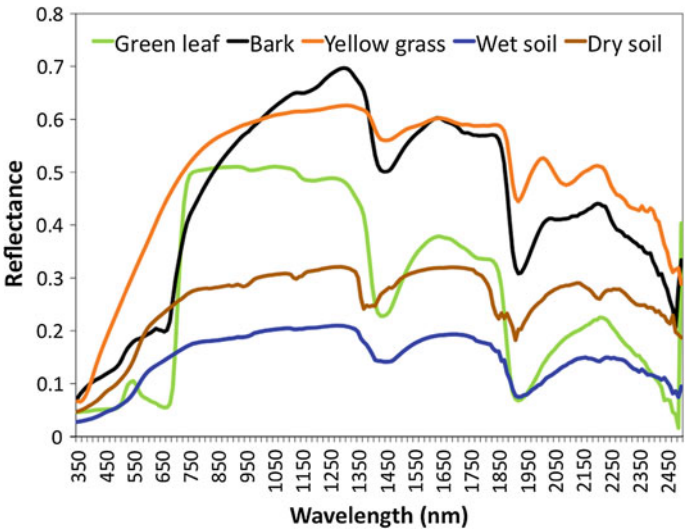

Fig. 1.1 Field spectral signatures of green leaf, senesced grass, woody bark, and dry and wet soil. As measured in situ with an Analytical Spectral Devices-Pro, ASD spectroradiometer

ratios and differences (Gallo and Eidenshink 1988), weighted differences and normalized differences (Tucker 1979), linear spectral band combinations, angle-based VIs (Jiang et al. 2006a), and optimized spectral band combinations (Gobron et al. 2000; Verstraete and Pinty 1996; Huete 1988; Qi et al. 1994). All VIs relate positively with plant canopy biophysical properties, and to a certain extent, some are functionally equivalent. Despite this, there are important differences in how they depict vegetation foliage and multiple VIs offer a more complete characterization of vegetation canopies. For example, in Fig. 1.2 there is a twofold difference in enhanced vegetation index (EVI) values (0.30–0.65) across forest canopy types where there is a much smaller range in normalized difference vegetation index (NDVI) values (0.70–0.90).

The Simple Ratio (SR), computed as a ratio of NIR and Red reflectances, is the most fundamental greenness measure of vegetation in a pixel (Rouse et al. 1973),

$$\mathrm{SR} = \rho_{\mathrm{NIR}} / \rho_{\mathrm{red}} \tag{1.1}$$

where ρ is reflectance. Similarly a vegetation water index (WI) is constructed as the ratio of NIR with a water-absorbing SWIR band, as in the Moisture Stress Index (MSI) (Hunt and Rock 1989),

$$\mathrm{MSI} = \rho_{\mathrm{NIR}} / \rho_{\mathrm{SWIR}} \tag{1.2}$$

Normalized versions of these ratios constrain values between −1 and +1, e.g., the NDVI (Tucker 1979), which is functionally equivalent to SR,

$$\mathrm{NDVI} = (\mathrm{SR} - 1) / (\mathrm{SR} + 1) = (\rho_{\mathrm{NIR}} - \rho_{\mathrm{red}}) / (\rho_{\mathrm{NIR}} + \rho_{\mathrm{red}}) \tag{1.3}$$

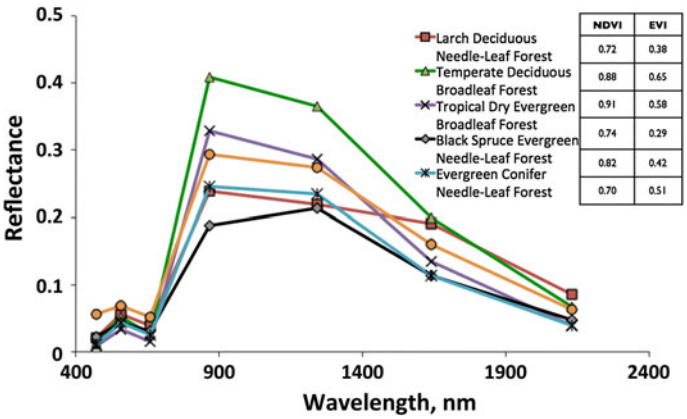

Fig. 1.2 Satellite-derived spectral signatures of various forest canopy types as measured from MODIS. The corresponding NDVI and EVI values for each forest canopy are shown in the *inset*. Sites include Siberian Yakutsk Larch, Hubbard Brook Deciduous Broadleaf Forest, Chamela Tropical Dry Evergreen Broadleaf Forest, Black Spruce Evergreen Needle-Leaf Forest, H.J. Andrews Pacific Northwest Evergreen Needle-Leaf Forest, and MaeKlong Tropical Evergreen Broadleaf Forest

Similarly, the normalized difference water index (NDWI) and land surface water index (LSWI) are normalized versions of NIR and water absorption band ratios (Gao 1996; Xiao et al. 2004),

$$\text{NDWI} = (\rho_{\text{NIR}} - \rho_{1240\text{nm}}) / (\rho_{\text{NIR}} + \rho_{1240\text{nm}}) \tag{1.4}$$

$$\text{LSWI} = (\rho_{\text{NIR}} - \rho_{1600\text{nm}}) / (\rho_{\text{NIR}} + \rho_{1600\text{nm}}), \tag{1.5}$$

The global vegetation moisture index (GVMI) has also been used for retrieval of equivalent water thickness (EWT) in a canopy (Ceccato et al. 2002a, b),

$$\text{GVMI} = [(\rho_{\text{NIR}} + 0.1) - (\rho_{\text{SWIR}} + 0.02)] / [(\rho_{\text{NIR}} + 0.1) + (\rho_{\text{SWIR}} + 0.02)] \tag{1.6}$$

In combination, VIs and WIs are important in analyzing canopy ecophysiological functioning, and some model-based studies have suggested that they can independently estimate canopy chlorophyll and water contents (Zarco-Tejada et al. 2003). Vegetation water indices are further deemed useful in assessing canopy drying and fire vulnerability (Caccamo et al. 2011). However, there are several studies showing little if any evidence that SWIR-based indices can sense water stress (Bates and Hall 1981). For example, Waring et al. (1979) found very small changes in leaf water content in needle-leaf evergreen conifers subjected to drought stress.

The ratio- and normalized difference-based VIs have the advantage of minimizing noise and influences attributed to variations in irradiance, clouds and cloud shadows. Their main disadvantage involve inherent non-linearities associated with

ratios and potential scaling issues (Yoshioka et al. 2000). Ratios also fail to account for canopy-background and mutual canopy shadowing associated with bidirectional reflectance anisotropies.

1.2.2 Vegetation Index and Vegetation Biophysical Isolines

Key theoretical differences among VIs can be depicted through NIR-Red band cross plots (Fig. 1.3a). A triangular cloud of points delineated by vegetation and soil end members characterize pixels of varying vegetation amounts and different canopy backgrounds representing a range of landscape surface conditions. The canopy background baseline is located close to the 1:1 line and represents the boundary condition of 'zero' vegetation, sometimes known as the "soil line" (Richardson and Wiegand 1977). The end members consist of dense green vegetation at the highest NIR and lowest Red reflectances, bright canopy backgrounds (dry soil, cement, or snow) and dark backgrounds (wet soil, organic soil, or standing water). The dense green apex exhibits the maximum Red-NIR contrast while the soil baseline shows the least differences between Red and NIR reflectances.

The points inside the triangular structure are mixed pixels composed of spectral signals from vegetation and canopy backgrounds. As noted by Graetz (1990), over 70 % of the Earth's terrestrial surface is classified as open canopies, with mixed background and vegetation signals. Relative to surfaces devoid of plants, partially vegetated pixels shift away from the lower baseline toward the apex of maximum NIR and lowest Red reflectance in a manner dependent upon the optical and structural properties of the canopy and soil background type (Fig. 1.3a). The greater the amount of green vegetation present in a pixel, the greater will be its' Red-NIR contrast and shift from the lower soil line, and there is also a convergence toward the apex of maximum vegetation density. The theoretical basis and defining characteristic of VIs are in how they model these spectrally mixed pixels, their boundary conditions, and associated variations in time and space.

The SR and NDVI characterize variations in NIR-Red space with vegetation index isolines of increasing slopes diverging out from the origin, i.e., isoline slopes become steeper with increasing vegetation amounts but their NIR intercepts are constant, and at zero (Fig. 1.3b). Isolines of constant VI values define the manner in which the VI quantifies the subpixel amounts of vegetation present. The NDVI approximates the soil baseline with an isoline defined by an NIR-Red slope between 1.25–1.5, which yields NDVI values of 0.10–0.20 for non-vegetated areas (see Eq. 1.3).

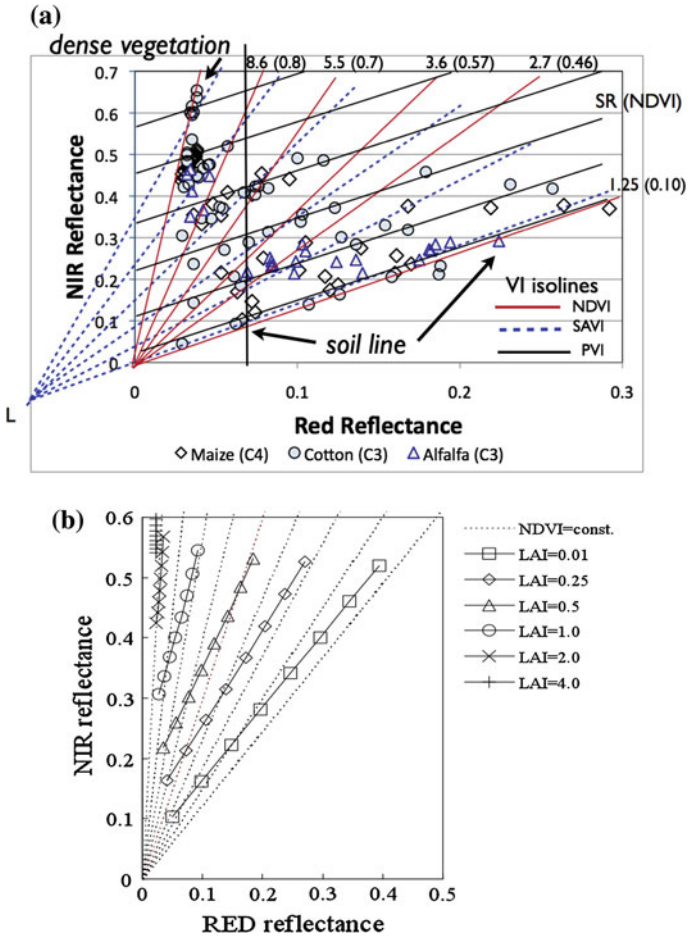

Fig. 1.3 **a** Vegetation index isolines representing NDVI, SAVI, and PVI in NIR-Red crossband space. These lines are diagrammed over the triangular cloud of crop canopy spectral measurements (cotton, corn, wheat) over a growing season. The *numbers* on *top* and *right* side are simple NIR/Red ratio and NDVI values of their isolines. **b** Vegetation biophysical isolines of constant LAI (symbols connected by *solid lines*) plotted alongside NDVI isolines (*dotted*). The NIR- Red reflectances for varying LAI were derived with the SAIL model. Each biophysical isoline has an NIR-intercept and the soil line is estimated by the LAI = 0.01 case. ©[2000] Adapted and reprinted with permission from Yoshioka et al. (2000)

1.2.3 Linear Combination and Optimized Indices

Linear spectral band combination indices are also widely used to measure foliage greenness and water status (Gobron et al. 2000; Huete and Glenn 2011). The Tasseled Cap (TC) greenness and wetness indices, as well as the perpendicular vegetation index (PVI) and spectral mixture analysis (SMA) schemes, are all

examples of linear combination indices of 2 or more spectral bands that have been applied to Landsat imagery and coarse resolution Moderate Resolution Imaging Spectroradiometer (MODIS) (Justice et al. 1998; Crist and Cicone 1984; Lobser and Cohen 2007). These indices have the added advantage of generating multiple measures of subpixel components, including vegetation, soil, shade, and other scene elements (Souza et al. 2003). The shade fractional component in SMA provides a useful measure of canopy shadowing that has been used to diagnose tropical forest structural properties (Anderson et al. 2011).

Linear combination spectral indices form parallel isolines of constant slope and increasing NIR intercepts, in Red-NIR space, significantly departing from how ratio-based and normalized difference VIs characterize vegetation spectral variations in time and space (Fig. 1.3a). Soil and vegetation are modeled as non-interacting horizontal, or checkerboard, fractions within a pixel, and the vegetation fraction is retrieved using linear mixing theory. The shade fraction in SMA is sometimes used to account for non-linear mixing of soil and vegetation components as expressed by canopy shading from vertical tree and shrub canopy structures.

In the case of optimized indices, simplified radiative transfer theory on soil-vegetation interactions is utilized. This involves formulating a VI equation so that the VI isolines line up with the vegetation biophysical isolines (Figs. 1.3, 1.4). The enhanced vegetation index (EVI) gains its heritage from the soil-adjusted vegetation index (SAVI) and the atmosphere resistance vegetation index (ARVI, Kaufman and Tanre 1992), and is an optimized combination of blue, red and NIR bands, designed to extract canopy greenness, independent of the underlying soil background and atmospheric aerosol variations,

$$\mathrm{SAVI} = (1+\mathrm{L})\,(\rho_{\mathrm{NIR}}-\rho_{\mathrm{Red}})\,/\,(\mathrm{L} + \rho_{\mathrm{NIR}} + \rho_{\mathrm{Red}}) \tag{1.7}$$

$$\mathrm{EVI} = 2.5(\rho_{\mathrm{NIR}}-\rho_{\mathrm{Red}})\,/\,(\mathrm{L} + \rho_{\mathrm{NIR}} + \mathrm{C}_1\rho_{\mathrm{Red}} - \mathrm{C}_2\rho_{\mathrm{Blue}}), \tag{1.8}$$

where ρ are reflectances in the NIR, Red, and Blue bands, respectively; L is the canopy background adjustment factor; and C_1 and C_2 are the aerosol resistance

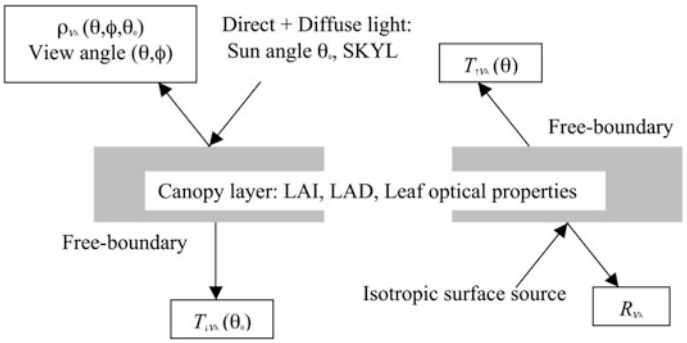

Fig. 1.4 Illustration of first order two layer canopy model of canopy layer and background used in theoretical studies of isoline patterns and interactions with atmosphere, sensor-canopy-sun geometry, and in formulating optimized vegetation indices. © [2000] Adapted and reprinted with permission from Yoshioka et al. (2000)

weights. The coefficients of the EVI equation for Landsat Enhanced Thematic Mapper (ETM+) and MODIS bands are $L = 1$; $C_1 = 6$ and $C_2 = 7.5$ (Huete et al. 2002). A greater weighing of the NIR band extends greenness sensitivity in high biomass areas, while the Blue reflectance term stabilizes aerosol influences and mis-corrections of Red reflectance retrievals, as originally developed in ARVI.

The NIR and Red reflectances for a constant canopy (e.g. any fixed LAI and structural arrangement) with variable underlying backgrounds is represented with a line connecting the various background-dependent spectra, with a slope and Y-intercept specific to that value of LAI (Baret and Guyot 1991; Huete 1988). This line of constant vegetation is known as a 'biophysical isoline', and includes the information needed to minimize or remove the background influences from vegetation indices. We can distinguish between biophysical isolines and VI isolines with a SAIL radiative transfer model simulation of NDVI isolines (Fig. 1.3b). The discrepancies between the two types of isolines are related to optical influences other than the vegetation layer, and provide methods for improving or designing optimal VIs so as to align the VI isolines with the biophysical isolines.

Canopy background signals are inherent to most canopies, and are non-linearly coupled to the vegetation signal to various extents dependent on the structural arrangement of the vegetation in a canopy. Red and NIR transmittance (extinction) through a photosynthetically-active canopy differs significantly with much higher optical thickness in the Red, due to the highly absorptive properties of leaf pigments, and relatively low NIR optical extinction due to the highly scattered (transmitted and reflected) signal (Fig. 1.4).

A primary difference among ratio-based, linear combination, and optimized indices is in the 'L' parameter, which optimizes the measure of greenness through a simple, first-order application of Beer-Lambert's law to describe differential red and NIR extinction through vegetation canopies,

$$\rho_c = \rho_v + t_c^2 \rho_s \tag{1.9}$$

where canopy reflectance, ρ_c, is the sum of the vegetation layer reflectance, ρ_v, and the two-way canopy transmitted- soil reflected signal, $t_c^2\ \rho_s$. When 'L' is optimized correctly, the VI signal becomes blind to soil background variations as the relative optical depths of the two bands are more closely adjusted to only see the greenness of the canopy. The NDVI represents the special case of $L = 0$, in contrast to $L = 1$ in the EVI. Larger values of L ($L > 10$), on the other hand, approximate the linear combination and SMA derived indices.

The use of multiple VIs offers a more complete characterization of canopy properties. The PVI, EVI and TC greenness are more spectrally sensitive to the NIR and will contain information from multiple canopy leaf layers, due to the higher canopy optical penetration depths. In contrast, the NDVI is most sensitive to the canopy-absorbing Red band and will sense primarily the uppermost leaf layers. As a result, the first set of indices presents higher canopy penetration, allowing extended sensitivity over higher LAI/biomass areas where the NDVI saturates (Fensholt et al. 2004; Huete et al. 2006).

1.3 Development of Satellite VI Products

A primary aim of a satellite VI product is to produce cloud-free, atmosphere-corrected, and globally consistent VI values. A sequence of data processing steps is generally made to achieve retrievals of higher quality satellite VI values. The at-satellite radiances are normalized by top-of-atmosphere solar irradiances to calculate 'apparent reflectances'. The derived 'apparent VI' values will contain both surface and atmosphere signals that confuse the interpretation of spatial and temporal VI variations, since atmosphere scattering and absorption processes alter the Red and NIR spectral contrasts of vegetated surfaces, thereby contaminating the VI values. Atmosphere corrections are utilized to minimize this contamination and produce top-of-canopy VI values that are more consistent with field-based and tower-sensor VI measurements.

The VIs will remain particularly sensitive to any disproportionate atmospheric correction of the Red and NIR bands. The inclusion of the Blue band in the EVI was found to stabilize atmospheric aerosol effects in Northern Asia (Xiao et al. 2003) and in the Amazon during the biomass burning season (Miura et al. 2001).

There may also be sun-target-sensor geometry effects, described by the bidirectional reflectance distribution function (BRDF), that alter the effective proportion of sunlit and shaded vegetation viewed by a sensor (Fig. 1.5). These

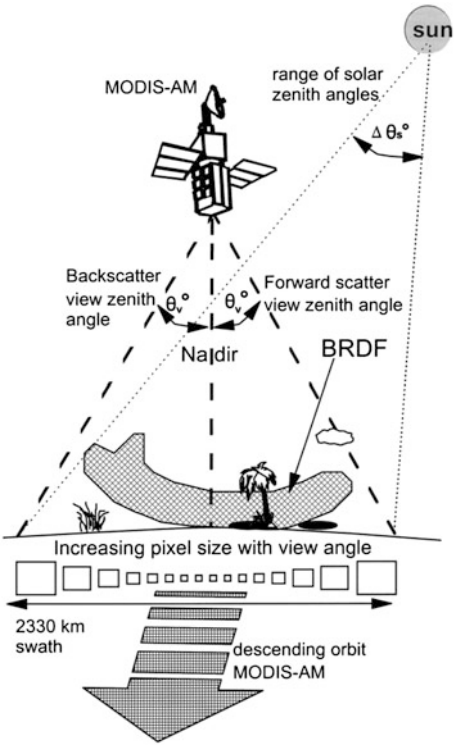

Fig. 1.5 Illustration of bidirectional reflectance distribution function (*BRDF*) satellite observations with sensor view angle and solar zenith angles. Note the canopy shadow effect, clouds, and cloud shadow, and in the case of sensor cross-track scanning pixel size shifts. Adapted from van Leeuwen et al. (1999), Copyright (1999), reprinted with permission from Elsevier

anisotropic influences can dramatically alter the spectral contrast between Red and NIR reflectances and result in angular biases (Cihlar et al. 1997; Schaaf et al. 2002). BRDF effects become more pronounced when atmosphere corrections are applied to satellite VI data sets (van Leeuwen et al. 1999).

Fensholt et al. (2006) studied the dependence of NDVI on solar and viewing geometries with MODIS and the Meteosat Second Generation (MSG) Spinning Enhanced Visible and Infrared Imager (SEVIRI) sensor, and found higher Red reflectances relative to NIR under backscatter conditions resulting in a decrease of NDVI, while in the forward scatter direction, Red reflectances were more strongly reduced due to shadowing relative to the scattered NIR, resulting in higher NDVI. The EVI responds in an opposite manner, and has a positive bias in the more sunlit, backscatter canopy view orientation due to the much stronger NIR signal (Fig. 1.5).

1.3.1 Compositing Approaches

Coarse resolution sensors with wide swath and near-daily imaging are important in obtaining sufficient acquisitions of cloud-free data necessary to improve temporal and spatial monitoring of surface vegetation dynamics. However, their wide swaths of over 2,000 km result in pronounced BRDF effects associated with sensor-surface-sun observation geometries. The sequential VI imagery is thus composited over set time intervals to reduce cloud and cloud shadow contamination as well as improve the viewing geometry quality of selected pixels in the final product.

Standard compositing methods used in coarse resolution satellite data are based on the maximum value composite (MVC) concept developed for the Advanced Very High Resolution Radiometer (AVHRR) NDVI time series data (Holben 1986). The MVC method selects the highest NDVI value over a compositing cycle to best represent the greenness status of an area for that period. In the early AVHRR era, this was applied to non-atmosphere and non-BRDF corrected satellite data and accurately presumed that the highest NDVI would occur on the day with least cloud and aerosol contamination and smallest atmosphere optical path length (i.e., the most nadir viewing geometry).

However, recent advancements in atmospheric correction have rendered the MVC approach less useful as surface anisotropy influences are more prominently revealed in the data. The MVC approach confuses higher VI values associated with lower residual cloud/aerosol contamination from high VI values caused by off-nadir viewing angles, i.e., the highest NDVI value within a compositing period does not necessarily correspond to near-nadir sensor viewing angles or to the least contaminated measurement (van Leeuwen et al. 1999). Lastly, higher VIs may also result from over-correction of atmosphere contamination, resulting in a negative bias in Red reflectances and positive bias in NDVI.

A constrained view angle MVC (CV-MVC) has been adopted for use with MODIS VI products (Huete et al. 2011). This method attempts to restrict pixel selections to within ±30° by choosing the closest to nadir view pixel from a set of 2 or 3 highest NDVI values in the compositing period. Additionally, a per-pixel QA-based methodology is used to filter out known problematic and noisy pixels contaminated by residual clouds, shadow, high aerosol loadings, and large viewing geometries. The CV-MVC method is then applied to the remaining higher quality pixels. The selected VI value represents an actual observation (not modeled) for the local solar zenith angle and close to nadir view geometry, and retain full traceability to the sensor acquisition. Thus, they are not BRDF-corrected, but rather minimized for BRDF influences. In a compositing study of MODIS and AVHRR daily data for mapping burned area over the Iberian Peninsula, Chuvieco et al. (2005) found this VI compositing procedure provided close to nadir observation angles and good spatial coherency, while the traditional MVC compositing criterion of maximizing NDVI values provided poor results. An example of daily to 16-day composite image generation for the Amazon is illustrated in Fig. 1.6.

In general, satellite products now provide per-pixel observation geometry information, including sensor zenith view angle, solar zenith angle, and relative azimuth observation geometry, and the selected day of year (DOY). Thus, added

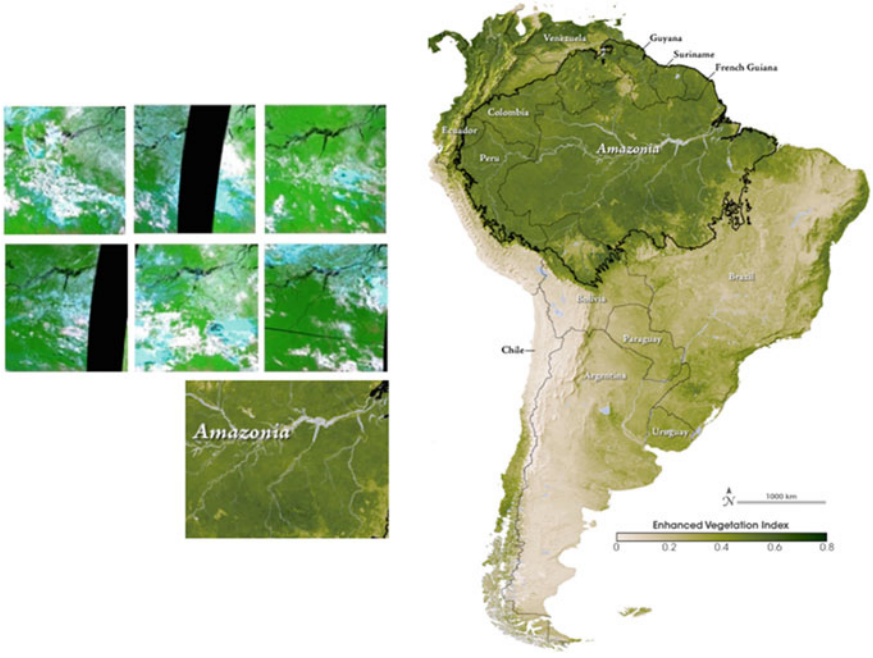

Fig. 1.6 Example of a 16-day composited product derived from single daily MODIS images over an Amazon tile (*left*) to all of South America (*right*). The composited product aims to remove clouds and select best quality with minimal aerosol contamination and near nadir sensor viewing conditions. Courtesy of Robert Simmons, NASA

value BRDF applications may be employed to further reduce angular variations. This has been accomplished in the Nadir BRDF-Adjusted Reflectance (NBAR) MODIS product, which generates nadir reflectances through BRDF model inversions applied to seven or more good quality, cloud-free acquisitions within a composite cycle. The MODIS VI and NBAR products are produced at local solar zenith and local solar noon angle, respectively, and thus still contain latitudinal and seasonal sun angle influences. Although a sun angle seasonal bias may be present, it is less of a problem in inter-annual time series data and trend analyses, providing there is no sensor orbital drift. Los (1993) documented AVHRR orbital drift issues in the NDVI time series (Pathfinder AVHRR Land) and adjusted the data to a standard illumination and viewing geometry by applying MODIS derived kernels, resulting in a 50–85 % reduction of BRDF effects.

1.4 Validation

As one of the most widely used satellite data products by the research and applications user community, the validation of VIs is essential to assess their quality, accuracy, and reliability. Previous validation efforts have involved finer resolution airborne and satellite imagery, field radiometer measurements, biophysical field sampling, and automated ground observation networks (Privette et al. 2000), with the objective of validating VIs through independent radiometric and biophysical measures.

Radiometrically, VIs are considered validated by independent, top-of-canopy reflectance measurements as uncertainties in VI measures of greenness are solely attributed to atmosphere correction accuracies and BRDF influences. VIs are readily computed with in situ spectroradiometers, tower-mounted sensors, and airborne instruments. Calibrated and traceable "transfer radiometers" mounted on light aircraft and unmanned airborne vehicles (UAVs) can be flown at altitudes of 150–300 m above ground level (AGL) and acquire top-of-canopy reflectances with nadir looks and prescribed sun angles for independent characterization of VIs. This extends locally-constrained, sub-canopy scale field radiometric measurements to kilometer length scales enabling sampling of site heterogeneity. Airborne sensors can also be flown at higher altitudes (1–20 km AGL) for scaling and larger area analyses encompassing a range of terrestrial biome types. The MODLAND Quick Airborne Looks (MQUALS) is an example of light aircraft sensor and spectral-digital camera deployment flown at the Jornada Experimental Range for ground truth characterization of surface conditions and sampling of landscape variability (Huete et al. 1999).

The quality of satellite-based VI retrievals vary in space and time due to geographic and seasonal variations in cloud persistence, unresolved clouds, aerosols, quality of atmosphere correction, view-sun angle geometries, topography, and sensor performance (Wolfe et al. 1998; Miura et al. 2000; Samanta et al. 2010; Kobayashi and Dye 2005). Cloud and aerosol residual effects and artifacts

will invariably persist at subpixel scales in satellite imagery, given the coarse nature of cloud detection algorithms and aerosol optical depth determinations. High aerosol pixels will generally not be corrected to the same accuracy as low aerosol pixels, and often there will be under- or over-estimations (and corrections) for aerosols. Kaufman et al. (2005) noted difficulties in aerosol correction attributed to residual cirrus as well as defining cloud contamination versus aerosol growth. Accuracy and precision values for the MODIS VIs are generally within 0.02–0.05 VI values (http://landval.gsfc.nasa.gov/ProductStatus.php?ProductID=MOD13, accessed November 2013).

1.4.1 Ground Observation Networks

In-situ observation networks are evolving into highly calibrated and traceable sensor systems that offer great potential in providing in situ temporally continuous data to complement field and airborne validation data acquired as 'spatial' snapshots in time. These networks can provide higher quality (finer spatial and temporal resolution) measurements than the satellite, and can facilitate various methods of quality, uncertainty, and cross-sensor continuity assessments involving multiple satellites. They include the AERONET-based Surface Reflectance Validation Network (ASRVN), the baseline surface radiation network (BSRN), various phenology networks, and FLUXNET. These provide in situ measurements of surface and atmosphere conditions that enable independent assessments of vegetation canopy states and phenophases.

The ASRVN collects operational satellite data from over 100 AERONET sites, equipped with automated sun photometers that provide atmospheric properties to enable an independent rigorous atmospheric correction of satellite measurements and allow computed VIs to be compared against their equivalent satellite products (Wang et al. 2009; Holben et al. 1998). Compared to ground-based, aircraft, and finer resolution satellite measurements, this approach has the advantage of identical spectral, spatial, and observation geometry sampling consistent with the satellite measurement. The sun-photometer based atmosphere correction is applicable to relatively large areas around an AERONET site for more rigorous spatial analysis. Further, ASRVN also outputs top-of-canopy bidirectional reflectances that provide realistic assessments of accuracies and uncertainties in VIs due to variability in atmosphere and sensor observation view angles.

In Fig. 1.7a, in situ VI measures from ASRVN results are compared with simultaneous day MODIS VI values, while in Fig. 1.7b, the nadir view angle ASRVN in situ results are compared with the MODIS 16-day composited VI product that attempts to retrieve near-nadir values, hence such a comparison allows one to ascertain the accuracy and uncertainty of such retrievals. These comparisons are applicable to all compositing schemes, including the assessment of NBAR nadir-view retrievals. The ASRVN data is not completely independent, however, in that the same sensor is used to generate both the VI product and the

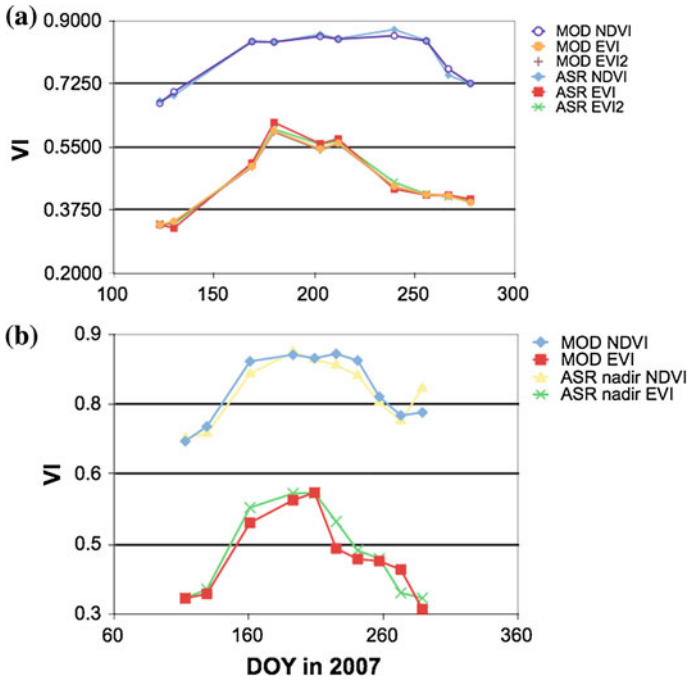

Fig. 1.7 **a** Relationship between MODIS VIs (NDVI, EVI, and two-band EVI, EVI2 (Jiang et al. 2008)) and ASRVN derived VIs for clear day observations, and **b** comparisons of nadir-derived ASRVN VIs with standard MODIS VI composite values. This analysis was conducted over the Howland Temperate Conifer Forest Aeronet and Fluxnet site for year 2007

in situ VI version of that product (i.e., it is only the atmosphere correction that is independently accomplished). Thus, sensor degradation artifacts, drifts in calibration, cross-band (Red, NIR, Blue) loss in spectral integrity and geolocation error would be present in both data sets and not be readily detected.

Many towers are now instrumented with shortwave and longwave radiation sensors that enable computation of broadband versions of the NDVI. The Baseline Surface Radiation Network (BSRN), for example, enables the measurement of visible (Q_{par}) and shortwave solar radiation (R_g) with quantum sensors and pyranometers, respectively, that can be used to represent contributions from reflected NIR and visible radiation (Wilson and Meyers 2007) as,

$$NDVI_{tower} = \left[\left(R_g - Q_{par} \right) \big|_{NIR} - Q_{par} \big|_{VIS} \right] / \left[\left(R_g - Q_{par} \right) \big|_{NIR} + Q_{par} \big|_{VIS} \right] \tag{1.10}$$

which simplifies to

$$NDVI_{tower} = 1 - 2^{*} \, Q_{par} / R_g \tag{1.11}$$

The BSRN network is primarily used to validate the theoretical computations of radiative fluxes by models, and has been endorsed by the World Climate Research Programme (WCRP) as the global surface radiation network for the Global Climate Observing System (GCOS). Wilson and Meyers (2007) demonstrated how well these tower sensors could trace MODIS NDVI across numerous tower sites as independent verifications of NDVI data over smaller, but homogeneous footprint areas (Fig. 1.8). Figure 1.8, however, shows the tower-based broadband NDVI to be somewhat poor in the Pine Needle Forest, temperate grasses, and deciduous forests. Wang et al. (2004) used the tower-based broadband NDVI calculated from observed upward and downward PAR and global radiation measurements and found the broadband NDVI to be a good index to describe physiological activity of a pine forest during certain periods, and a means for obtaining other physiological parameters that are required by ecosystem models.

Increasingly, automated sensors are being mounted on towers for canopy spectra measurements. Light-emitting diode (LED) sensors are now readily mounted at tower sites to collect continuous diurnal and seasonal time series data (e.g. Soudani et al. 2012; Ryu et al. 2010) (Fig. 1.9). Richardson et al. (2007)

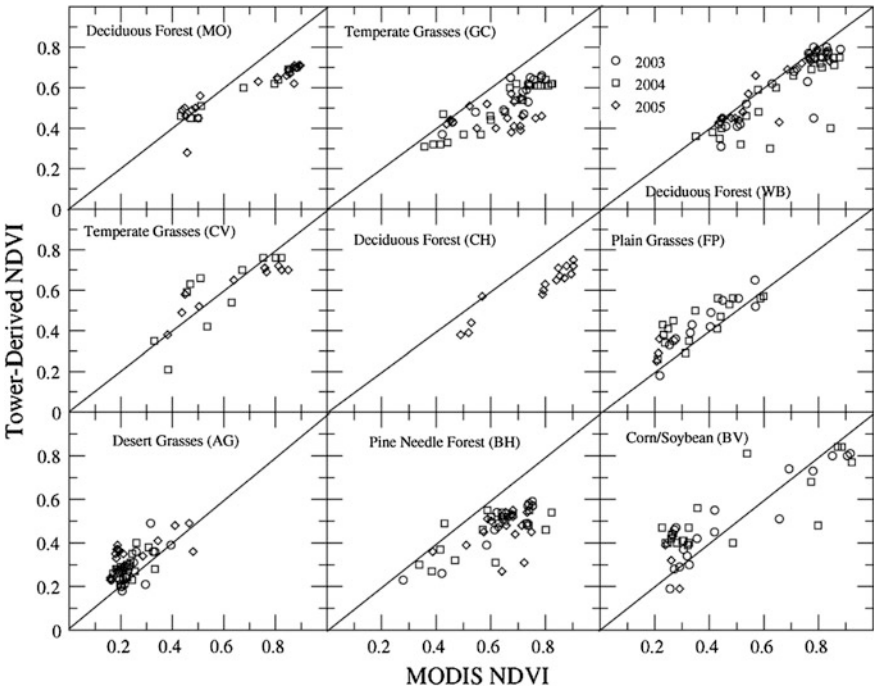

Fig. 1.8 Relationship between MODIS NDVI and tower derived broadband NDVI using PAR and shortwave radiation sensors for 9 GEWEX sites in North America during 2003–2005. Adapted from Wilson and Meyers (2007). Copyright (2007) Reprinted with permission form Elsevier

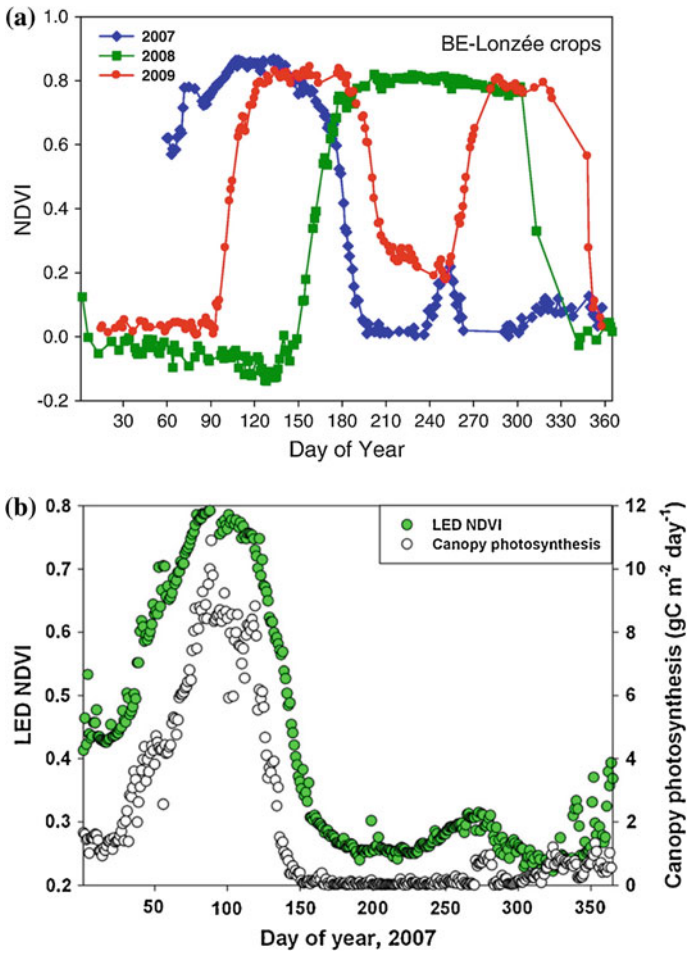

Fig. 1.9 In-situ automated sensors provide continuous spectral measures of vegetation indices for diurnal, seasonal, and interannual comparisons with satellite data. **a** Example of in situ NDVI time series over varying crops (wheat, sugar beet, and mustard) in Belgium (adapted from Soudani et al. 2012) and **b** comparisons of daily canopy photosynthesis from eddy flux tower and midday LEDs derived NDVI over a California annual grassland site (Adapted from Ryu et al. 2010. Copyright (2010) Reprinted with permission from Elsevier)

demonstrated the use of digital webcam, RGB imagery and ratios of green and red components for detection of forest phenology. An automated tower-based, multi-angular spectroradiometer platform (AMSPEC) provides continuous spectral measures of a canopy through a range of viewing angles over all azimuthal directions (Hilker et al. 2011).

The global network known as FLUXNET coordinates observations from a multitude of micrometeorological tower sites (Running et al. 1999). The tower sites use eddy covariance methods for continuous measurements of carbon, water,

and energy exchanges between ecosystems and atmosphere. This provides valuable opportunities for evaluation of satellite VI measures of vegetation growth, phenology, and seasonal dynamics. Monteith and Unsworth (1990) noted that VIs can legitimately be used to estimate the rate of processes that depend on absorbed light, such as gross primary production (GPP, photosynthesis) and transpiration.

Several studies have shown potential satellite data validation opportunities via FLUXNET, e.g., strong, multiple-biome satellite EVI relationships have been reported with tower GPP flux measurements across AmeriFlux tower sites and tropical forests in the Amazon and Southeast Asia with MODIS and SPOT-VGT satellite data (Rahman et al. 2005; Sims et al. 2006; Xiao et al. 2004, 2005; Huete et al. 2006, 2008) (Fig. 1.10).

1.4.2 Biophysical Validation

Field-based vegetation sampling is fundamental for validating and assessing VI performance in depicting vegetation dynamics and biophysical phenomena. A good correspondence between VIs and field measurements lends confidence in their use as biophysical surrogates for variables that are otherwise difficult to sample in the field. VI relationships with biophysical properties are mostly derived from empirical field measurements and canopy radiative transfer models, where numerous and often ambiguous relationships have been reported (Sellers 1985). Hence, although VIs have been validated within numerous environments, the resulting biophysical relationships tend to be local-based and with limited spatial extent that rarely extend to landscape-relevant temporal and spatial scales.

The biophysical validation of VIs is complicated by a lack of consensus on what VIs explicitly measure about a canopy and how to interpret a VI value. VIs respond to upper sunlit leaves to a greater extent than lower leaves, resulting in strongly non-linear relationships with field-derived LAI values. NDVI sensitivity to LAI variations is generally restricted to values below 2 or 3 with differing correlations between broadleaf vs needle-leaf canopy stands (Fassnacht et al. 1997; Chen et al. 2005). NDVI-LAI relationships may further vary across different canopy phenophases, as was found in a beech deciduous forest in Europe (Wang et al. 2005) (Fig. 1.11).

Linear combination and optimized indices provide extended LAI sensitivity and are less prone to saturate in high-biomass areas (Fensholt et al. 2004). Houborg and Soegaard (2004) found EVI from MODIS to accurately describe the variations in green LAI up to 5 in agriculture areas in Denmark ($r^2 = 0.91$). However, in comparison with relationships reported using fine resolution Landsat satellite data, poorer relationships are commonly found when using coarser resolution VIs, such as MODIS and SPOT-VEGETATION (VGT). In a multi-biome validation field campaign known as Bigfoot, Cohen et al. (2003) found only weak correlations between field measured LAI and several MODIS products, including LAI and VIs.

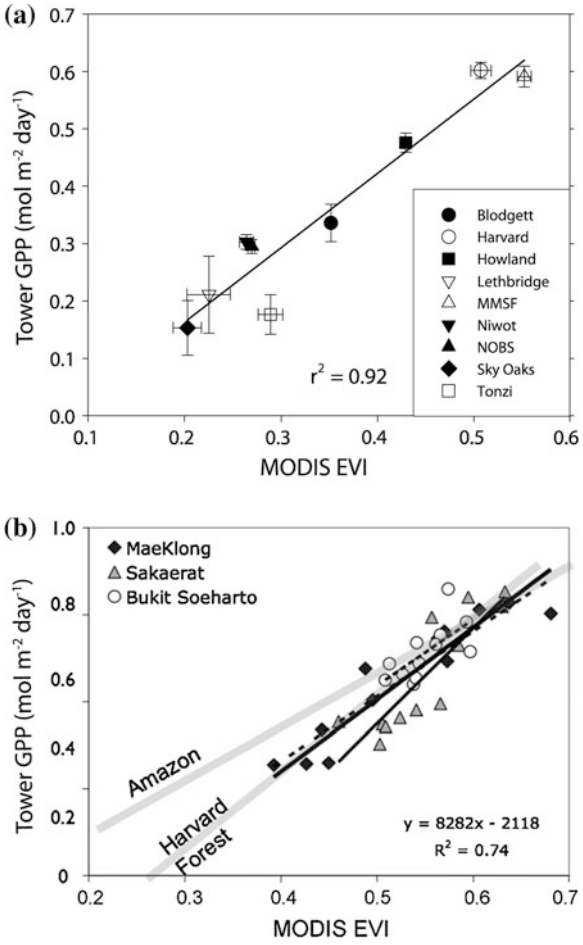

Fig. 1.10 Relationships of tower-derived flux measurements of gross primary productivity (*GPP*) and MODIS EVI for (**a**) annual averages for a range of North America temperate ecosystems (forest, savanna, grassland), and (**b**) monthly averages for tropical forests in SE Asia (dry and humid tropical broadleaf forests) and the Amazon (humid tropical evergreen broadleaf forest). Adapted from (**a**) Sims et al. (2006), Copyright (2006), Reprinted with permission from John Wiley and Sons and (**b**) Huete et al. (2008), Copyright (2008), Reprinted with permission from Elsevier

Several field studies have shown NDVI more strongly and linearly related with the fraction of absorbed PAR, f_{APAR}, over a range of land cover types (Huemmrich et al. 2005). Fensholt et al. (2004) found a strong linear relationship between in situ f_{APAR} and NDVI across three different vegetation types, suggesting that covariance between f_{APAR} and NDVI is insensitive to variations in leaf angle distribution (LAD) and vegetation heterogeneity. However, the type of soil background and PAR absorption by non-photosynthetic vegetation (NPV) can alter

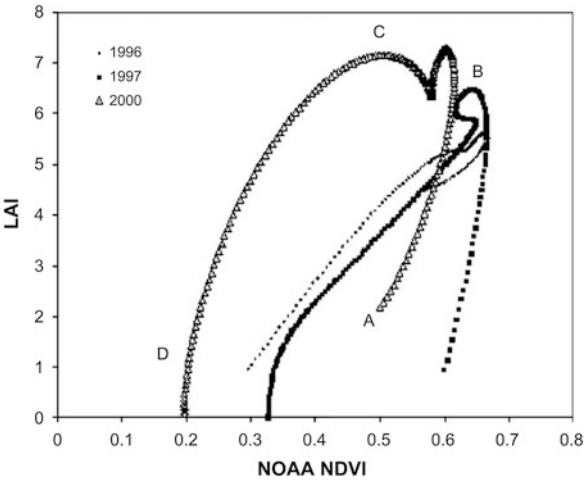

Fig. 1.11 Local-based biophysical relationships between in situ LAI with NOAA-AVHRR NDVI in the Hesse Beech Forest highlighting strong phenological dependencies with unique green-up and dry-down relationships. Adapted from Wang et al. (2005), Copyright (2005), reprinted with permission from Elsevier

the NDVI- f_{APAR} relationship and affect its linearity with important consequences to scaling (Jiang et al. 2006b). The f_{APAR} measured in a Kalahari woodland field campaign also varied distinctly with NDVI during phenologic green-up and dry-down periods (Huemmrich et al. 2005). In an attempt to encompass cross-biome variations, Sims et al. (2006) empirically derived a global-based, linear f_{APAR}–NDVI relationship as,

$$f_{APAR} = 1.24 \times \text{NDVI} - 0.168 \tag{1.12}$$

The SAVI and EVI have also been found useful in estimating f_{APAR} in vegetated canopies, with relationships that are largely independent of soil background and NPV (Gao et al. 2000; Xiao et al. 2004). Lastly, Zhang et al. (2005) combined MODIS data with a radiative transfer model to separate f_{APAR} into chlorophyll-, leaf-, and canopy-absorbed components. They showed large differences in the f_{APAR} absorbed by chlorophyll versus that absorbed by the canopy and noted that only chlorophyll-absorbed f_{APAR} is used in photosynthesis. They found NDVI to be correlated with total canopy f_{APAR}, while EVI was better correlated with the chlorophyll f_{APAR}, presumably more closely related to the green f_{APAR}.

Gitelson et al. (2003) have conducted extensive field measurements relating canopy chlorophyll content with satellite vegetation indices, including chlorophyll spectral measures. The MERIS instrument onboard ENVISAT has a Total Chlorophyll Index (MTCI) product derived from inverse canopy reflectance modeling, in which maps of canopy chlorophyll content (CCC) and leaf area index (LAI) are derived simultaneously. The MTCI product is output at 300 m spatial resolution and validated with indirect field measurements (Vuolo et al. 2012).

VIs have also been successfully related with the fraction of vegetation cover in Landsat data, but with strong relationship dependencies associated with extent of tree clumping, LAI, and tree species (Smith et al. 2009; Carlson and Ripley 1997). There also remains a phenologic dependence similar to that with f_{APAR}.

The validation of VIs with specific in situ biophysical quantities across a vegetation, phenologic growing season is made more complicated by the large number of co-varying canopy properties that make it difficult to explicitly quantify one variable from the others without constructing generalizations and assumptions about the canopy. Phenologic canopy development often involve simultaneous changes in LAI, specific leaf area, chlorophyll content, fractional cover, leaf angle, leaf phenology, litterfall, and canopy shadows (Hilker et al. 2008). Each of these variables result in unique spectral variations and the retrieval of specific biophysical details from the integrative 'greenness' signal would require the use of radiative transfer (RT) models, productivity models, or for local site conditions, empirical models.

1.5 Findings

Vegetation indices have been remarkably successful in providing coherent data sets with large spatial coverage for mapping and characterization of landscape vegetation dynamics. Satellite VI products are seamlessly computed across all pixels and at high temporal frequencies. A wide range of the earth science, modeling, and applications user group community are using VI time-series data in natural resource management, agriculture, public health, and hydrology and biogeochemical models. In this section we highlight some recent examples of important findings involving the use of vegetation indices within the earth science research and applications communities.

1.5.1 Phenology Studies

High temporal frequency vegetation index time series data from coarse resolution sensors, including MODIS, AVHRR, SPOT-VGT, MERIS are now widely used to trace and characterize land surface seasonal dynamics and phenology with quantifiable metrics, such as the onset date of greening, peak greenness date, browning, and growing season length, all critical to understanding ecosystem functioning (Fig. 1.12) (Zhang et al. 2006; Reed et al. 2003). Phenology is the study of recurring biological events, such as the timing of leaf emergence and development, senescence, and litterfall (Schwartz and Hanes 2010). It is an important integrative science for quantifying vegetation responses and feedbacks to climate variability (Penuelas et al. 2009).

Using AVHRR-NDVI time series data, Myneni et al. (1997) showed evidence of a lengthening of the plant growing season at northern latitudes in response to global temperature increases. Vegetation phenologies in high latitude environments are difficult to interpret due to the short growing seasons, long periods of darkness, and persistent snow cover in winter. More recently, Beck et al. (2006) were able to estimate biophysical parameters related to the timing of spring and

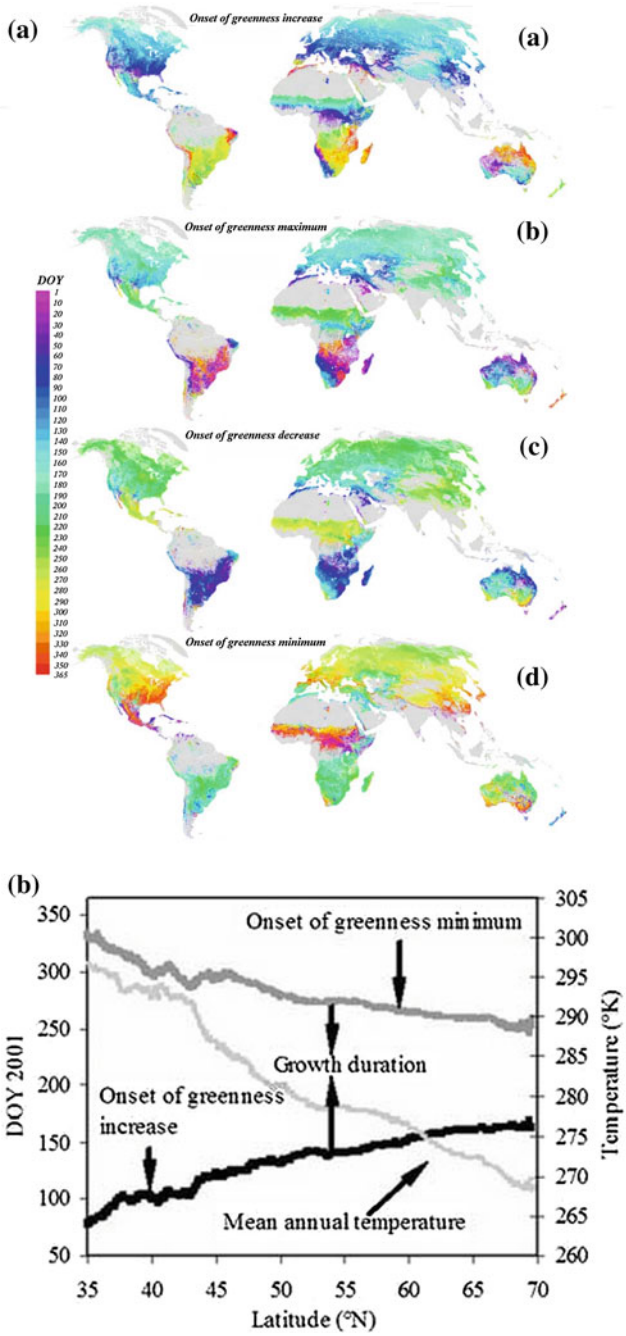

Fig. 1.12 **a** Global maps of phenological transition dates from MODIS phenology product (MODQ12) using NBAR-EVI, and **b** zonal averages (0.1°) for phenological transition dates and MODIS land surface temperature in Europe/Asia. Adapted from Zhang et al. (2006), Copyright (2006). Reprinted with permission from John Wiley and Sons

autumn phenology events in northern Scandinavia by applying double logistic functions (Fischer 1994) to MODIS NDVI time series data.

MODIS VIs have been used to characterize the phenology patterns of varying physiognomic vegetation classes in the Brazilian cerrado biome (Ratana et al. 2005). Kawamura et al. (2005) monitored short-term phenological changes in rangeland forage conditions with EVI in the semi-arid Xilingol steppe in Inner Mongolia. They were able to estimate forage quantity and derive seasonal changes in live biomass and standing crude protein amounts over areas with different grazing intensities, useful in providing timing information for hay cutting based on nutritive value to range managers. NDVI data from the MODIS sensor has provided timely monitoring of locust outbreaks in East China based on its accurate assessments of vegetation conditions (Zha et al. 2005). Xiao et al. (2006) developed a MODIS-based VI phenology algorithm using NDVI, EVI, and LSWI for mapping paddy rice distributions in support of irrigation, food security, trace gas emission estimates, and risk assessment of avian flu over South and Southeast Asia.

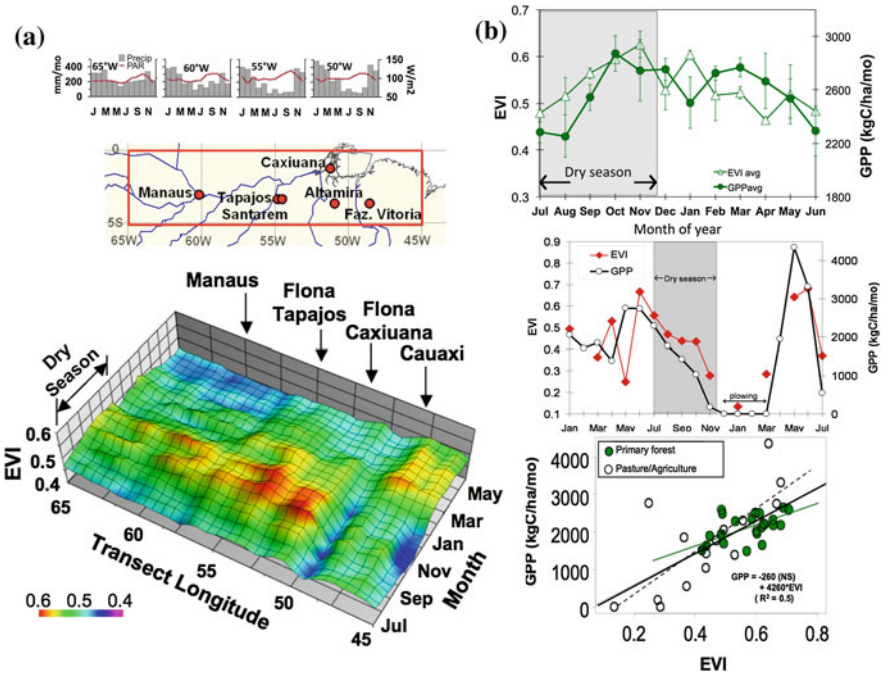

Fig. 1.13 **a** Three-dimensional phenological transition dates of MODIS EVI along an east to west transect in which seasonally dry rainforest grades to a perhumid rainforest. The eastern portion is an area of forest clearing and disturbance; and **b** tower flux measurements of gross primary productivity (*GPP*) compared with MODIS EVI at the seasonally dry Tapajos forest site and adjacent forest disturbance area. Adapted from Huete et al. (2006), Copyright (2006). Reprinted with permission from John Wiley and Sons

The extended sensitivity of the EVI has facilitated phenology studies in dense tropical rainforests, where MODIS and SPOT-VGT EVI were shown to discriminate phenology cycles in Amazon rainforests (Huete et al. 2006; Xiao et al. 2005, 2006) (Fig. 1.13a). Using 250 m and 0.05°EVI data from MODIS, Huete et al. (2006) found Amazon rainforests to green-up by 25 % in the dry season in response to the increased availability of sunlight. Disturbed forest areas, on the other hand, showed dry-season declines in EVI, presumably because the more shallow-rooted vegetation had reduced access to deep soil water. This was verified by a strong linear and consistent relationship between seasonal EVI and tower-calibrated GPP measurements of carbon fluxes in both intact rainforest and forest conversion to pasture/agriculture sites in the Amazon (Fig. 1.13b).

Saleska et al. (2007) later analyzed Amazon rainforest EVI response to drought and found a positive greening response to a short drought event in 2005, rather than the expected negative response. Samanta et al. (2010) reported a much smaller spatial extent in greening after more rigorous screening of contaminated pixels, however, the proportion of acceptable quality pixels that showed greening remained the same, and there was little drought-induced browning observed. Other studies have confirmed the positive greening response to the 2005 drought, while reporting a definitive negative response to a more severe drought in 2010 that clearly suppressed photosynthetic activity (Xu et al. 2011; Anderson 2012; Brando et al. 2010).

The MODIS vegetation phenology product (MOD12Q2) uses maximum inflections in seasonal NBAR-EVI profiles to produce a global set of phenology metrics based on key transition dates related to vegetation growth activity (Zhang et al. 2003; Ganguly et al. 2010). The NBAR-EVI has been successfully used to map the phenology of single, double, and triple rice cropping patterns in the Mekong delta where previously this was only accomplished with SAR data (Sakamoto et al. 2006). NBAR-EVI was also used to show the effect of urban climates on vegetation phenology transition dates in North American cities (Zhang et al. 2004). Strong heat island effects were found in urban areas with increases in the growing season of $\sim$15 days and delays in the onset of dormancy, relative to adjacent non-disturbed ecosystems, a pattern that decays exponentially with distance from urban areas.

1.5.2 Carbon and Water Science

Vegetation indices have demonstrated their utility in studies of ecosystem functions which affect net ecosystem exchange of CO_2 and water between the land and the atmosphere. Most carbon exchange models use a light-use efficiency (LUE) relationship in which gross primary productivity (GPP) is related to the amount of PAR absorbed by green vegetation multiplied by the efficiency with which the absorbed light is used in carbon fixation, or photosynthesis (Monteith and Unsworth 1990),

$$\mathrm{GPP} = \mathrm{LUE} \times \ \mathrm{APAR} = \mathrm{LUE} \times f_{\mathrm{APAR}} \times \mathrm{PAR}. \tag{1.13}$$

f_{APAR} is derived through VI relationships and LUE is scaled down with meteorological information available, normally, at much coarser resolution. In the BIOME-BGC (BioGeochemical Cycles) model, biome specific LUE_{max} values are scaled down using meteorological data (Running et al. 2004). Net Primary Productivity (NPP) has been modeled with AVHRR-NDVI inputs to the NASA-CASA (Carnegie Ames Stanford Approach) model, and more recently, Potter et al. (2007) found monthly EVI inputs to the CASA model significantly improved both predicted high- and low-seasonal carbon fluxes, associated with peak growing season uptake rates of CO_2 in irrigated croplands and moist temperate forests.

There is also much interest in estimating GPP solely with remote sensing methods in order to avoid the large uncertainties in LUE estimates based on land cover generalizations and coarse meteorological inputs. In the Vegetation Photosynthesis Model (VPM) LUE_{max} is downscaled using remotely-sensed temperature (T), canopy moisture status (W), and phenology (P) scalars (Xiao et al. 2004),

$$GPP = (LUE_{max} \times T \times W \times P)_{APAR} \times PAR \tag{1.14}$$

in which f_{APAR} is derived from EVI and W is derived from LSWI. VPM has produced tower-calibrated predictions of GPP across a wide series of biomes, including evergreen and deciduous forests, grasslands, and shrub sites in temperate North America and in seasonally moist tropical evergreen forest in the Amazon (Mahadevan et al. 2008; Xiao et al. 2005).

Several studies have shown the EVI to estimate GPP with relatively high accuracy without direct consideration of LUE, thus potentially simplifying carbon balance models over most vegetation types (Rahman et al. 2005; Sims et al. 2006). Strong linear relationships between EVI and tower GPP were shown in North American temperate forests, Southeast Asia tropical dry forests, and Amazon tropical humid forests with the strength of the relationship greater for seasonally contrasting deciduous forests compared with evergreen forests (Xiao et al. 2004; Sims et al. 2006; Huete et al. 2006, 2008) (Figs. 1.11,1.13b). These relationships were independent of the need for climatic drivers and LUE, thus greatly simplifying carbon balance and water flux models.

However there are also studies showing limitations of satellite vegetation products in predicting GPP, including VIs, demonstrating the need to include information on radiation and temperature environmental drivers, including land surface temperature (LST) (Jahan and Gan 2009; Sims et al. 2008; Schubert et al. 2010; Ryu et al. 2011). Li et al. (2008) also demonstrated limitations associated with disparate footprints between satellite and tower flux measurements and the need for Landsat spatial resolutions for flux footprint matching in non-forested canopies.

Ichii et al. (2007) combined EVI from MODIS with the BIOME-BGC (BioGeochemical Cycles) model to constrain spatial variability in rooting depths of forest trees over the Amazon and improve the assessments of carbon, water and energy cycles in tropical forests. They simulated seasonal variations in GPP with different rooting depths from 1 to 10 m and determined which rooting depths best

estimated GPP consistent with satellite-based EVI, and hence were able to map rooting depths at regional scales across the Amazon with satellite data.

Combined remote sensing and in situ tower flux measurements have also yielded close relationships with water fluxes (Glenn et al. 2007, 2011). Guerschman et al. (2009) developed an algorithm for estimating monthly actual evapotranspiration (AET) across varying sites in Australia. They used EVI and GVMI from MODIS data, scaled to Priestley-Taylor potential evapotranspiration. The EVI provided information on LAI while GVMI provided information on surface water, bare soil and vegetation water content. Yang et al. (2006) derived continental-scale estimates of evapotranspiration (ET) by combining MODIS data with eddy covariance flux tower measurements using an inductive machine learning technique called support vector machines (SVM). EVI was found to be the most important explanatory factor in their fairly accurate estimates of ET (root mean square of 0.62 mm d^{-1}). ET measurements at regional scales, from 9 flux towers established in riparian plant communities on the Middle Rio Grande, Upper San Pedro River, and Lower Colorado River were also found to correlate strongly with EVI values and the inclusion of maximum daily air temperatures (T_a) measured at the tower sites further improved this relationship ($r^2 = 0.74$) (Nagler et al. 2005a). Other ET studies at flux tower sites in semiarid riparian and upland grass and shrub plant communities were also found strongly correlated with MODIS EVI ($r = 0.80–0.94$) (Nagler et al. 2005b, 2007).

The AVHRR-NDVI has a long history of vegetation drought and climate variability studies. Anyamba and Tucker (2005) demonstrated the strong correspondence of 20+ year NDVI trends and anomalies with rainfall in the Sahel (Fig. 1.14), and Breshears et al. (2005) showed large scale, drought-induced vegetation mortality over the western U.S. with AVHRR- NDVI satellite data. Many ecologists are concerned of the potential impacts on biodiversity and forest ecosystem services resulting from major shifts in climate and wish to develop predictive relationships between tree species richness and forest productivity under current climate conditions (Turner et al. 2003). Waring et al. (2006) found a good relationship between EVI, as a surrogate of productivity, and tree species richness measured across the forest eco-regions of the conterminous USA (Fig. 1.15). They used phenology metrics of growing season EVI values from MODIS in developing their species diversity relationships and found climate- independent satellite methods to be more useful in assessing tree biodiversity than models requiring climate data owing to the problem in extrapolating such data accurately.

Various studies have found much utility in VI products for landscape disturbance mapping and impacts of invasive species. As an example, Jin and Sader (2005) successfully used MODIS NDVI to detect and quantify forest disturbances in northern Maine. The MODIS-based Global Disturbance Index (MGDI) was designed to provide information on the timing, location, and extent of large scale disturbances on ecosystems, involving fires, hurricanes, pests, and woody plant species mortality (Mildrexler et al. 2009). Large scale disturbance events have major impacts on the global carbon cycle and can result in sudden and large pulses

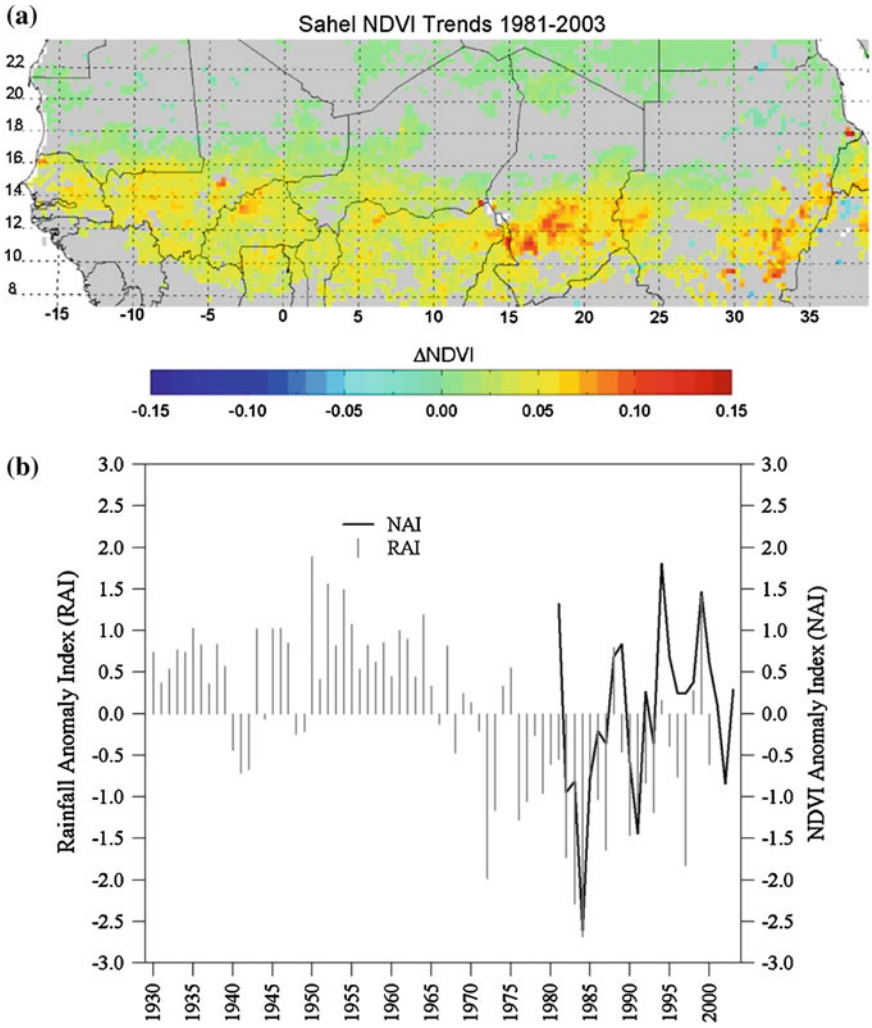

Fig. 1.14 **a** NDVI trends in the Sahel from 1981 to 2003. *Yellow* to *red* colors indicate areas of significant change and *gray* areas show no significant trend, **b** comparisons of Sahel rainfall anomaly index (RAI, 1930–2000) and NDVI anomaly index (NAI, 1981–2003). Adapted from Anyamba and Tucker (2005), Copyright (2008), reprinted with permission from Elsevier

of CO_2 and other trace gases released into the atmosphere. The MGDI combines LST and EVI data from the Aqua-MODIS sensor and detects and maps event-specific disturbances based on anomalous changes in EVI and LST that exceed the normal ranges of natural variability (Fig. 1.16). VI time series data have also been used to predict potential invasive species habitats so that control or preventative measures can be applied before irreversible changes occur. Using MODIS NDVI, Franklin et al. (2006) studied the negative impacts of an invasive African grass

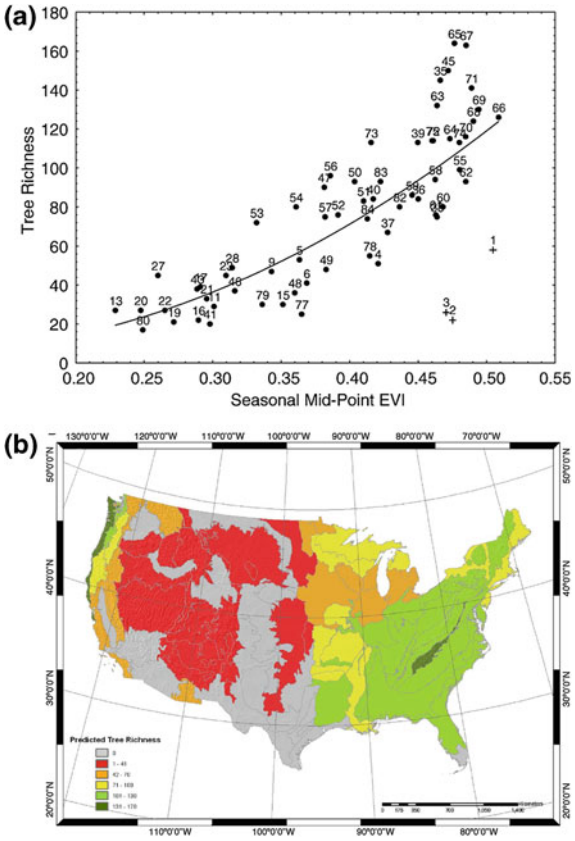

Fig. 1.15 **a** Relationship between tree species richness and seasonal mid-point EVI values derived from MODIS using forest field survey plots; and **b** map of predicted tree richness delineated by ecoregions into five classes derived from mid-season MODIS EVI values. Adapted from Waring et al. (2006), Copyright (2006), reprinted with permission from Elsevier

species, buffelgrass (*Pennisetum ciliare*), on diversity of native rangeland plant communities in Sonora, Mexico.

1.6 Future Directions and Challenges

The remote sensing literature of the past 30 years attests to the enormous utility and applications of VIs for landscape monitoring and vegetation health assessments. Nevertheless, new challenges and demands for robust remote sensing tools exist in order to address upcoming ecological challenges that require more accurate and long term VI data records for climate studies, ecosystem sustainability, and a more explicit understanding of the biophysical information contained in VI measurements. Advancements in hyperspectral and combined optical-thermal indices offer much potential in advancing remote sensing based landscape monitoring and applications.

1.6.1 VI Continuity and Long Term Data Records

The Intergovernmental Panel on Climate Change report (IPCC 2007) emphasized the need to assess climate change impacts on forest resources through repeatable, long term, and accurate satellite measures. VIs derived from the numerous Earth Observing satellites partly fill this critical need by providing frequent temporal satellite measurements that can be used to generate a seamless, long-term data record for global change and climate change studies. Relative to more complex satellite algorithms, VIs are more easily fused across multiple sensor systems facilitating the underlying need to ensure continuity for long term monitoring (Fig. 1.17).

Numerous investigations have empirically evaluated NDVI continuity and consistency across AVHRR sensors (e.g. Los 1993; Roderick et al. 1996) and confirmed the feasibility of NDVI translation across MODIS, SPOT-VGT, Sea-viewing Wide Field-of-view Sensor (SeaWiFS), AVHRR, and the Landsat ETM+ sensors (Fensholt 2004; Gallo et al. 2005; Gitelson and Kaufman 1998; Miura et al. 2006; Trishchenko et al. 2002; Tucker et al. 2005; Yoshioka et al. 2012; van Leeuwen et al. 2006). The Visible Infrared Imaging Radiometer Suite (VIIRS) instrument on the Joint Polar Satellite System (JPSS) program will extend the VI data record of essential measurements begun by the NOAA-AVHRR and

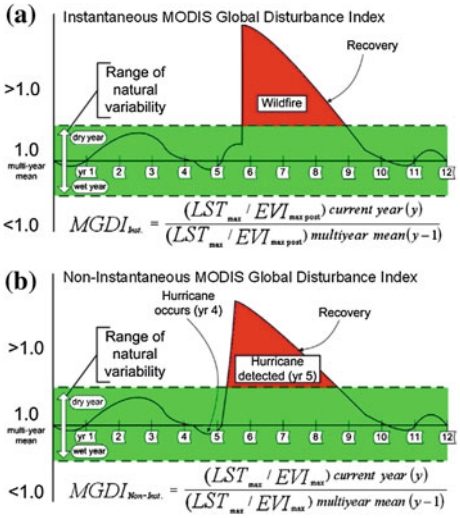

Fig. 1.16 Illustration of the MODIS Global Disturbance Index (*MGDI*) concept for detection and mapping large-scale landscape disturbances. Disturbances will cause departures from normal variations dependent on the type and severity of the event. **a** In the case of wildfire, there are instantaneous changes in MODIS LST and EVI, while in the case of hurricanes (**b**), there is no immediate spike on LST and MGDI values increase the year after the disturbance event. Adapted from Mildrexler et al. (2009), Copyright (2009), reprinted with permission from Elsevier

EOS MODIS. Both the NDVI and EVI have been selected as one of JPSS Environmental Data Records (EDR's). The first VIIRS sensor onboard the current Suomi National Polar-orbiting Partnership (NPP) provides a bridge between EOS-MODIS and the operational JPSS VIIRS planned for launch in 2016 (Fig. 1.17).

Intercalibration across these sensors and more rigorous translation approaches are desired and will be critical to long term VI data continuity in support of climate science. In a study of cross-sensor influences on NDVI-LAI relationships with NOAA-14 AVHRR, SPOT-4 VGT, and Terra MODIS data, Wang et al. (2005) found significant differences in slope, intercept, and strengths of relationships, despite empirical NDVI agreements among the sensors. Yoshioka et al. (2012) developed bottom-to-top approaches in translating the NDVI from one sensor to another using Red and NIR cross-sensor isolines. This theoretical approach provided a better mechanistic understanding and predictive modeling of cross-sensor relationships for the NDVI and input reflectances as well as other VIs, such as EVI. The EVI can be computed from many sensors that carry a blue channel, and SPOT-VGT and Advanced Earth Orbiting Satellite (ADEOS-II) GLI have provided EVI values compatible with Aqua and Terra MODIS EVI (Yamamoto et al. 2005). Fensholt et al. (2006) explored the consistency of EVI values across different sensors and suggested the EVI may be more problematic due to the additional variations associated with the blue band. Jiang et al. (2008) developed a functionally equivalent 2-band version of EVI, or EVI2, for use in sensors without a blue band,

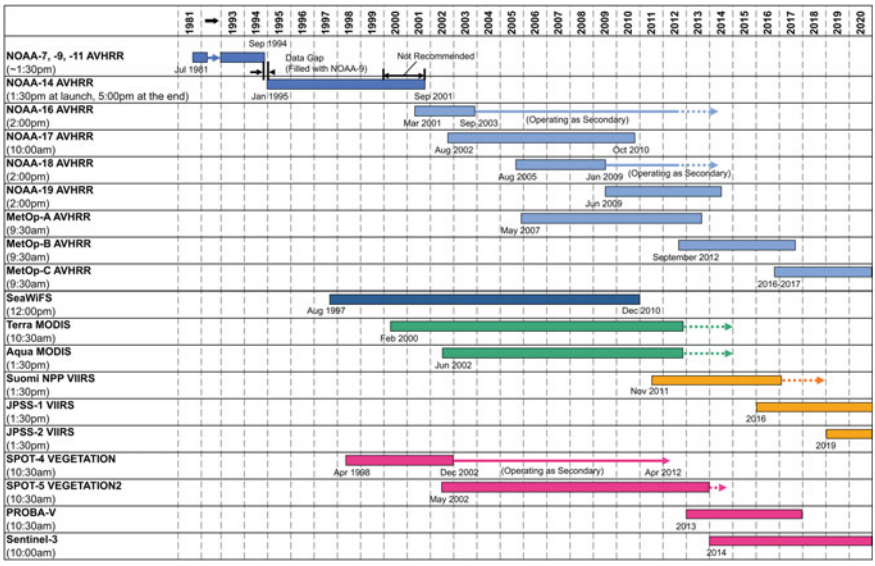

Fig. 1.17 Vegetation index long term time series continuity across the NOAA-AVHRR, EOS-Terra and Aqua MODIS, and VIIRS Suomi National Polar-orbiting Partnership (*NPP*) and JPSS VIIRS, in support of climate studies

$$\text{EVI2} = 2.5(\rho_{NIR} - \rho_{Red}) / (L + \rho_{NIR} + C_1 \times \rho_{Red}) \quad (1.15)$$

where $L = 1$ and $C_1 = 2.4$. A backward compatibility of the EVI2 (and other 2-band VIs) to the historical AVHRR record to complement the NDVI is highly desirable. Rocha and Shaver (2009) applied the EVI2 to a burn severity gradient in the arctic tundra and found EVI2 was best able to resolve LAI variations along the gradient consisting of highly variable background soil albedo variations associated with the burns. Soil darkening positively biased NDVI values requiring separate relationships between LAI and NDVI for burned and unburned areas. Yang et al. (2012) combined EVI2 from MODIS with meteorological records to develop a regional phenology model in New England, U.S.

1.6.2 Multi-sensor Fusion

Multiple sensor systems with different combinations of spectral, spatial and temporal resolutions will be needed to characterize ecosystem structure and function and effectively capture the important spatiotemporal complexities of landscapes. Coarse spatial resolution sensors provide consistent and timely information of ecosystem health, functioning, and large scale disturbance events, whereas species dynamics, and more subtle land degradation processes, fragmentation and land use modifications are better resolved with finer spatial resolution satellite imagery. By realizing the spectral-spatial detail present in finer resolution data, one is able to fully interpret and characterize the spatial patterns hidden inside pixels of coarser spatial resolution satellite imagery.

Global mosaics of Landsat imagery, including the Landsat Multi Spectral Scanner (MSS), Thematic Mapper (TM), and Enhanced Thematic Mapper (ETM+) have recently been made freely available for detailed mapping of landscapes from the early 1970s (Tucker et al. 2004; Roy et al. 2010) and numerous studies have demonstrated their tremendous value to global change mapping studies (e.g. Giri et al. 2011; Broich et al. 2011a, Potapov et al. 2012). High temporal frequency MODIS satellite data are increasingly being blended with fine spatial resolution Landsat data for applications that require high resolution in both time and space. Two methods for generating dense, synthetic time series of high spatial resolution imagery are the spatial and temporal adaptive reflectance fusion model (STARFM) algorithm (Gao et al. 2006) and the multi-temporal MODIS–Landsat data fusion method (Roy et al. 2008). Such methods to integrate multi-resolution satellite sensor data provide better resolution properties than the individual data sources and are vital to better understand interactions and processes that influence carbon stocks, water resources, and land use activities. For example, Asner (2009) demonstrated that forest degradation and selective logging potentially contribute as much carbon loss as larger scale clear-cutting. Whereas, coarse resolution satellites may detect large-scale clearings, the finer resolution data is needed for forest degradation assessments. Broich et al. (2011b) provided the first

annual map of forest loss for persistently cloudy Indonesia at Landsat spatial resolution. Their approach used annual MODIS forest loss detections to temporally disaggregate epochal Landsat-mapped forest loss.

Schmidt et al. (2012) investigated the utility of the STARFM algorithm with MODIS and Landsat time series to map and monitor subtle changes in vegetation cover in a heterogeneous savanna and wetland landscape. They found that the synthesized high spatial and temporal resolution time series allowed the detailed phenological description of various vegetation communities that would have not been possible across large areas otherwise.

The majority satellite sensor measurements are made using broad spectral bands that are limited in their ability to capture fine resolution biochemical spectral variability associated with multi-species canopies, leaf age spectral variations, and variable plant stress responses. Broadband vegetation and water indices often lack the fidelity to capture subtle absorption variations associated with vegetation stress and changes in biochemistry. Hyperspectral remote sensing measurements add spectral fidelity that enable the retrieval of important biochemical canopy features. Their fusion with high temporal frequency satellite measurements can provide powerful monitoring tools for the characterization of landscape phenology, ecosystem processes, and ecosystem health.

Hyperspectral indices can be formulated with narrow bandwidths that offer greater sensitivity in the retrieval of foliage biochemical properties (Carter and Knapp 2001), and many narrow-band indices have been developed that aim to quantify canopy absorption processes associated with pigments, water, and lignocellulose compounds from litter and woody material (see Ustin et al. 2004). The photochemical reflectance index (PRI) is a hyperspectral index that provides a scaled LUE measure as (Middleton et al. 2011; Gamon et al. 1992),

$$\mathrm{PRI} = \left(\rho_{531\mathrm{nm}} - \rho_{570\mathrm{nm}}\right) / \left(\rho_{531\mathrm{nm}} + \rho_{570\mathrm{nm}}\right) \tag{1.16}$$

Spectral variations at 531 nm are closely associated with the dissipation of excess light energy by xanthophyll pigments in order to protect the photosynthetic leaf apparatus (Ripullone et al. 2011). The upcoming potential launches of new hyperspectral missions, such as Hyperspectral Infrared Imager (HyspIRI), will provide future data fusion opportunities for the scaling and extension of leaf physiologic processes and phenology from species and ecosystem to regional and global scales.

Opportunities to fuse dynamic VI optical measurements and hyperspectral data with Lidar (light detection and ranging) sensors also have promising potentials to improve the assessments of standing wood biomass, forest disturbance and biomass loss, carbon accumulation through forest regrowth, and mapping the spread of invasive species (Lefsky et al. 2002; Baccini et al. 2008; Asner et al. 2011).

1.6.3 VI Biophysical Definition

Despite the success of vegetation indices, there are increasing demands to better define what VI values represent and measure about a canopy. VIs, as measures of canopy *greenness,* depict integrative spatial and temporal variations in canopy biophysics (fractional cover and LAI), leaf physiology (pigments, age, nitrogen), and structure (leaf thickness, leaf angles and shading). A temporal sequence of VI values will most likely include simultaneous changes in many of these variables, and the retrieval of specific variables will either require multiple indices or inverse radiative transfer models with required implicit assumptions and generalizations about land cover type, leaf phenology, and biochemistry.

To a large extent VIs are used opportunistically with the aim of finding the best correlation between a local site experimental data set and a selection of VIs. A VI correlation made with seasonal LAI will incorporate, and confuse, simultaneous changes in leaf chemistry and traits that accompany the measured changes in LAI. There is a tendency to search for the "best VI", although such studies rarely offer insight into the mechanisms of the VI relationships to specific variables. There are far less multi-site studies and spatial and temporal extension analyses of VI-biophysical relationships. This contributes to the overall lack of consensus as to what VIs measure about a canopy and how to further interpret VI values. EVI may provide a more direct relationship with photosynthesis (GPP) in high biomass canopies by relying on the more sensitive NIR reflectances that are able to sense to a greater canopy depth compared with the chlorophyll-sensitive Red band that only senses the uppermost leaf layer. However, Vickers et al. (2012) noted that VIs can only be used to determine the upper limits of canopy exchange processes (photosynthesis and transpiration) as environmental drivers, such as water vapor deficits and soil drought, will influence these processes without affecting canopy spectral properties.

However, it may not always be necessary to deconstruct canopy spectral signals into their biophysical components (LAI, chlorophyll, etc.). The convergence of relationships between VIs and tower fluxes across different ecosystems (Figs. 1.10, 1.13) is surprising since, in theory CO_2 and water exchanges can vary considerably over short time periods; and are related not just to foliage density but environmental variables (PAR, air temperature, vapor pressure deficit, etc.), which can vary considerably over short time periods. VIs provide both a measure of the capacity to absorb photosynthetically active radiation, as well as reflect recent environmental forcings acting on the canopy. Ecological processes tend to adjust plant characteristics over time periods of weeks or months to match the capacity of the environment to support photosynthesis and maximize growth. This is known as the resource balance or resource optimization theory (Field et al. 1995), which treats photosynthesis or primary production as integrators of resource availability.

Acknowledgments This work was partly carried out under a NOAA Cooperative Agreement, CICS-NC (NESDIS-NESDISPO-2009-2002050), and NASA NPP grant NNX11AH25G (Miura, P.I). The authors are very grateful for the review and challenging comments provided by Richard Waring.

References

Anderson LO (2012) Biome-scale forest properties in Amazonia based on field and satellite observations. Remote Sens Basel 4(5):1245–1271. doi:10.3390/Rs4051245

Anderson LO, Aragao LEOC, Shimabukuro YE, Almeida S, Huete A (2011) Fraction images for monitoring intra-annual phenology of different vegetation physiognomies in Amazonia. Int J Remote Sens 32(2):387–408. doi:10.1080/01431160903474921

Anyamba A, Tucker CJ (2005) Analysis of Sahelian vegetation dynamics using NOAA-AVHRR NDVI data from 1981–2003. J Arid Environ 63(3):596–614

Asner GP (2009) Tropical forest carbon assessment: integrating satellite and airborne mapping approaches. Environ Res Lett 4(3):1748–9326

Asner GP, Martin RE, Knapp DE, Tupayachi R, Anderson C, Carranza L, Martinez P, Houcheime M, Sinca F, Weiss P (2011) Spectroscopy of canopy chemicals in humid tropical forests. Remote Sens Environ 115(12):3587–3598

Baccini A, Laporte N, Goetz SJ, Sun M, Dong H (2008) A first map of tropical Africa's above-ground biomass derived from satellite imagery. Environ Res Lett 3(4):045011

Baret F, Guyot G (1991) Potentials and limits of vegetation indexes for LAI and APAR assessment. Remote Sens Environ 35(2–3):161–173

Bates LM, Hall AE (1981) Stomatal closure with soil-water depletion not associated with changes in bulk leaf water status. Oecologia 50(1):62–65. doi:10.1007/Bf00378794

Beck PSA, Atzberger C, Hogda KA, Johansen B, Skidmore AK (2006) Improved monitoring of vegetation dynamics at very high latitudes: a new method using MODIS NDVI. Remote Sens Environ 100(3):321–334

Brando PM, Goetz SJ, Baccini A, Nepstad DC, Beck PSA, Christman MC (2010) Seasonal and interannual variability of climate and vegetation indices across the Amazon. Proc Natl Acad Sci USA 107(33):14685–14690

Breshears DD, Cobb NS, Rich PM, Price KP, Allen CD, Balice RG, Romme WH, Kastens JH, Floyd ML, Belnap J, Anderson JJ, Myers OB, Meyer CW (2005) Regional vegetation die-off in response to global-change-type drought. Proc Natl Acad Sci USA 102(42):15144–15148. doi:10.1073/Pnas.0505734102

Broich M, Hansen M, Stolle F, Potapov P, Margono BA, Adusei B (2011a) Remotely sensed forest cover loss shows high spatial and temporal variation across Sumatera and Kalimantan, Indonesia 2000–2008. Environ Res Lett 6(1). doi:10.1088/1748-9326/6/1/014010

Broich M, Hansen MC, Potapov P, Adusei B, Lindquist E, Stehman SV (2011b) Time-series analysis of multi-resolution optical imagery for quantifying forest cover loss in Sumatra and Kalimantan, Indonesia. Int J Appl Earth Obs 13(2):277–291. doi:10.1016/J.Jag.2010.11.004

Caccamo G, Chisholm LA, Bradstock RA, Puotinen ML (2011) Assessing the sensitivity of MODIS to monitor drought in high biomass ecosystems. Remote Sens Environ 115(10):2626–2639

Carlson TN, Ripley DA (1997) On the relation between NDVI, fractional vegetation cover, and leaf area index. Remote Sens Environ 62(3):241–252

Carter GA, Knapp AK (2001) Leaf optical properties in higher plants: linking spectral characteristics to stress and chlorophyll concentration. Am J Bot 88(4):677–684

Ceccato P, Flasse S, Gregoire JM (2002a) Designing a spectral index to estimate vegetation water content from remote sensing data. Part 2. Validation and applications. Remote Sens Environ 82(2–3):198–207

Ceccato P, Gobron N, Flasse S, Pinty B, Tarantola S (2002b) Designing a spectral index to estimate vegetation water content from remote sensing data. Part 1. Theoretical approach. Remote Sens Environ 82(2–3):188–197

Chen X, Vierling L, Deering D, Conley A (2005) Monitoring boreal forest leaf area index across a Siberian burn chronosequence: a MODIS validation study. Int J Remote Sens 26(24): 5433–5451

Chuvieco E, Ventura G, Martin MP, Gomez I (2005) Assessment of multitemporal compositing techniques of MODIS and AVHRR images for burned land mapping. Remote Sens Environ 94(4):450–462

Cihlar J, Ly H, Li ZQ, Chen J, Pokrant H, Huang FT (1997) Multitemporal, multichannel AVHRR data sets for land biosphere studies—artifacts and corrections. Remote Sens Environ 60(1):35–57

Cohen WB, Maiersperger TK, Yang ZQ, Gower ST, Turner DP, Ritts WD, Berterretche M, Running SW (2003) Comparisons of land cover and LAI estimates derived from ETM plus and MODIS for four sites in North America: a quality assessment of 2000/2001 provisional MODIS products. Remote Sens Environ 88(3):233–255

Crist EP, Cicone RC (1984) A physically-based transformation of thematic mapper data—the TM tasseled cap. IEEE Trans Geosci Remote Sens 22(3):256–263

Fassnacht KS, Gower ST, MacKenzie MD, Nordheim EV, Lillesand TM (1997) Estimating the leaf area index of North Central Wisconsin forests using the Landsat Thematic Mapper. Remote Sens Environ 61(2):229–245

Fensholt R (2004) Earth observation of vegetation status in the Sahelian and Sudanian West Africa: comparison of terra MODIS and NOAA AVHRR satellite data. Int J Remote Sens 25(9):1641–1659

Fensholt R, Sandholt I, Rasmussen MS (2004) Evaluation of MODIS LAI, fAPAR and the relation between fAPAR and NDVI in a semi-arid environment using in situ measurements. Remote Sens Environ 91(3–4):490–507

Fensholt R, Sandholt I, Stisen S, Tucker C (2006) Analysing NDVI for the African continent using the geostationary meteosat second generation SEVIRI sensor. Remote Sens Environ 101(2):212–229

Field CB, Randerson JT, Malmstrom CM (1995) Global net primary production—combining ecology and remote-sensing. Remote Sens Environ 51(1):74–88

Fischer A (1994) A model for the seasonal-variations of vegetation indexes in coarse resolution data and its inversion to extract crop parameters. Remote Sens Environ 48(2):220–230

Franklin KA, Lyons K, Nagler PL, Lampkin D, Glenn EP, Molina-Freaner F, Markow T, Huete AR (2006) Buffelgrass (*Pennisetum ciliare*) land conversion and productivity in the plains of Sonora, Mexico. Biol Conserv 127(1):62–71

Gallo KP, Eidenshink JC (1988) Differences in visible and near-IR responses, and derived vegetation indexes, for the NOAA-9 and NOAA-10 AVHRRS—a case-study. Photogramm Eng Remote Sens 54(4):485–490

Gallo K, Li L, Reed B, Eidenshink J, Dwyer J (2005) Multi-platform comparisons of MODIS and AVHRR normalized difference vegetation index data. Remote Sens Environ 99(3):221–231

Gamon JA, Penuelas J, Field CB (1992) A narrow-waveband spectral index that tracks diurnal changes in photosynthetic efficiency. Remote Sens Environ 41(1):35–44

Ganguly S, Friedl MA, Tan B, Zhang XY, Verma M (2010) Land surface phenology from MODIS: characterization of the collection 5 global land cover dynamics product. Remote Sens Environ 114(8):1805–1816

Gao BC (1996) NDWI—a normalized difference water index for remote sensing of vegetation liquid water from space. Remote Sens Environ 58(3):257–266

Gao X, Huete AR, Ni WG, Miura T (2000) Optical-biophysical relationships of vegetation spectra without background contamination. Remote Sens Environ 74(3):609–620

Gao F, Masek J, Schwaller M, Hall F (2006) On the blending of the Landsat and MODIS surface reflectance: predicting daily Landsat surface reflectance. IEEE Trans Geosci Remote Sens 44(8):2207–2218

Giri C, Ochieng E, Tieszen LL, Zhu Z, Singh A, Loveland T, Masek J, Duke N (2011) Status and distribution of mangrove forests of the world using earth observation satellite data. Global Ecol Biogeogr 20(1):154–159

Gitelson AA, Kaufman YJ (1998) MODIS NDVI optimization to fit the AVHRR data series spectral considerations. Remote Sens Environ 66(3):343–350

Gitelson AA, Gritz Y, Merzlyak MN (2003) Relationships between leaf chlorophyll content and spectral reflectance and algorithms for non-destructive chlorophyll assessment in higher plant leaves. J Plant Physiol 160(3):271–282

Glenn EP, Huete AR, Nagler PL, Hirschboeck KK, Brown P (2007) Integrating remote sensing and ground methods to estimate evapotranspiration. Crit Rev Plant Sci 26(3):139–168

Glenn EP, Huete AR, Nagler PL, Nelson SG (2008) Relationship between remotely-sensed vegetation indices, canopy attributes and plant physiological processes: what vegetation indices can and cannot tell us about the landscape. Sensors Basel 8(4):2136–2160

Glenn EP, Doody TM, Guerschman JP, Huete AR, King EA, McVicar TR, Van Dijk AIJM, Van Niel TG, Yebra M, Zhang YQ (2011) Actual evapotranspiration estimation by ground and remote sensing methods: the Australian experience. Hydrol Process 25(26):4103–4116. doi:10.1002/Hyp.8391

Gobron N, Pinty B, Verstraete MM, Widlowski JL (2000) Advanced vegetation indices optimized for up-coming sensors: design, performance, and applications. IEEE Trans Geosci Remote Sens 38(6):2489–2505

Graetz RD (1990) Remote sensing of terrestrial ecosystem structure: an ecologist's pragmatic view. In: Hobbs RJ, Mooney HA (eds) Remote sensing of biosphere functioning. Springer, New York

Guerschman JP, Van Dijk AIJM, Mattersdorf G, Beringer J, Hutley LB, Leuning R, Pipunic RC, Sherman BS (2009) Scaling of potential evapotranspiration with MODIS data reproduces flux observations and catchment water balance observations across Australia. J Hydrol 369(1–2):107–119. doi:10.1016/J.Jhydrol.2009.02.013

Hilker T, Coops NC, Schwalm CR, Jassal RS, Black TA, Krishnan P (2008) Effects of mutual shading of tree crowns on prediction of photosynthetic light-use efficiency in a coastal Douglas-fir forest. Tree Physiol 28(6):825–834

Hilker T, Gitelson A, Coops NC, Hall FG, Black TA (2011) Tracking plant physiological properties from multi-angular tower-based remote sensing. Oecologia 165(4):865–876

Holben BN (1986) Characteristics of maximum-value composite images from temporal AVHRR data. Int J Remote Sens 7(11):1417–1434

Holben BN, Eck TF, Slutsker I, Tanre D, Buis JP, Setzer A, Vermote E, Reagan JA, Kaufman YJ, Nakajima T, Lavenu F, Jankowiak I, Smirnov A (1998) AERONET—a federated instrument network and data archive for aerosol characterization. Remote Sens Environ 66(1):1–16

Houborg RM, Soegaard H (2004) Regional simulation of ecosystem CO2 and water vapor exchange for agricultural land using NOAA AVHRR and Terra MODIS satellite data. Application to Zealand, Denmark. Remote Sens Environ 93(1–2):150–167

Huemmrich KF, Privette JL, Mukelabai M, Myneni RB, Knyazikhin Y (2005) Time-series validation of MODIS land biophysical products in a Kalahari woodland, Africa. Int J Remote Sens 26(19):4381–4398

Huete A (1988) A soil-adjusted vegetation index (SAVI). Remote Sens Environ 25(3): 295–309

Huete AR, Glenn EP (2011) Recent advances in remote sensing of ecosystem structure and function. In: Weng Q (ed) Advances in environmental remote sensing: sensors, algorithms, and applications. CRC Press/Taylor and Francis Group, New York

Huete A, Didan, K, van Leeuwen W, Miura T, Glenn E (2011) MODIS Vegetation Indices, In: Ramachandran B, Justice CO, Abrams M (eds) Land remote sensing and global environmental change: NASA's earth observing system and the science of ASTER and MODIS, vol 11. Springer, Berlin

Huete A, Didan K, Miura T, Rodriguez EP, Gao X, Ferreira LG (2002) Overview of the radiometric and biophysical performance of the MODIS vegetation indices. Remote Sens Environ 83(1–2):195–213

Huete AR, Didan K, Shimabukuro YE, Ratana P, Saleska SR, Hutyra LR, Yang WZ, Nemani RR, Myneni R (2006) Amazon rainforests green-up with sunlight in dry season. Geophys Res Lett 33(6):L06405

Huete A, Keita F, Thome K, Privette J, van Leeuwen WJD, Justice C, Morisette J (1999) A light aircraft radiometric package for MODLAND quick airborne looks (MQUALS). The Earth Observer 11(1):22

Huete AR, Restrepo-Coupe N, Ratana P, Didan K, Saleska SR, Ichii K, Panuthai S, Gamo M (2008) Multiple site tower flux and remote sensing comparisons of tropical forest dynamics in Monsoon Asia. Agric For Meteorol 148(5):748–760

Hunt ER, Rock BN (1989) Detection of changes in leaf water-content using near-infrared and middle-infrared reflectances. Remote Sens Environ 30(1):43–54

Ichii K, Hashimoto H, White MA, Potter C, Hutyra LR, Huete AR, Myneni RB, Nemanis RR (2007) Constraining rooting depths in tropical rainforests using satellite data and ecosystem modeling for accurate simulation of gross primary production seasonality. Global Change Biol 13(1):67–77

IPCC (2007) Climate change 2007: the physical science basis. In: Solomon S, Qin D, Manning M, Chen Z, Marquis M, Averyt KB, Tignor M, Miller HL (eds) Contribution of working group I to the fourth assessment report of the intergovernmental panel on climate change. Cambridge University Press, Cambridge

Jahan N, Gan TY (2009) Modeling gross primary production of deciduous forest using remotely sensed radiation and ecosystem variables. J Geophys Res Biogeosci 114

Jiang ZY, Huete AR, Chen J, Chen YH, Li J, Yan GJ, Zhang XY (2006a) Analysis of NDVI and scaled difference vegetation index retrievals of vegetation fraction. Remote Sens Environ 101(3):366–378

Jiang ZY, Huete AR, Li J, Chen YH (2006b) An analysis of angle-based with ratio-based vegetation indices. IEEE Trans Geosci Remote Sens 44(9):2506–2513

Jiang Z, Huete A, Didan K, Miura T (2008) Development of a two-band enhanced vegetation index without a blue band. Remote Sens Environ 112(10):3833–3845

Jin SM, Sader SA (2005) MODIS time-series imagery for forest disturbance detection and quantification of patch size effects. Remote Sens Environ 99(4):462–470

Justice CO, Vermote E, Townshend JRG, Defries R, Roy DP, Hall DK, Salomonson VV, Privette JL, Riggs G, Strahler A, Lucht W, Myneni RB, Knyazikhin Y, Running SW, Nemani RR, Wan ZM, Huete AR, van Leeuwen W, Wolfe RE, Giglio L, Muller JP, Lewis P, Barnsley MJ (1998) The Moderate Resolution Imaging Spectroradiometer (MODIS): land remote sensing for global change research. IEEE Trans Geosci Remote Sens 36(4):1228–1249

Kaufman YJ, Tanre D (1992) Atmospherically resistant vegetation index (ARVI) for EOS-MODIS. IEEE Trans Geosci Remote Sens 30(2):261–270

Kaufman YJ, Remer LA, Tanre D, Li RR, Kleidman R, Mattoo S, Levy RC, Eck TF, Holben BN, Ichoku C, Martins JV, Koren I (2005) A critical examination of the residual cloud contamination and diurnal sampling effects on MODIS estimates of aerosol over ocean. IEEE Trans Geosci Remote Sens 43(12):2886–2897

Kawamura K, Akiyama T, Yokota H, Tsutsumi M, Yasuda T, Watanabe O, Wang G, Wang S (2005) Monitoring of forage conditions with MODIS imagery in the Xilingol steppe, Inner Mongolia. Int J Remote Sens 26(7):1423–1436

Kerr JT, Ostrovsky M (2003) From space to species: ecological applications for remote sensing. Trends Ecol Evol 18(6):299–305

Kobayashi H, Dye DG (2005) Atmospheric conditions for monitoring the long-terrn vegetation dynamics in the Amazon using normalized difference vegetation index. Remote Sens Environ 97(4):519–525

Lefsky MA, Cohen WB, Parker GG, Harding DJ (2002) Lidar remote sensing for ecosystem studies. Bioscience 52(1):19–30

Li FQ, Kustas WP, Anderson MC, Prueger JH, Scott RL (2008) Effect of remote sensing spatial resolution on interpreting tower-based flux observations. Remote Sens Environ 112(2):337–349. doi: 10.1016/J.Rse.2006.11.032

Lobser SE, Cohen WB (2007) MODIS tasselled cap: land cover characteristics expressed through transformed MODIS data. Int J Remote Sens 28(22):5079–5101

Los SO (1993) Calibration adjustment of the NOAA-AVHRR normalized difference vegetation index without recourse to component channel 1 and 2 data. Int J Remote Sens 14(10): 1907–1917

Mahadevan P, Wofsy SC, Matross DM, Xiao XM, Dunn AL, Lin JC, Gerbig C, Munger JW, Chow VY, Gottlieb EW (2008) A satellite-based biosphere parameterization for net ecosystem CO2 exchange: vegetation photosynthesis and respiration model (VPRM). Global Biogeochem Cycle 22(2). doi:10.1029/2006gb002735

Middleton EM, Huemmrich KF, Cheng YB, Margolis HA (2011) Spectral bio-indicators of photosynthetic efficiency and vegetation stress. In: Thenkabail PS, Lyon JG, Huete AR (eds) Hyperspectral remote sensing of vegetation. Taylor & Francis Group, London

Mildrexler DJ, Zhao MS, Running SW (2009) Testing a MODIS global disturbance index across North America. Remote Sens Environ 113(10):2103–2117

Miura T, Huete AR, Yoshioka H (2000) Evaluation of sensor calibration uncertainties on vegetation indices for MODIS. IEEE Trans Geosci Remote Sens 38(3):1399–1409

Miura T, Huete AR, Yoshioka H, Holben BN (2001) An error and sensitivity analysis of atmospheric resistant vegetation indices derived from dark target-based atmospheric correction. Remote Sens Environ 78(3):284–298

Miura T, Huete A, Yoshioka H (2006) An empirical investigation of cross-sensor relationships of NDVI and red/near-infrared reflectance using EO-1 hyperion data. Remote Sens Environ 100(2):223–236

Monteith JL, Unsworth MH (1990) Principles of environmental physics, 2nd edn. Edward Arnold, London

Myneni RB, Keeling CD, Tucker CJ, Asrar G, Nemani RR (1997) Increased plant growth in the northern high latitudes from 1981 to 1991. Nature 386(6626):698–702

Nagler PL, Cleverly J, Glenn E, Lampkin D, Huete A, Wan ZM (2005a) Predicting riparian evapotranspiration from MODIS vegetation indices and meteorological data. Remote Sens Environ 94(1):17–30

Nagler PL, Scott RL, Westenburg C, Cleverly JR, Glenn EP, Huete AR (2005b) Evapotranspiration on western US rivers estimated using the enhanced vegetation index from MODIS and data from eddy covariance and Bowen ratio flux towers. Remote Sens Environ 97(3):337–351

Nagler PL, Glenn EP, Kim H, Emmerich W, Scott RL, Huxman TE, Huete AR (2007) Relationship between evapotranspiration and precipitation pulses in a semiarid rangeland estimated by moisture flux towers and MODIS vegetation indices. J Arid Environ 70(3):443–462

Penuelas J, Rutishauser T, Filella I (2009) Phenology feedbacks on climate change. Science 324(5929):887–888

Pettorelli N, Vik JO, Mysterud A, Gaillard JM, Tucker CJ, Stenseth NC (2005) Using the satellite-derived NDVI to assess ecological responses to environmental change. Trends Ecol Evol 20(9):503–510

Potapov PV, Turubanova SA, Hansen MC, Adusei B, Broich M, Altstatt A, Mane L, Justice CO (2012) Quantifying forest cover loss in Democratic Republic of the Congo, 2000–2010, with Landsat ETM+data. Remote Sens Environ 122:106–116. doi:10.1016/j.rse.2011.08.027

Potter C, Klooster S, Huete A, Genovese V (2007) Terrestrial carbon sinks for the United States predicted from MODIS satellite data and ecosystem modeling. Earth Interact 11. doi:10.1175/Ei228.1

Privette JL, Asner GP, Conel J, Huemmrich KF, Olson R, Rango A, Rahman AF, Thome K, Walter-Shea EA (2000) The EOS prototype validation exercise (PROVE) at Jornada: overview and lessons learned. Remote Sens Environ 74(1):1–12

Qi J, Chehbouni A, Huete AR, Kerr YH, Sorooshian S (1994) A modified soil adjusted vegetation index. Remote Sens Environ 48(2):119–126

Rahman AF, Sims DA, Cordova VD, El-Masri BZ (2005) Potential of MODIS EVI and surface temperature for directly estimating per-pixel ecosystem C fluxes. Geophys Res Lett 32(19):L19404

Ratana P, Huete AR, Ferreira L (2005) Analysis of cerrado physiognomies and conversion in the MODIS seasonal-temporal domain. Earth Interact 9:1–22

Reed BC, White M, Brown JF (2003) Remote sensing phenology. In: Schwartz MD (ed) Phenology: an integrative environmental science. Kluwer Academic Publishers, The Netherlands

Richardson AJ, Wiegand CL (1977) Distinguishing vegetation from soil background information. Photogramm Eng Remote Sens 43(12):1541–1552

Richardson AD, Jenkins JP, Braswell BH, Hollinger DY, Ollinger SV, Smith ML (2007) Use of digital webcam images to track spring green-up in a deciduous broadleaf forest. Oecologia 152(2):323–334

Ripullone F, Rivelli AR, Baraldi R, Guarini R, Guerrieri R, Magnani F, Penuelas J, Raddi S, Borghetti M (2011) Effectiveness of the photochemical reflectance index to track photosynthetic activity over a range of forest tree species and plant water statuses. Funct Plant Biol 38(3):177–186

Rocha AV, Shaver GR (2009) Advantages of a two band EVI calculated from solar and photosynthetically active radiation fluxes. Agric For Meteorol 149(9):1560–1563

Roderick M, Smith R, Cridland S (1996) The precision of the NDVI derived from AVHRR observations. Remote Sens Environ 56(1):57–65

Rouse JW, Haas RH, Schell JA, Deering DW (1973) Monitoring vegetation systems in the Great Plains with ERTS. In: 3rd ERTS symposium, NASA SP-351, pp 309–317

Roy DP, Ju J, Lewis P, Schaaf C, Gao F, Hansen M, Lindquist E (2008) Multi-temporal MODIS-Landsat data fusion for relative radiometric normalization, gap filling, and prediction of Landsat data. Remote Sens Environ 112(6):3112–3130. doi:10.1016/J.Rse.2008.03.009

Roy DP, Ju JC, Kline K, Scaramuzza PL, Kovalskyy V, Hansen M, Loveland TR, Vermote E, Zhang CS (2010) Web-enabled Landsat Data (WELD): Landsat ETM plus composited mosaics of the conterminous United States. Remote Sens Environ 114(1):35–49

Running SW, Baldocchi DD, Turner DP, Gower ST, Bakwin PS, Hibbard KA (1999) A global terrestrial monitoring network integrating tower fluxes, flask sampling, ecosystem modeling and EOS satellite data. Remote Sens Environ 70(1):108–127

Running SW, Nemani RR, Heinsch FA, Zhao MS, Reeves M, Hashimoto H (2004) A continuous satellite-derived measure of global terrestrial primary production. Bioscience 54(6):547–560

Ryu Y, Baldocchi DD, Verfaillie J, Ma S, Falk M, Ruiz-Mercado I, Hehn T, Sonnentag O (2010) Testing the performance of a novel spectral reflectance sensor, built with light emitting diodes (LEDs), to monitor ecosystem metabolism, structure and function. Agr For Meteorol 150(12):1597–1606

Ryu Y, Baldocchi DD, Kobayashi H, van Ingen C, Li J, Black TA, Beringer J, van Gorsel E, Knohl A, Law BE, Roupsard O (2011) Integration of MODIS land and atmosphere products with a coupled-process model to estimate gross primary productivity and evapotranspiration from 1 km to global scales. Global Biogeochem Cycle 25

Sakamoto T, Van Nguyen N, Ohno H, Ishitsuka N, Yokozawa M (2006) Spatio-temporal distribution of rice phenology and cropping systems in the Mekong Delta with special reference to the seasonal water flow of the Mekong and Bassac rivers. Remote Sens Environ 100(1):1–16

Saleska SR, Didan K, Huete AR, da Rocha HR (2007) Amazon forests green-up during 2005 drought. Science 318(5850):612

Samanta A, Ganguly S, Hashimoto H, Devadiga S, Vermote E, Knyazikhin Y, Nemani RR, Myneni RB (2010) Amazon forests did not green-up during the 2005 drought. Geophys Res Lett 37:L05401

Schaaf CB, Gao F, Strahler AH, Lucht W, Li XW, Tsang T, Strugnell NC, Zhang XY, Jin YF, Muller JP, Lewis P, Barnsley M, Hobson P, Disney M, Roberts G, Dunderdale M, Doll C,

d'Entremont RP, Hu BX, Liang SL, Privette JL, Roy D (2002) First operational BRDF, albedo nadir reflectance products from MODIS. Remote Sens Environ 83(1–2):135–148

Schmidt M, Udelhoven T, Gill T, Roder A (2012) Long term data fusion for a dense time series analysis with MODIS and Landsat imagery in an Australian Savanna. J Appl Remote Sens 6. doi:10.1117/1.Jrs.6.063512

Schubert P, Eklundh L, Lund M, Nilsson M (2010) Estimating northern peatland CO2 exchange from MODIS time series data. Remote Sens Environ 114(6):1178–1189

Schwartz MD, Hanes JM (2010) Continental-scale phenology: warming and chilling. Int J Climatol 30(11):1595–1598

Sellers PJ (1985) Canopy reflectance, photosynthesis and transpiration. Int J Remote Sens 6(8):1335–1372

Sims DA, Rahman AF, Cordova VD, El-Masri BZ, Baldocchi DD, Flanagan LB, Goldstein AH, Hollinger DY, Misson L, Monson RK, Oechel WC, Schmid HP, Wofsy SC, Xu LK (2006) On the use of MODIS EVI to assess gross primary productivity of North American ecosystems. J Geophys Res Biogeosci 111(G4)

Sims DA, Rahman AF, Cordova VD, El-Masri BZ, Baldocchi DD, Bolstad PV, Flanagan LB, Goldstein AH, Hollinger DY, Misson L, Monson RK, Oechel WC, Schmid HP, Wofsy SC, Xu L (2008) A new model of gross primary productivity for North American ecosystems based solely on the enhanced vegetation index and land surface temperature from MODIS. Remote Sens Environ 112(4):1633–1646

Smith AMS, Falkowski MJ, Hudak AT, Evans JS, Robinson AP, Steele CM (2009) A cross-comparison of field, spectral, and lidar estimates of forest canopy cover. Can J Remote Sens 35(5):447–459

Soudani K, Hmimina G, Delpierre N, Pontailler JY, Aubinet M, Bonal D, Caquet B, de Grandcourt A, Burban B, Flechard C, Guyon D, Granier A, Gross P, Heinesh B, Longdoz B, Loustau D, Moureaux C, Ourcival JM, Rambal S, Saint André L, Dufrêne E (2012) Ground-based network of NDVI measurements for tracking temporal dynamics of canopy structure and vegetation phenology in different biomes. Remote Sens Environ 123(0):234–245. doi:10.1016/j.rse.2012.03.012

Souza C, Firestone L, Silva LM, Roberts D (2003) Mapping forest degradation in the Eastern Amazon from SPOT 4 through spectral mixture models. Remote Sens Environ 87(4):494–506

Trishchenko AP, Cihlar J, Li Z (2002) Effects of spectral response function on surface reflectance and NDVI measured with moderate resolution satellite sensors. Remote Sens Environ 81(1):1–18

Tucker CJ (1979) Red and photographic infrared linear combinations for monitoring vegetation. Remote Sens Environ 8(2):127–150

Tucker CJ, Grant DM, Dykstra JD (2004) NASA's global orthorectified landsat data set. Photogramm Eng Remote Sens 70(3):313–322

Tucker CJ, Pinzon JE, Brown ME, Slayback DA, Pak EW, Mahoney R, Vermote EF, El Saleous N (2005) An extended AVHRR 8-km NDVI dataset compatible with MODIS and SPOT vegetation NDVI data. Int J Remote Sens 26(20):4485–4498

Turner W, Spector S, Gardiner N, Fladeland M, Sterling E, Steininger M (2003) Remote sensing for biodiversity science and conservation. Trends Ecol Evol 18(6):306–314

Ustin SL, Roberts DA, Gamon JA, Asner GP, Green RO (2004) Using imaging spectroscopy to study ecosystem processes and properties. Bioscience 54(6):523–534

van Leeuwen WJD, Huete AR, Laing TW (1999) MODIS vegetation index compositing approach: a prototype with AVHRR data. Remote Sens Environ 69(3):264–280

van Leeuwen WJD, Orr BJ, Marsh SE, Herrmann SM (2006) Multi-sensor NDVI data continuity: uncertainties and implications for vegetation monitoring applications. Remote Sens Environ 100(1):67–81

Verstraete MM, Pinty B (1996) Designing optimal spectral indexes for remote sensing applications. IEEE Trans Geosci Remote Sens 34(5):1254–1265

Vickers D, Thomas CK, Pettijohn C, Martin JG, Law BE (2012) Five years of carbon fluxes and inherent water-use efficiency at two semi-arid pine forests with different disturbance histories. Tellus B 64. doi:10.3402/Tellusb.V64i0.17159

Vuolo F, Dash J, Curran PJ, Lajas D, Kwiatkowska E (2012) Methodologies and uncertainties in the use of the terrestrial chlorophyll index for the Sentinel-3 mission. Remote Sens Basel 4(5):1112–1133

Wang Q, Tenhunen J, Dinh NQ, Reichstein M, Vesala T, Keronen P (2004) Similarities in ground- and satellite-based NDVI time series and their relationship to physiological activity of a Scots pine forest in Finland. Remote Sens Environ 93(1–2):225–237

Wang Q, Adiku S, Tenhunen J, Granier A (2005) On the relationship of NDVI with leaf area index in a deciduous forest site. Remote Sens Environ 94(2):244–255

Wang YJ, Lyapustin AI, Privette JL, Morisette JT, Holben B (2009) Atmospheric correction at AERONET locations: a new science and validation data set. IEEE Trans Geosci Remote Sens 47(8):2450–2466

Waring RH, Whitehead D, Jarvis PG (1979) The contribution of stored water to transpiration in Scots pine. Plant Cell Environ 2(4). doi:10.1111/j.1365-3040.1979.tb00085.x

Waring RH, Coops NC, Fan W, Nightingale JM (2006) MODIS enhanced vegetation index predicts tree species richness across forested ecoregions in the contiguous USA. Remote Sens Environ 103(2):218–226

Wilson TB, Meyers TP (2007) Determining vegetation indices from solar and photosynthetically active radiation fluxes. Agric For Meteorol 144(3–4):160–179

Wolfe RE, Roy DP, Vermote E (1998) MODIS land data storage, gridding, and compositing methodology: level 2 grid. IEEE Trans Geosci Remote Sens 36(4):1324–1338

Xiao XM, Braswell B, Zhang QY, Boles S, Frolking S, Moore B (2003) Sensitivity of vegetation indices to atmospheric aerosols: continental-scale observations in Northern Asia. Remote Sens Environ 84(3):385–392

Xiao XM, Zhang QY, Braswell B, Urbanski S, Boles S, Wofsy S, Berrien M, Ojima D (2004) Modeling gross primary production of temperate deciduous broadleaf forest using satellite images and climate data. Remote Sens Environ 91(2):256–270

Xiao XM, Zhang QY, Saleska S, Hutyra L, De Camargo P, Wofsy S, Frolking S, Boles S, Keller M, Moore B (2005) Satellite-based modeling of gross primary production in a seasonally moist tropical evergreen forest. Remote Sens Environ 94(1):105–122

Xiao XM, Boles S, Frolking S, Li CS, Babu JY, Salas W, Moore B (2006) Mapping paddy rice agriculture in South and Southeast Asia using multi-temporal MODIS images. Remote Sens Environ 100(1):95–113

Xu LA, Samanta A, Costa MH, Ganguly S, Nemani RR, Myneni RB (2011) Widespread decline in greenness of Amazonian vegetation due to the 2010 drought. Geophys Res Lett 38. doi:10.1029/2011gl046824

Yamamoto H, Matsumura Y, Sawayama S (2005) Evaluation of supply potential of energy crops in Japan considering cases of improvement of crop productivity. Biomass Bioenerg 29(5):355–359

Yang FH, White MA, Michaelis AR, Ichii K, Hashimoto H, Votava P, Zhu AX, Nemani RR (2006) Prediction of continental-scale evapotranspiration by combining MODIS and AmeriFlux data through support vector machine. IEEE Trans Geosci Remote Sens 44(11):3452–3461

Yang X, Mustard JF, Tang J, Xu H (2012) Regional-scale phenology modeling based on meteorological records and remote sensing observations. J Geophys Res 117(G3):1–18. doi:10.1029/2012JG001977

Yoshioka H, Miura T, Obata K (2012) Derivation of relationships between spectral vegetation indices from multiple sensors based on vegetation isolines. Remote Sens 4(3):583–597. doi:10.3390/rs4030583

Yoshioka H, Huete AR, Miura T (2000) Derivation of vegetation isoline equations in red-NIR reflectance space. IEEE Trans Geosci Remote Sens 38(2):838–848

Zarco-Tejada PJ, Rueda CA, Ustin SL (2003) Water content estimation in vegetation with MODIS reflectance data and model inversion methods. Remote Sens Environ 85(1):109–124

Zha Y, Gao J, Ni S, Shen N (2005) Temporal filtering of successive MODIS data in monitoring a locust outbreak. Int J Remote Sens 26(24):5665–5674

Zhang XY, Friedl MA, Schaaf CB, Strahler AH, Hodges JCF, Gao F, Reed BC, Huete A (2003) Monitoring vegetation phenology using MODIS. Remote Sens Environ 84(3):471–475

Zhang XY, Friedl MA, Schaaf CB, Strahler AH, Schneider A (2004) The footprint of urban climates on vegetation phenology. Geophys Res Lett 31(12)

Zhang QY, Xiao XM, Braswell B, Linder E, Baret F, Moore B (2005) Estimating light absorption by chlorophyll, leaf and canopy in a deciduous broadleaf forest using MODIS data and a radiative transfer model. Remote Sens Environ 99(3):357–371

Zhang XY, Friedl MA, Schaaf CB (2006) Global vegetation phenology from Moderate Resolution Imaging Spectroradiometer (MODIS): evaluation of global patterns and comparison with in situ measurements. J Geophys Res Biogeosci 111(G4)

Chapter 2
Green Leaf Area and Fraction of Photosynthetically Active Radiation Absorbed by Vegetation

Sangram Ganguly, Ramakrishna R. Nemani, Frederic Baret, Jian Bi, Marie Weiss, Gong Zhang, Cristina Milesi, Hirofumi Hashimoto, Arindam Samanta, Aleixandre Verger, Kumaresh Singh and Ranga B. Myneni

Abstract Leaf Area Index (LAI), the area of leaves per unit ground area, and the Fraction of Photosynthetically Active Radiation (FPAR; 400–700 nm) absorbed by vegetation are important biophysical variables for quantifying the cycling of water, carbon and nutrients through ecosystems. The LAI/FPAR products from the Advanced Very High Resolution Radiometer (AVHRR), the Moderate Resolution Imaging Spectroradiometer (MODIS) sensor and the Système Pour l'Observation de la Terre (SPOT) sensor have a large Earth science community user base and the ease of access, provision of pixel quality and validation information have greatly aided the use of these products. Recent research efforts focusing on inter-sensor product consistencies have developed a foundation upon which mature algorithms and a validation framework can act synergistically to further refine the accuracy and precision of these existing long-term products. This chapter provides a brief

S. Ganguly (✉) · G. Zhang
Bay Area Environmental Research Institute (BAERI)/NASA Ames Research Center, Moffett Field, CA, USA
e-mail: sangramganguly@gmail.com

J. Bi · R. B. Myneni
Department of Earth and Environment, Boston University, Boston, MA, USA

R. R. Nemani
NASA Advanced Supercomputing Division, Moffett Field, CA, USA

F. Baret · M. Weiss · A. Verger
INRA-EMMAH, Avignon, France

C. Milesi · H. Hashimoto
Department of Science and Environmental Policy, California State University at Monterey Bay/NASA Ames Research Center, Moffett Field, CA, USA

A. Samanta
Atmospheric and Environmental Research (AER) Inc., Lexington, MA, USA

K. Singh
Risk Management Solutions, Newark, CA, USA

J. M. Hanes (ed.), *Biophysical Applications of Satellite Remote Sensing*,
Springer Remote Sensing/Photogrammetry, DOI: 10.1007/978-3-642-25047-7_2,

overview of the recent progresses in LAI/FPAR estimation algorithms and resulting biophysical products from the AVHRR, MODIS, SPOT and Landsat data.

2.1 Introduction

Leaf Area Index (LAI), the one-sided green leaf area per unit ground area, and the Fraction of Photosynthetically Active Radiation (FPAR; 400–700 nm) absorbed by vegetation are important biophysical variables for quantifying the cycling of water, carbon and nutrients through ecosystems (Demarty et al. 2007; Sellers et al. 1996; Tian et al. 2004). LAI characterizes the functioning surface area of a vegetation canopy (Myneni et al. 2002). The interactions between the vegetation surface and the atmosphere, for example, radiation exchange, transpiration rates, precipitation interception, momentum and gas exchange, is predominantly determined by leaf area (Monteith and Unsworth 1990). An increase in leaf area, for example, increases the uptake of CO_2 from the atmosphere due to greater sunlight absorption and hence results in increased canopy conductance and transpiration rates (Field and Mooney 1983). Field measurements of LAI include hemispherical photography and optical instruments like TRAC, LAI-2000 or LI-3000C (Chen et al. 1997; Weiss et al. 2004). Satellite remote sensing enables retrieval of LAI globally at different spatial resolutions and temporal frequency with algorithms based on the physics of radiative transfer. Another parameter that characterizes the energy absorption capacity of a vegetation canopy is FPAR, defined as the fraction of photosynthetically active radiation (0.4–0.7 μm) absorbed by the vegetation canopy. FPAR depends on the incident radiation field, architecture and absorption, reflectance and transmission spectra of the canopy as well as the reflectance of the soil and/or understory background. FPAR is well related to NDVI and usually increases with fractional canopy cover and plant leaf area (Myneni and Williams 1994). It is one of the fundamental parameters used to estimate net primary production and for modeling of terrestrial carbon processes (Knorr and Kattge 2005; Pitman 2003; Sellers et al. 1986). Similar to LAI, FPAR has also been identified as one of the fundamental terrestrial state variables in the context of global change studies (GCOS 2006).

The LAI/FPAR products from the Advanced Very High Resolution Radiometer (AVHRR), the Moderate Resolution Imaging Spectroradiometer (MODIS) sensor and the Système Pour l'Observation de la Terre (SPOT) sensor have a large Earth science community user base and the ease of access, provision of pixel quality and validation information have greatly aided the use of these products. Recent research efforts focusing on inter-sensor product consistencies have developed a foundation upon which mature algorithms and a validation framework can act synergistically to further refine the accuracy and precision of these existing long-term products (Brown et al. 2006; Ganguly et al. 2008b; Tarnavsky et al. 2008;

Van Leeuwen et al. 2006). Multi-decadal, validated, consistent global and regional data sets of LAI/FPAR from the AVHRR, MODIS, and the SPOT-VGT sensors are now available at resolutions of 1 km to 1° in service of several national and international initiatives (Chen 2002; Fernandes and Butson 2003; Ganguly et al. 2008a; Myneni et al. 2002). Long-term records of LAI and FPAR are required by various terrestrial biosphere models, like the Terrestrial Ecosystem Model (TEM) (Melillo et al. 1993), Biome-BGC (Running and Gower 1991), Simple Biospheric Model (SiB) (Sellers et al. 1986), Integrated Biosphere Simulated Model (IBIS) (Foley et al. 1996), Lund-Potsdam-Jena (LPJ) dynamic global vegetation model in Land Surface Model (LSM) (Bonan et al. 2003) and the Atmospheric-Vegetation Interactive Model (AVIM) (Jinjun 1995), for the investigation of the response of ecosystems to the changes in climate, carbon cycle, land cover and land use. The Landsat series of sensors also provides a unique opportunity to characterize terrestrial ecosystem processes at a spatial scale at which most natural resources management decisions are made. Although regional- to continental-scale multi-temporal mosaics of Landsat data have been constructed for pilot studies of national land use change monitoring and disturbance mapping (Chander et al. 2009; Hansen et al. 2008; Wulder et al. 2002), the Landsat archive has not yet been exploited to derive long-term biophysical products. This chapter provides a brief overview of the recent progresses in some of the key LAI/FPAR estimation algorithms and resulting biophysical products from the AVHRR, MODIS, SPOT and Landsat data at global to continental scales.

2.2 Algorithmic Theoretical Basis

There is considerable literature on the estimation of LAI from vegetation indices like the Normalized Difference Vegetation Index (NDVI), Simple Ratio and Reduced Simple Ratio (RSR) (Asrar et al. 1984; Chen and Cihlar 1996; Stenberg et al. 2004; Brown et al. 2000). In particular, (Sellers et al. 1996) introduced an empirical algorithm that calculated FPAR as a function of the simple ratio. Lu and Shuttleworth (2002) used this definition of FPAR and approximated the relationship between LAI and FPAR to be exponential (Monteith and Unsworth 1990) for evenly distributed vegetation. Strong positive correlations were found between LAI and NDVI for various vegetation types (Myneni et al. 1997), as well as with simple ratio in coniferous forests (Chen and Cihlar 1996). Site-specific NDVI/RSR-LAI empirical relationships have been used in various ecosystems (Colombo et al. 2003; Fassnacht et al. 1997; Stenberg et al. 2004), but with limited success when applied across sites and vegetation classes.

The sensitivity of NDVI or RSR to LAI is controlled by the relationship between NDVI/RSR and fractional vegetation cover when LAI is in the range of about 2–4 (Carlson and Ripley 1997; Stenberg et al. 2004). Steltzer and Welker (2006) incorporated fractional cover of photosynthetic vegetation for multiple species into the exponential NDVI-LAI model for a regional scale analysis, and

suggested that species composition affects the NDVI-LAI relationship through leaf-level properties (leaf optics, leaf structure and orientation) and canopy-level structural properties that influence the vertical and horizontal distribution of leaf area within a canopy. Relationships between RSR and LAI in closed canopy regimes suggest that the inclusion of the short-wave band decreases the effect of understory reflectance on the retrieval of LAI below a certain threshold value of crown-closure (Nemani et al. 1993; Rautiainen 2005). It is evident that NDVI/RSR-LAI empirical relationships do vary across different species and are sensitive to canopy structure and fractional ground cover. These empirical relationships can also vary both seasonally and inter-annually with respect to phenological development of the vegetation. Thus, a relationship established between LAI and NDVI in a particular year may not be applicable in other years (Wang 2004). Consequently, the empirical relationships will be site-, time-, and species-specific, and, therefore, poorly suited for large-scale operational use (Houborg et al. 2007).

An alternate approach is to use physically based models that describe the interaction of radiation inside a canopy based on physical principles and provide an explicit connection between biophysical variables and canopy reflectance (Combal et al. 2002). The physical models of radiation transfer and interaction in vegetation canopies are usually categorized into four broad types: (1) radiative transfer models (Knyazikhin et al. 1998; Myneni et al. 1989), (2) geometrical optical models (Li and Strahler 1992), (3) hybrid models that incorporate both radiative transfer as well geometric optics (Welles and Norman 1991), and (4) Monte-Carlo simulation models (Lewis 1999; Ross and Marshak 1988). In Sects. 2.1 and 2.2, we describe in brief two state-of-the art physical algorithms in retrieving LAI and FPAR that have evolved over time.

2.3 Modis LAI/FPAR Algorithm: Scaling to AVHRR and Landsat

The MODIS LAI/FPAR algorithm retrieves LAI and FPAR values given sun and view directions, Bidirectional Reflectance Factor (BRF) for each MODIS spectral band, uncertainties in input BRFs, and land cover classes based on a 8-biome classification map (Myneni et al. 2002; Yang et al. 2006). The retrieval technique compares observed and modeled BRFs stored in a Look_Up_Table (LUT) for a suite of canbiome-opy structures and soil patterns that represent an expected range of typical conditions for a given biome type. The modeled BRFs are simulated using a canopy 3D stochastic radiative transfer model. All canopy/soil patterns for which modeled and observed BRFs differ within a specified uncertainty level are considered acceptable solutions. The mean values of LAI averaged over all acceptable solutions and the dispersion are reported as the output of the algorithm (Knyazikhin et al. 1998). The algorithm currently requires: (a) atmospherically corrected surface reflectances at Red and NIR bands, and (b) an 8-biome Land

Cover classification map distinguishing the following biomes types: (1) grasses and cereal crops, (2) shrubs, (3) broadleaf crops, (4) savannas, (5) evergreen broadleaf forests, (6) deciduous broadleaf forests, (7) evergreen needle leaf forests, (8) deciduous needle leaf forests. The biome map reduces the number of unknowns of the inverse problem through the use of simplifying assumptions (e.g., biome-specific models of leaf orientation distributions; Knyazikhin et al. 1998) and standard constants (e.g., biome-specific leaf and soil optical properties at given wavelengths). Over 11 years of Terra MODIS and about 10 years of Aqua MODIS LAI/FPAR products have been generated with this algorithm. Figure 2.1 shows global fields of annual average LAI and FPAR derived from 10 years of Terra MODIS Collection 5 data.

A consistent retrieval of LAI/FPAR from different sensors depends on the parameterization of the physically-based algorithm by adjusting for sensor-specific features of the BRF measurements (spatial resolution, bandwidth, calibration, atmospheric correction, information content, etc.). The theory of canopy spectral invariants provides the required BRF parameterization via a small set of well-defined measurable variables that specify the relationship between the spectral response of vegetation canopy bounded be biome-specific canopy architecture low by a non-reflecting surface to the incident radiation at the leaf and canopy scales (Huang et al. 2007; Yuri Knyazikhin et al. 2011; Lewis and Disney 2007; Smolander and Stenberg 2005). The core theory provides a more easy and efficient way of simulating wavelength dependent BRFs as a function of biome-specific canopy structural attributes. The first order approximation of the BRF for a vegetation canopy bounded below by a non-reflecting surface (Ganguly et al. 2008b; Huang et al. 2007) is approximated as:

$$BRF_{BS,\lambda}(\Omega) = \omega_\lambda R_1(\Omega) + \frac{\omega_\lambda^2}{1 - p\omega_\lambda} R_2(\Omega), \tag{2.1}$$

where ω_λ is the leaf single scattering albedo, R_1 and R_2 are escape probabilities expressed relative to the number of incident photons and p refers to the recollision probability, which is defined as the probability that a photon scattered by a foliage element in the canopy will interact within the canopy again. The spectral absorptance, $a_{\mathrm{BS},\lambda}$ of the vegetation canopy with non-reflecting background can be expressed as:

$$a_{BS,\lambda} = \frac{1 - \omega_\lambda}{1 - p\omega_\lambda} i_0, \tag{2.2}$$

where i_0 is the probability of initial collisions, or canopy interceptance, defined as the portion of photons from the incident beam that are intercepted, i.e., collide with phytoelements for the first time. The FPAR is a weighted integral of Eq. (2.2) over the photosynthetically active radiation (PAR) spectral region (Knyazikhin et al. 1998). The formulation in Eq. (2.1) permits decoupling of the structural and radiometric components of any optical sensor signal, and requires a set of sensor-specific values of configurable parameters, namely the "single scattering albedo"

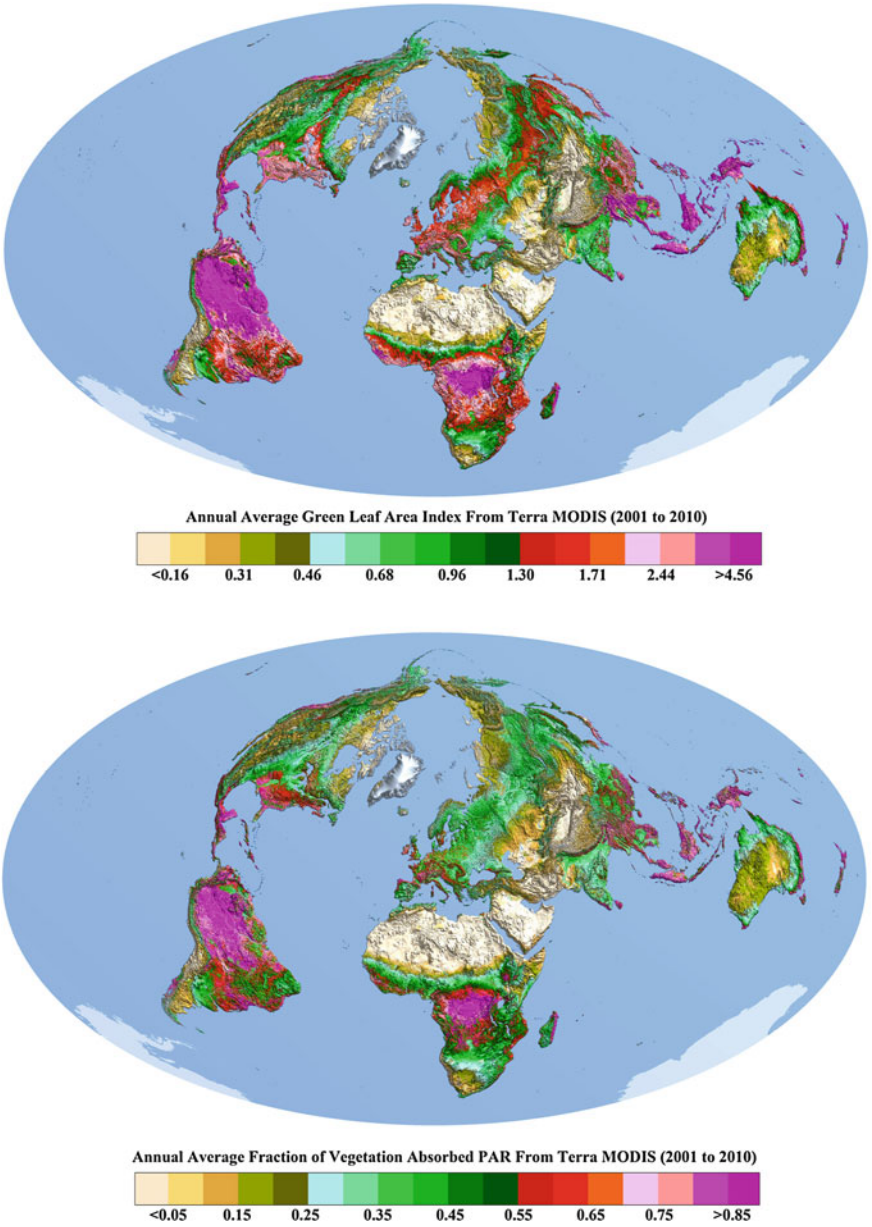

Fig. 2.1 Global *color-coded* maps of Terra MODIS Collection 5 annual average LAI and FPAR. These maps were generated from nearly 10 years of Terra MODIS data (January 2001 to December 2010). Leaf area index (LAI) is defined as the one-sided *green leaf* area per unit ground area in broadleaf canopies and as one-half the total needle surface area per unit ground area in coniferous canopies. FPAR is defined as the fraction of incident photosynthetically active radiation (400–700 nm) absorbed by the green elements of a vegetation canopy. Both quantities are dimensionless

and "uncertainties in surface reflectances" that allow to maintain consistency in the retrieved LAI (Ganguly et al. 2008b). The analytical expressions for the total BRF formulation (e.g. contributions from understory and canopy that are related to reflectance, transmittance and absorptance simulations) are documented in (Ganguly et al. 2012) and are not provided here for the sake of brevity.

To achieve accurate retrievals from a particular sensor like Landsat, the *simulated* surface reflectances making up the LUT should be adjusted to be consistent with the expected range of *measured* surface reflectances. The simulated surface reflectances are highly sensitive to leaf single scattering albedo for medium-to-high LAI and to soil reflectances for low LAI. The single scattering albedo is a function of spatial resolution and accounts for the variation in BRF with sensor spatial resolution and spectral bandwidth (c.f. Sects. 4 and 5 of Ganguly et al. 2008b). The theoretical scaling of the algorithm has been demonstrated by (Ganguly et al. 2008a) to derive LAI from the AVHRR dataset that is consistent with LAI products from other sensors such as MODIS and SPOT. In essence, the BRF can be computed for the sensor-specific resolution and spectral bands by adjusting the single scattering albedo. For Landsat, the initial set of single scattering albedos for the red, NIR and SWIR bands are calculated for each biome as the mean single scattering albedo, such that

$$\overline{\omega} = \int_{\alpha}^{\beta} \omega_{\lambda} f(\lambda) d\lambda \tag{2.3}$$

where $f(\lambda)$ is the relative spectral response function for the Landsat spectral bands. α and β represents the lower and upper bounds for wavelengths in the red and NIR bands and ω_{λ} for different biomes is obtained from field measured leaf spectral measurements (Tian et al. 2004). $\overline{\omega}$ is further tuned to achieve the best possible overlap of simulated BRFs with Landsat observed surface reflectances over a suite of biomes (Ganguly et al. 2012). The dominant factors in classifying the biomes, based on RED, NIR, and SWIR bands, are soil reflectances and single scattering albedos in the respective bands.

The LAI retrieval algorithm exploits the location information in the reflectance cross planes by attributing each point in the spectral space to a specific physical state that is characterized by a background brightness and LAI (Knyazikhin et al. 1998). A pixel can have a background ranging from dark to bright depending on the type of soil, and the LAI can vary over a range for each specific instance of background brightness. Given a Landsat pixel with a reflectance triplet (RED, NIR, SWIR), a merit function is used to select the set of acceptable solutions such that

$$\Delta^2 = \frac{BRF_{NIR} - BRF_{NIR,sim}}{\sigma^2_{NIR}} + \frac{BRF_{RED} - BRF_{RED,sim}}{\sigma^2_{RED}} + \frac{BRF_{SW} - BRF_{SW,sim}}{\sigma^2_{SW}} + \tag{2.4}$$

Here, BRF_{NIR}, BRF_{RED} and BRF_{SW} denote values of measured surface reflectances in the NIR, Red and SWIR spextral bands, while $BRF_{NIR,sim}$, $BRF_{RED,sim}$ and $BRF_{SW,sim}$ correspond to respective simulated reflectances from the LUT. The dispersions σ^2_{NIR}, σ^2_{RED} and σ^2_{SW} quantify combined model and observational uncertainties in NIR, RED and SWIR spectral bands and are configurable parameters in the retrieval approach (Wang et al. 2001). The dispersions are represented as $\sigma_{NIR} = \varepsilon_{NIR} \cdot NIR$, $\sigma_{RED} = \varepsilon_{RED} \cdot RED$, and $\sigma_{SWIR} = \varepsilon_{SWIR} \cdot SWIR$, where ε_{NIR}, ε_{RED}, *and* ε_{SWIR} are the corresponding relative uncertainties (Wang et al. 2001). The optimum values of relative uncertainties used in this study (Ganguly et al. 2008a) are those that result in maximizing the retrieval index without loss of information content. The variable Δ^2, characterizing how close the measured surface reflectances are to the simulated ones, has a Chi square distribution with three degrees of freedom. A value of $\Delta^2 \leq 3$ (3-band inversion) indicates good proximity between observations and simulations. All LAI and soil reflectance values satisfying this criterion constitute the set of acceptable solutions for a particular Landsat observation (NIR, RED and SWIR). In the situation in which $\Delta^2 \leq 3$ fails to localize a solution set, Eq. (2.4) limits to a two band based merit function (excluding SWIR and $\Delta^2 \leq 2$). If the reflectance based inversion fails, an empirical relationship between Simple Ratio and LAI is used to retrieve LAIs. (Ganguly et al. 2012) shows the implementation of the algorithm to derive LAI from Landsat derived surface reflectances. Figure 2.2 shows a 30 m forest LAI for the Conterminous United States derived from the Landsat Global Land Survey (GLS) 2005 dataset.

2.4 Spot GEOV2 LAI/FPAR Algorithm

The GEOV2 LAI and FPAR products derive from the past experience gained in the development of GEOV1 products from the SPOT VEGETATION (GEOV1/VGT) instrument (Baret et al. 2010, 2013) and AVHRR (GEOV1/AVHRR) (A Verger et al. 2012). The theoretical framework for GEOV1/VGT capitalizes on the MODIS and CYCLOPES products development. A database of sites representative at the global scale was populated with MODIS (Myneni et al. 2002; Shabanov et al. 2005) and CYCLOPES (Baret et al. 2007) products that were combined to retain the advantages while minimizing their deficiencies shown in few validation exercises (Garrigues et al. 2008; Weiss et al. 2007; McCallum et al. 2010). The resulting LAI or FPAR products values were used to train a neural network with VEGETATION derived top of the canopy directionally normalized reflectance values as inputs. This approach provided improved performances as compared to both MODIS and CYCLOPES products as demonstrated by few validation exercises (Camacho et al. 2012). However, these GEOV1/VGT products did not improve the continuity of the original MODIS and CYCLOPES products. Further, the pre-processing steps used to normalize the directional effects was based on a 30 days compositing window, making at least a 15 days delay between the actual date of the product and its delivery. Several operational applications require real

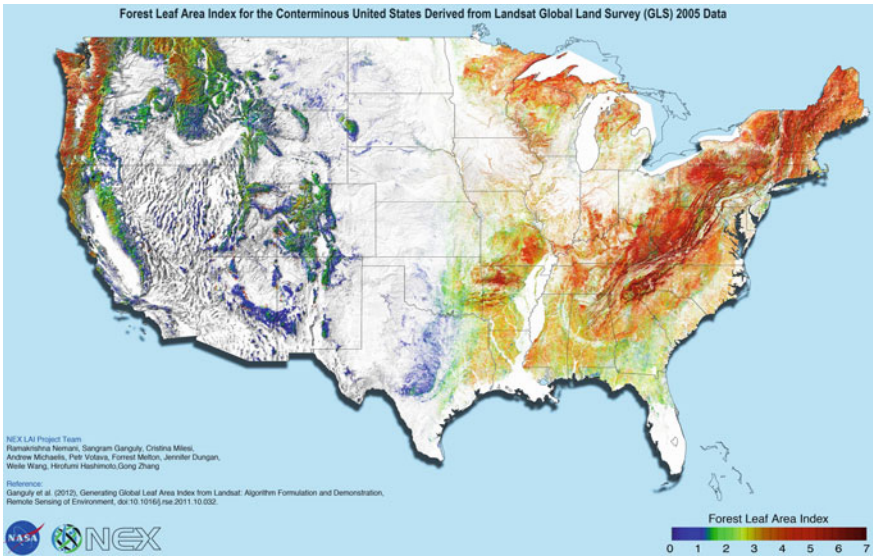

Fig. 2.2 A 30 m Forest LAI for the Conterminous United States derived from the Landsat Global Land Survey (GLS) 2005 dataset. Most of the GLS Landsat scenes are acquired during the peak of growing season. The forested pixels are delineated from the National Land Cover Dataset (NLCD 2006) classification map. The Landsat Ecosystem Disturbance Adaptive Processing System (LEDAPS) framework is used to convert the GLS Landsat data to surface reflectances at the *Red*, NIR and Shortwave Infrared (SWIR) bands. Following the approach as detailed in Ganguly et al. (2012), a radiative transfer based inversion methodology was implemented to retrieve LAI for each pixel given the surface reflectances at the *Red*, NIR and SWIR bands

time delivery of the products and the 15 days delay was clearly a limitation for these users. Finally, the VEGETATION observations were starting only from 1998, while several applications require long time series.

The AVHRR archive was consequently exploited to derive the GEOV1/AVHRR products that extend the GEOV1/VGT products back to 1981. For this purpose, the 1999–2000 years where both VEGETATION and AVHRR overlap were used to train a neural network with GEOV1/VGT products as output and AVHRR reflectance as inputs. The AVHRR LTDR reflectance products (Devadiga et al. 2007) were used here. They correspond to atmospherically corrected and directionally normalized daily values. The corresponding daily LAI and FPAR products were smoothed using TSGF algorithm (Verger et al. 2011) and gap filled using the climatology as background information when limited observations are available. The GEOV1/AVHRR products have been demonstrated to be highly consistent with the GEOV1/VGT product values while improving largely the continuity, with almost no gaps (Verger et al. 2012). Figure 2.3a shows a global map of the GEOV1/VGT LAI product for the first dekad of May 2002 and Fig. 2.3b demonstrates the consistency between the GEOV1/VGT and GEOV1/AVHRR products for the overlapping time period.

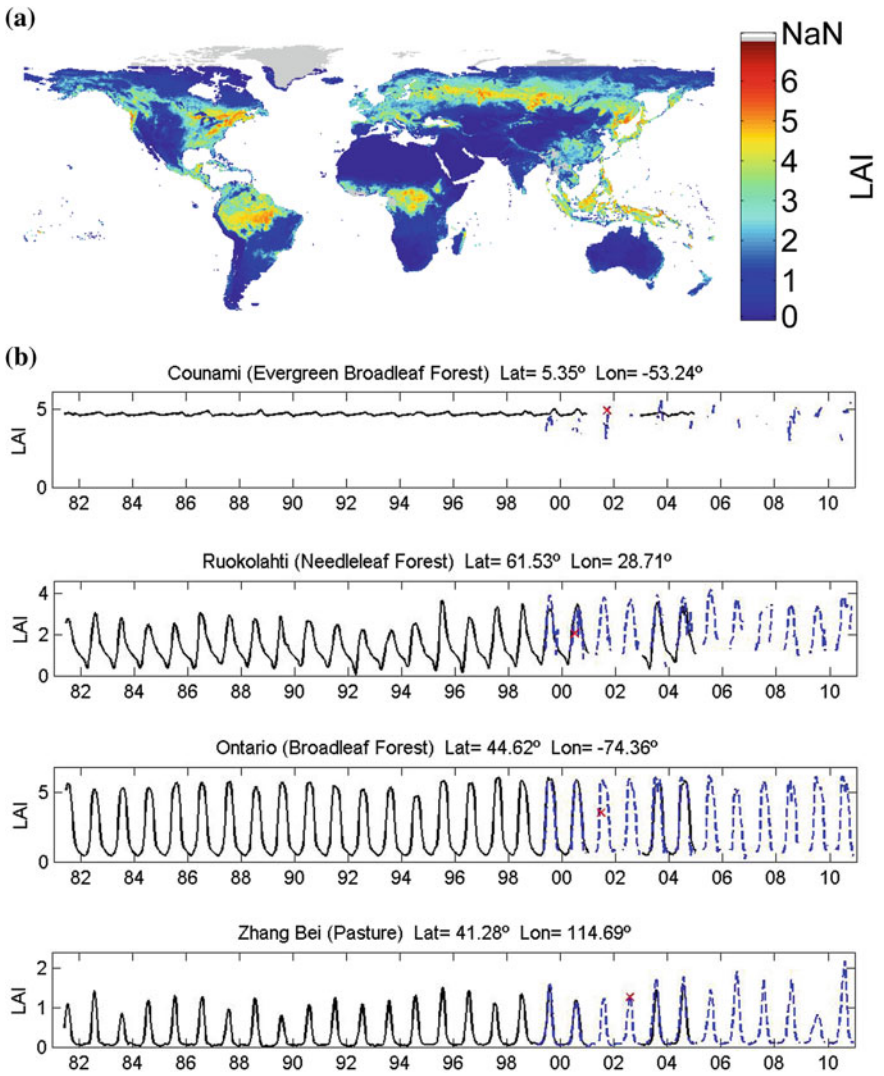

Fig. 2.3 **a** GEOV1/VGT LAI global map for the first dekad of May 2002. **b** Typical temporal profiles derived from GEOV1/AVHRR (*black*) and GEOV1/VGT (*blue*). The overlap period in 1999–2000 shows good consistency between both products. The *red* crosses correspond to available ground measurements of LAI

The GEOV2/VGT products were later developed to improve the continuity of GEOV1/VGT as well as to provide real time estimates of the products. The MODIS and CYCLOPES products were first combined similarly as what was achieved with GEOV1/VGT over a globally representative data set. Then the daily VEGETATION reflectances were used as input to train a neural network to estimate the LAI and FPAR computed from the combination of MODIS and

CYCLOPES products. The resulting daily LAI and FPAR estimates were gap filled and smoothed with the time series-processing algorithm developed previously for GEOV1/AVHRR. The use of the background climatology information on LAI and FPAR values, as well as the smoothing algorithm allowed for short-term projections required for deriving real time estimates of the products. The resulting GEOV2/VGT products were demonstrated to be highly consistent with GEOV1/VGT values with a large improvement in the continuity of the data (Baret et al. 2013). GEOV2/VGT is also fairly consistent with GEOV1/AVHRR and provides thus a time series of more than 32 years of LAI and FPAR products. The GEOV series of products are shown below in Table 2.1.

2.5 Availability of Data Products

The LAI/FPAR products as described above are available to use by the scientific research community. The standard MODIS Collection 5 LAI/FPAR products are available via the Reverb/ECHO web service at http://reverb.echo.nasa.gov/reverb/. The standard MODIS products from 2000 till present are available at a spatial resolution of 1 km and at 8 day temporal frequency. The long-term multi-year (1981 till present) monthly AVHRR LAI/FPAR dataset based on a scaled version of the MODIS algorithm is available upon request at the Climate and Vegetation Research Group at http://cliveg.bu.edu/modismisr/index.html. The GEOV2 LAI/FPAR products can be downloaded freely from the GEOLAND2 web portal located at http://www.geoland2.eu/portal/. They are available at the dekadal time step with 0.05° and 0.0089° spatial sampling interval in lat-lon geographic projection system. The MODIS LAI products at a spatial resolution of 250 m is also available upon request via the NASA Earth Exchange (NEX) web portal located at https://c3.nasa.gov/nex/. NEX in collaboration with USGS EROS is also currently making Landsat derived LAI available to research community on demand basis.

2.6 Validation Efforts

There has been an extensive effort since the inception of the NASA EOS era to validate biophysical products. Validation campaigns from existing network of sites like the BigFoot, AERONET, FLUXNET, EOS Land Validation Core Sites, and Valeri with sustained efforts from several research teams across the globe have provided the necessary platform to validate these biophysical products (Garrigues et al. 2008; Morisette et al. 2006; Pisek and Chen 2007). Both the MODIS and SPOT derived LAI/FPAR products have been extensively validated over a suite of vegetation types and climatic regimes. It is to be noted that "validation" refers to both (a) direct and (b) indirect validation, where the former refers to comparing satellite derived measures with ground truth while the later refers to an exercise

Table 2.1 Table showing the different GEOV products

	GEOV1/VGT	GEOV1/AVHRR	GEOV2/VGT
Sensors	Vegetation	AVHRR	Vegetation
Period	1999-present	1981–1998	1999-present
Spatial sampling	0.0089°	0.05°	0.0089°
Temporal sampling	10 days	10 days	10 days
Near real time	No	No	Yes
Products used for training	MODIS and CYCLOPES	GEOV1/VGT	MODIS and CYCLOPES
Input reflectance	Composited ToC normalized reflectance (CYCLOPES L3a)	Daily ToC directionally normalized	Daily ToA i original view configuration
Output products	LAI, FPAR, FCOVER	LAI, FPAR, FCOVER	LAI, FPAR, FCOVER
Gap filling	No	Yes (using climatology)	Yes (using climatology)
Smoothing	Using BRDF model (30 days window)	Using TSGF and CACAO (variable window)	Using TSGF and CACAO (variable window)
Uncertainties	Based on training data set	Based on local differences with daily estimates	Based on local differences with daily estimates
Definition domain	Yes	Yes	Yes

intercomparing products from different sensor systems to test consistency. Both direct and indirect validation provides a comprehensive knowledge about the accuracy of these products and level of uncertainties that may results due to input data and modeling errors.

Direct validation results for the MODIS LAI/FPAR over vegetation types representative of all the major biome types suggest that the product provides reasonable estimates of LAI for most cover types and land use types (Garrigues et al. 2008; Huang et al. 2006; Kauwe et al. 2011; Pisek and Chen 2007; Sea et al. 2011; Tan et al. 2005; Yang et al. 2006). The MODIS LAI/FPAR products are categorized as a Stage 2 land validated product (http://landval.gsfc.nasa.gov/ProductStatus.php?ProductID=MOD15) that have the following characteristics: (a) LAI accuracy of 0.5 LAI units (uncertainty of 0.66 LAI), FPAR accuracy of 0.1; (b) spatial resolution from 500 m to 1 km; (c) temporal frequency from 4 days to monthly (Yang et al. 2006). Direct validation of the GEOV-1 products also shows a satisfactory agreement with field observations. An indirect validation implementing a scaled version of the MODIS algorithm to derive an LAI dataset from AVHRR shows satisfactory agreement with the MODIS and CYCLOPES LAI products at a range of spatial resolutions and field data (Ganguly et al. 2008a). The Landsat based LAI products are not rigorously validated, however an indirect validation with MODIS shows comparable results (Ganguly et al. 2012). Figure 2.4 briefly demonstrates the results obtained from validation exercises performed with the AVHRR, MODIS and GEOV suite of LAI products.

2.7 Concluding Remarks

Current scientific research and application studies have demonstrated the usefulness of physically derived LAI/FPAR products at local-to-regional scales; however, there are certain limitations in physically based approaches. First, data measurement uncertainties from different sensors can impact the retrieval of a biophysical product. Data uncertainties mostly result from calibration ambiguities, current state of the atmospheric correction algorithm and other effects introduced by solar/view angle corrections. Second, global retrievals of LAI/FPAR products utilize land cover classification maps. Classification inaccuracies are a critical source of error in the LAI retrieval process, especially for those regions undergoing dynamic land cover change (e.g. changes from herbaceous to woody biomes). There are intrinsic limitations in the retrieval algorithms that mostly include (1) accurately modeling the uncertainty of the input reflectances and incorporating the variability in model and input uncertainties with biome types; (2) incorporating a better understory reflectance characterization in simulating the soil reflectance behavior and (3) using constrained definitions of leaf spectral properties as defined by the broad biome types. Finally, a global validation of coarse-to-fine resolution

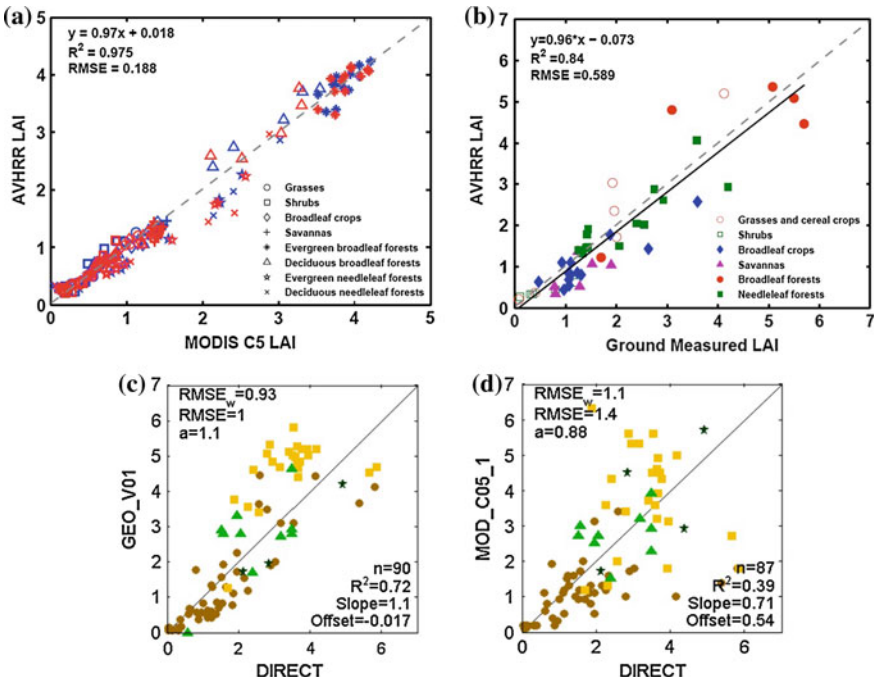

Fig. 2.4 Validation of global LAI/FPAR products. Panel **a** shows comparison between MODIS Collection 5 and AVHRR LAI product from Ganguly et al. (2008b) for the year 2001 (*blue color*) and 2002 (*red color*) for different vegetation classes. The LAI values are globally averaged values for the respective vegetation pixels. Panel **b** shows a comparison of AVHRR LAI as in **a** with field measurements for the six major vegetation classes. Altogether 44 field data values were used (Table B2 of Appendix B in Ganguly et al. 2008b). Panel **c** shows comparison between GEOV1 (GEO_V01 on y-axis) LAI product and ground measurements (DIRECT on x-axis). All ground measurements for the period January, 1999 till August, 2012 are used. Panel **d** shows a similar comparison as in **c** but with MODIS Collection 5 LAI product. Reprinted from Remote Sensing of Environment, 112, Ganguly, S., Samanta, A., Schull, M. A., Shabanov, N. V., Milesi, C., Nemani, R. R., Knyazikhin, Y., Myneni, R.B., Generating vegetation leaf area index Earth system data record from multiple sensors. Part 2: Implementation, analysis and validation, 4318–4332, Copyright (2008), with permission from Elsevier

LAI/FPAR products with ground measurements is a complicated task because of issues with aggregation of plot-level measurements to sensor resolution, limited temporal and spatial sampling of the ground data, field instrument calibrations, sampling errors, etc.

Future research on LAI/FPAR product development will continue along the following directions:

(a) Implementation of physical algorithms to derive high-resolution LAI/FPAR products—this will involve characterizing land cover types at a sufficiently high resolution.

(b) Continued validation of coarse-to-high resolution LAI/FPAR products with available and future acquisitions of field measurements in enhancing the accuracy of the satellite-derived products. Field measurements that provide synoptic knowledge about biome-specific spectral characteristics, will be an integral part of product assessment efforts that feed into algorithm refinement.
(c) Utilization of high-resolution LAI products for estimating above ground biomass and Net Primary Productivity (NPP) estimates. Current algorithms in fusing Landsat derived LAI and canopy height estimates from the ICESat GLAS instrument have shown significant potential in estimating biomass over forested regions.
(d) Enhancing the MODIS experience to Landsat LAI/FPAR products to monitor long-term changes and trends in land surface characteristics due to climatic variability and human-induced changes.

References

Asrar G, Fuchs M, Kanemasu ET, Hatfield JL (1984) Estimating absorbed photosynthetic radiation and leaf-area index from spectral reflectance in wheat. Agron J 76(2):300–306

Baret F, Weiss M, Lacaze R, Camacho F, Makhmara H, Pacholcyzk P, Smets B (2013) GEOV1: LAI and FAPAR essential climate variables and FCOVER global time series capitalizing over existing products. Part1: principles of development and production. Remote Sens Environ 137:299–309

Baret F, Weiss M, Lacaze R, Camacho F, Pacholcyzk P, Smets B (2010) Consistent and accurate LAI, FAPAR, and FCover global products: principles and evaluation of GEOV1 products. In: Proceedings of 3rd RAQRS, 27th Sept.- 1st Oct., Torrent, pp 208–213

Baret F, Hagolle O, Geiger B, Bicheron P, Miras B, Huc M, Berthelot B et al (2007) LAI, fAPAR and fCover CYCLOPES global products derived from VEGETATION: Part 1: Principles of the algorithm. Remote Sens Environ 110(3):275–286. http://www.sciencedirect.com/science/article/B6V6V-4NKJ1K0-1/2/29e421e7954752424d9bfbf9b697ca68

Bonan GB, Levis S, Sitch S, Vertenstein M, Oleson KW (2003) A dynamic global vegetation model for use with climate models: concepts and description of simulated vegetation dynamics. Glob Change Biol 9(11):1543–1566. doi:10.1046/j.1529-8817.2003.00681.x

Brown L, Chen JM, Leblanc SG, Cihlar J (2000) A shortwave infrared modification to the simple ratio for LAI retrieval in boreal forests an image and model analysis. Remote Sens Environ 71(1):16–25. doi:10.1016/S0034-4257(99)00035-8

Brown M, Pinzon JE, Didan K, Morisette JT, Tucker CJ (2006) Evaluation of the consistency of long-term NDVI time series derived from AVHRR, SPOT-vegetation, SeaWiFS, MODIS, and Landsat ETM + sensors. IEEE Trans Geosci Remote Sens 44(7):1787–1793. doi:10.1109/TGRS.2005.860205

Camacho F, Baret F, Cernicharo J, Lacaze R, Weiss M (2012) Quality assessment of the first version of Geoland-2 biophysical variables produced at global scale. In: Sobrino J. (Ed.), Third international symposium on recent advances in quantitative remote sensing. Torrent

Carlson TN, Ripley DA (1997) On the relation between NDVI, fractional vegetation cover, and leaf area index. Remote Sens Environ 62(3):241–252

Chander G, Huang C, Yang L, Homer C, Larson C (2009) Developing consistent landsat data sets for large area applications: the mrlc 2001 protocol. IEEE Geosci Remote Sens Lett 6(4):777–781. doi:10.1109/LGRS.2009.2025244

Chen J (2002) Derivation and validation of Canada-wide coarse-resolution leaf area index maps using high-resolution satellite imagery and ground measurements. Remote Sens Environ 80(1):165–184. doi:10.1016/S0034-4257(01)00300-5

Chen JM, Cihlar J (1996) Retrieving leaf area index of boreal conifer forests using landsat TM images. Remote Sens Environ 55(2):153–162

Chen JM, Rich PM, Gower ST, Norman JM, Plummer S (1997) Leaf area index of boreal forests: Theory, techniques, and measurements. J Geophys Res-Atmos 102(D24):29429–29443

Colombo R, Bellingeri D, Fasolini D, Marino CM (2003) Retrieval of leaf area index in different vegetation types using high resolution satellite data. Remote Sens Environ 86(1):120–131. doi:10.1016/s0034-4257(03)00094-4

Combal B, Baret F, Weiss M, Trubuil A, Mace D, Pragnere A, Myneni RB et al (2002) Retrieval of canopy biophysical variables from bidirectional reflectance using prior information to solve the ill-posed inverse problem. Remote Sens Environ 84(1):1–15. doi:10.1016/S0034-4257(02)00035-4

Demarty J, Chevallier F, Friend AD, Viovy N, Piao S, Ciais P (2007) Assimilation of global MODIS leaf area index retrievals within a terrestrial biosphere model. Geophys Res Lett 34(15):L15402 doi:10.1029/2007GL030014

Devadiga S, Masuoka E, Brown M, Pinzon J, Tucker CJ, Roy DP, Ju J et al (2007) Generating a long-term land data record from the AVHRR and MODIS Instruments. In: IEEE geoscience and remote sensing symposium, 2007, IGARSS 2007. pp 1021–1025 doi:10.1109/IGARSS.2007.4422974

Fassnacht KS, Gower ST, MacKenzie MD, Nordheim EV, Lillesand TM (1997) Estimating the leaf area index of North Central Wisconsin forests using the Landsat Thematic Mapper. Remote Sens Environ 61(2):229–245

Fernandes R, Butson C (2003) A Landsat TM/ETM + based accuracy assessment of leaf area index products for Canada derived from SPOT4/VGT data. Can J Remote Sens 29(2):241–258. http://scholar.google.com/scholar?q=A+Landsat+TM/ETM++basedaccuracy+assessment+of+leaf+area+index+products+for+Canada+derived+from+SPOT4/VGT+data&hl=en&btnG=Search&as_sdt=1,5&as_sdtp=on#0

Field C, Mooney HA (1983) Leaf age and seasonal effects on light, water, and nitrogen use efficiency in a California shrub. Oecologia 56(2–3):348–355

Foley JA, Prentice IC, Ramankutty N, Levis S, Pollard D, Sitch S, Haxeltine A (1996) An integrated biosphere model of land surface processes, terrestrial carbon balance, and vegetation dynamics. Global Biogeochem Cycles 10(4):603–628

GCOS (2006) Systematic observation requirements for satellite-based products for climate. WMO/TD No. 1338 p 103. http://www.wmo.ch/web/gcos/gcoshome.html

Ganguly S, Nemani RR, Zhang G, Hashimoto H, Milesi C, Michaelis A, Wang W et al (2012) Generating global Leaf Area Index from Landsat: Algorithm formulation and demonstration. Remote Sens Environ 122:185–202. doi:10.1016/j.rse.2011.10.032

Ganguly S, Samanta A, Schull MA, Shabanov NV, Milesi C, Nemani RR, Knyazikhin Y et al (2008a) Generating vegetation leaf area index Earth system data record from multiple sensors. Part 2: Implementation, analysis and validation. Remote Sens Environ 112(12):4318–4332. doi:10.1016/j.rse.2008.07.013

Ganguly S, Schull M, Samanta A, Shabanov N, Milesi C, Nemani R, Knyazikhin Y et al (2008b) Generating vegetation leaf area index earth system data record from multiple sensors. Part 1: Theory. Remote Sens Environ 112(12):4333–4343. doi:10.1016/j.rse.2008.07.014

Garrigues S, Lacaze R, Baret F, Morisette JT, Weiss M, Nickeson JE, Fernandes R et al (2008) Validation and intercomparison of global Leaf Area Index products derived from remote sensing data. J Geophys Res 113(G2):G02028. doi:10.1029/2007JG000635

Hansen M, Roy D, Lindquist E, Adusei B, Justice C, Altstatt A (2008) A method for integrating MODIS and Landsat data for systematic monitoring of forest cover and change in the Congo Basin. Remote Sens Environ 112(5):2495–2513. doi:10.1016/j.rse.2007.11.012

Houborg R, Soegaard H, Boegh E (2007) Combining vegetation index and model inversion methods for the extraction of key vegetation biophysical parameters using Terra and Aqua MODIS reflectance data. Remote Sens Environ 106(1):39–58. doi:10.1016/j.rse.2006.07.016

Huang D, Knyazikhin Y, Dickinson RE, Rautiainen M, Stenberg P, Disney M, Lewis P et al (2007) Canopy spectral invariants for remote sensing and model applications. Remote Sens Environ 106(1):106–122

Huang D, Yang WZ, Tan B, Rautiainen M, Zhang P, Hu JN, Shabanov NV et al (2006) The importance of measurement errors for deriving accurate reference leaf area index maps for validation of moderate-resolution satellite LAI products. IEEE Trans Geosci Remote Sens 44(7):1866–1871. doi:10.1109/tgrs.2006.876025

Jinjun J (1995) A climate-vegetation interaction model: simulating physical and biological processes at the surface. J Biogeogr 22:445–451

Kauwe MGD, Disney MI, Quaife T, Lewis P, Williams M (2011) An assessment of the MODIS collection 5 leaf area index product for a region of mixed coniferous forest. Remote Sens Environ 115(2):767–780. doi:10.1016/j.rse.2010.11.004

Knorr W, Kattge J (2005) Inversion of terrestrial ecosystem model parameter values against eddy covariance measurements by Monte Carlo sampling. Glob Change Biol 11(8):1333–1351. doi:10.1111/j.1365-2486.2005.00977.x

Knyazikhin Y, Martonchik JV, Myneni RB, Diner DJ, Running SW (1998) Synergistic algorithm for estimating vegetation canopy leaf area index and fraction of absorbed photosynthetically active radiation from MODIS and MISR data. J Geophys Res 103(D24):32257–32275. doi:10.1029/98JD02462

Knyazikhin Y, Schull MA, Xu L, Myneni RB, Samanta A (2011) Canopy spectral invariants. Part 1: A new concept in remote sensing of vegetation. J Quant Spectrosc Radiat Transfer 112(4):727–735. doi:10.1016/j.jqsrt.2010.06.014

Lewis P (1999) Three-dimensional plant modelling for remote sensing simulation studies using the Botanical Plant Modelling System. Agronomie 19(3–4):185–210

Lewis P, Disney M (2007) Spectral invariants and scattering across multiple scales from within-leaf to canopy. Remote Sens Environ 109(2):196–206

Li XW, Strahler AH (1992) Geometric-optical bidirectional reflectance modeling of the discrete crown vegetation canopy–effect of crown shape and mutual shadowing. IEEE Trans Geosci Remote Sens 30(2):276–292

Lu LX, Shuttleworth WJ (2002) Incorporating NDVI-derived LAI into the climate version of RAMS and its impact on regional climate. J Hydrometeorology 3(3):347–362

McCallum I, Wagner W, Schmullius C, Shvidenko A, Obersteiner M, Fritz S, Nilsson S (2010) Comparison of four global FAPAR datasets over Northern Eurasia for the year 2000. Remote Sens Environ 114(5):941–949. doi:10.1016/j.rse.2009.12.009

Melillo JM, McGuire AD, Kicklighter DW, Moore B, Vorosmarty CJ, Schloss AL (1993) Global climate-change and terrestrial net primary production. Nature 363(6426):234–240

Monteith JL, Unsworth MH (1990) Principles of environmental physics (p 291). Edward Arnold, London

Morisette JT, Baret F, Privette JL, Myneni RB, Nickeson JE, Garrigues S, Shabanov NV et al (2006) Validation of global moderate-resolution LAI products: a framework proposed within the CEOS land product validation subgroup. IEEE Trans Geosci Remote Sens 44(7):1804–1817. doi:10.1109/TGRS.2006.872529

Myneni RB, Hoffman S, Knyazikhin Y, Privette JL, Glassy J, Tian Y, Wang Y et al (2002) Global products of vegetation leaf area and fraction absorbed PAR from year one of MODIS data. Remote Sens Environ 83(1–2):214–231

Myneni RB, Keeling CD, Tucker CJ, Asrar G, Nemani RR (1997) Increased plant growth in the northern high latitudes from 1981 to 1991. Nature 386(6626):698–702. doi:10.1038/386698a0

Myneni RB, Ross J, Asrar G (1989) A review on the theory of photon transport in leaf canopies. Agric For Meteorol 45(1–2):1–153

Myneni RB, Williams DL (1994) On the relationship between FAPAR and NDVI. Remote Sens Environ 49(3):200–211

Nemani R, Pierce L, Running S, Band L (1993) Forest ecosystem processes at the watershed scale: Sensitivity to remotely-sensed Leaf Area Index estimates. Int J Remote Sens 14(13):2519–2534. doi:10.1080/01431169308904290

Pisek J, Chen JM (2007) Comparison and validation of MODIS and VEGETATION global LAI products over four BigFoot sites in North America. Remote Sens Environ 109(1):81–94. doi:10.1016/j.rse.2006.12.004

Pitman AJ (2003) The evolution of, and revolution in, land surface schemes designed for climate models. Int J Climatol 23(5):479–510. doi:10.1002/joc.893

Rautiainen, M (2005) Retrieval of leaf area index for a coniferous forest by inverting a forest reflectance model. Remote Sens Environ 99:295–303

Ross JK, Marshak AL (1988) Calculation of canopy bidirectional reflectance using the Monte-Carlo method. Remote Sens Environ 24(2):213–225

Running SW, Gower ST (1991) Forest-BGC, a general-model of forest ecosystem processes for regional applications.2. Dynamic carbon allocation and nitrogen budgets. Tree Physiol 9(1–2):147–160

Sea WB, Choler P, Beringer J, Weinmann RA, Hutley LB, Leuning R (2011) Documenting improvement in leaf area index estimates from MODIS using hemispherical photos for Australian savannas. Agric For Meteorol 151(11):1453–1461. doi:10.1016/j.agrformet.2010.12.006

Sellers PJ, Mintz Y, Sud YC, Dalcher A (1986) A simple biosphere model (sib) for use within general-circulation models. J Atmos Sci 43(6):505–531

Sellers PJ, Randall DA, Collatz GJ, Berry JA, Field CB, Dazlich DA, et al. (1996) A revised land surface parameterization (SiB2) for atmospheric GCMs. Part1: Model formulation. J Clim 9(4):676–705

Shabanov NV, Huang D, Yang W, Tan B, Knyazikhin Y, Myneni RB, Ahl DE et al (2005) Analysis and optimization of the MODIS leaf area index algorithm retrievals over broadleaf forests. IEEE Trans Geosci Remote Sens 43(8):1855–1865. doi:10.1109/TGRS.2005.852477

Smolander S, Stenberg P (2005) Simple parameterizations of the radiation budget of uniform broadleaved and coniferous canopies. Remote Sens Environ 94(3):355–363. doi:10.1016/j.rse.2004.10.010

Steltzer H, Welker JM (2006) Modeling the effect of photosynthetic vegetation properties on the NDVI–LAI relationship. Ecology 87(11):2765–2772

Stenberg Pauline, Rautiainen Miina, Manninen T (2004) Reduced simple ratio better than NDVI for estimating LAI in Finnish pine and spruce stands. Silva Fennica 38:3–14

Tan B, Hu JN, Huang D, Yang WZ, Zhang P, Shabanov NV, Knyazikhin Y et al (2005) Assessment of the broadleaf crops leaf area index product from the Terra MODIS instrument. Agric For Meteorol 135(1–4):124–134. doi:10.1016/j.agrformet.2005.10.008

Tarnavsky E, Garrigues S, Brown M (2008) Multiscale geostatistical analysis of AVHRR, SPOT-VGT, and MODIS global NDVI products. Remote Sens Environ 112(2):535–549. doi:10.1016/j.rse.2007.05.008

Tian, Y. (2004) Comparison of seasonal and spatial variations of leaf area index and fraction of absorbed photosynthetically active radiation from Moderate Resolution Imaging Spectroradiometer (MODIS) and Common Land Model. J Geophys Res 109(D1), D01103. doi:10.1029/2003JD003777 American Geophysical Union

Van Leeuwen W, Orr B, Marsh S, Herrmann S (2006) Multi-sensor NDVI data continuity: uncertainties and implications for vegetation monitoring applications. Remote Sens Environ 100(1):67–81. doi:10.1016/j.rse.2005.10.002

Verger A, Baret F, Weiss M, Lacaze R, Makhmara H, and Vermote E (2012) Long term consistent global GEOV1 AVHRR biophysical products. 1st EARSeL workshop on temporal analysis of satellite images, Mykonos (Greece) (pp 1–6)

Verger Aleixandre, Baret F, Weiss M (2011) A multisensor fusion approach to improve LAI time series. Remote Sens Environ 115(10):2460–2470. doi:10.1016/j.rse.2011.05.006

Wang Y (2004) Evaluation of the MODIS LAI algorithm at a coniferous forest site in Finland. Remote Sens Environ 91(1):114–127. doi:10.1016/j.rse.2004.02.007

Wang Y, Tian Y, Zhang Y, El-Saleous N, Knyazikhin Y, Vermote E, Myneni RB (2001) Investigation of product accuracy as a function of input and model uncertainties Case study with SeaWiFS and MODIS LAI/FPAR algorithm. Remote Sens Environ 78(3):299–313. doi:10.1016/S0034-4257(01)00225-5

Weiss M, Baret F, Smith GJ, Jonckheere I, Coppin P (2004) Review of methods for in situ leaf area index (LAI) determination Part II. Estimation of LAI, errors and sampling. Agric For Meteorol 121:37–53

Weiss M, Baret F, Garrigues S, Lacaze R (2007) LAI and fAPAR CYCLOPES global products derived from VEGETATION. Part 2: validation and comparison with MODIS collection 4 products. Remote Sens Environ 110(3):317–331. http://www.sciencedirect.com/science/article/B6V6V-4NKB1YP-1/2/7fc55dac10c40359f085241851a6fa37

Welles JM, Norman JM (1991) Instrument for indirect measurement of canopy architecture. Agron J 83(5):818–825

Wulder M, Loubier E, Richardson D (2002) Landsat-7 ETM + orthoimage coverage of Canada. Can J Remote Sens 28(5):667–671

Yang W, Tan B, Huang D, Rautiainen M, Shabanov NV, Wang Y, Privette JL et al (2006) MODIS leaf area index products: from validation to algorithm improvement. IEEE Trans Geosci Remote Sens 44(7):1885–1898. doi:10.1109/TGRS.2006.871215

Chapter 3
Remote Sensing of Forest Biomass

Xiaoyang Zhang and Wenge Ni-meister

Abstract Forest biomass reflects sequestration or release of carbon between terrestrial ecosystems and the atmosphere. Measuring the size and complexity of forest biomass over large areas can enable us to better understand the environmental processes, availability of renewable energy, and global carbon cycle. This chapter reviews recent progress in measuring forest biomass from remote sensing. In quantifying forest biomass, forest properties are often characterized from three types of remote sensing data. Passive optical spectral reflectances are sensitive to vegetation structure (leaf area index, crown size and tree density), texture and shadow. Radar data measure dielectric and geometrical properties of forests. Lidar data characterize vegetation vertical structure and height. Because these instruments have their advantages and disadvantages in reflecting forest properties, data fusion techniques can combine data from multiple sensors and related information from associated databases to achieve improved accuracy in biomass estimation. The remote sensing data or derived forest attributes are commonly correlated to forest biomass using empirical regression models, non-parametric methods, and physically-based allometric models. Although forest biomass is widely estimated at various scales from remote sensing data, models tend to underestimate large biomass densities and overestimate small ones because of saturation issues. Finally, the assessment and validation of forest biomass obtained from remote sensing is critical because current biomass estimates at large area are of large uncertainties.

X. Zhang (✉)
Geospatial Sciences Center of Excellence, South Dakota State University, Brookings, South Dakota, USA
e-mail: xiaoyang.zhang@sdstate.edu

W. Ni-meister
Department of Geography, Hunter College City University of New York, New York, NY, USA
e-mail: wnimeist@hunter.cuny.edu

J. M. Hanes (ed.), *Biophysical Applications of Satellite Remote Sensing*, Springer Remote Sensing/Photogrammetry, DOI: 10.1007/978-3-642-25047-7_3,

3.1 Introduction

Biomass is defined as the mass per unit area of live or dead plant organic matter. Forest ecosystem covers about a third of the Earth's land surface, and it stores about 80 % of all above-ground and 40 % of all below-ground terrestrial organic carbon (IPCC 2001). Forest significantly affects the exchange of gases and energy between the atmosphere and the surface, through photosynthesis and the production of woody plant matter. During productive seasons, forests take up carbon dioxide (CO_2) from the atmosphere and store as plant biomass (Losi et al. 2003; Phat et al. 2004), while they release CO_2 to atmosphere during deforestation, decomposition, and biomass burning (Chambers et al. 2000; Van der Werf et al. 2010; Zhang et al. 2012). Changes of forest biomass in time can be used as an essential climate variable, because it is a direct measure of sequestration or release of carbon between terrestrial ecosystems and the atmosphere. Measuring the size and complexity of forest biomass over large areas would enable scientists to better understand the environmental processes, availability of renewable energy, and global carbon cycle.

Forest biomass consists of above-ground biomass (AGB) and below-ground biomass. AGB represents all living biomass above the soil including stem, stump, branches, bark, seeds, and foliage, while below-ground biomass consists of all living roots excluding fine roots (less than 2 mm in diameter) (FAO 2004). Because it is relatively easy to measure and it accounts for the majority of the total accumulated biomass in forest ecosystem, AGB is usually estimated in many studies to refer as to forest biomass (Aboal et al. 2005; Brown 1997; Kraenzel et al. 2003; Laclau 2003; Losi et al. 2003; Segura and Kanninen 2005).

Forest biomass has been traditionally estimated at field plot scales (usually less than one acre). To calculate tree biomass, a large number of studies have focused on the development of species and site specific allometric models depending on bole diameter at breast height (e.g., Paster et al. 1984; Ter-Mikaelian and Korzukin 1997). The plot estimates of national forest inventories are commonly aggregated to represent forest biomass at national or regional scales (Brown et al. 1999; Jenkins et al. 2001).

Recently, remote sensing has been extensively used as a robust tool in deriving forest structure and AGB because it provides a practical means of acquiring spatially-distributed forest biomass from local, continental, to global areas (Dobson 2000; Saatchi et al. 2007a, b; Houghton et al. 2007; Baccini et al. 2004; Blackard et al. 2008; Zhang and Kondragunta 2006; Zheng et al. 2004; Lu 2006; Le Toan et al. 2011). Three types of remote sensing data are often used, which are passive optical remote sensing, radar (radio detection and ranging, microwave) data, and lidar (light detection and ranging) data. Optical spectral reflectances are sensitive to vegetation structure (leaf area index, crown size and tree density), texture and shadow, which are strongly correlated with AGB. Radar data are related to AGB through measuring dielectric and geometrical properties of forests (Le Toan et al. 2011). Lidar remote sensing is promising in characterizing vegetation vertical structure and height which are then associated to ABG (Lefsky et al. 2005; Drake et al. 2002).

3.2 General Principles

Remote sensing measures the amount of radiation energy in the electromagnetic spectrum that is emitted or reflected by the object or surrounding area being observed. Passive optical remote sensing is particularly sensitive to forest foliage which provides a synoptic view of the area of interest that enables the estimation of biomass values over a large area. Satellite observations represent the top-of-atmosphere (TOA) radiance which is a combination of top-of-canopy (TOC) and atmospheric radiance. TOC reflectance reflects forest properties, particularly, leaf area index (Jarvis and Leverenz 1983), which can be retrieved using vegetation radiative transfer models from satellite data by minimizing atmospheric effects. Canopy green leaves scatter strongly solar radiation in both near-infrared wavelength (0.7–1.3 μm) with a value of about 40–50 % of incident light and green wavelength while the leaves absorb radiation in blue and red wavelengths by chlorophyll and foliage water (Hofer 1978; Ripple 1986). The radiation measured in spectral bands helps us to distinguish the forest properties. A combination of two or more spectral bands produces a vegetation index (VI), which can be calculated by rationing, differencing, rationing differences, and linear combinations of spectral bands. Vegetation index generally enhances vegetation signal while it minimizes the influences from solar irradiance, solar angle, sensor view angle, atmospheric and soil background effects.

Spectral reflectance and vegetation index characterize forest properties and forest biomass. Biomass is basically calculated using the density of unit biomass and the area of forest growth. The unit biomass of AGB (foliage, branch, and stem) can be estimated from optical remote sensing in two different ways. First, forest biomass is generally estimated using models that are statistically established in a relationship between spectral responses and field samples of biomass measurements. The models are generated using either regression analyses or non-parametric imputation approaches. The model parameters or coefficients are affected by various factors that include the atmosphere, sun angle, satellite view angle, phenological state of vegetation growth at the time of image acquisition, topography, and imperfections in radiometric calibration and geo-metric registration. Second, forest biomass is calculated using satellite-based allometric models. Such models are physically meaningful because biomass is associated with forest components (attributes) which include leaf area index (LAI) and canopy structure (crown closure and height). These components can be directly estimated from optical remotely sensed data.

Radar wavelengths range from less than 1 mm to 1 m. They are sensitive to dielectric and geometrical properties of forests, and are thus more closely related to measurements of AGB than optical data, which mainly respond to chemical properties of the vegetation constituents. Theory and observations show that the radar backscattering coefficient (i.e. the normalized backscattered power) varies with increasing forest biomass for lower levels of biomass, but saturates (remains approximately constant) for higher levels.

Light Detection And Ranging (Lidar) use laser ranging to measure the distance between a sensor and target based on half the elapsed time between the emission of a pulse and the detection of a reflected return. Lidar is an active optical remote sensing technology and has been used to measure three dimension vegetation structure.

Lidar systems are classified as small footprint lidar (laser footprint less than 1 m scale) and large footprint lidar (laser footprint 10 m or greater) based on the size of laser footprint or profiling lidar (recording only along a narrow ling at nadir along the flight path) versus scanning lidar (recording across a wide swath along the flight path) systems or discrete return and full waveform recording (Dubayah and Drake 2000; Lefsky et al. 2002; Lim et al. 2003). Discrete return systems record single or multiple returns from a given laser pulse. As the laser signal is reflected back to the sensor, large peaks (i.e., bright returns) represent discrete objects in the path of the laser beam and are recorded as discrete points. Most small footprint lidar systems record discrete energy returns. In contrast, full waveform recording lidar systems digitize the entire reflected energy from a return, resulting in complete sub-meter vertical vegetation profiles. The waveform is a function of canopy height and vertical distribution of foliage, as it is made up of the reflected energy from the surface area of canopy components such as foliage, trunks, twigs, and branches, at varying heights within the large footprint. The total waveform is therefore a measure of both the vertical distribution of vegetation surface area and the distribution of the underlying ground height. Waveform recording instruments are mainly large footprint lidar systems; however, recent advances have seen full waveform instruments with increasingly smaller footprint sizes (Wagner et al. 2006, 2008).

Lidar measures the three-dimensional distribution of plant canopies. The measured canopy structure parameters include vegetation height, cover, and canopy structure. Canopy height is calculated as the distance between the first significant return above threshold and the ground. Canopy cover, the fraction of background obscured by vertically projected foliage and woody area above a certain height, is calculated using the cumulative laser returns from the canopy to that height divided by the total returns from the canopy and the ground. Canopy height profile (CHP) quantitatively represents the relative vertical distribution of canopy surface area. All the lidar measured vegetation structure parameters are closely related to field measurements and are then used to derive AGB estimates.

3.3 Approaches

3.3.1 Field Samples

In situ data of forest biomass are inevitable in biomass estimates. These data serve as a tool to establish biomass predictive models from remote sensing, to evaluate the developed models, and to validate the accuracy of biomass calculations. In situ data can be obtained using a destructive method for a single tree or on an area

(plot) basis (Brown et al. 1989; Brown and Iverson 1992; Brown and Lugo 1992; Gillespie et al. 1992). This method entails harvesting plants, drying them, and then weighing the biomass. The destructive measurement is most accurate but it is very expensive and time consuming.

A non-destructive method is first to measure tree variables, such as canopy crown size, crown depth, tree height, and stem diameter. These components on randomly selected sample trees are then converted to tree biomass using allometric models (Brown et al. 1989; Brown and Iverson 1992; Brown and Lugo 1992; Gillespie et al. 1992; Paster et al. 1984; Ter-Mikaelian and Korzukin 1997). The allomatric models are developed in various forms for biomass estimates (e.g., Ter-Mikaelian and Korzukin 1997; Paster et al. 1984), but the simplest and most commonly used model is:

$$AGB = \alpha D^{\gamma} \tag{3.1}$$

where AGB is above-ground biomass (kg), D is the diameter of tree at breast height (DBH) (m), α and γ are coefficients.

Field data of biomass are commonly measured based on sample plots designed for a specified study. Such field data can be aggregated to generate National Forest Inventories (NFI) (Brown et al. 1999; Jenkins et al. 2001; Chojnacky et al. 2004). The NFI dataset currently contains the most accurate biomass estimates in various countries, such as in Finland and Sweden (Tomppo 1991; Reese et al. 2003), Norway (Gjersten 2005), Austria (Koukal et al. 2005), New Zealand (Tomppo et al. 1999), China (Tomppo et al. 2001), Germany (Diemer et al. 2000), Italy (Maselli et al. 2005), and the United States (Franco-Lopez et al. 2001; McRoberts 2006; McRoberts et al. 2002, 2007). However, it is challenging to extrapolate plot estimates to unit ground area of high-quality geo-referenced ground-truth (Gibbs et al. 2007; Goetz et al. 2009).

3.3.2 Forest Biomass from Passive Optical Remote Sensing

Forest biomass is a function of remote sensing metrics that are closely related to vegetation function (leaf area, volume, photosynthetic activity) and horizontal structure (crown cover). Particularly, forest biomass is estimated using spectral reflectance and vegetation indices from various satellite instruments of passive optical remote sensing. Both empirical regression techniques (Hall et al. 2006; Jakubauskas and Price 1997; Lefsky et al. 2001; Rahman et al. 2008; Zheng et al. 2004; Labrecque et al. 2006; Powell et al. 2010) and nonlinear nonparametric approaches (Baccini et al. 2004; Fraser and Li 2002) are developed to estimate forest biomass following the basic strategy as presented in Fig. 3.1. In contrast, satellite-based allometric models calculate forest biomass using forest attributes derived from satellite data, which is described in Fig. 3.2 (Zhang and Kondragunta 2006; Soenen et al. 2010).

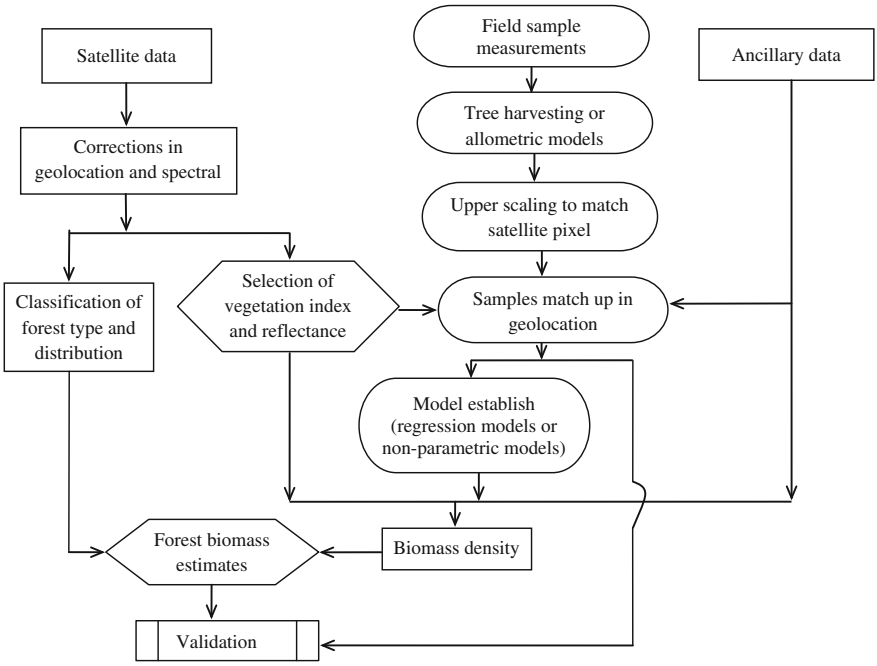

Fig. 3.1 Flowchart of forest biomass estimates from satellite data using empirical models

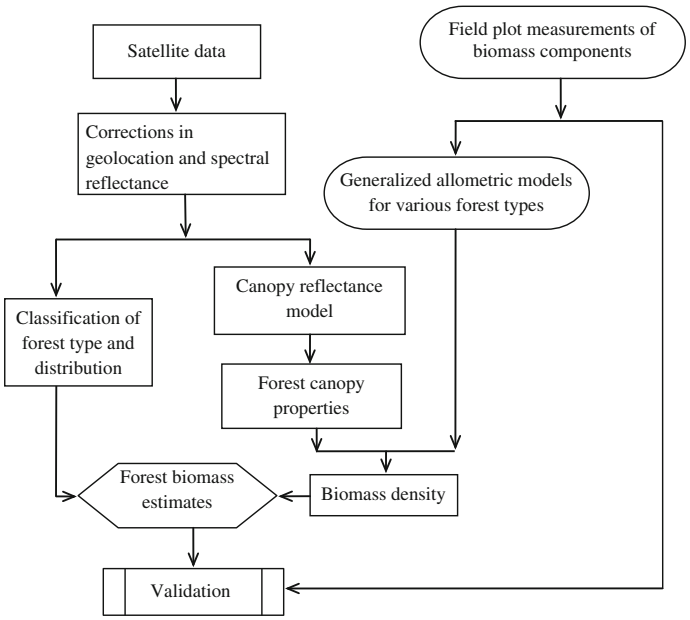

Fig. 3.2 Flowchart of forest biomass estimates from satellite data using physically-based models

3.3.2.1 Satellite-Derived Variables for Biomass Estimates

Several passive optical satellite instruments are available for determining the spatial coverage of biomass. NOAA Advanced Very High Resolution Radiometer (VAHRR) and Moderate Resolution Imaging Spectroradiometer (MODIS) data at a spatial resolution from 250 m to 1,000 m are frequently used to produce biomass estimates at long term and global scales (Dong et al. 2003; Baccini et al. 2004, 2008; Zhang and Kondragunta 2006). Landsat Thematic Mapper (TM), Enhanced Thematic Mapper Plus (ETM+), and Advanced Spaceborne Thermal Emission and Reflection Radiometer (ASTER) with a spatial resolution of 30 m are the most frequently used data to quantify biomass at local and regional scales (e.g., Fazakas et al. 1999; Häme et al. 1997; Krankina et al. 2004; Tomppo et al. 2002; Turner et al. 2004; Muukkonen and Heiskanen 2005). Local tree biomass is usually calculated from high-resolution satellite imagery (HRSI) on QuickBird and IKONOS (Leboeuf et al. 2007; Gonzalez, et al. 2010; Palace et al. 2008). The IKONOS has a spatial resolution of 3.2 m in multispectral and 0.82 m in panchromatic at nadir while QuickBird has a resolution of 2.44 and 0.61 m, separately.

Spectral reflectances of optical remote sensing are the simplest variables in biomass estimates. Spectral bands from visible to short-wave infrared wavelength are all applicable in biomass investigation although the band wavelength varies slightly in various satellite instruments (Table 3.1). Moreover, both IKONOS and QuickBird capture panchromatic, blue, green, red, and near infrared reflectances (NIR).

Vegetation index is particularly useful in biomass observations because it enhances green vegetation signals and minimizes the impacts from surface and atmospheric effects (Bausch 1993; Huete et al. 1985; Ben-Ze'ev et al. 2006; Kaufman and Tanré 1992; Miura et al. 1998). Most frequently used VI is Normalized Difference Vegetation Index (NDVI) because green vegetation has high NIR but low red reflectance. The tasseled cap (TC) transformation or

Table 3.1 Satellite spectral bands (nm) and spatial resolution of optical remote sensing

ETM+	MODIS	SPOT	ASTER	AVHRR	
450–520 (30 m)	450–520 (500 m)				Blue (ρ_B)
530–610 (30 m)	530–610 (500 m)	500–590 (20 m)	520–600 (15 m)		Green (ρ_G)
630–690 (30 m)	630–690 (250 m)	610–680 (20 m)	630–690 (15 m)	0.58–0.68 (1.1 km)	Red (ρ_R)
780–900 (30 m)	780–900 (250 m)	790–890 (20 m)	760–860 (15 m)	0.72–1.0 (1.1 km)	Near Infrared (ρ_{NIR})
	1,230–1,250 (500 m)				Near Infrared (ρ_{NIR2})
1,550–1,750 (30 m)	1,550–1,750 (500 m)	1,580–1,750 (20 m)	1,600–1,700 (30 m)	1.58–1.64 (1.1 km)	Short-wave Infrared (ρ_{SWIR1})
2,090–2,350 (30 m)	2,090–2,350 (500 m)				Short-wave Infrared (ρ_{SWIR2})

Principal Component Analysis (PCA) is another widely applicable tool because it compresses spectral data into a few bands associated with physical scene characteristics (Crist and Cicone 1984). It produces three important variables that are brightness index (TC_b), greenness index (TC_g) and wetness index (TC_w). However, the TC coefficients are sensor-dependent, so that the coefficients have been developed for Landsat TM (Crist and Cicone 1984), Landsat ETM/ETM+ (Huang et al. 2002), MODIS data (Zhang et al. 2002), and IKONOS (Horne 2003), separately. Furthermore, the spatial texture of spectral bands, which is a characteristic for identifying objects or regions of interest in an image, is also used to enhance biomass estimates (Sarker and Nichol 2011). Although there are numerous vegetation indices developed (e.g., Foody et al. 2003; Heiskanen 2006a, b), Table 3.2 lists several commonly used vegetation indices for biomass estimates.

Alternatively, tree canopy attributes are derived from optical satellite data and are considered to be effective proxies of AGB. Tree components are physically correlated in allometric functions (Nelson et al. 1999; Phua and Saito 2003; Popescu et al. 2003), so that several canopy variables that are retrieved from satellites are frequently applied to estimate forest biomass.

(1) LAI is one half the total green leaf area per unit ground surface area and is expressed in terms of square meters of leaf (half surface area) per square meter of ground. This biophysical parameter can be related to photosynthesis, evaporation and transpiration, rainfall interception, and carbon flux. LAI can be estimated from spectral vegetation index using either various regression models (e.g., Heiskanen 2006a, b) or radiative transfer (RT) algorithm (Myneni et al. 1997; Knyazikhin et al. 1998; Myneni et al. 2002). The latter simulates the surface reflectances (bidirectional reflectance factors) as a function of biome type, view/illumination geometry, LAI/FPAR, canopy structure, leaf optical properties, and soil patterns. The final LAI estimate is the average of all acceptable solutions within specified uncertainties from the algorithm outputs which are retrieved from all canopy and soil patterns (Myneni et al. 2002).
(2) Canopy structure, such as tree crown size (area), height, and density, is effective parameters in calculating foliage biomass and total standing biomass (Franklin and Hiernaux 1991; Wu and Strahler 1994; Soenen et al. 2010). The crown size and density in each satellite pixel can be estimated using Li–Strahler geometric-optical (GO) canopy reflectance model (Li and Strahler 1985, 1986). The Li-Strahler model is a three-dimensional model in describing individual plant canopies, which characterizes the variation in reflectance due to different vegetation properties, illumination (solar) and view (sensor) angles. This model treats vegetation cover as a collection of discrete objects and the reflectance from vegetation cover is modeled as a function of the pattern of plants, shadows, and soil visible from a given viewing position.
The GO model has been used to derived meaningful canopy structural parameters from multiangle data (Zeng and Schaepman 2009; Chopping et al. 2008, 2009, 2012; Wang et al. 2011; and Laurent et al 2011). Using data from

Table 3.2 Commonly used vegetation index in biomass estimates

Index	Function	References
Normalized difference vegetation index	NDVI = (ρNIR − ρR)/(ρNIR + ρR)	Rouse et al. (1973)
Simple ratio	SR = ρNIR/ρR	Birth and McVey (1968)
MIR index	MIRI = (ρMIR − ρR)/(ρMIR + ρR)	Roy and Ravan (1996)
Difference vegetation index	DVI = ρNIR − ρR	Tucker (1979)
Modified soil adjusted vegetation index 1	MSAVI1 = (ρNIR − ρR)(1 + L)/(ρNIR + ρR + L)); where L is a soil adjustment factor	Qi et al. (1994)
Modified soil adjusted vegetation index 2	MSAVI2 = ρNIR + 0.5 − ((ρNIR + 0.5)2 − 2(ρNIR − ρR))1/2	Qi et al. (1994)
Enhanced vegetation index	EVI = G(ρNIR − ρR)/(ρNIR + C1*ρR − C2ρB + L); where L = 1, C1 = 6, C2 = 7.5, G = 2.5	Huete et al. (2002)
Chlorophyll based difference index	CI = (ρ850 − ρ710)/(ρ850 − ρ680)	Datt (1999)
MSI	MSI = ρSWIR/ρNIR	Rock et al. (1986)
Tasseled cap transformation	Greenness (TCg), brightness (TCb) and wetness indices (TCw)	Crist 1985; Huang et al. 2002; Zhang et al. 2002; Horne 2003
NDVIc index	NDVIc = ((ρNIR − ρR)/(ρNIR + ρR))(1 − (ρSWIR − ρSWIRmin)/(ρSWIRmax − ρSWIRmin)); where ρSWIRmax and ρSWIRmin are the minimum and mavximum reflectance observed in field plots	Nemani et al. (1993)

NASA's Multi-angle Imaging SpectroRadiometer (MISR), GO model retrieved distributions of crown cover and mean canopy height for forested areas in New Mexico and Arizona (Chopping et al. 2008), which showed good matches with data from US Forest Service (USFS) Interior West (FS-IW) maps, with R^2 values of 0.78 and 0.69, and absolute mean errors of 0.10 and 2.2 m respectively.

Moreover, forest canopy structure can also be derived from multiangle reflectance data using empirical methods and physical or semi-empirical models (Nolin 2004; Chopping et al. 2012). Specifically, a neural network was used to derive canopy height estimates ($R^2 = \sim 0.9$) from the Airborne MISR (AirMISR) after trained by height data from the NASA Laser Vegetation Imaging Sensor (LVIS, a waveform lidar) (Kimes et al. 2006), and from MISR data at 275 m and 1.1 km resolutions after trained and assessed by high-resolution biotope inventory data, where the tree cover estimates had a RMSE of 6.5 % (relative RMSE 56.1 %) at 275 m resolution and of 4.1 % (36.9 %) at 1.1 km resolution, and the tree height estimates had a RMSE of 2.0 m (37.6 %) and 1.3 m (25.4 %), respectively (Heiskanen 2006a, b). Moreover, the multivariate linear regression models were developed to estimate LVIS height measures from 28 AirMISR multi-angle spectral reflectances and from the spectrally invariant escape probability at 7 AirMISR view angles (Schull et al. 2007).

(3) Tree shadow fraction (SF) is defined as the sum of individual tree shadow (TS) areas divided by a ground reference area. Individual TS is composed of both shadowed crown and crown shadow cast on the ground (Li and Strahler 1985). Although it is not a physical attribute of forests, the SF is a suitable variable for estimating forest biomass, LAI, and chlorophyll concentration (Greenberg et al. 2005; Peddle et al. 2001). Besides using canopy reflectance model, SF can also be inferred from medium resolution spectral images (e.g. ETM/ETM+) using spectral unmixing models (Hall et al. 1995; Peddle et al. 1995; Peddle and Johnson 2000). For the HRSI data, TS in a given local or plot area can be calculated by applying a threshold to the digital values of individual pixels (Leboeuf et al. 2007).

3.3.2.2 Simple Models of Biomass Estimates

Forest biomass models in a local area can be produced by comparing single vegetation index or spectral reflectance with samples of field biomass measurements (Roy and Ravan 1996; Calvao and Palmeririm 2004; Salvador and pons 1998; Steininger 2000; Heiskanen 2006a, b). The frequently used empirical model format is:

$$Y = a + bX + \varepsilon \tag{3.2}$$

where Y is forest biomass, a and b are regression coefficients, X is a independent parameter including a vegetation index, spectral reflectance, or satellite-based forest attribute, and ε is the residual.

The variables of either X or Y in this simple format of model could be a logarithm transformation value. In this way, the non-linear correlation between biomass and satellite-derived variables are easily established. The model coefficients (a and b) are commonly determined using the ordinary least-squares (OLS) approach with the assumption that the independent variable is accurately measured. The regression slope from OLS will be biased if spectral bands and vegetation indices are measured with errors. Alternatively, the Reduced Major Axis (RMA) regression, an orthogonal regression technique that minimizes error in both the X and Y directions (Larsson 1993), is believed to be more appropriate at modeling forest biomass (Powell et al. 2010).

Either vegetation index or spectral reflectance has been correlated to AGB in numerous simple linear equations in a local region (Foody et al. 2003; Lu et al. 2004; Rhaman et al. 2005; Roy and Ravan 1996; Heiskanen 2006a, b). The model significance varies greatly with the type of spectral variables and local environment conditions (Foody et al. 2003; Lu 2006). Indeed, spectral biomass models developed using shortwave infrared bands are more reliable as compared to the visible bands which are more sensitive to atmospheric changes (Roy and Ravan 1996*)*. Vegetation indices involving the red spectral band correlates poorly to forest biomass in Brazilian but strongly in Malaysia (Lu et al. 2004). AGB in Canadian forests has no relation to red, NIR, and SWIR reflectance ($R^2 = 0.01$, 0.05, and 0.09, respectively) or to the NDVI ($R^2 = 0.03$) and it is also weakly associated with the SWVI (short-wave vegetation index) computed from the NIR and SWIR (short-wave infrared) channels ($R^2 = 0.25$) (Fraser and Li 2002). Simple band ratios produce higher correlation with AGB than complex vegetation indices do (Lu et al. 2004). TC brightness and wetness parameters show very strong relationship with the biomass values (Roy and Ravan 1996).

SF from QuickBird HRSI linearly correlates to tree biomass and is able to produce a biomass map effectively in a high spatial resolution (Leboeuf et al. 2007) while the RMSE varies from 11 to 18 Mg/ha and bias from 2 to 5 Mg/ha in different test sites. In contrast, SF from IKONOS is related to biomass in a logarithmic form and exhibits a saturation level in large biomass values (Hall et al. 1995; Jasinski and Crago 1999). SF at sub-pixel of SPOT imagery from spectral mixture modeling produces AGB at both deciduous and conifer plots with a RMSE of 32.6 Mg/ha (Soenen et al. 2010).

LAI is also strongly correlated to AGB as demonstrated by regression equations. The linear relationships are generally significant in the deciduous forests in the Western Ghats of Karnataka, India ($R^2 = 0.63$) (Madugundu et al. 2008) and the logarithmic relationship works well in low-density forests and savanna woodlands during the dry season ($R^2 = 0.66$) (Saatchi et al. 2007a, b).

Evidently, although strong relationships between a spectral variable and biomass have been found in various studies, transferring those predictive relationships to different regions remains problematic (Foody et al. 2003).

3.3.2.3 Multiple Regression Models

Biomass estimates can be improved by combining satellite raw spectral bands, spectral vegetation indices, and biophysically-related variables (Hall et al. 2006; Zheng et al. 2004). These variables are usually integrated in multiple regression models to qualify AGB. The basic model format is:

$$Y = b_0 + b_1 X_1 \ldots b_i X_i + \varepsilon \tag{3.3}$$

where Y is the forest biomass; X_i is the independent variable for the *ith* observation assumed to be measured without error; b_0, b_1, b_i are constant parameters of the model that need to be determined; and ε is the error term.

Multiple regression analysis is conducted in several ways. Multiple regression from OLS approach takes all variables into account even though variables themselves are significantly correlated and some variables may have little relationship with biomass. Stepwise regression analysis selects the most significant variables while eliminating less significant variables. Canonical correlation analysis (CCA) enables multiple regression analysis in a simple linear context (Cohen et al. 2003), maximizes the correlation between variables, and provides a set of weights for the spectral bands that aligns them with the variation in the forest variables (Heiskanen 2006a). Basically, multiple regression models assume that the independent variables are uncorrelated and that a linear relationship exists between the remotely sensed data and the biophysical property.

A large number of multiple regression models have been established for the estimates of forest biomass (Table 3.3). Model variables vary greatly in various case studies. It is not always apparent which sets of independent and uncorrelated variables are optimal for a given research.

3.3.2.4 Non-Parametric Imputation Approaches

The non-parametric approach is a computing tool for general purposes. It performs recursive partitioning of data sets, makes no assumptions regarding the distribution and correlation of the input data, effectively solves complex non-linear relationships between the response and predictor variables, and provides easily understandable output. Unlike both simple linear models and multiple regression models, this approach can handle a large number of variables from satellite and ancillary data.

Table 3.3 Multiple regression models from various studies (see Tables 3.1 and 3.2 for definitions of variables)

Model	Satellite instruments	Authors
$AGB = 48.8(\rho_{NIR}/\rho_R) + 2.3Age\text{-}454MASVI\text{-}38;$ $AGB = 111(NDVIc^{10.3}/(NDVIc^{10.3} + 0.35^{10.3}))$ $AGB = 232.5\rho_{NIR} + 2.7Age\text{-}71$ Age is forest age	Single ETM+	Zheng et al. (2004)
$AGB = 122.288 - 1.078TCb\text{-}128.913VARtm2\_9$ $AGB = 64.037 - 1.65\ \rho_{NIR} + 1.405SKtm4\_9$ VARtm2_9 is variance texture with window size of 9 × 9 in TM2 SKtm4_9 is skewness with window size of 9 × 9 in TM4	Single TM	Lu (2005)
$Log(AGB) = 2.99 + 0.18LHH + 0.0467QH + 0.218QV + 0.0028LAI + 0.00059NDVI + 0.0133VCF$	JERS-1, QSCAT H and V MODIS dry season NDVI, percent tree cover (VCF), dry season LAI AGB < 150 Mg/ha	Saatchi et al. (2007a, b)
$AGB = 7.938Log(\rho_G)213.286\ Log(\rho_R) + 9.309\ \rho_{NIR} + 9.953Log(\rho_{SWIR3})$ ρ_{SWIR3} is band 9	ASTER	Heiskanen (2006a, b)
Thailand $AGB = 168 - 9984\rho_B + 8081\rho_G + 4793\rho_R - 238\rho_{NIR} - 436\rho_{SWIR1} - 1338\rho_{SWIR2}$ Brazil $AGB = 195 - 628\rho_B - 3493\rho_G - 1442\rho_R - 532\rho_{NIR} + 2487\rho_{SWIR1} - 1821\rho_{SWIR2}$ Malaysia $AGB = 28\ 343 - 8160\rho_B + 7613\rho_G - 6432\rho_R + 781\rho_{NIR} - 3625\rho_{SWIR1} + 6226\rho_{SWIR2}$	Single ETM+	Foody et al. (2003)
$Log10\ AGB = 3{\cdot}7163 - 0{\cdot}01078TC_b + 0{\cdot}007065TC_w$ $AGB = 73709{\cdot}9241 - 48420{\cdot}44\ NDVI + 67242{\cdot}43MIRI$	Single ETM+	Roy and Ravan (1996)
$1/AGB = \alpha + \beta[(1/NDVI)/Latitude^2] + \gamma Latitude$	Growing season AVHRR	Dong et al. (2003)
ETM bands + spectral indices ETM bands + spectral indices + topographic variables ETM bands + spectral indices + topographic variables + climate variables TC indices + spectral indices TC indices + spectral indices + topographic variables TC indices + spectral indices + topographic variables + climate variables	ETM	Powell et al. (2010)

Neural network

Neural networks typically comprise a large number of simple processing units linked by weighted connections according to a specified architecture. Such networks are typically massively parallel in nature and can learn by example and then generalize (Foody et al. 2001). In the estimates of forest biomass, a variety of neural networks have been used. In mapping the biomass of tropical forests in north-eastern Borneo from Landsat TM data, Foody et al. (2001) found that the multi-layer perception (MLP) performed better than both radial basis function (RBF) and generalized regression neural networks (GRNN). Using SPOT data in Canada, six artificial neural network models containing between 5 and 35 neurons all predicted forest biomass in test set with an accuracy of 60 %, $R^2 = 0.80$, and RMS = 32 Mg/ha (Fraser and Li 2002).

k-Nearest Neighbor Algorithm

The k-nearest neighbor (k-NN) technique is a means to determine points that are most similar or nearest in a covariate space (McRoberts et al. 2002, 2007; Tomppo 1991; Tomppo and Halme, 2004). Given a set of n points, defined in real d-dimensional space, and a query point q, the k-NN technique is simply to calculate the minimum Euclidean distances for the n points to the query point q (Finley and Mcroberts 2008). This technique is generic, which does not specify both the similarity or distance metric and the number of nearest neighbor sampling units on which predictions are based. The biomass estimate in point q is calculated by a weighted value of the biomass value of the k nearest reference points, where the weight is determined by spectral distance. Several methods have been proposed in defining the d-dimensional space within which the nearest neighbor search is executed (Finley and Mcroberts 2008). The methods include the Euclidean distance or a weighted Euclidean distance (Franco-Lopez et al. 2001; Reese et al. 2003), most similar neighbor (MSN) (Moeur and Stage 1995), and gradient nearest neighbor (GNN) (Ohmann and Gregory 2002). The k-NN technique has been frequently applied to calculate forest attributes by combining strategic inventory data, TM imagery, and other ancillary variables (Franco-Lopez et al. 2001; Halme and Tomppo 2001; Katila and Tomppo 2001; McRoberts et al. 2007; Trotter et al. 1997; Fazakas et al. 1999; Ohmann and Gregory 2002; Pierce et al. 2009). When mapping biomass from Landsat TM and inventory data in Canada, k-NN method produces a RMSE of 59 Mg/ha compared with inventory plots (Labrecque et al. 2006).

Regression tree model

Tree-based models, such as Random Forests (RF), establish a large number of trees, in which different bootstrap samples of the data are used to estimate each tree. RF constructs numerous small regression trees that vote on predictions and is robust to over-fitting (Breiman 2001). Similar to other non-parametric approaches, RF models are built up using training samples of biomass (such as Forest Inventory data), satellite data, and other ancillary variables. The tree is composed of a root node (comprised of all of the data), a set of internal nodes which are split using a randomly selected sub-set of the predictor variables, and a set of terminal

nodes (leaves). The splitting procedure stops either when the variability within a node is considered sufficiently low (based on the deviance within the node) or when a prescribed minimum number of cases is reached.

A regression tree approach has been widely used in biomass estimates from time series MODIS data at large scales. Baccini et al. (2004) generated tree-based models using MODIS Nadir BRDF (Bidirectional Reflectance Distribution Function) Adjusted Reflectance (NBAR), climate, and topographic variables in California. The model produced forest biomass in 1 km pixels with an RMSE of 44.4 Mg/ha. Similarly, time series of MODIS NBAR was employed to establish regression tree models to predict AGB in Africa (Baccini et al. 2008), which revealed that the model explained 82 % of the variance in AGB ranging from 0 to 545 Mg/ha, with a RMSE of 50.5 Mg/ha. Houghton et al. (2007) applied bootstrapped regression trees to develop associations between mean MODIS reflectance and biomass in Russia. After creating 500 regression trees using different random samples of the data at 500 m resolution, forest biomass was calculated with an error of $\sim$40 %.

The regression tree approach was also applied to calculate AGB at a spatial resolution of 250 m across conterminous United States (CONUS) (Blackard et al. 2008). The variables used in the model were MODIS-derived land cover, Landsat-derived National Land Cover Dataset (NLCD), topographic variables, monthly and annual climate parameters, and time series of MODIS land surface reflectance and vegetation index. The estimated biomass shows that pixel-based error ranges from 42 to 163 Mg/h and relative error from 0.51 to 0.92 in different regions where the western regions had substantially better results than the eastern regions.

Powell et al. (2010) established RF models using a set of variables that were Landsat TM Tasseled Cap indices, spectral indices, topographic variables, and climate variables. The model was served to calculate biomass in Arizona and Minnesota with a RMSE of 32 and 39 Mg/ha, respectively. A comparison indicates that the RF model consistently yields smaller RMSE than both multiple regression models and a k-NN algorithm (Gradient Nearest Neighbor) do while RF model produces relatively larger variance.

3.3.2.5 Satellite-Based Generalized Allometric Models

Generalized allometric model is a physically-based approach in forest biomass determinations. Although the tree allometric models are generally species-specific and site-specific, they are also generalized to estimate biomass in mixed species across large regions (e.g., Jenkins et al. 2003; Wirth et al. 2004).

Foliage-based generalized allometric model can link remotely sensed data to forest biomass over a continental scale (Zhang and Kondragunta 2006). Unlike DBH, canopy leaf properties are sensitively reflected in passive optical remote sensing and are widely measured from optical satellite data. Thus, a foliage-based allometric model has been developed (Zhang and Kondragunta 2006):

$$AGB = \delta M_f^{\gamma} \tag{3.4}$$

where M_f is foliage biomass, γ and δ are coefficients.

The foliage-based generalized allometric model was applied to estimate forest biomass over North America after coefficients γ and δ were determined using a set of simulated samples (Fig. 3.3, Zhang and Kondragunta 2006). The biomass samples were derived for broadleaf forests and needleleaf forests, respectively, using the existing diameter-based models in literature (e.g., Gholz et al. 1979; Ter-Mikaelian and Korzukin 1997). Foliage biomass was functionally associated with maximum forest LAI and specific leaf area (SLA) (Zhang and Kondragunta 2006). In the processing, the maximum monthly forest LAI derived from MODIS LAI products at a spatial resolution of 1 km (Myneni et al. 2002) was unmixed for needleleaf trees, broadleaf trees, and mixed trees, respectively. Comparison of AGB indicates that estimates from MODIS data and allometric models match the average of Forest Inventory and Analysis (FIA) values at a state level with a RMSE of 21 Mg/ha in eastern US and at a pixel level with a RMSE of 46 Mg/ha in California (Zhang and Kondragunta 2006).

An alternative satellite-based biomass allometric model is established using tree crown surface area (SA) which is a function of horizontal crown radius (r) and vertical crown radius (b). The general allometric models are generated using field measurements for conifer and deciduous trees, separately, using linear least

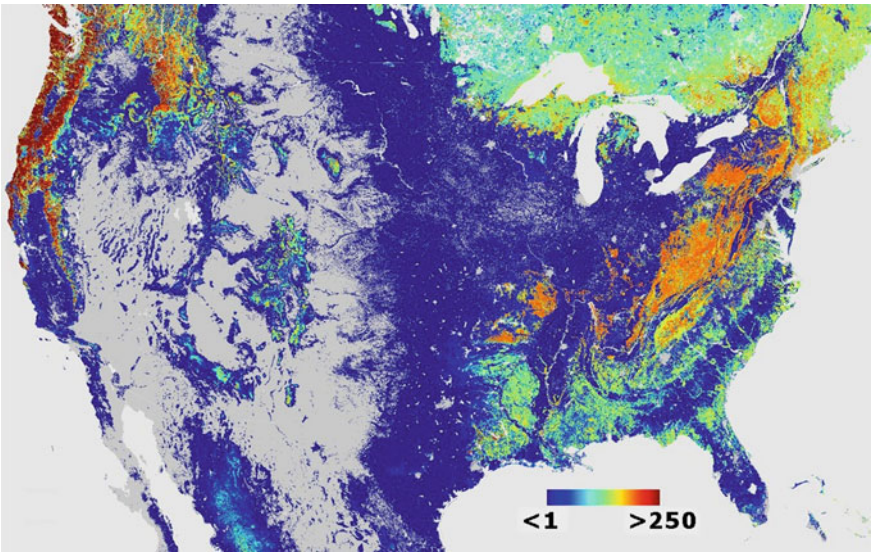

Fig. 3.3 AGB (tons/ha) derived from MODIS land data (1 km) and foliage-based generalized allometric models (from Zhang and Kondragunta 2006)

squares regression. After derived from a geometric-optical canopy reflectance model (Soenen et al. 2010; Chopping et al. 2011), SA is applied to calculate biomass based on general allometric relationships in a large regional area. This approach has been demonstrated to successfully calculate biomass in Canada using 10 m multispectral SPOT data with a plot-based accuracy of 31.7 Mg/ha, which is superior to empirical methods (NDVI and shadow fraction) (Soenen et al. 2010). Similarly, the canopy structure parameters have also been retrieved from MODIS and MISR data for biomass calculation (Chopping et al. 2011).

The satellite-based generalized allometric model has advantages over others although the model construction requires a set of spatially representative samples acquired from field plots. Once the parameters of canopy properties are derived from satellite data, the model could be applied to calculate forest biomass in a broad area without regeneration and calibration of models. As a result, the biomass can be easily updated interannually. Moreover, this approach does not require geo-referenced plots to match satellite-derived parameters. This avoids the model errors caused by matching samples between field measurements and satellite pixels.

3.3.3 Forest Biomass from Radar

Radar data physically measure biomass through the interaction of the radar waves with tree scattering elements. The widely used active radar data are from space-borne synthetic aperture radar (SAR) sensors, such as the L-band ALOS PALSAR, the C-band ERS/SAR, RADARSAT/SAR or ENVISAT/ASAR and the X-band TerraSAR-X instruments, which transmit microwave energy at wavelengths from 3.0 (X-band) to 23.6 cm (L-band). The proposed ESAEarth Explorer Mission BIOMASS is the prime candidate to be the first P-band SAR satellite (Le Toan et al. 2011). The major advantage of all SAR systems is their weather- and day-light-independency.

The ability of radar sensors to measure biomass mainly depends on how deep the radar signals can penetrate into the canopy. The longer the wavelength is, the deeper the penetration is. The L- and P-band backscatter, particularly single polarization HV (horizontal transmit and vertical receive) and HH (horizontal transmit and horizontal receive) polarized backscatter, is strongly dependent on biomass amount (e.g., Le Toan et al. 1992; Ranson and Sun 1994; Imhoff 1995; Saatchi et al. 2007a, b). P-band backscatter shows stronger dependence on biomass than L-band backscatter. The radar backscatter increases approximately linearly with increasing biomass until it is saturated at a certain biomass level that varies with the radar wavelength (Dobson et al. 1992). The biomass level for backscatter saturation is about 200 Mg/ha at P-band, 100 Mg/ha at L-band, and 30–50 Mg/ha at X- and C-bands (Le Toan et al. 2011).

The observed relationship between radar backscatter and biomass can be physically illustrated using electromagnetic scattering models (Ulaby et al. 1990;

Sun and Ranson 1995). HV backscatter is dominated by volume scattering from the woody elements in the trees, so that HV is strongly related to AGB. For the HH and VV polarisations, ground conditions can affect the biomass-backscatter relationship, because HH backscatter comes mainly from trunk-ground scattering while VV backscatter results from both volume and ground scattering.

Forest biomass can be retrieved from radar data using regression models and inversion models. Ranson and Sun (1994, 2000) and Saatchi et al. (2007a, b) used nonlinear regression models to estimate AGB from polarimetric or dual-polarimetic measurements (e.g., HV and HH) by simplifying the complex modeling formulation. At L-band frequency, the regression method can estimate AGB with a 20 % precision up to 200 Mg/ha in boreal and temperate forests and 150 Mg/ha over tropical forests (Saatchi et al. 2007a, b).

The inversion of scattering physical models is often categorized as either random-media or structure-based methods. The random-media approach models the canopy as layers of homogeneous random media (Treuhaft et al. 1996; Treuhaft and Siqueira 2000). However, the structure-based method "grows" realizations of high fidelity, naturally-varying tree structures, and then examines the scattering from a sample of trees to determine canopy scattering properties (Sun and Ranson 1995). In a three-dimensional forest backscatter model, a ray tracing method calculates backscattering components from crowns, trunk, and ground, and scattering between crowns and back-ground, and between trunk and ground (Sun and Ranson 1995).

Because the sensitivity of the backscattering coefficient to biomass decreases at high levels of biomass, inversion methods based solely on intensity are insufficient to cover the full range of the world's biomass. To overcome this problem, polarimetric interferometry is used to derive height of vegetation phase scattering center, which is closely related to vegetation height characteristics. The interferometric coherence can be calculated using two images of a scene acquired at different times (for a repeat pass system) and with slightly different geometries, which is decomposed into the noise decorrelation, the temporal coherence, and the volume decorrelation. The latter is effectively correlated to vegetation height. A major advantage of this approach is that both height and biomass measurements are provided independently by the same radar sensor. In addition, the sensitivity of Polarimetric SAR Interferometry (Pol-InSAR) to height increases with height (and hence biomass), whereas the sensitivity of intensity to biomass decreases with biomass, so that the two measurements complement each other when used jointly in retrieval (Treuhaft and Siqueira 2000).

Application of the radar biomass estimation at continental or globe scale is best at 1.0 ha scale (100 × 100 m pixel size). At this scale, the distribution of AGB over the landscape is both stationary and normal, so that the radar resolution is large enough to reduce the speckle noise and the geolocation error between radar pixel and the plot location. Errors associated with the biomass estimation from radar backscatter or height measurements at this scale can be reduced to acceptable levels (10–20 %) for mapping the aboveground biomass globally (Saatchi et al. 2011).

3.3.4 Biomass from Lidar

Recently lidar data have become widely available to study the linkage between lidar signals and vegetation structure characteristics. AGB is strongly related to lidar measured tree height, ranging from boreal conifers to equatorial rain forests. Lidar data are mainly from airborne discrete-return lidar (Lim and Treitz 2004; Lim et al. 2003; Popescu 2007; García et al. 2010), airborne profiling lidar (e.g., Nelson et al. 1988), airborne waveform lidar (Drake et al. 2002; Lefsky et al. 1999a, b, c; Ni-Meister et al. 2010), satellite waveform lidar (Boudreau et al. 2008; Nelson 2010; Lefsky et al. 2002, 2005), and ground-based lidar (Ni-Meister et al. 2010). Lidar is recognized as the state-of-the-art remote sensing technology for mapping AGB because it is much less sensitive to the saturation problem, compared to conventional optical remote sensing and radar data. In the following, we summarize recent progress on lidar-based biomass mapping activities from small footprint discrete return lidar and large footprint full waveform lidar.

3.3.4.1 Small Footprint Discrete Return Lidar

Small-footprint discrete multiple return lidar data has been collected in many small regions of the globe. Such small footprint airborne lidar systems are available on a commercial basis and are now operationally used for forest resource inventories (Næsset and Gobakken 2008). With many ground lidar systems, complex and detailed vegetation structure data have been recorded over various study sites. These global, regional, and local lidar data can provide the detailed vegetation structure and biomass maps necessary for carbon models and ecosystem processes studies.

AGB has been successfully estimated using small footprint discrete lidar data (Lim et al. 2003; Næsset 2004; Nelson et al. 1988; Popescu et al. 2007; García et al. 2010). Tree height obtained from airborne lidar is a good predictor of biomass for large area averages (Nelson et al. 2003, 2004), which can explain 88 and 85 % of the variability in aboveground and belowground biomass, respectively, for 1,395 sample plots in the coniferous boreal zone of Norway (Næsset and Gobakken 2008). Regardless of the type of lidar system used, however, estimation of biomass is generally conducted based on regression equations relating vegetation biomass to lidar-derived variables across different scales from individual tree to plot and stand scales.

At plot scale, field-measured biomass is regressed against derived statistics from plot-level lidar data. The lidar statistics can be obtained from the individual returns or from the height of canopy (also called canopy height model (CHM)) where lidar return values are interpolated to a certain size raster. This approach adopts distributional metrics such as the mean canopy height and the standard deviation of the canopy height derived from CHM or the raw returns. These metrics are then used in conjunction with regression equations to predict forest

properties (Nelson et al. 1988, 2004; Lim et al. 2003; Lim and Treitz 2004; and García et al. 2010). However, lidar intensity or height combined with intensity data provides better biomass estimate than height metrics alone (García et al. 2010; Lim et al. 2003).

At individual tree level, biomass is estimated based on individual tree structure parameters. The properties are located and measured using different tree segmentation approaches (Popescu and Wynne 2003, 2004). Specifically, the parameters, including tree height, crown width, and tree locations, are derived from CHM using a local maximum filtering approach with a variable circular window to locate individual trees. Crown width is estimated using polynomial fitting on two perpendicular vertical profiles through each identified tree crown. The crown base height for each lidar-derived tree is calculated with the lidar voxel-based approach (Popescu and Zhao 2008).

3.3.4.2 Large Footprint Full Waveform Lidar

Large footprint full-waveform systems can accurately estimate AGB in various forest types. The commonly used airborne lidar data over the past decade are collected from the Scanning Lidar Imager of Canopies by Echo Recovery (SLICER) with a ~15 m footprint and the Laser Vegetation Imaging Sensor (LVIS) with a ~25 m footprint (Blair et al. 1999). These data have been successfully used to retrieve AGB over various biomes across the US, which includes SLICER for estimating AGB in Cascade Mountain Range in Oregon and Washington States (Lefsky et al. 2005) and in Annapolis in Maryland (Lefsky et al. 1999a), and LVIS for AGB in La Selva (Drake et al. 2002), White Mountain (Anderson et al. 2006; Ni-Meister et al. 2010), Sierra Nevada in California (Hyde et al. 2005; Swatantran et al., 2011), and Costa Rica (Drake et al. 2002, 2003). In most studies, stepwise multiple regressions are adapted to predict ground-based measures of stand structure from both conventional canopy structure indices (including mean and maximum canopy surface height and canopy cover) and indices derived from CHP (the height relative to the ground elevation, at which 100, 75, 50 and 25 %, respectively, of the accumulated full waveform energy occurs) (Blair et al. 2004).

The spaceborne Geoscience Laser Altimeter System (GLAS), part of the Ice, Cloud and land Elevation Satellite (ICESat) mission, provides global lidar data with a variable diameter of ~70 m footprint spaced at ~170 m (Zwally et al. 2002; Harding et al. 2005; Lefsky et al. 2005). GLAS is a full waveform digitizing lidar system that acquires information of topography and vertical vegetation structure (Zwally et al. 2002; Harding and Carabajal 2005). The GLAS data have been applied for estimating forest biomass on ground plots in tropical, temperate and conifer forests (Boudreau et al. 2008; Lefsky et al. 2005, 2007; and Nelson et al. 2009). One major limitation of current spaceborne lidar systems is the lack of imaging capabilities, which only provides sparse sampling information on the forest structure. To overcome this problem, it has been fused with other data to

map AGB at large scales. For example, Boudreau et al. (2008) and Nelson et al. (2009) used a multiphase sampling approach to relate GLAS waveforms to airborne profiling lidar measurements which relate to field AGB estimates. Another issue is that the lidar waveform mixes lidar energy returns from both vegetation and underneath topography. The impact of underneath topography needs to be removed using waveform shapes (Lefsky et al. 2005, 2007) and other physical approaches (Yang et al. 2011).

3.3.5 Biomass from Multisensors

Data fusion techniques combine data from multiple sensors and related information from associated databases to achieve improved accuracy. In essence, the methods statistically combine or fuse information from multiple sensors to take advantage of the highly detailed vertical measurements provided by lidar and the broad scale mapping capabilities of horizontal and vertical structure afforded by radar and passive optical remote sensing data.

The fusion methods can lie on employing an approach to stratify field plots with lidar samples of AGB with environmental controls through a stratification or regression approach for scaling up to regions outside of lidar coverage. Stratification of a region is employed by vegetation type, topography and other environmental datasets measured by passive optical and radar remote sensing data (Saatchi et al. 2007a, b, 2011). These methods make it possible to map forest structure and biomass at intermediate scales. Currently, data fusion methods of two or more sensors are based primarily on empirical analyses (Hyde et al. 2007; Walker et al. 2007) although it is suggested to develop physical-based models as a needed advancement.

Most recently, a multisensor dataset has been used to produce a high-resolution "National Biomass and Carbon Dataset for the year 2000 (NBCD2000)" (Kellndorfer et al. 2010, 2013). This dataset includes baseline estimates of basal area-weighted canopy height, aboveground live dry biomass, and standing carbon stock for CONUS at a 30 m spatial resolution. The dataset was developed using an empirical modeling approach that combines USFS FIA data with high-resolution InSAR data acquired from the 2000 Shuttle Radar Topography Mission (SRTM) and optical remote sensing data acquired from the Landsat ETM+ sensor. Both the USGS National Land Cover Dataset 2001(landcover and canopy density) (NLCD 2001) and the existing vegetation type from the LANDFIRE project as well as topographic information from the USGS National Elevation Dataset (NED) were used as spatial predictor layers for canopy height and biomass estimation. The USFS FIA canopy height and biomass were used in model development and validation.

Multisensor data have also been applied to generate a "benchmark" map of biomass carbon stocks over 2.5 billion ha of forests on three tropical continents (Saatchi et al. 2007a, b, 2011). The map was developed through a combination of data from inventory plots, samples of forest structure from ICESat GLAS in

combination of optical and microwave imageries (1-km resolution) of leaf area index, vegetation cover, vegetation types and topography. The uncertainty of biomass estimate ranges from 6 to 53 % at the pixel level (100 ha) and 5 and 1 % at the typical project (10,000 ha) and national (>1,000,000 ha) scales, respectively.

Moreover, a multisensory system has been developed to fully probe forest structure, function and composition of ecosystems at the macroscale (Asner et al. 2012a). For example, the Carnegie Airborne Observatory (CAO) Airborne Taxonomic Mapping System (AToMS) was developed, which includes a high fidelity visible-to-shortwave infrared (VSWIR) imaging spectrometer (280–2,510 nm), dual-laser waveform lidar scanner, and high spatial resolution visible-to-near infrared (VNIR) imaging spectrometer (365–1,052 nm). CAO-2 AToMS is a newer version of CAO Alpha system (Asner et al. 2007), which can measure not only high spatial resolution AGB (Asner et al. 2012b), but also ecosystem physiology, biogeochemistry, species and biodiversity.

There are several other fusion studies in biomass estimates using empirical and physical methods. Hudak et al. (2002) developed an empirical relationship between VIR and lidar data based on kriging and cokriging, which concluded that the spacing of the lidar data should be <250 m for accurate extrapolation. Kellendorfer et al. (2004) extrapolated lidar heights by regressing with SRTM (InSAR), Landsat (tasseled-cap), and a canopy density layer, which resulted in a RMSE of 3 meters. Hyde et al. (2007) and Nelson et al. (2007) developed linear regression models to relate biomass with lidar height metrics, low frequency, low wavelength (VHF), GOESAR (a dual-frequency, dual-polarimetic interferometric airborne SAR instrument), and SAR data, which proved that lidar is most useful for predicting forest biomass and radar adds little improvement in biomass estimation. Slatton et al. (2001) used a physical modeling with Kalman Filter based multiscale estimation to retrieve surface topography and vegetation height from lidar and InSAR data, which demonstrated significant improvement of bare surface topography and vegetation height estimates obtained from InSAR alone. Kimes et al. (2006) studied fusion of lidar with multi-angle data using an optical model to exploit both spectral information and tree structure.

3.4 Validation Efforts Using In-Situ Measurements

The assessment and validation of forest biomass obtained from remote sensing is a critical but challenging task. This requires a large set of reliable in situ data or other estimates of biomass. In-situ measurements are generally obtained using either destructive method or species-specific allometric models in field plots as described in Sect. 3.1. The plots should be designed in homogeneous areas located with GPS (Sarker and Nichol 2011; Soenen et al. 2010; Heiskanen 2006a). Because field measurements are time consuming and expensive, the plot size is generally small (<30 m) and the plot number is limited. These types of data are

applicable for matching with pixels of moderate-high resolution data, such as HRSI and Landsat TM, at local regions.

In-situ data that are comparable with moderate resolution instrument (including MODIS, AVHRR, MISR, and SPOT VGT) pixels are basically not available. As a result, assessment instead of direct validation is implemented for continental biomass estimates. Generally, biomass estimates from MODIS data are evaluated using values estimated from lidar, panchromatic imagery of IKONOS and QuickBird, Landsat TM data (Palace et al. 2008; Chopping 2010; Baccini et al. 2004; Zhang and Kondragunta 2006). To evaluate biomass estimates appropriately at large scales, efforts are needed to upscale biomass measurements from plot (or lidar measurements) to HRSI, Landsat TM and then to MODIS pixels.

Moreover, there are no standard approaches to validate biomass estimates from satellites. The commonly used indices for validation/assessment of biomass are: correlation of determination (R^2), total biomass, mean biomass, root mean square error (RMSE), relative RMSE, bias, and relative bias (Heiskanen 2006a; Labrecque et al. 2006; Powell et al. 2010). High quality of biomass results demonstrated from one index is not necessary to correspond to high quality based on other indices. In a given area, therefore, high quality of biomass estimates needs to be qualified by considering various indices described above.

3.5 Major Findings

Selecting an optimal method from numerous models and satellite instruments for biomass calculations needs to follow several principles. Broadly, methods are acceptable if they meet their objectives or design requirements. Simply speaking, the reasonableness of the methods and the availability of data are the main principles when selecting a method. All biomass models seek to simplify the complexity of forest properties by selectively exaggerating the fundamental variables. Several simple rules are suggested to estimate forest biomass from satellite data. First, a simplest method that will provide acceptable accuracy should then be adopted. Secondly, the assumptions and limitations of the method (model) should always be remembered, and the degree of uncertainty associated with model predictions should always be known. More complex variables used in a model are clearly more versatile, but such method may also be difficult to use widely. Because the presence or absence of available input data constraints the method selection, the availability of data will determine which method may be selected.

Numerous regression modeling approaches have been proposed for empirical estimation of aboveground biomass with satellite variables and biophysical data. A regression model is commonly created by selecting samples in field biomass and satellite variables from one single scene, such as Landsat data. The model is then applied to the entire scene, which is expected to work well in the given condition and satellite scene. However, it is impracticable to directly transfer the model across biomes and the time periods of satellite data because spectral properties

from satellites are strongly dependent on tree canopy phenology, forest types, and local environmental conditions. As a result, each study region should design its own models to match its own condition and to suit related satellite data, or to use the same variables but different coefficients.

Among various regression models, it is difficult to conclude outright that one model is superior to another. Model applicability is dependent upon the locations that a model applied and the criteria (such as RMS, R^2, variance, bias, and overall accuracy) that a validation/assessment is used (Powell et al. 2010). The latter are always inconsistent. Generally, the models including multiple variables produce relatively better estimates than single variable, and vegetation index-based models better than single band models. Because of the uncertainty in the samples and model establishment, linear regression models are recommended since non-linear models could not always enhance the reliability statistics (Heiskanen 2006a, b). Because there is no widely acceptable satellite variables across a range of forest conditions, efforts are needed on comparisons of possible models in practical purpose in a given region.

The non-parametric approach is optimal and robust for biomass estimates using large number of input variables. It can implement various datasets, such as annual time series of MODIS data, radar data, lidar, and other climate parameters. The level of precision of biomass map is strongly dependent on the details of training samples (Labrecque et al. 2006). If the training samples represent a very detailed and broad range of real biomass values, the resultant biomass could be highly accurate. Like the spectral-based regression models (Labrecque et al. 2006), the non-parameteric methods rely on image-specific relationships and the transferability of these relationships to other images is usually difficult. In other words, sufficient field samples over a research area are required to train the non-parametric models. Moreover, to implement the non-parametric methods effectively, it would be important to conduct a feature selection to extract variables which are highly sensitive to forest biomass.

Satellite-based allometric models based on forest structural variables are applicable across biomes once the models are established. The challenge is to retrieve forest canopy attributes appropriately from satellite data. From passive optical satellite data, canopy reflectance models are promising in retrieving forest structural parameters using little or no field data (Soenen et al. 2010). As a result, the satellite-based generalized allometric models are particularly useful for the regions where little field measurements are available (Zhang and Kondragunta 2006). Radar and lidar data have advantages in calculating forest structures for allometric biomass models.

Different satellite instruments serve as a tool to estimate biomass in various spatial resolution and coverage. Lidar data and high-resolution passive satellite imagery, such as QuickBird and IKNOS data, are optimal for the generation of forest inventory at an individual tree crown scale in local areas (Bauer et al. 1997; Wu and Strahler 1994; Gougeon and Leckie 1999; Wulder et al. 2000; García et al. 2010). Optical data at a medium–high spatial resolution produce biomass distributions in a spatial stratification of vegetation. Data such as 30 m Landsat

TM/ETM+ data are most frequently used for calculating forest biomass in regional areas.

MODIS data seem the best option for the investigation of forest biomass in national and continental scales. Although the spatial resolution is relatively coarse (250–1,000 m), time series of MODIS data contain forest phenological variation which is an important variable in producing a trained model that generally represents forest properties well for biomass estimates. However, MODIS pixels are generally a mixture of forests and non-forests, which affect the accuracy of results. Indeed, models established from field plots of a single tree species are better than those with multiple species (Eklundh et al. 2003) and most errors and unexplained variation in the biomass models are from complex vegetation composition (Heiskanen 2006a, b).

Using discrete small footprint lidar data, the individual tree-based approach provides biomass estimates at different levels. This approach permits the estimation of parameters at the tree level rather than at the plot or stand level. It has advantages in highly fragmented forests. However the individual tree-based approach may not be able to separate individual trees in dense forests.

Large footprint full waveform lidar data, based on statistical regression models, can provide accurate estimates of AGB at plot and stand levels. This method predicts field-measured AGB with a large variation of accuracies and uncertainties with the correlation coefficients ranging from 0.65 to 0.96 and with RMSEs from 4 to 80 Mg/ha (Lefsky et al. 1999a, b, c, 2002; Drake et al. 2002, 2003; Nelson et al. 1988; Popescu et al. 2004; Lim et al. 2003; Lim and Treitz 2004; Ni-Meister et al. 2010). The large variations come from using different lidar systems, different lidar sensed vegetation structure parameters, and different site conditions. In general, the higher the lidar point cloud density is, the better the accuracy is. Using combination of different height metrics achieves better accuracies than using maximum canopy height as an AGB predictor. However it remains challenging to accurately estimate biomass over dense deciduous forests at present.

Rader data have the advantage of weather- and daylight-independency. These data are quite useful in the investigation of biomass in tropical forests where cloud-free satellite data are rare. The current use of radar sensors to measure biomass is limited mainly in low biomass regions and biomass change due to deforestation using L- and P-band backscattering.

Finally, saturation is a common issue in biomass estimates using passive optimal satellite and radar data. Because of the saturation of reflectance values, models tend to underestimate large biomass densities and overestimate small ones (Cohen et al. 2003; Blackard et al. 2008). The threshold of saturation varies with satellite data. From MODIS data, aboveground biomass is slightly underestimated for the areas where the biomass is larger than $\sim$300 Mg/ha in tropical Africa (Baccini et al. 2008) and 250 Mg/ha and it is over-predicted biomass values below 45Mg/ha in California (Baccini et al. 2004; Zhang and Kondragunta 2006).

3.6 Future Research Directions

The validation and accuracy analysis of satellite-derived forest biomass is one of the most important and challenging tasks. The accurate estimation of forest biomass is crucial for monitoring fuel wood availability, modeling global carbon consequences, and managing forest change. Unfortunately, current biomass estimates of regional area are widely inconsistent. For example, seven products in Uganda produce total AGB estimates that range from 343 to 2,201 Tg and also present different spatial distribution patterns (Avitabile et al. 2011). Thus, it is necessary to generate a set of reliable true measures of biomass from various ecosystems and plant species, which are sufficient to account for spatial heterogeneity and to represent forest types. It is recognized that reconciliation of the ground and satellite-based biomass is extremely challenging and that in situ datasets collected across ecosystems at spatial scales commensurate with moderate-coarse resolution data are urgently required. To make substantial validation possible in future, it is urgent to generate a series of core validation data sets by up-scaling intensive field data or HRSI and lidar data to the Landsat pixel scale and MODIS pixel scales.

In the mean time, biomass estimates from remote sensing currently still rely heavily on field based training data sets. At regional and global scales, these field measurements are always far from sufficient to represent complex forest properties. Thus, using physically-based or physical approaches to retrieve forest attributes and biomass seems the most promising and avenues of advancement. However to accomplish this, more efforts are needed to investigate canopy reflectance models and forest allometric models which can provide the possibility to estimate biomass at continental scales with limited ground-based training samples.

It must be acknowledged that forest biomass is a dynamic process governed by disturbance and subsequent re-growth processes (Harmon et al. 1990; Wofsy and Harris 2002; Kennedy et al. 2007). Currently biomass at two specific times (images) is generally produced and the difference between the two different periods (images) is commonly used to detect change (Coppin et al. 2004). The detection of trajectory-based changes (Kennedy et al. 2007) is a more meaningful method of monitoring forest biomass. Given that the global archive of long-term Landsat data is being made available for free in a standard processing format (Woodcock et al. 2008) and the time series of global MODIS and VIIRS data is available for more than a decade, robust approaches are required to automatically retrieve forest biomass trajectories.

Passive optical remote sensing, lidar, and microwave remote sensing have advantages and disadvantages in forest biomass estimates. Fusion of both data would be a promising tool. Lidar provides accurate measure of woody volume while accurate estimates of AGB require vegetation types, which can be obtained from passive optical remote sensing. The small footprint lidar data is only limited to small regions. Large footprint lidar can directly measure the horizontal and

vertical vegetation structure of ecosystems at regional and continental scales; however it lacks the imaging capabilities. Fusion of lidar remote sensing with imaging capability from radar or passive optical remote sensing provides a promising in mapping above-ground biomass in future.

References

Aboal JR, Areval JR, Fernandez A (2005) Allometric relationships of different tree species and stand above ground biomass in the Gomera laurel forest (Canary Island). Flora 200:264–274

Anderson HE, Reutebuch SE, McGaughey RJ (2006) A rigorous assessment of tree height measurements obtained using airborne Lidar and conventional field methods. Can J Remote Sens 32(5):355–366

Asner GP, Knapp DE, Kennedy-Bowdoin T, Jones MO, Martin RE, Boardman J, Field CB (2007) Carnegie Airborne Observatory: in-flight fusion of hyperspectral imaging and waveform light detection and ranging (Lidar) for three-dimensional studies of ecosystems. J Appl Remote Sens 1. http://dx.doi.org/10.1117/1111.2794018

Asner GP, Knapp DE, Boardman J, Green RO, Kennedy-Bowdoin T, Eastwood M, Martin RE, Anderson C, Field CB (2012a) Carnegie Airborne Observatory-2: increasing science data dimensionality via high-fidelity multi-sensor fusion. Remote Sens Environ 124:454–465

Asner GP, Clark JK, Mascaro J, Galindo Garcia GA, Chadwick KD, Navarrete Encinals DA, Paez-Acosta G, Cabrera Montenegro E, Kennedy-Bowdoin T, Dugue A, Balaji A, von Hildebrand P, Maatoug L, Phillips Bernal JF, Yepes Quintero AP, Knapp D E, Garcia Davila MC, Jacobson J, Ordones MF (2012b) High-resolution mapping of forest carbon stocks in the Colombian Amazon. Biogeosciences 9:2683–2696

Avitabile V, Herold M, Henry M, Schmullius C (2011) Mapping biomass with remote sensing: a comparison of methods for the case study of Uganda. Carbon Balance Manag 6(7):1–14

Baccini A, Friedl MA, Woodcock CE, Warbington R (2004) Forest biomass estimation over regional scales using multisource data. Geophys Res Lett 31(10):L10501

Baccini A, Laporte N, Goetz SJ, Sun M, Dong H (2008) A first map of tropical Africa's above-ground biomass derived from satellite imagery. Environ Res Lett 3:045011

Bauer G, Schulze E-D, Mund M (1997) Nutrient contents and concentrations in relation to growth of *Picea abies* and *Fagus sylvatica* along a European transect. Tree Physiol 17:777–786

Bausch WC (1993) Soil background effects on reflectance-based crop coefficients for corn. Remote Sens Environ 46:213–222

Ben-Ze'ev E, Karnieli A, Agam N, Kaufman Y, Holben B (2006) Assessing vegetation condition in the presence of biomass burning smoke by applying the aerosol-free vegetation index (AFRI) on MODIS. Int J Remote Sens 27:3203–3221

Birth GS, Mcvey GR (1968) Measuring the colour of growing turf with a reflectance spectrophotometer. Agron J 60:640–643

Blackard JA, Finco MV, Helmer EH, Holden GR, Hoppus ML, Jacobs DM, Lister AJ, Moisen GG, Nelson MD, Riemann R, Ruefenacht B, Salajanu D, Weyermann DL, Winterberger KC, Brandeis TJ, Czaplewski RL, McRoberts RE, Patterson PL, Tymcio RP (2008) Mapping U.S. forest biomass using nationwide forest inventory data and moderate resolution information. Remote Sens Environ 112:1658–1677

Blair JB, Rabine DL, Hofton MA (1999) The laser vegetation imaging sensor: a medium-altitude, digitisation-only, airborne laser altimeter for mapping vegetation and topography. ISPRS J Photogramm Remote Sens 54:115–122

Blair JB, Hofton MA, Rabine DL (2004) Processing of NASA LVIS elevation and canopy (LGE, LCE and LGW) data products, version 1.0. (http://lvis.gsfc.nasa.gov)

Boudreau J, Nelson RF, Margolis HA, Beaudoin A, Guindon L, Kimes DS (2008) Regional aboveground forest biomass using airborne and spaceborne lidar in Quebec. Remote Sens Environ 112:3876–3890

Breiman L (2001) Random forests. Mach Learn 45:5–32

Brown S (1997) Estimating biomass and biomass change of tropical forests: a primer. FAO Forestry Paper 134. FAO, Rome

Brown S, Iverson LR (1992) Biomass estimates for tropical forests. World Resour Rev 4:366–384

Brown S, Lugo AE (1992) Above ground biomass estimates for tropical moist forests of the Brazilian Amazon. Interciencia 17:8–18

Brown S, Gillespie AJR, Lugo AE (1989) Biomass estimation methods for tropical forests with applications to forest inventory data. For Sci 35:881–902

Brown SL, Schroeder P, Kern JS (1999) Spatial distribution of biomass in forests of the eastern USA. For Ecol Manag 123:81–90

Calvao T, Palmeirim JM (2004) Mapping Mediterranean scrub with satellite imagery: biomass estimation and spectral behaviour. Int J Remote Sens 25:3113–3126

Chambers JQ, Higuchi N, Schimel JP, Ferreira LV, Melack JM (2000) Decomposition and carbon cycling of dead trees in tropical forests of the central Amazon. Oecologia 122:380–388

Chojnacky DC, Mickler RA, Meath LS, Woodall CW (2004) Estimates of down woody materials in eastern US forests. Environ Manag 33:S44–S55

Chopping M (2010) CANAPI: canopy analysis with panchromatic imagery. Remote Sens Lett 2(1):21–29

Chopping M, Moisen G, Su L, Laliberte A, Rango A, Martonchik JV et al (2008) Large area mapping of southwestern forest crowncover, canopy height, and biomass using MISR. Remote Sens Environ 112:2051–2063

Chopping M, Nolin A, Moisen GG, Martonchik JV, Bull M (2009) Forest canopy height from the multiangle imaging spectroradiometer (MISR) assessed with high resolution discrete return lidar. Remote Sens Environ 113:2172–2185

Chopping M, Schaaf CB, Zhao F, Wang Z, Nolin AW, Moisen GG, Martonchik JV, Bull M (2011) Forest structure and aboveground biomass in the southwestern United States from MODIS and MISR. Remote Sens Environ 115:2943–2953. doi:10.1016/j.rse.2010.08.031

Chopping M, North M, Chen J, Schaaf CB, Blair JB, Martonchik JV, Bull MA (2012) Forest Canopy cover and height from MISR in topographically complex Southwestern US landscapes assessed with high quality reference data. IEEE J Sel Topics Appl Earth Obs Remote Sens 5:44–58

Cohen WB, Maiersperger TK, Gower ST, Turner DP (2003) An improved strategy for regression of biophysical variables and Landsat ETM + data. Remote Sens Environ 84:561–571

Coppin P, Jonckheere I, Nackaerts K, Muys B (2004) Digital change detection methods in ecosystem monitoring: A review. Int J Remote Sens 25(9):1565–1596

Crist EP (1985) A TM tasseled cap equivalent transformation for reflectance factor data. Remote Sens Environ 17:301–306

Crist EP, Cicone RC (1984) A physically-based transformation of thematic Mapper data—the TM Tasseled Cap. IEEE Trans Geosci Remote Sens GE-22:256–263

Datt B (1999) A new reflectance index for remote sensing of chlorophyll content in higher plants: tests using *Eucalyptus* leaves. J Plant Physiol 154:30–36

Diemer C, Lucaschewski I, Spelsberg G, Tomppo E, Pekkarinen A (2000) Integration of terrestrial forest sample plot data, map information and satellite data. An operational multisource-inventory concept. In: Ranchin T, Wald L (eds) Proceedings of the third conference fusion of earth data: merging point measurements, raster maps and remotely sensed images, Sophia Antipolis, France, 26–28 Jan 2000, pp 143–150. SEE/URISCA, Nice

Dobson MC (2000) Forest information from synthetic aperture Rader. J For 98(6):41–43

Dobson M, Ulaby F, LeToan T, Beaudoin A, Kasischke E and Christensen N (1992) Dependence of radar backscatter on coniferous forest biomass. IEEE Trans Geosci Remote Sens 30(2):412–415

Dong J, Kaufmann RK, Myneni RB, Tucker CJ, Kauppi PE, Liski J, Buermann W, Alexeyev V, Hughes MK (2003) Remote sensing estimates of boreal and temperate forest woody biomass: carbon pools, sources, and sinks. Remote Sens Environ 84:393–410

Drake JB, Dubayah RO, Clark DB, Knox RG, Blair JB, Hofton MA, Chazdon RL, Weishampel JF, Prince SD (2002) Estimation of tropical forest structural characteristics using large-footprint lidar. Remote Sens Environ 79:305–319. Remote Sens Environ 112:3876–3890

Drake JB, Knox RG, Dubayah RO, Clark DB, Condit R, Blair JB, Hofton M (2003) Above-ground biomass estimation in closed canopy Neotropical forests using lidar remote sensing: factors affecting the generality of relationships. Glob Ecol Bio-geogr 12(2):147–159

Dubayah R, Drake JB (2000) Lidar remote sensing for forestry applications. J For 98:44–46

Eklundh L, Hall K, Eriksson H, Ardö J, Pilesjö P (2003) Investigating the use of LANDSAT thematic mapper data for estimation of forest leaf area index in southern Sweden. Can J Remote Sens 29:349–362

Fazakas Z, Nilsson M, Olsson H (1999) Regional forest biomass and wood volume estimation using satellite data and ancillary data. Agric For Meteorol 98–99:417–425

Finley AO, McRoberts RE (2008) Efficient k-nearest neighbor searches for multi-source forest attribute mapping. Remote Sens Environ 112:2203–2211

Foody GM, Cutler ME, Mcmorrow J, Pelz D, Tangki H, Boyd DS, Douglas I (2001) Mapping the biomass of Bornean tropical rain forest from remotely sensed data. Glob Ecol Biogeogr 10:379–387

Foody GM, Boyd DS, Cutler MEJ (2003) Predictive relations of tropical forest biomass from Landsat TM data and their transferability between regions. Remote Sens Environ 85:463–474

Franco-Lopez H, Ek AR, Bauer ME (2001) Estimation and mapping of forest stand density, volume, and cover type using k-nearest neighbors method. Remote Sens Environ 77:251–274

Franklin J, Hiernaux PYH (1991) Estimating foliage and woody biomass in Sahelian and Sudanian woodlands using a remote sensing model. Int J Remote Sens 12:1387–1404

Fraser RH, Li Z (2002) Estimating fire-related parameters in boreal forest using SPOT VEGETATION. Remote Sens Environ 82:95–110

García M, Riaño D, Chuvieco E, Danson FM (2010) Estimating biomass carbon stocks for a Mediterranean forest in Spain using height and intensity LiDAR data. Remote Sens Environ 114:816–830

Gholz HL, Grier CC, Campbell AG, Brown AT (1979) Equations for estimating biomass and leaf area of plants in the Pacific Northwest, Res. Pap. 41, Oregon State University, For. Res. Lab., Corvallis, p 39

Gibbs HK, Brown S, Niles JO, Foley JA (2007) Monitoring and estimating tropical forest carbon stocks: making REDD a reality. Environ Res Lett 2. Doi: 10.1088/1748-9326/2/4/045023

Gillespie AJR, Brown S, Lugo AE (1992) Tropical forest biomass estimation from truncated stand tables. For Ecol Manage 48:69–88

Gjertsen A (2005) Accuracy of forest mapping based on Landsat TM data and a kNN method. In: Olsson H (ed) Proceedings of ForestSat 2005, Borås, Sweden, 31 May–3 June 2005, pp 7–11. http://www.skogsstyrelsen.se

Goetz SJ, Baccini A, Laporte N, Johns T, Walker WS, Kellndorfer JM, Houghton RA, Sun M (2009) Mapping and monitoring carbon stocks with satellite observations: a comparison of methods. Carbon Balance Manag 4(2): doi: 10.1186/1750-0680-1184-1182

Gonzalez P, Asner GP, Battles JJ, Lefsky MA, Waring KM, Palace M (2010) Forest carbon densities and uncertainties from Lidar, QuickBird, and field measurements in California. Remote Sens Environ 114:1561–1575

Gougeon FA, Leckie D (1999) Forest regeneration: individual tree crown detection techniques for density and stocking assessment. Proceedings of the international forum on automated interpretation of high spatial resolution digital imagery for forestry, Feb 10–12, Natural Resources Canada, Canadian Forest Service, Pacific Forestry Centre, Victoria, B.C., pp 169–177

Greenberg JA, Dobrowski SZ, Ustin SL (2005) Shadow allometry estimating tree structural parameters using hyperspatial image analysis. Remote Sens Environ 97:15–25

Hall FG, Shimabukuro YE, Huemmrich KF (1995) Remote sensing of forest biophysical structure in boreal stands of Picea Mariana using mixture decomposition and geometric reflectance models. Ecol Appl 5(4):993–1013

Hall RJ, Skakun RS, Arsenault EJ, Case BS (2006) Modeling forest stand structure attributes using Landsat ETM + data: Application to mapping of aboveground biomass and stand volume. For Ecol Manag 225:378–390

Halme M, Tomppo E (2001) Improving the accuracy of multisource forest inventory estimates by reducing plot location error—a multicriteria approach. Remote Sens Environ 78:321–327

Harding DJ Carabajal CC (2005) ICESat waveform measurements of withinfootprint topographic relief and vegetation vertical structure. Geophys Res Lett 32:L21S10, doi: 10.1029/2005GL023471

Häme T, Salli A, Andersson K, Lohi A (1997) A new methodology for the estimation of biomass of conifer-dominated boreal forest using NOAA AVHRR data. Int J Remote Sens 18:3211–3243

Harmon ME, Ferrell WK, Franklin JF (1990) Effects on carbon storage of conversion of old-growth forests to young forests. Science 247(4943):699–702

Heiskanen J (2006a) Estimating aboveground tree biomass and leaf area index (LAI) in a mountain birch forest using ASTER satellite data. Int J Remote Sens 27:1135–1158

Heiskanen J (2006b) Tree cover and height estimation in the Fennoscandian tundrataiga transition zone using multiangular MISR data. Remote Sens Environ 103:97–114

Hoffer RM (1978) Biological and physical considerations in applying computer-aided analysis techniques to remote sensor data. In: Swain PH, Davis SM (eds) Remote sensing: the quantitative approach, McGraw-Hill Book Company, New York, pp 227–289

Horne JH (2003) A tasseled cap transformation for IKONOS images. ASPRS 2003 Annual Conference Proceedings, May 2003, Anchorage, Alaska

Houghton RA, Butman D, Bunn AG, Krankina ON, Schlesinger P, Stone TA (2007) Mapping Russian forest biomass with data from satellites and forest inventories. Environ Res Lett 2: doi: 10.1088/1748-9326/2/4/045032

Huang C, Wylie B, Homer C, Yang L, Zylstra G (2002) Derivation of a Tasseled cap transformation based on Landsat 7 at-satellite reflectance. Int J Remote Sens 23:1741–1748

Hudak AT, Lefsky MA, Cohen, WB, Berterretche M (2002) Integration of lidar and Landsat ETM+ data for estimating and mapping forest canopy height. Remote Sens Environ 82:397–416

Huete AR, Jackson RD, Post DF (1985) Spectral response of a plant canopy with different soil backgrounds. Remote Sens Environ 17:37–53

Huete AR, Didan K, Miura T, Rodriguez EP, Gao X, Ferreira LG (2002) Overview of the radiometric and biophysical performance of the MODIS vegetation indices. Remote Sens Environ 83:195–213

Hyde P, Dubayah R, Peterson B, Blair JB, Hofton M, Hunsaker C et al (2005) Mapping forest structure for wildlife habitat analysis using waveform LiDAR: validation of montane ecosystems. Remote Sens Environ 96:427–437

Hyde P, Nelson R, Kimes D, Levine E (2007) Exploring LiDAR-RaDAR synergy predicting aboveground biomass in a southwestern ponderosa pine forest using LiDAR, SAR, and InSAR. Remote Sens Environ 106:28–38

Imhoff M (1995) Radar backscatter and biomass saturation: ramifications for global biomass inventory. IEEE Trans Geosci Remote Sens 33(2):511–518

Jakubauskas ME, Price KP (1997) Empirical relationships between biotic and spectral factors of Yellowstone lodgepole pine forests. Photogramm Eng Remote Sens 63(12):1375–1381

Jarvis PG, Leverenz JW (1983) Productivity of temperate, deciduous and evergreen forests. Encycl Plant Physiol No.12D:233–280

Jasinski MF, Crago RD (1999) Estimation of vegetation aerodynamic roughness of natural regions using frontal area density determined from satellite imagery. Agric For Meteorol 94:65–99

Jenkins JC, Birdsey RA, Pan Y (2001) Biomass and NPP estimation for the mid-Atlantic region (USA) using plot-level forest inventory data. Ecol Appl 11:1174–1193

Jenkins JC, Chojnacky DC, Heath LS, Birdsey RA (2003) National-scale biomass estimators for United States tree species. For Sci 49(1):12–35

Katila M, Tomppo E (2001) Selecting estimation parameters for the Finnish multisource National Forest Inventory. Remote Sens Environ 76:16–32

Kaufman YJ, Tanré D (1992) Atmospherically resistant vegetation index (ARVI) for EOS-MODIS. IEEE Trans Geosci Remote Sens 30:261–270

Kellndorfer J, Walker W, Pierce L, Dobson C, Fites JA, Hunsaker C, Vona J, Clutter M (2004) Vegetation height estimation from shuttle radar topography mission and national elevation datasets. J Remote Sens 93(5):339−358

Kellndorfer J, Walker W, LaPoint E, Kirsch K (2010) Statistical fusion of LiDAR, InSAR, and optical remote sensing data for forest stand height characterization: a regional-scale method based on LVIS, SRTM, Landsat ETM+, and ancillary data sets. Geophys Res Lett 115:G00E08

Kellndorfer J, Walker W, LaPoint E, Cormier T, Bishop J, Fiske G, Kirsch K (2013) Vegetation height, biomass, and carbon stock for the conterminous United States: a high-resolution dataset from Landsat ETM+, SRTM-InSAR, National Land Cover Database, and Forest Inventory and Analysis data fusion (in review)

Kennedy RE, Cohen WB, Schroeder TA (2007) Trajectory-based change detection for automated characterization of forest disturbance dynamics. Remote Sens Environ 110:370–386

Kimes DS, Ranson KJ, Sun G, Blair JB (2006) Predicting lidar measured forest vertical structure from multi-angle spectral data. Remote Sens Environ 100:503–511

Knyazikhin Y, Martonchik JV, Myneni RB, Diner DJ, Running SW (1998) Synergistic algorithm for estimating vegetation canopy leaf area index and fraction of absorbed photosynthetically active radiation from MODIS and MISR data. J Geophys Res 103:32257–32274

Koukal T, Suppan F, Schneider W (2005) The impact of radiometric calibration on kNN predictions of forest attributes. In: Olsson H (ed) Proceedings of ForestSat 2005. Borås, Sweden, 31May–3 June 2005, pp 17–21. http://www.skogsstyrelsen.se

Kraenzel M, Castillo A, Moore T, Potvin C (2003) Carbon storage of harvest-age teak (*Tectona grandis*) plantations, Panama. For Ecol Manage 173:213–225

Krankina ON, Harmon ME, Cohen WB, Oetter DR, Zyrina O, Duane MV (2004) Carbon stores, sinks, and sources in forests of Northwestern Russia: can we reconcile forest inventories with remote sensing results? Clim Chang 67:257–272

Labrecque S, Fournier RA, Luther JE, Piercey D (2006) A comparison of four methods to map biomass from Landsat-TM and inventory data in western Newfoundland. For Ecol Manag 226:129–144

Laclau P (2003) Biomass and carbon sequestration of ponderosa pine plantations and native cypress forests in northwest Patagonia. For Ecol Manag 180:317–333

Larsson H (1993) Linear regression for canopy cover estimation in Acacia woodlands using Landsat-TM, -MSS, and SPOT HRV XS data. Int J Remote Sens 14:2129–2136

Laurent VCE, Verhoef W, Clevers JGPW, Schaepman M E (2011) Estimating forest variables from top-of-atmosphere radiance satellite measurements using coupled radiative transfer models. Remote Sens Environ 115:1043–1052

Le Toan T, Beaudoin A, Riom J, Guyon D (1992) Relating forest biomass to SAR data. IEEE Trans Geosci Remote Sens 30:403–411

Le Toan T, Quegan S, Davidson MWJ, Balzter H, Paillou P, Papathanassiou K, Plummer S, Rocca F, Saatchi S, Shugart H, Ulander L (2011) The BIOMASS mission: mapping global forest biomass to better understand the terrestrial carbon cycle. Remote Sens Environ 115:2850–2860

Leboeuf A, Beaudoin A, Fournier RA, Guindon L, Luther JE, Lambert M-C (2007) A shadow fraction method for mapping biomass of northern boreal black spruce forests using QuickBird imagery. Remote Sens Environ 110:488–500

Lefsky MA, Harding D, Cohen W, Parker G, Shugart H (1999a) Surface lidar remote sensing of basal area and biomass in deciduous forests of eastern Maryland, USA. Remote Sens Environ 67:83–96

Lefsky MA, Harding D, Cohen WB, Parker G, Shugart HH (1999b) Surface lidar remote sensing of basal area and biomass in deciduous forests of eastern Maryland, USA. Remote Sens Environ 67:83–98

Lefsky MA, Cohen WB, Acker SA, Parker GG, Spies TA, Harding D (1999c) Lidar remote sensing of the canopy structure and biophysical properties of Douglas-fir western hemlock forests. Remote Sens Environ 70:339–361

Lefsky MA, Cohen WB, Spies TA (2001) An evaluation of alternate remote sensing products for forest inventory, monitoring, and mapping of Douglas-fir forests in western Oregon. Can J For Res 31:78–87

Lefsky MA, Cohen WB, Harding DJ, Parker GG, Acker SA, Gower ST (2002) Lidar remote sensing of above-ground biomass in three biomes. Glob Ecol Bio-geogr 11(5):393–399

Lefsky MA, Hudak AT, Cohen WB, Acker SA (2005) Geographic variability in lidar predictions of forest stand structure in the Pacific Northwest. Remote Sens Environ 95:532–548

Lefsky MA, Keller M, Pang Y, de Camargo P, Hunter MO (2007) Revised method for forest canopy height estimation from the geoscience laser altimeter system waveforms. J Appl Remote Sens 1:013537. doi:10.1117/1.2795724

Li X, Strahler AH (1985) Geometric-optical modeling of a coniferous forest canopy. IEEE Trans Geosci Remote Sens GE-23:207–221

Li X, Strahler AH (1986) Geometric-optical bidirectional reflectance modeling of a coniferous forest canopy. IEEE Trans Geosci Remote Sens GE-24:281–293

Lim KS, Treitz PM (2004) Estimation of above ground forest biomass from airborne discrete return laser scanner data using canopy-based quantile estimators. Scand J For Res 19:558–570

Lim K, Treitz P, Wulder MA, St-Onge B, Flood M (2003) Lidar remote sensing of forest structure. Prog Phys Geogr 27:88–106

Losi CJ, Siccama TG, Condit R, Morales JE (2003) Analysis of alternative methods for estimating carbon stock in young tropical plantations. For Ecol Manage 184(1–3):355–368

Lu D (2005) Aboveground biomass estimation using Landsat TM data in the Brazilian Amazon Basin. Int J Remote Sens 26:2509–2525

Lu D (2006) The potential and challenge of remote sensing-based biomass estimation. Int J Remote Sens 27(7):1297–1328

Lu D, Mausel P, Brondizio E, Moran E (2004) Relationships between forest stand parameters and landsat thematic mapper spectral responses in the Brazilian Amazon Basin. For Ecol Manag 198:149–167

Madugundu R, Nizalapur V, Jha CS (2008) Estimation of LAI and above-ground biomass in deciduous forests: Western Ghats of Karnataka, India. Int J Appl Earth Obs Geoinf 10(2):211–219

Maselli F, Chirici G, Bottai L, Corona P, Marchetti M (2005) Estimation of Mediterranean forest attributes by the application of k-NN procedures to multitemporal Landsat ETM+ images. Int J Remote Sens 26(17):3781–3796

McRoberts RE (2006) A model-based approach to estimating forest area. Remote Sens Environ 103:56–66

McRoberts RE, Nelson MD, Wendt DG (2002) Stratified estimation of forest area using satellite imagery, inventory data, and the k-Nearest Neighbors technique. Remote Sens Environ 82:457–468

McRoberts RE, Tomppo EO, Finley AO, Heikkinen J (2007) Estimating areal means and variances of forest attributes using the k-nearest neighbors technique and satellite imagery. Remote Sens Environ 111(4):466–480

Miura T, Huete AR, van Leeuwen WJD (1998) Vegetation detection through smoke-filled AVHRIS images: An assessment using MODIS band passes. J Geophys Res 103(D24):32,001–32,011

Moeur M, Stage A (1995) Most similar neighbor: an improved sample inference procedure for natural resource planning. For Sci 41(2):337–359
Muukkonen P, Heiskanen J (2005) Estimating biomass for boreal forests using ASTER satellite data combined with standwise forest inventory data. Remote Sens Environ 99:434–447
Myneni RB, Nemani RR, Running SW (1997) Estimation of global leaf area index and absorbed PAR using radiative transfer models. IEEE Trans Geosci Remote Sens 35:1380–1393
Myneni RB et al (2002) Global products of vegetation leaf area and fraction absorbed PAR from year one of MODIS data. Remote Sens Environ 83:214–231
Næsset E, Gobakken T (2008) Estimation of above- and below-ground biomass across regions of the boreal forest zone using airborne laser. Remote Sens Environ 112:3079–3090
Næsset E, Gobakken T, Holmgren J, Hyyppa H, Hyyppa J, Maltamo M et al (2004) Laser scanning of forest resources: the Nordic experience. Scand J For Res 19:482–499
Nelson R (2010) Model effects on GLAS-based regional estimates of forest biomass and carbon. Int J Remote Sens 31:1359–1372
Nelson R, Swill R, Krabill W (1988) Using airborne lasers to estimate forest canopy and stand characteristics. J For 86:31–38
Nelson BW, Mesquita R, Pereira JLG, de Souza SGA, Batista GT, Couta LB (1999) Allometric regressions for improved estimate of secondary forest biomass in the Central Amazon. For Ecol Manag 117:149–167
Nelson R, Parker G, Hom M (2003) A portable airborne laser system for forest inventory. Photogramm Eng Remote Sens 69(3):267–273
Nelson R, Short A, Valenti M (2004) Measuring biomass and carbon in Delaware using and airborne profiling lidar. Scand J For Res 19:500–511
Nelson RF, Hyde P, Johnson P, Emessiene B, Imhoff ML, Campbell R, Edwards W (2007) Investigating RaDAR-LiDAR synergy in a North Carolina pine forest. Remote Sens Environ 110:98–108
Nelson R, Ranson KJ, Sun G, Kimes DS, Kharuk V, Montesano P (2009) Estimating Siberian Timber volume Using MODIS and ICESat/GLAS. Remote Sens Environ 113:691–701
Nemani RR, Pierce LL, Band LE, Running SW (1993) Forest ecosystem processes at the watershed scale: Sensitivity to remotely sensed leaf area index estimates. Int J Remote Sens 14:2519–2534
Ni-Meister W, Lee S, Strahler AH, Woodcock CE, Schaaf C, Yao T et al (2010) Assessing general relationships between aboveground biomass and vegetation structure parameters for improved carbon estimate from lidar remote sensing. J Geophys Res 115:1–12
Nolin A W (2004) Towards retrieval of forest cover density over snow from the Multiangle Imaging SpectroRadiometer (MISR). Hydrol Process 18:3623–3636
Ohmann JL, Gregory MJ (2002) Predictive mapping of forest composition and structure with direct gradient analysis and nearest neighbor imputation in coastal Oregon, USA. Can J For Res 32:725–741
Palace M, Keller M, Asner GP, Hagen S, Braswell B (2008) Amazon forest structure from IKONOS satellite data and the automated characterization of forest canopy properties. Biotropica 40(2):141–150, doi: 10.1111/j.1744-7429.2007.00353.x
Paster J, Aber J, Melillo JM (1984) Biomass prediction using generalized allometric regressions for some Northeast tree species. For Ecol Manag 7:265–274
Peddle DR, Johnson RL (2000) Spectral mixture analysis of airborne remote sensing imagery for improved prediction of leaf area index in mountainous terrain, Kananaskis, Alberta. Can J Remote Sens 26:176–187
Phat NK, Knorr W, Kim S (2004) Appropriate measures for conservation of terrestrial carbon stocks—Analysis of trends of forest management in Southeast Asia. For Ecol Manage 191:283–299
Phua M, Saito H (2003) Estimation of biomass of a mountainous tropical forest using Landsat TM data. Can J Remote Sens 29:429–440

Peddle DR, Brunke SP, Hal, FG (2001) A comparison of spectral mixture analysis and ten vegetation indices for estimating boreal forest biophysical information from airborne data. Can Remote Sens 27(6):627–635

Pierce KB, Ohmann JL, Wimberly MC, Gregory MJ, Fried JS (2009) Mapping wildland fuels and forest structure for land management: a comparison of nearest neighbor imputation and other methods. Can J For Res 39:1901–1916

Popescu SC (2007) Estimating biomass of individual pine trees using airborne lidar. Biomass and Bioenergy 31(9):646–655

Popescu SC, Zhao K (2008) A voxel-based lidar method for assessing crown base height. Remote Sens Environ 112(3):767–781

Popescu SC, Wynne RH, Nelson RF (2003) Measuring individual tree crown diameter with lidar and assessing its influence on estimating forest volume and biomass. Can J Remote Sens 29(5):564–577

Popescu SC, Wynne RH, Scrivani JA (2004) Fusion of small-footprint lidar and multispectral data to estimate plot-level volume and biomass in deciduous and pine forests in Virginia, USA. For Sci 50:551–565

Powell SL, Warren B, Cohen WB, Healey SP, Kennedy RE, Moisen GG, Pierce KB, Ohmann JL (2010) Quantification of live aboveground forest biomass dynamics with Landsat time-series and field inventory data: a comparison of empirical modeling approaches. Remote Sens Environ 114:1053–1068

Qi J, Chehbouni A, Huete AR, Kerr YH (1994) Modified Soil adjusted vegetation index (MSAVI). Remote Sens Environ 48:119–126

Rahman MM, Csaplovics E, Koch B (2005) An efficient regression strategy for extracting forest biomass information from satellite sensor data. Int J Remote Sens 26:1511–1519

Rahman MH, Okubo A, Kawai S, Sugiyama S (2008) Assessing microbial community in andisol differing in management practices by biochemical and molecular fingerprinting methods. Int J Soil Sci 3:1–10

Ranson KJ, Sun G (1994) Northern forest classification using temporal multifrequency and multipolarimetric SAR images. Remote Sens Environ 47(2):142–153

Ranson KJ, Sun G (2000) Effects of environmental conditions on boreal forest classification and biomass estimates with SAR. IEEE Trans Geosci Remote Sens 38(3):1242–1252.

Reese H, Nilsson M, Granqvist Pahlén T, Hagner O, Joyce S, Tingelöf U, Egberth M, Olsson H (2003) Countrywide estimates of forest variables using satellite data and field data from the National Forest Inventory. Ambio 32:542–548

Ripple WJ (1986) Spectral reflectance relationship to leaf water stress. Photogramm Eng Remote Sens 52:1669–1675

Rock BN, Vogelmann JE, Williams DL, Vogelmann AF, Hoshizaki T (1986) Remote detection of forest damage. Bioscience 36:439–445

Rouse J, Haas R, Schell J, Deering D, Harlan J (1973) Monitoring the vernal advancements and retrogradation (greenwave effect) of nature vegetation. NASA/GSFC Final Report, NASA, Greenbelt

Roy PS, Ravan SA (1996) Biomass estimation using satellite remote sensing data—an investigation on possible approaches for natural forest. J Biosci 2:535–561

Saatchi SS, Houghton RA, Dos Santos Alvala RC, Soares JV, Yu Y (2007a) Distribution of aboveground live biomass in the Amazon Basin. Glob Change Biol 13:816–837. doi:10.1111/j.1365-2486.2007.01323.x

Saatchi SS, Houghton RA, Dos Santos Alvala RC, Soares JV, Yu Y (2007b) Distribution of aboveground live biomass in the Amazon basin. Glob Change Biol 13:816–837

Saatchi SS, Harris NL, Brown S, Lefsky M, Mitchard ETA, Salas W, Zutta BR, Buermann W, Lewis SL, Hagen S, Petrova S, White L, Silman M, Morel A (2011) Benchmark map of forest carbon stocks in tropical regions across three continents. Proc Natl Acad Sci 108(24):9899–99044

Salvador R, Pons X (1998) On the reliability of Landsat TM for estimating forest variables by regression techniques: a methodological analysis. IEEE Trans Geosci Remote Sens 36:1888–1897

Sarker LR, Nichol JE (2011) Improved forest biomass estimates using ALOS AVNIR-2 texture indices. Remote Sens Environ 115:968–977

Schull MA, Ganguly S, Samanta A, Huang D, Shabanov NV, Jenkins JP, Chiu JC, Marshak A, Blair JB, Myneni RB, Knyazikhin Y (2007) Physical interpretation of the correlation between multiangle spectral data and canopy height. Geophys Res Lett 34:L18405. doi:10.1029/2007GL031143

Segura M and Kanninen M (2005) Allometric models for tree volume and total aboveground biomass in atropical humid forest in Costa Rica. Biotropica 37:2–8

Slatton KC, Crawford MM, Evans BL (2001) Fusing interferometric radar and laser altimeter data to estimate surface topography and vegetation heights. IEEE Trans Geosci Remote Sens 39(11):2470–2482

Soenen SA, Peddle DR, Hall RJ et al (2010) Estimating aboveground forest biomass from canopy reflectance model inversion in mountainous terrain. Remote Sens Environ 114(7):1325–1337. doi:10.1016/j.rse.2009.12.012

Steininger MK (2000) Satellite estimation of tropical secondary forest above-ground biomass: data from Brazil and Bolivia. Int J Remote Sens 21:1139–1157

Sun G, Ranson KJ (1995) A three-dimensional radar backscatter model of forest canopies. IEEE Trans Geosci Remote Sens 33(2):372–382

Swatantran A, Dubayah R, Roberts D, Hofton M, Blair JB (2011) Mapping biomass and stress in the Sierra Nevada using lidar and hyperspectral data fusion. Remote Sens Environ 115:2917–2930

Ter-Mikaelian MT, Korzukin MD (1997) Biomass equations for sixty-five North America tree species. For Ecol Manag 97:1–24

Tomppo E (1991) Satellite Image-Based National Forest Inventory of Finland. In: Proceedings of the symposium on Global and Environmental Monitoring, Techniques and Impacts. September 17–21, 1990 Victoria, British Columbia Canada. International Archives of Photogrammetry and Remote Sensing, Vol 28, Part 7-1, pp 419–424

Tomppo E, Halme M (2004) Using coarse scale forest variables as ancillary information and weighting of variable sin k-NN estimation: a genetic algorithm approach. Remote Sens Environ 92:1–20

Tomppo E, Goulding C, Katila M (1999) Adapting Finnish multi-source forest inventory techniques to the New Zealand preharvest inventory. Scand J For Res 14:182–192

Tomppo E, Korhonen KT, Heikkinen J, Yli-Kojola H (2001) Multisource inventory of the forests of the Hebei Forestry Bureau, Heilongjiang, China. Silva Fennica 35(3):309–328

Tomppo E, Czaplewski R, Mäkisara K (2002) The role of remote sensing in global forest assessment. FAO Forest Resource Assessment Programme Working Paper 61.pp 90

Treuhaft RN, Siqueira PR (2000) Vertical structure of vegetated land surfaces from interferometric and polarimetric radar. Radio Sci 35:141–177

Treuhaft RN, Madsen SN, Moghaddam M, Van Zyl JJ (1996) Vegetation characteristics and surface topography from interferometric radar. Radio Science 31:1449–1485

Trotter CM, Dymond JR, Goulding CJ (1997) Estimation of timber volume in a coniferous plantation forest using Landsat TM. Int J Remote Sens 18:2209–2223

Tucker CJ (1979) Red and photographic infrared linear combinations for monitoring vegetation. Remote Sens Environ 8:127–150

Turner DP, Ollinger SV, Kimball JS (2004) Integrating remote sensing and ecosystem process models for landscape- to regional-scale analysis of the carbon cycle. Bioscience 54:573–584

Ulaby FT, Sarabandi K, McDonald K, Whitt M, Dobson MC (1990) Michigan Microwave Canopy Scattering Model. Int J Remote Sens 11(7):1223–1253

Van der Werf GR, Randerson JT, Giglio L, Collatz GJ, Mu M, Kasibhatla PS, Morton DC DeFries RS, Jin Y, and van Leeuwen TT (2010) Global fire emissions and the contribution of

deforestation, savanna, forest, agricultural, and peat fires (1997–2009). Atmos Chem Phys 10:11707–11735

Wagner W, Ullrich A, Ducic V, Melzer T, Studnicka N (2006) Gaussian decomposition and calibration of a novel small-footprint full-waveform digitizing airborne laser scanner. ISPRS J Photogramm Remote Sens 60:100–112

Wagner W, Hollaus M, Briese C, Ducic V (2008) 3D vegetation mapping using small-footprint full-waveform airborne laser scanners. Int J Remote Sens 29:1433–1452

Wang Z, Schaaf CB, Lewis P, Knyazikhin Y, Schull MA, Strahler AH, Yao T, Myneni RB, Chopping M (2011) Retrieval of canopy vertical structure using MODIS data. Remote Sens Environ 115(6):1595–1601

Walker WS, Kellndorfer JM, LaPoint E, Hoppus M, Westfall J (2007) An empirical InSAR optical fusion approach to mapping vegetation height. Remote Sens Environ 109:482–499

Wirth C, Schumacher J, Schulze E (2004) Generic biomass functions for Norway spruce in Central Europe-a meta-analysis approach toward prediction and uncertainty estimation. Tree Physiol 24:121–139

Wofsy SC, Harris RC (2002) The North American carbon program (NACP): report of the NACP Committee of the U.S. Interagency Carbon Cycle Science Program. U.S. Global Change Research Program, Washington, D.C.

Woodcock CA, Allen R, Anderson M, Belward A, Bindschadler R, Cohen W et al (2008) Free access to landsat imagery. Science 320(5879):1011

Wu Y, Strahler AH (1994) Remote estimation of crown size, stand density, and biomass on the Oregon transect. Ecol Appl 4:299–312

Wulder M, St-Onge B, Treitz P (2000) Three-dimensional analysis of forest structure and terrain using LIDAR technology. GEOIDE Calgary 2000, From Ideas to Innovation-Geomatics for a New Millennium, Calgary, 25–26 May 2000

Yang W, Ni-Meister W, Lee S (2011) Assessment of the impacts of surface topography, off-nadir pointing and vegetation structure on vegetation lidar waveforms using an extended geo-metric optical and radiative transfer model. Remote Sens Environ 15(11):2810–2822

Zeng Y, Schaepman ME (2009) Quantitative forest canopy structure assessment using an inverted geometric-optical model and up-scaling. Int J Remote Sens 30(6):1385–1406

Zhang X, Kondragunta S (2006) Estimating forest biomass in the USA using generalized allometric model and MODIS product data. Geophys Res Lett 33:L09402. doi:10.1029/2006GL025879

Zhang X, Schaaf CB, Friedl MA, Strahler AH, Gao F, Hodges JC (2002) MODIS tasseled cap transformation and its utility. Proceedings of IEEE 2002 international geoscience and remote sensing symposium and the 24th Canadian symposium on remote sensing, 24–28 June 2002, Toronto, pp 1149–1151

Zhang X, Kondragunta S, Ram J, Schmidt C, Huang HC (2012) Near-real-time global biomass burning emissions product from geostationary satellite constellation. J Geophys Res 117:D14201. doi:10.1029/2012JD017459

Zheng D, Rademacher J, Chen J, Crow T, Bressee M, Moine JL, Ryu S (2004) Estimating aboveground biomass using Landsat ETM+ data across a managed landscape in northern Wisconsin, USA. Remote Sens Environ 93(3):402–411

Zwally HJ, Schutz B, Abdalati W, Abshire J, Bentley C, Brenner A, Bufton J, Dezio J, Hancock D, Harding . (2002) ICESat's laser measurements of polar ice, atmosphere, ocean, and land. J Geodyn 34(3–4):405–445

Chapter 4
Land Surface Phenology

Jonathan M. Hanes, Liang Liang and Jeffrey T. Morisette

Abstract Certain vegetation types (e.g., deciduous shrubs, deciduous trees, grasslands) have distinct life cycles marked by the growth and senescence of leaves and periods of enhanced photosynthetic activity. Where these types exist, recurring changes in foliage alter the reflectance of electromagnetic radiation from the land surface, which can be measured using remote sensors. The timing of these recurring changes in reflectance is called land surface phenology (LSP). During recent decades, a variety of methods have been used to derive LSP metrics from time series of reflectance measurements acquired by satellite-borne sensors. In contrast to conventional phenology observations, LSP metrics represent the timing of reflectance changes that are driven by the aggregate activity of vegetation within the areal unit measured by the satellite sensor and do not directly provide information about the phenology of individual plants, species, or their phenophases. Despite the generalized nature of satellite sensor-derived measurements, they have proven useful for studying changes in LSP associated with various phenomena. This chapter provides a detailed overview of the use of satellite remote sensing to monitor LSP. First, the theoretical basis for the application of satellite remote sensing to the study of vegetation phenology is presented. After establishing a theoretical foundation for LSP, methods of deriving and validating LSP metrics are discussed. This chapter concludes with a discussion of major research findings and current and future research directions.

J. M. Hanes (✉)
Department of Geography, University of Wisconsin-Milwaukee, Milwaukee, WI, USA
e-mail: jmhanes@uwm.edu

L. Liang
Department of Geography, University of Kentucky, Lexington, KY, USA

J. T. Morisette
North Central Climate Science Center, U.S. Geological Survey, Fort Collins, CO, USA

J. M. Hanes (ed.), *Biophysical Applications of Satellite Remote Sensing*,
Springer Remote Sensing/Photogrammetry, DOI: 10.1007/978-3-642-25047-7_4,

4.1 Introduction

Vegetation phenology is the study of the timing of recurring plant life cycle events that are driven by environmental factors (Morisette et al. 2009). The occurrence of particular life cycle events, such as the emergence, growth, and senescence of leaves, is driven predominantly by weather and climate (Hanes et al. 2013) and has feedback effects on ecosystem processes (Baldocchi et al. 2005; Richardson et al. 2009b; Schwartz and Hanes 2010) and climate variables (Schwartz 1996; Hayden 1998; Fitzjarrald et al. 2001; Hanes 2012). The integrated nature of vegetation phenology has motivated many to use it as an indicator of climate change, as evidenced by the Intergovernmental Panel on Climate Change's contention that phenology "…is perhaps the simplest process in which to track changes in the ecology of species in response to climate change." (Rosenzweig et al. 2007).

The timing of phenological events has traditionally been documented using in situ, visual observations of selected plants. While these observations have proven useful, the lack of spatially and temporally-extensive in situ data inhibits systematic assessments of vegetation phenology at large spatial scales (e.g., continental, global). Given this limitation of conventional phenology data, researchers utilize satellite sensor-derived measurements of reflected electromagnetic radiation from the land surface to study vegetation phenology over large geographic areas. These measurements of land surface reflectance exhibit recurring changes that are determined by vegetation phenology. The timing of these recurring changes in reflectance is called land surface phenology (LSP).

During recent decades, a variety of methods has been used to derive metrics of LSP from time series of satellite observations (White et al. 2009; Schwartz and Hanes 2010). Although LSP metrics do facilitate large-scale assessments of seasonal vegetation dynamics, they are different than conventional phenology data. In contrast to conventional phenology data, which typically include the timing of specific phenophases for individual plants, metrics of LSP represent the timing of reflectance changes that are driven by the aggregate activity of vegetation within the areal unit measured by satellite sensors, such as the Advanced Very High Resolution Radiometer (AVHRR) and the Moderate Resolution Imaging Spectroradiometer (MODIS) (see Table 1 in Reed et al. 2009 for a list of satellite sensors used commonly in LSP studies and the spatial resolution of their measurements). Therefore, these satellite-derived LSP metrics do not provide specific information about the phenology of individual plants, species, or their phenophases (e.g., buds open, leaf emergence, leaf unfolding). Despite the generalized nature of satellite sensor-derived measurements, they have proven useful for studying changes in LSP associated with various phenomena, including climate (Myneni et al. 1997; Hanes and Schwartz 2011), institutional changes (de Beurs and Henebry 2004), and urban heat islands (White et al. 2002; Zhang et al. 2004; Fisher et al. 2006).

This chapter provides a detailed overview of the use of satellite remote sensing to monitor LSP. First, the theoretical basis for the application of satellite remote

sensing to the study of vegetation phenology is presented. After establishing a theoretical foundation for LSP, methods of deriving and validating LSP metrics are discussed. This chapter concludes with a discussion of major research findings and current and future research directions.

4.2 Theoretical Basis

The emission of electromagnetic radiation from the Sun and its reflection from the Earth's surface provide a basis for satellite remote sensing and, consequently, for LSP. Therefore, our discussion of the theoretical basis for LSP begins by describing briefly the nature of electromagnetic radiation. We then present the reflectance characteristics of foliage, which are subsequently used to describe how the timing of recurring changes in vegetation can be studied using satellite remote sensing.

Electromagnetic radiation (hereafter referred to as "radiation") is energy emitted in the form of waves by objects possessing heat (Anderson and Strahler 2008). The amount and wavelengths of radiation are of particular interest in the field of remote sensing, which focuses on monitoring and analyzing characteristics of the Earth from afar by measuring its emitted or reflected radiation. The amount of radiation emitted by an object is proportional to its temperature, with warmer temperatures leading to larger emissions of radiation and cooler temperatures resulting in lower emissions of radiation. The peak wavelength of emitted radiation is inversely proportional to the temperature of the emitting object. Because different objects have different temperatures, radiation can be emitted at a variety of wavelengths. The various wavelengths of radiation are classified commonly into different categories, or types, of radiation and represented as a continuous spectrum beginning with those that are shortest and ending with those that are longest. Progressing from shorter to longer wavelengths, the general types of radiation are gamma-rays, x-rays, ultraviolet radiation, visible light, near-infrared radiation, middle infrared radiation, thermal infrared radiation, microwaves, and radio waves (Shellito 2012).

Measurements of emitted and reflected radiation have facilitated the development of numerous methods to monitor the Earth from afar. In the context of land surface phenology, methods of documenting and analyzing the timing of seasonal changes in vegetation have relied primarily on visible and near-infrared radiation (NIR) emitted by the Sun. Variable amounts of visible light and NIR emitted by the Sun are transmitted through the atmosphere and received by the Earth's surface. When the Earth receives this radiation from the Sun, it is absorbed, transmitted, or reflected. Sensors (often called radiometers or spectroradiometers) mounted on satellites orbiting the Earth effectively measure the amount of visible light and NIR reflected from the land surface. The measured reflectances of visible light and NIR from a specified areal unit on the Earth's surface are assigned digital

numbers that provide an indication of how much radiation is reflected. The digital numbers from multiple areal units (or pixels) are used to create images that display the reflection of radiation from the land surface (Shellito 2012).

The surface characteristics of the Earth primarily determine the amounts of visible light and NIR that are reflected and captured by the sensors mounted on satellites. As evidenced by the spectral profile of a trembling aspen leaf in Fig. 4.1, healthy green foliage strongly reflects NIR (~0.8–0.9 μm), but reflects small proportions of the visible light (~0.4–0.7 μm) received. The high proportion of reflected NIR is related to leaf structural characteristics [e.g., internal cellular structure (Knipling 1970); leaf thickness (Knapp and Carter 1998), leaf bicoloration and the presence of a thick leaf cuticle (Slaton et al. 2001)]. The low reflectance of visible light by healthy green foliage is attributed to the strong absorption of these wavelengths by leaf pigments (most notably chlorophyll). While chlorophyll strongly absorbs visible light, it does not absorb all wavelengths of visible light equally. Chlorophyll is a stronger absorber of blue and red wavelengths than green wavelengths, which gives healthy foliage its green color (as indicated by the "spike" in reflectance between 0.5 and 0.6 μm in Fig. 4.1). Unlike blue wavelengths (~0.4–0.5 μm), which are also absorbed by carotenoids (Ollinger 2011), the absorption of red wavelengths (~0.6–0.7 μm) is a primary indicator of chlorophyll content (Filella and Peñuelas 1994; Peñuelas and Filella 1998). Any changes in leaf area and pigmentation will cause corresponding changes in the reflectance of NIR and red wavelengths, respectively. Consequently, the remote sensing community has paid special attention to reflectance in the near-infrared and red sections of the electromagnetic spectrum (either separately or in the form of vegetation indices) when attempting to measure and study green leaf biomass (Gamon et al. 1995), leaf area and the fraction of absorbed photosynthetically active radiation (Myneni et al. 1997; Yang et al. 2006), and discriminate between land cover types (Loveland et al. 1991; DeFries et al. 1995).

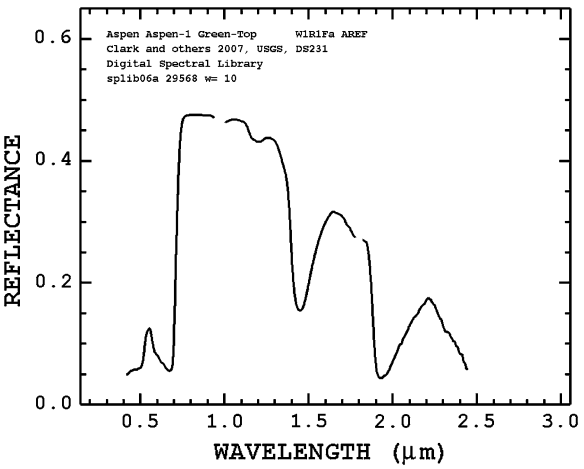

Fig. 4.1 Spectral profile of a trembling aspen leaf (*Populus tremuloides*) (Clark et al. 2007)

Certain vegetative land cover types (e.g., deciduous shrubs, deciduous trees, grasslands) have distinct life cycles marked by the growth and senescence of leaves and periods of enhanced photosynthetic activity. Where these land cover types exist, the growth and senescence of leaves cause changes in the reflectance of NIR and visible light from the land surface. For example, the emergence and growth of new leaves are associated with increases in chlorophyll concentration and leaf area, which increase the absorption of red wavelengths (Richardson et al. 2007) and the reflectance of NIR. During leaf senescence, the collapse of the mesophyll reduces the proportion of reflected NIR (Knipling 1970; but see Castro and Sanchez-Azofeifa 2008). In addition, declining chlorophyll concentrations and de novo synthesis of anthocyanins in senescing leaves (Lee et al. 2003) increase the reflectance of red wavelengths (Richardson et al. 2009a). The close correspondence between leaf growth and senescence and the reflectance of NIR and visible light makes it possible to study vegetation phenology using reflectance measurements acquired by remote sensors.

Annual time series of satellite-derived vegetation indices [e.g., normalized difference vegetation index (NDVI), enhanced vegetation index (EVI) (Huete et al. 2002)] and biophysical metrics [e.g., leaf area index (LAI), fraction of absorbed photosynthetically active radiation (FPAR) (Myneni et al. 2002)] that incorporate the reflectance of NIR and red wavelengths generally capture the spectral changes associated with leaf growth and senescence in the large areal units monitored by the sensor. Therefore, these metrics can be used to document the phenology of the land surface with variable accuracy and precision (White et al. 2009; Schwartz and Hanes 2010). With this said, it must be noted that the degree to which these satellite-derived metrics can be used to study LSP depends on the surface characteristics of the entire areal unit measured. Considering that the large areal units measured from space can integrate a variety of land cover types (vegetative and non-vegetative, deciduous and evergreen), there has been some effort to restrict the analysis of LSP to pixels containing land cover types that exhibit distinct phenologies that are most observable from space [e.g., deciduous forests (Fisher et al. 2006)] and have a strong response to climate (White et al. 2005).

4.3 Methods

Remote sensing indices characterizing vegetation conditions form the basis of deriving LSP metrics. The most ubiquitous algorithm is the Normalized Difference Vegetation Index (NDVI), which utilizes chlorophyll and leaf structure-induced reflectance contrast between red and near-infrared spectral bands from live vegetation (Rouse et al. 1974). Using the normalized difference [(NIR − R)/(NIR + R)] rather than quantifications of single bands effectively captures the relative reflectance difference between the red and near-infrared bands. Specifics regarding algorithms of this and the following vegetation indices discussed here may be found in Chap. 3 of this book. The NDVI is able to effectively differentiate

vegetated and non-vegetated areas, and capture the overall condition, magnitude, and phenology of vegetation growth. Additional vegetation indices are formulated on essentially the similar principle as NDVI with additional improvement such as accounting for atmospheric noise through adding the blue band information to specific indices, etc. Examples of these alternative vegetation indices include the soil adjusted vegetation index (SAVI, Huete 1988), the atmospherically resistant vegetation index (ARVI, Kaufman and Tanre 1992), and the soil and atmospherically resistant vegetation index (SARVI, Huete and Liu 1994), which integrates the former two algorithms. These efforts culminated in the development of the enhanced vegetation index (EVI, Huete and Justice 1999), which was specifically targeted at improved vegetation monitoring through the MODIS platforms. The EVI corrects both soil and atmospheric effects akin to SARVI and has improved sensitivity to high biomass, which leads to NDVI saturation (Huete et al. 2002). Both NDVI and EVI are widely employed vegetation indices and are used for LSP metrics derivation and studies. For boreal regions where snow cover affects vegetation recognition, the normalized difference water index (NDWI; Gao 1996) is useful for more accurate LSP analysis, as NDWI decreases with snowmelt and increases with canopy growth (from leaf water content) versus NDVI, which increases with snowmelt and therefore introduces biases if used alone (Delbart et al. 2005). Recent development also includes an attempt to combine the use of NDVI and the normalized difference infrared index (NDII) to produce a remote sensing phenology index (PI) to better overcome the background soil and snow contaminations (Gonsamo et al. 2012),

Biophysical variables corresponding to detailed vegetation processes can also be estimated from satellite data and in turn used for LSP metric development. Such variables include notably the leaf area index (LAI) and fraction of absorbed photosynthetically active radiation (FAPAR or FPAR) as described in another chapter of this book. The field observation-originated LAI can be remotely sensed and is more directly related to vegetation properties and functions, such as structure, evapotranspiration, and primary production. The FPAR relates to similar vegetation activities and is a basis for remote sensing of the gross and net primary productions (GPP and NPP; Running et al. 2004). Chapters 2 and 5 of this book outline the details of these aspects of vegetation parameterization. Therefore, in addition to the use of vegetation indices, there were studies deriving LSP metrics from LAI and/or FPAR (Ahl et al. 2006; Kang et al. 2003; Wang et al. 2005). The LAI and/or FPAR are strongly correlated with NDVI. In particular, LAI has an approximately linear correspondence with NDVI when LAI is low, yet a highly non-linear relationship when LAI is higher (http://earthobservatory.nasa.gov/Features/LAI/LAI3.php). The NDVI, along with EVI, is still most commonly used for generating phenology information from data acquired through earth resource satellites.

The remote sensing data used for LSP monitoring and studies are primarily derived from multispectral sensors onboard sun-synchronous polar orbiting satellites. The AVHRR onboard NOAA series polar orbiting environmental satellites (POES) has provided long-term global NDVI products since the early 1980s

(Goward et al. 1985; Tarpley 1991; Eidenshink 1992). AVHRR acquires global coverage daily with its broad scanning swath (2700 km) and as a tradeoff it has a relatively coarse (1.1 km) spatial resolution. At the turn of the century, a type of sensor with improved spectral, radiometric, and geometric quality was implemented. The MODIS onboard NASA's Terra (1999–present) and Aqua (2002–present) satellites began operating to provide better remote sensing data for multidisciplinary research on global change (Justice et al. 1998). The MODIS instruments provide similar global and near-daily repeat coverage and improved spatial resolutions: 250 m (bands 1–2), 500 m (bands 3–7), and 1 km (bands 8–36). In addition, the EVI was developed along with the implementation of this sensor, increasing the ability to extract vegetation information. Both AVHRR and MODIS allow frequent monitoring of vegetation conditions for large geographic regions and, therefore, are ideal for LSP monitoring at continental and global scales. However, the presence of clouds has been a major hindrance to acquiring high temporal resolution image time series of vegetation at a given location. A maximum value composite method is hence employed to remove cloud contamination for both AVHRR and MODIS vegetation indices time series, with nominal temporal resolutions of resultant products reduced to about 2 weeks (Thayn and Price 2008).

Specifically, the available vegetation indices (VI) values from satellite observation over a year comprise time series corresponding to annual growing seasons of vegetation. Given the cloud contamination problem mentioned previously, the cloud-free images that allow vegetation of a specific location to be seen are often few for a growing season. Besides atmospheric interference, the quality of data is also affected by noises from sensor systems, surface properties, and solar and sensor viewing angles. Therefore data smoothing approaches from simple running median to curve-fitting models are employed as a necessary procedure in image preprocessing (Reed et al. 1994; Bradley et al. 2007). Obvious spurious data points such as extremely low VI values caused by snow, clouds, or water bodies can also be removed manually. Such an approach is meant to reduce the signal contaminations and retain the essence of annual and interannual variations of phenology. As stated earlier, VI products available are typically processed with the maximum value composite method to remove cloud effects (Holben 1986). For a 16-day composite window, the maximum VI value is retained to indicate the vegetation condition during that time period. This temporal limitation of applicable data entails the use of interpolation approaches for generating continuous VI curves for LSP estimation.

Curve geometry of VI time series is used for further extracting satellite pixel-based phenological patterns, because VI values fluctuate in annual cycles in accordance with vegetation phenology. For instance, the rise and drop of VI levels reflect respectively the increase and decrease of vegetation activities. Conventional phenology studies pay most attention to the critical annual events, such as leaf bud burst, flower bloom, and sometimes leaf fall and growing season length. Remotely sensed phenology has been mostly focused on leaf phenology, given the spatial resolution available that makes detecting flower phenology in mixed landscapes

very difficult. Based on annual variations of VI time series, phenological parameters such as dates of the start of season (SOS) and end of season (EOS) and consequently the growing season length can be estimated. Additional parameters may also include the dates when vegetation activities reach a stably high level in the summer (maturity) and a subsequent transitional autumn phase when foliage starts to decline (senescence) (Zhang et al. 2001).

Various methods have been adopted to estimate the threshold points or phenologically important dates using multi-temporal VI imagery (Lloyd 1990; Reed et al. 1994; White et al. 1997, 1999, 2002; Zhang et al. 2001, 2003). An early attempt using fixed threshold values was made to mark the SOS in selected ecosystems (Lloyd 1990). Lloyd (1990) employed a constant value of 0.099 for AVHRR NDVI time series as the threshold to mark the start and end of the growing season. This threshold selection was based on tests in selected regions and the general assumption was that vegetation growth is unlikely to be occurring if the NDVI value is below the specified threshold (Henricksen and Durkin 1986; Justice et al. 1986). Given that the same criterion is applied to all land cover types, geographic variations of LSP may be highlighted using this approach. However, whether a unified threshold corresponds to the vegetation greenness onset for a large region is difficult to verify. The assumption of land cover homogeneity puts a fundamental limit to simple threshold-based phenology for representing spatially variant biophysical reality in vegetated landscapes. Depending on the vegetation types and background reflectance properties, the NDVI threshold marking SOS may be different across locations. Hence, more accurate determination of phenological transition points and growing season length requires land cover/pixel-specific extraction methods that account for the heterogeneous nature of LSP.

More accurate and also more computationally intensive approaches were later developed in the same era marked with prevalent vegetation studies using AVHRR NDVI, especially driven by an increased need to monitor LSP for continental and global-scale coverage (Reed et al. 1994; White et al. 1997). Reed et al. (1994) derived phenological metrics using primarily a delayed moving average (DMA) method and compared the results for agricultural crops, grasslands, and forests. Biweekly composited NDVI time series were interpolated to remove gaps between adjacent data points, and cloud contamination was further removed using a running median line-smoother. Moving averages of previous n observations (sum of all values divided by the time interval) were calculated for all pixels. Through repetitive testing, a nine-value composite period was selected and new DMA time series were generated. A new time series represents a predicted trend based on NDVI values in the past. The time when an observed value exceeds the predicated trend (smoothed NDVI curve crosses the DMA curve) was designated as the onset of greenness or start of the growing season (SOS). This crossing indicates an abrupt change of vegetation activities that have surpassed the preexisting tendency. A chronologically reversed DMA procedure was performed in like manner to derive a metric for the end of the growing season.

White et al. (1997) developed a NDVI ratio-based approach for deriving phenological markers. Instead of using biweekly composite NDVI data, the raw data

points were used. In order to remove contaminations from clouds and the atmosphere, a best index slope extraction (BISE) method was employed. The essence of the BISE approach is to extract the phenological development curve from NDVI raw data points based on the assumptions that vegetation growth is consistent (free from erratic changes) and cloud effects depress the NDVI as reflected by aberrantly low values. A continuous NDVI curve is then extracted from the unswerving boundary of the annual data point distribution (see White et al. 1997 for details). An NDVI ratio [$(NDVI–NDVI_{min})/(NDVI_{max}–NDVI_{min})$] was computed for each pixel, and a constant ratio value of 0.5 was used to mark the SOS. White et al. (1999, 2002) further simplified this approach to the seasonal midpoint NDVI (SMN) method, which computes the midpoint between minimum and maximum NDVI values for each pixel as the threshold (maximum composite data were used in these follow-up studies). Thus, the determined SOS is proportional to site-specific NDVI amplitude and is therefore sensitive to spatial and temporal phenological variations.

Among the algorithms used for phenological signal extraction from annual VI profiles, a method using the growth curve (modeled with a logistic function) bears a closer resemblance to actual springtime vegetation development (Fischer 1994; Zhang et al. 2003). The logistic function is a common type of sigmoid model that approximates an s-shaped curve, which is used to simulate a natural process with an initial stage of exponential growth, followed with a tapering growth rate as saturation begins, indicating maturity of development. The formula of this model according to Zhang et al. (2003) is given as follows:

$$y(t) = \frac{c}{1 + e^{a+bt}} + d$$

where t is time in day of year, $y(t)$ is the VI value at time t, a and b are fitting parameters, $c + d$ is the maximum VI value, and d is the initial background VI value. Parameter a dictates the date of the onset of the rise in greenness and b dictates the steepness of the VI curve. This model corresponds well with the phenological development of deciduous vegetation, which is characterized with a flush of greening at first, followed with a steady increase in foliage expansion throughout the spring, and a plateau of growth in the summer. A second logistic function is used to quantify the decline of vegetation activities due to growth cessation in the fall, approximately mirroring the spring phases. Fischer (1994) applied a double logistic method to NDVI time profiles to characterize the phenological cycle of crops. Inflection points (when the concavity of a logistic curve changes signs) were used to mark the start and end of the growing season. As these inflection points are found approximately at the mid-point of steady increasing/decreasing segments of a logistic curve, the growing season duration may be underestimated. Zhang et al. (2001, 2003) modeled the AVHRR and MODIS VI-based phenology with logistic functions with an improved method for deriving transition dates. The time points at which a VI curve experiences fastest changes are related to the thresholds of phenological phase shift. The curvature and curvature change rates can be calculated using formulas detailed in Zhang et al. (2003).

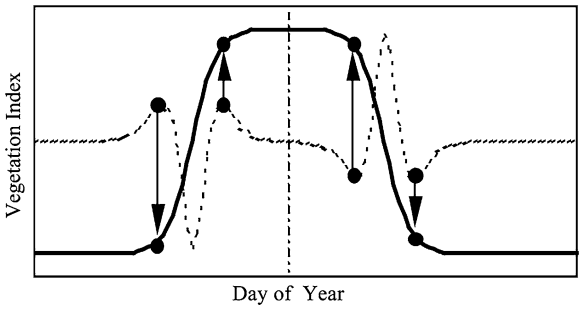

Fig. 4.2 A schematic showing how transition dates are calculated using minimum and maximum values in the rate of change in curvature. The *solid line* is an idealized time series of VI data, and the *dashed line* is the rate of change in curvature from the VI data. The *circles* indicate transition dates. The extreme values located between *circles* indicate the points at which the curvature changes sign. The figure is reprinted from Zhang et al. (2003) with permission from Elsevier

The maxima (on the ascending segment) and minima (on the descending segment) of curvature change rate correspond to transition dates of an annual phenology cycle (Fig. 4.2). The initiation and ending of fast vegetation growth are marked by the time when curvature changes are greatest on the ascending segment of an annual curve and the start and finish of vegetation senescence are indicated with times at which minimum curvature change rates (negative) on the descending segment are reached. These four phenological markers are related specifically to the onset dates of green-up, maturity, senescence, and dormancy of seasonal vegetation growth. The inflection points corresponding to the extreme curvature change rates occur half way between each pair of transition dates, the slopes at which may be used to characterize the average green-up and brown-down rates. Besides, a further effort was made to refine brown-down date estimation, which is usually more uncertain given the foliage coloration processes (Zhang and Goldberg 2011).

The LSP metrics extraction algorithm of Zhang et al. (2003) is used in MODIS Land Cover Dynamics products (MCD12Q2). An alternative curve smoothing and SOS derivation approach akin to that of Zhang et al. (2003) was developed using an asymmetric Gaussian model (Jönsson and Eklundh 2004; Gao et al. 2008; Tan et al. 2008; 2010). Jönsson and Eklundh (2004) developed an open source LSP extraction software (TIMESAT), which includes both the double logistic and asymmetric Gaussian algorithms. Gao et al. (2008) employed the asymmetric Gaussian method for smoothing MODIS LAI time series. Tan et al. (2008) and Tan et al. (2010) developed a modified TIMESAT method for generating MODIS LSP for the North American Carbon Program (NACP). This enhanced TIMESAT approach utilizes asymmetric Gaussian curve fitting and the third derivative of a fitted curve to determine key phenological dates. Both double logistic and asymmetric Gaussian methods utilize semilocal curve geometry to characterize LSP time series and extract transition dates. The two curve fitting approaches were found to generate similar results with the exception that the asymmetric Gaussian method is less sensitive to an incomplete time series with many data gaps (Beck et al. 2006; Gao et al. 2008).

4.4 Validation Efforts Using In Situ Measurements

Satellite-derived phenology has advantages of covering broad geographic regions, integrating information from multiple species, and providing regular multi-temporal capability that is useful for change detection. However, common limitations and signal contaminations associated with remote sensing data reduce the accuracy of LSP estimates. The primary limitations include the relatively coarse spatial resolution (250 m–1 km) and the fairly large temporal resolution of useable observations at a given location caused primarily by clouds. The standard VI products are usually available as 8–16 day maximum value composites, but there have been attempts to use daily MODIS surface reflectance to compute customized NDVI for optimized temporal precision in LSP derivation (Graham et al. 2010; Ju et al. 2010). Other uncertainties may be from additional atmospheric path radiance effects, sensor systematic errors, and ground reflectance noises. The different approaches used for the extraction of phenology metrics may also contain inherent biases. Therefore, validation of LSP with appropriate ground measurements is essential for improving phenological monitoring abilities (Schwartz and Reed 1999).

Given the lack of in situ data that are comparable with LSP in spatial coverage and landscape representativeness, the initial attempt to bridge ground phenology with satellite phenology was through using bioclimatic models (Schwartz and Reed 1999; Schwartz et al. 2002). A suite of climate data-driven phenological models (spring indices, SI) was developed using phenological records of indicator species: *Syringa chinensis* (a lilac) and two varieties of honeysuckle (*Lonicera tararica* and *Lonicera korolkowii*) distributed across eastern North America (Schwartz 1990, 1994, 1997). Schwartz (1994, 1997) outlined the utility of SI as a "backbone" to produce spatially continuous phenological measures for large regions and thus enable comparison of surface phenology with satellite phenology. Simulated phenology as derived according to ground-based phenology and independently from LSP serves as a proxy of in situ phenology to compare with LSP over broad regions where actual phenology data are not available. An initial comparison was made between satellite-derived SOS and SI first leaf and first bloom estimates using a land cover stratified correlation approach (Schwartz and Reed 1999). The first bloom phenology was used as a reference of late spring events rather than to correspond with the landscape greening as detected by satellites. The SOS dates were calculated from 1 km AVHRR NDVI data using an updated version of the DMA approach described previously and in Reed et al. (1994). This study found that satellite-derived SOS was systematically earlier than the SI first leaf, suggesting that satellite signals record the greening of understory vegetation before the onset of tree foliage growth. A follow-up study compared SI with both DMA SOS and SMN SOS over the conterminous United States (Schwartz et al. 2002). Results pointed out that SMN SOS corresponds more closely in timing with the late spring phenology event (e.g., SI first bloom date). Regardless of the lack of explicit linkages with ground biophysical processes,

these SOS measures showed the ability to detect general interannual and large-scale geographic variations of LSP.

An alternative approach to bridging in situ phenology with satellite phenology was attempted using Landsat data as an intermediary (Fisher et al. 2006; Fisher and Mustard 2007). Relatively high spatial resolution (30 m) data from Landsat TM and ETM + have a repeat coverage of 16 days (can be reduced to 8 days if data from multiple platforms are used). Due to the data loss from cloud effects, estimating vegetation phenology using data from a single year of Landsat data is not practical. Fisher et al. (2006) utilized multi-year Landsat data to approximate phenological development over an annual cycle. A modified double logistic model akin to that of Zhang et al. (2003) was used to fit a growth season curve. Fractional vegetation cover, which was estimated using a sub-pixel spectral mixture analysis (SMA) method (estimating vegetation percentage cover at the subpixel level), was used instead of vegetation indices. Fisher et al. (2006) suggested that the SOS is marked when vegetation reaches half maximum greenness, similar to the SMN approach of White et al. (1997).

The Fisher et al. (2006) approach accepted a compromise in using 19-year composited time series to take advantage of the higher spatial resolution of Landsat data. In spite of the unavoidable loss of interannual change information when multi-year data are merged, results seemed to show spatial variations of phenology with interesting details. In particular, the micro-topographic and microclimatological gradients seem to play an evident role in influencing spring leaf phenology. Cold air drainage in the New England area delays the phenology of trees grown in low laying areas. The sequence of phenological development as observed onsite with both visual estimates and photography agreed with findings from satellite data. Further, maritime effects seem to be responsible for the delayed coastal vegetation phenology due to a lag of spring temperature increase. The urban heat island effect that advances phenology is also documented in the Landsat-based LSP estimates.

The effort to relate ground and satellite phenology is furthered from considering only Landsat data to using Landsat data as a bridge to connect to MODIS data (Fisher and Mustard 2007). This is a necessary step because most of the large-scale vegetation studies are carried out at coarser spatial resolutions as provided by MODIS (250 m–1 km) or AVHRR (1 km), which are better suited for global monitoring. In this follow-up study, Fisher and Mustard (2007) attempted to address the need of interannual phenology comparison in relation to detecting climatic influences on phenology. This was not possible in the previous study with time-integrated Landsat data. The investigation of interannual change mainly relied on the MODIS time series and field-observed data. The spatial variation was checked mainly between Landsat-based and MODIS-based phenological measurements. These two sets of independent satellite measurements appeared to show relatively coherent spatial variations when averaged phenology is of concern. This study further compared MODIS phenology with field-observed phenology at two sites, incorporating interannual variations. Year-to-year change of MODIS phenology seemed to match the general variations observed in situ at the field sites,

with satellite-derived onset dates situated between the earlier bud break-based onset dates and later leaf expansion-based onset dates.

Two notable efforts to validate different LSP methodologies developed for AVHRR NDVI and MODIS NDVI/EVI highlighted large uncertainties in the connection between satellite and ground phenology measurements (White et al. 2009; Schwartz and Hanes 2010). Both studies were conducted at the continental scale and were specifically aimed towards validating SOS estimates. White et al. (2009) performed an inter-comparison among 10 selected SOS derivation techniques using 8 km 15-day composite AVHRR NDVI data for 1982–2006. Ground-based measurements used included phenology network records, phenology model predictions, as well as cryospheric/hydrologic seasonality data. Results indicated that SOS dates predicted by different methods deviate from each other up to 2 months, in addition to large variations across geographic regions. Schwartz and Hanes (2010) utilized 1 km 16-day composite MODIS NDVI and EVI data from 2000 to 2006, and compared 10 sets of SOS estimates derived from selected methods. Some important SOS methods, such as those using double logistic functions (Zhang et al. 2003; Fisher et al. 2006) and modified TIMESAT (Tan et al. 2008), which were missing in the analyses of White et al. (2009), were covered. The inter-comparison was made for eastern North America against surface data, which included both modeled phenology (SI) and local species phenology data from several study sites across the region. The comparison results alike suggested a lack of significant correlations between the satellite and ground measurements and the performance of different SOS methods varied across sites. Though targeting on LSP estimates from different satellite data sources, both studies noted here implied that the differences in spatial scales and temporal resolutions of satellite and ground data are a major hurdle to validation tasks. These studies also demonstrated that ground phenology data as collected in an extensive manner at discrete locations (e.g., from the Nature's Notebook of the USA National Phenology Network) need to be complemented with more detailed field observations in order to be used for validating LSP.

More specifically, remote sensing and in situ observation of plant phenology both investigate essentially the same phenomena, but deviate in coverage and resolution, as well as in the forms of information recorded. Observer-based recording of phenology relies on the synthetic capability of human eyes in detecting integrated phenological development phases, such as bud burst or leaf expansion. Often some statistical criteria are employed to guide the characterization of differential growth within the same canopy. Human eyes do not provide quantitatively precise recordings when multiple observations are translated into a series of values, but do capture ordinal progression sequences. For key phenological events, visual observations are most reliable. Remote sensing, on the other hand, would allow quantification of vegetation growth at more differentiable levels as allowed by the sensor's radiometric resolution, but lacks the direct correspondence with traditionally defined phenological events. In addition, the majority of local species ground phenology data from observation networks are available for limited plant individuals registered to approximate geographic locations, while

continuous satellite data incorporate mixed signals from all plants as well as background substrates. Therefore, the exact biophysical meanings of LSP, in particular SOS, remain vague when ground data that lack landscape representativeness are employed for validation.

To meet this challenge, phenology data collection in a spatially concentrated manner which allows detailed characterization of landscape heterogeneity became crucial (Liang and Schwartz 2009; Liang et al. 2011; Schwartz et al. 2013). Beginning from 2006, high density phenology observations were carried out in a mixed forest located in northern Wisconsin, near an AmeriFlux tower site (Park Falls/WLEF). A high resolution spatial sampling of major canopy species was deployed at the study sites, initially for a 625 × 275 m area (2006 and 2007), and later for two 625 × 625 m expanded areas (since 2008). At least three of the largest trees at 288 plots were sampled. The coverage of sampling grids matched the size of MODIS pixels, and the density of sampling allowed capturing spatial variations within the pixels. As shown in Fig. 4.3, the spatial setting of in situ data collection allowed better compatibility with coarse resolution satellite pixels in both extent and representativeness. In addition to high spatial density, phenology observation was conducted with high temporal frequency. The field crew took measurements for all sampled trees every other day (modified to a 4-day interval since 2010) throughout the early spring time period (about a month). A detailed field protocol was used to describe phenology from buds to leaves and with

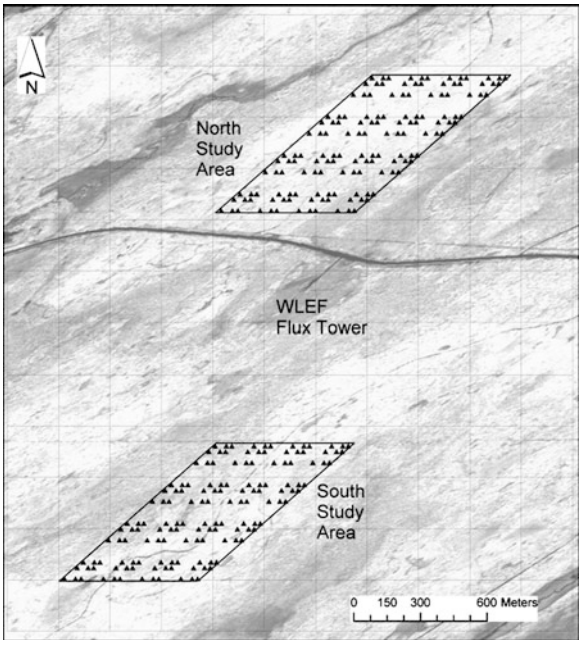

Fig. 4.3 High resolution sampling design for satellite phenology validation showing: (1) in situ phenological observation transects/plots (according to a cyclic sampling design, see Burrows et al. 2002); (2) MODIS pixel grids (250 × 250 m squares, sinusoidal projection); and (3) 2.4 m resolution NDVI image derived from a May 18, 2007 QuickBird image underlying the plots and MODIS pixel grids. This figure is reprinted from Liang et al. (2011) with permission from Elsevier

different percentage characterization for canopies undergoing a particular phenological stage transition.

To fully utilize the data from high resolution phenology for the purpose of validating satellite phenology, adequate scaling methods are required. Liang and Schwartz (2009) proposed the concept of landscape phenology, which integrates discrete phenology information to the synthetic levels of ecosystem organization. Observations for individual plants may be aggregated to form population, community, and landscape phenology representations with additional data related to species dominance, abundance, and distribution. The concept was fully implemented in a practical scaling ladder that effectively produced landscape phenology (LP) indices that are readily comparable with LSP metrics (Liang et al. 2011). Liang et al. (2011) developed a step-wise nested hierarchical scaling approach linking landscape phenology and hierarchical patch dynamics (Wu and Loucks 1995). This scaling design allowed practicality of data aggregation and simultaneously took into consideration the predefined ecosystem structure and coherence, as well as the patchiness of forest landscapes.

To achieve each step of scale transition following the individual-population-community-landscape (ecosystem patch) sequence, a suite of digital image processing techniques (with ancillary high resolution imagery) was employed to characterize the forest landscapes and provide required additional information for spatially aggregating phenology data (for details see Liang et al. 2011). Two sets of LP indices were developed with one being compatible with landscape spectral reflectance and the other retaining field protocol meanings. MODIS VI time series were first compared with the time series of reflectance calibrated LP index. Then full bud burst dates as estimated from the LP indices (which retained biological meanings) for deciduous and coniferous species respectively were compared with LSP SOS dates. The maximum curvature logistic approach (Zhang et al. 2003) was used to develop SOS estimates given its use in the MODIS global land cover dynamics products (Ganguly et al. 2010). With the high resolution field data, the spatial matching with MODIS satellite pixels was able to be conducted in a more precise manner. Pixel values were weighted with corresponding spectral contributions of the areal fractions overlapping with the study areas. Detailed comparisons revealed relatively close connections of satellite phenology with the ground observations. Instead of a linear relationship, the phenological development on the ground appeared to influence LSP exponentially. The phenology protocol used in the field describes the progression of canopy growth from buds to leaves. The primary impact of phenology on surface greening occurs after bud burst and accelerates with rapid leaf unfolding and expansion. This general trend also agrees with the initiating pattern of a logistic curve. Coniferous LP index time series lagged behind those of LSP and deciduous LP index, implying the major role of deciduous land covers in influencing LSP. Maximum absolute errors between LP deciduous full bud burst dates and SOS dates were 15 days and 2 days for NDVI and EVI, respectively.

In addition to the effort to validate LSP using traditional observer-based phenology, there has been much work done to utilize in situ observations from

near-surface remote sensors (Richardson et al. 2007, 2009a; Graham et al. 2010; Hufkens et al. 2012). In particular, networked webcams have been used to record repeat canopy phenology in association with the existing eddy covariance flux tower sites (cf. PhenoCam program, http://phenocam.sr.unh.edu/webcam/). Webcam-based phenology observation has the advantages of being more objective (free from observer biases) and low-cost in logistics, which allows for consistent and continuous monitoring of forest canopy conditions (Sonnentag et al. 2012). The tradeoff is that it provides optical signals akin to satellite remote sensing and does not give particular details of phenological development (e.g., bud break) that traditional observer-based protocols offer.

In particular, Huemmrich et al. (1999) and Richardson et al. (2007) employed a broad-band NDVI measured from flux tower-based radiometric measurements. The broad-band NDVI utilizes the entire visible spectrum ([NIR-VIS]/[NIR + -VIS]) instead of the red band as is typical for satellite-derived NDVI. However, more widely available near-surface remote sensing analyses have relied on visible light digital camera measurements. The visible light digital photos contain separate color bands (Red [R], Green [G], and Blue [B] respectively), which were used to derive band algebra-based greenness indices, such as the excess green (2G-R-B) and green chromatic coordinate (G/[R + G + B]; Sonnentag et al. 2012). Hufkens et al. (2012) performed a comparison of near-surface remote sensing-based phenology with satellite (i.e. MODIS) remote sensing-based phenology at four PhenoCam sites across the United States. Results from the study showed relatively consistent correspondence between the MODIS VI time series and camera excess green time series and suggested that the mismatch of camera field of view and satellite pixel-covered areas may contribute the major uncertainty in linking the two types of phenological measurements. Related studies also utilized webcam data to compare with MODIS-based LSP (Graham et al. 2010) and Landsat-based LSP (Elmore et al. 2012). The continuous monitoring of near-surface remote sensing also provided opportunities for validation in both the spring and autumn seasons (Hufkens et al. 2012; Elmore et al. 2012). Elmore et al. (2012) utilized a different index ([G-R]/[G + R]) other than the excess green utilized in other studies for deriving phenological information and attempted to use aerial photos to compare with Landsat-based autumn phenology. In summary, the webcam phenology data provide a valuable source of in situ observation for validating LSP. With the improvement of technology and data analyzing techniques, we anticipate the ground-based radiometric measurements of tree canopy phenology will provide more insights on the links between phenological processes of plants and corresponding remote sensing indices.

Recent validation efforts also include a study utilizing extensive data from the Canadian phenology network (PlantWatch) and AVHRR and MERIS-integrated LSP (Pouliot et al. 2011). Given that high resolution intensive phenology data are only available at specific study sites, the growing extensive ground phenology data from crowd-sourcing observation networks, such as PlantWatch (http://www.naturewatch.ca) and the USA National Phenology Network (http://www.usanpn.org), with real-time forest canopy monitoring using near-surface

remote sensing, will contribute to broader LSP validation efforts synergizing observations from different sources. Surface datasets from network volunteer observations, high resolution observations at intensive study sites, and the digital camera records are meant to be used to complement one another in order to achieve a more complete understanding of LSP and the corresponding surface processes. Overall, the validation efforts to date have significantly increased our confidence in using satellite-based LSP for deriving relatively accurate biospheric information for global change studies. Additional efforts may be directed towards validating new LSP products and investigating LSP performance within diversely vegetated environments, as well as for the autumn season.

4.5 Current and Future Research Directions

This section will describe some of the research findings that have emerged from the study of LSP as well as potential directions for future work. As described above, the community has developed a well-established theoretical basis for LSP and there have been advances in both methodology and validation. A Google Scholar search with the string "Land Surface Phenology" returned over 500 papers with an exponential growth pattern over the last 10 years (Fig. 4.4). It is important to note that there are many publications related to LSP that are not necessarily labeled as such. However, this query does reveal that the first paper found using this particular label was by Henebry and Su (1995) and that the term is becoming more established in the literature. With the large (and growing) body of LSP literature, it is beyond the scope of this chapter to do a full literature review of that body of work. Rather, the remainder of this chapter will summarize some of

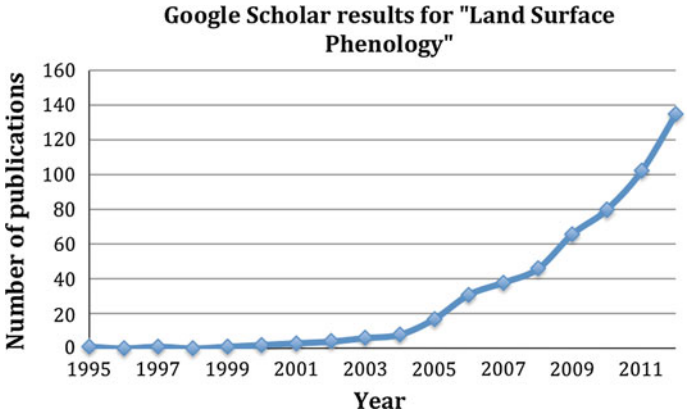

Fig. 4.4 Number of land surface phenology publications by year [This figure is similar to Fig. 21.1 in Henebry and de Beurs (2013), who also noted the trends in literature pertaining to Land Surface Phenology.]

the major findings related to climate and phenology connections, some of the limitations of current work, and how the advances in LSP research will help address these issues and lead to greater utility.

The earliest documented work we could find pertaining to remote sensing and phenology was a progress report from Texas A&M University on a project sponsored by NASA's Goddard Space Flight Center in the early 1970s (Rouse et al. 1974). That study concludes that satellite data can provide a quantitative description of vegetation conditions as phenological indicators for seasonal and climate effects. It is interesting to note this study was based on "Landsat 1" (originally called ERTS-1, Earth Resources Technology Satellite 1) Multispectral Sensor (MSS) data. The satellite was launched on July 23, 1972 and the report was written in the fall of 1973. While this is an impressive turnaround time, it is also an indication that, at least for some researchers, satellites clearly offered an approach to connect vegetation growth to climate drivers. Many similar (relatively) local studies using Landsat and other 10–30 m spatial resolution sensors have been done since then. However, to better understand climate and vegetation phenology connections, LSP studies needed to expand to the continental and global scales.

Within a few years of the earliest demonstration of how AVHRR could be used to monitor vegetation health (Gray and McCrary 1981, Schneider et al. 1981, Townshend and Tucker 1981), researchers started evaluating LSP from that sensor at regional scales far larger than then current Landsat studies. As an example of some of the earliest work on continental LSP, Justice et al. (1986) used AVHRR to monitor 1 year of phenology in Kenya. Particular emphasis was placed on quantifying the phenology of the Acacia Commiphora bushlands. Considerable variation was found and explained through the high spatial variability in the distribution of rainfall and the resulting green-up of the vegetation. They explored the relationship between rainfall and NDVI using meteorological stations existing within the bushland, which shows that the early AVHRR work also considered the relationship between satellite-observed LSP and annual weather patterns (Justice et al. 1986; Justice 1986).

Building on this and other studies demonstrating the utility of AVHRR to monitor vegetation for larger areas over time, much of which was led by the Global Inventory Monitoring and Modeling Studies (GIMMS) group at NASA/Goddard Space Flight Center (GSFC) (Justice 1986), NOAA and NASA initiated the AHVRR pathfinder program to produce global, 8 km NDVI. The pathfinder data were processed using the best available methods at that time to produce a consistent time series of data; including cross-satellite calibration, navigation using an orbital model and updated ephemerides, and correction for Rayleigh scattering. The data were made openly available to the community as both daily and composite data. Analysis of this initial global time series provided insight into terrestrial processes, seasonal and annual variability, and methods for handling large volume data sets and facilitated land surface phenology (James et al. .). As such, it truly did establish a path for subsequent global land vegetation products from MODIS, MERIS, and the Visible Infrared Imaging Radiometer Suite (VIIRS).

Perhaps one of the most seminal articles on large-scale land surface phenology was Myneni et al. (1997), which presented evidence from satellite data that the photosynthetic activity of terrestrial vegetation in northern latitudes increased from 1981 to 1991 in a manner that is suggestive of an increase in plant growth associated with a lengthening of the active growing season. This was one of first articles to link large-scale vegetation trends to a warming climate.

As the available time series of remote sensing data increases, so too have the time spans for LSP studies. As the time series increases, studies are able to better extract more "signal" from the "noise" and explore correlation between LSP and climate events and distinguish between natural variability and trends. Ivits et al. (2012) used LSP derived from the AVHRR from 1982 to 2006 to explore the correlations between phenology and climate and trends in both. Park et al. (2012) used two decades of AVHRR data to explore the relationship between El Niño–Southern Oscillation (ENSO) events and the onset of spring. These are just two examples among many where the long record from AVHRR is being used to explore how vegetation responds to a changing climate.

However, there is considerable uncertainty associated with LSP studies that link climate forcings with vegetation change. At the very heart of the problem is the uncertainty in methods and techniques used to extract phenology parameters from a satellite time series. The foundational intercomparison work of White et al. (2009) demonstrated that start of season estimates vary extensively within and among methods and that selecting the strongest method is difficult without some additional ecosystem information. In addition to differences in algorithms, specific regional phenomena may complicate the analysis. For example, Samanta et al. (2012) detail how clouds and aerosols complicate LSP studies in the Amazon.

Indeed, we can use the Amazon as an example to expose how uncertainty associated with LSP studies can lead to controversy and confusion. In 2010, a Boston University press release[1] stated that a recent study (Samanta et al. 2010) showed results that were contrary to a previously published report and claims by the Intergovernmental Panel on Climate Change (IPCC). Because of its potential relevance to national and international policy, the conclusions of the IPCC can be highly contentious. The uncertainly involved with discerning trends in the Amazon (Saleska et al. 2007; Samanta et al. 2010) provided considerable fodder for climate-related blogs,[2,3] On the technical side, it is not surprising that LSP products may indicate different, somewhat inconsistent results (White et al. 2009; Samanta et al. 2012). However, if LSP results are to contribute to policy-relevant information, it is important, at the very least, to quantify the uncertainty and, at best, provide consistent and reliable information. Hopefully advances in sensors, methods, and validation will help address this uncertainty and lead to greater utility.

---

[1] http://www.eurekalert.org/pub_releases/2010-03/bumc-nsd031110.php

[2] http://scienceblogs.com/deltoid/2010/03/14/its-always-bad-news-for-the-ip/

[3] http://www.realclimate.org/index.php/archives/2010/03/saleska-responds-green-is-green/

Referring back to Fig. 4.4, the increasing number of publications on LSP is likely to be connected to enhanced computational power and storage capacity, improved LSP product quality, and easier access to satellite imagery. However, the increase is likely also tied to the increasing relevance of LSP studies as the community is looking to explore the connection between climate variability and changes or trends in vegetation seasonality as well as the connection between observed LSP and ecosystem functions.

The future likely will bring more satellite imagery and a longer time series of data from which to construct ever-increasing LSP time series. This longer time series will help LSP distinguish between temporal variability, actual trends, and correlation with climate forcings. Perhaps the most pressing need for this line of research will be for common LSP products derived from multiple sensors. The works of Tucker et al. (2005) and Cao et al. (2008) have demonstrated the ability to extend the time series through a multi-sensor approach (see also the Long Term Data Record project at NASA[4]). Future work with LSP will need to build on such work as well as utilize the validation techniques described above to ensure that LSP derived from a multi-sensor time series are free from artifacts from the different data streams. Also, with the entire archive of Landsat data now available and efforts to mosaic and composite those data (Roy et al. 2010), there is the opportunity to consider kilo-, hecto-, and deca-resolution imagery (Morisette 2010) LSP products (Kovalskyy et al. 2012) for regional, continental, and even global LSP studies.

In addition to longer time series, the validation techniques described above will be able to take advantage of an increasing amount of coordinated phenology-related ground-based observations and modeling techniques that can integrate these observations with satellite data. In May 2012, the archive of observations within the USA National Phenology Network recorded its one millionth observation.[5] These offer an unprecedented archive of information with which to compare LSP products. Furthermore, there is now an expanding network of tower-based near-surface cameras to complement field-based phenology observations and help scale from the individual plant to a wider area representing a CO_2 flux tower footprint (Richardson et al. 2009a). The integration of plant phenology and LSP products with CO_2 monitoring and modeling has led the community to call for improved understanding of the environmental controls on vegetation phenology and incorporation of this knowledge into better phenological models (Richardson et al. 2012). Some work is being done toward this objective through data assimilation of empirical phenology models and remote sensing observations (Stockli et al. 2008, 2011). More connection and integration between the carbon modeling and LSP communities are likely to improve our understanding of the global carbon cycle and its impact on climate and feedback to phenological processes (Morisette et al. 2009).

[4] http://ltdr.nascom.nasa.gov

[5] http://www.usgs.gov/newsroom/article.asp?ID=3195#.UAQsGvXNkxE

Finally, it is worth mentioning the integration of LSP products into habitat assessment; including both the evaluation of plant species habitat with a time series of deca-resolution imagery (Evangelista et al. 2009) to animal species using kilo-resolution LSP products (Herfindal et al. 2006). The use of LSP products in habitat modeling can provide spatial predictions of species habitat at higher levels of ecological complexity, including the consideration of functional groups and species assemblages (Guisan and Thuiller 2005).

This section has described some of the foundational work in LSP research and some potential future directions. With the various challenges and opportunities related to this research, it is exciting to consider future research directions for LSP. As we head into the future there will be an ever-longer time series of satellite data from which to extract phenology metrics and look for trends across multiple decades. The expanding size, coordination, and communication among the ground-based phenological networks will offer opportunities for the validation of LSP products as well as a larger community of users who can use and understand LSP products. Finally, with the extended time series and a stronger connection to ground-based observations, it is likely that LSP can provide substantial input to improve carbon, climate, and ecological models.

References

Ahl DE, Gower ST, Burrows SN, Shabanov NV, Myneni RB, Knyazikhin Y (2006) Monitoring spring canopy phenology of a deciduous broadleaf forest using MODIS. Remote Sens Environ 104:88–95. doi:10.1016/j.rse.2006.05.003

Anderson BT, Strahler A (2008) Visualizing weather and climate. Wiley, New York

Baldocchi DD, Black TA, Curtis PS, Falge E, Fuentes JD, Granier A, Gu L, Knohl A, Pilegaard K, Schmid HP, Valentini R, Wilson K, Wofsy S, Xu L, Yamamoto S (2005) Predicting the onset of net carbon uptake by deciduous forests with soil temperature and climate data: a synthesis of FLUXNET data. Int J Biometeorol 49:377–387. doi:10.1007/s00484-005-0256-4

Beck PSA, Atzberger C, Høgda KA, Johansen B, Skidmore AK (2006) Improved monitoring of vegetation dynamics at very high latitudes: a new method using MODIS NDVI. Remote Sens Environ 100:321–334. doi:10.1016/j.rse.2005.10.021

Bradley BA, Jacob RW, Hermance JF, Mustard JF (2007) A curve fitting procedure to derive inter-annual phenologies from time series of noisy satellite NDVI data. Remote Sens Environ 106:137–145. doi:10.1016/j.rse.2006.08.002

Burrows S, Gower S, Clayton M, Mackay D, Ahl D, Norman JM & Diak G (2002) Application of geostatistics to characterize leaf area index (LAI) from flux tower to landscape scales using a cyclic sampling design. Ecosystems, 5:667–679

Cao C, Xiong X, Wu A, Wu X (2008) Assessing the consistency of AVHRR and MODIS L1B reflectance for generating fundamental climate data records. J Geophys Res Atmos 113:D09114. doi:10.1029/2007JD009363

Castro KL, Sanchez-Azofeifa GA (2008) Changes in spectral properties, chlorophyll content and internal mesophyll structure of senescing *Populus balsamifera* and *Populus tremuloides* leaves. Sensors 8:51–69

Clark RN, Swayze GA, Wise R, Livo KE, Hoefen TM, Kokaly RF, Sutley SJ (2007) USGS digital spectral library splib06a. U.S. Geological Survey, Data series 231

de Beurs KM, Henebry GM (2004) Land surface phenology, climatic variation, and institutional change: analyzing agricultural land cover change in Kazakhstan. Remote Sens Environ 89:497–509. doi:10.1016/j.rse.2003.11.006

DeFries R, Hansen M, Townshend J (1995) Global discrimination of land cover types from metrics derived from AVHRR pathfinder data. Remote Sens Environ 54:209–222

Delbart N, Kergoat L, Le Toan T, Lhermitte J, Picard G (2005) Determination of phenological dates in boreal regions using normalized difference water index. Remote Sens Environ 97:26–38. doi:10.1016/j.rse.2005.03.011

Eidenshink JC (1992) The 1990 conterminous United States AVHRR data set. Photogram Eng Rem S 58:809–813

Elmore AJ, Guinn SM, Minsley BJ, Richardson AD (2012) Landscape controls on the timing of spring, autumn, and growing season length in mid-Atlantic forests. Glob Change Biol 18:656–674. doi:10.1111/j.1365-2486.2011.02521.x

Evangelista PH, Stohlgren TJ, Morisette JT, Kumar S (2009) Mapping invasive tamarisk (*Tamarix*): a comparison of single-scene and time-series analyses of remotely sensed data. Remote Sens 1:519–533. doi:10.3390/rs1030519

Filella I, Peñuelas J (1994) The red edge position and shape as indicators of plant chlorophyll content, biomass and hydric status. Int J Remote Sens 15:1459–1470

Fischer A (1994) A model for the seasonal variations of vegetation indices in coarse resolution data and its inversion to extract crop parameters. Remote Sens Environ 48:220–230

Fisher JI, Mustard JF (2007) Cross-scalar satellite phenology from ground, landsat, and MODIS data. Remote Sens Environ 109:261–273. doi:10.1016/j.rse.2007.01.004

Fisher JI, Mustard JF, Vadeboncoeur MA (2006) Green leaf phenology at landsat resolution: scaling from the field to the satellite. Remote Sens Environ 100:265–279. doi:10.1016/j.rse.2005.10.022

Fitzjarrald D, Acevedo OC, Moore KE (2001) Climatic consequences of leaf presence in the Eastern United States. J Clim 14:598–614. doi:10.1175/1520-0442(2001)014<0598:CCOLPI>2.0.CO;2

Gamon JA, Field CB, Goulden ML, Griffin KL, Hartley AE, Joel G, Peñuelas J, Valentini R (1995) Relationships between NDVI, canopy structure, and photosynthesis in three Californian vegetation types. Ecol Appl 5:28–41

Ganguly S, Friedl MA, Tan B, Zhang X, Verma M (2010) Land surface phenology from MODIS: characterization of the collection 5 global land cover dynamics product. Remote Sens Environ 114:1805–1816. doi:10.1016/j.rse.2010.04.005

Gao B (1996) NDWI—a normalized difference water index for remote sensing of vegetation liquid water from space. Remote Sens Environ 58:257–266

Gao F, Morisette JT, Wolfe RE, Ederer G, Pedelty J, Masuoka E, Myneni R, Tan B, Nightingale J (2008) An algorithm to produce temporally and spatially continuous MODIS-LAI time series. IEEE Geosci Remote S 5:60–64. doi:10.1109/LGRS.2007.907971

Gonsamo A, Chen JM, Price DT, Kurz WA, Wu C (2012) Land surface phenology from optical satellite measurement and CO_2 eddy covariance technique. J Geophys Res 117:G03032. doi:10.1029/2012JG002070

Goward SN, Tucker CJ & Dye DG (1985) North American vegetation patterns observed with the NOAA-7 advanced very high resolution radiometer. Vegetatio (The Hague), 64:3–14

Graham EA, Riordan EC, Yuen EM, Estrin D, Rundel PW (2010) Public Internet-connected cameras used as a cross-continental ground-based plant phenology monitoring system. Glob Change Biol 16:3014–3023. doi:10.1111/j.1365-2486.2010.02164.x

Gray TI & McCrary DG (1981) The environmental vegetative index: the tool potentially useful for arid land management. Proceedings of the Fifth Conference on Biometeorology. Anaheim, California. p. 205

Guisan A, Thuiller W (2005) Predicting species distribution: offering more than simple habitat models. Ecol Lett 8:993–1009. doi:10.1111/j.1461-0248.2005.00792.x

Hanes JM (2012) Spring leaf phenology and the diurnal temperature range in a temperate maple forest. Int J Biometeorol. doi:10.1007/s00484-012-0603-1

Hanes JM, Schwartz MD (2011) Modeling land surface phenology in a mixed temperate forest using MODIS measurements of leaf area index and land surface temperature. Theor Appl Climatol 105:37–50. doi:10.1007/s00704-010-0374-8

Hanes JM, Richardson AD, Klostermann S (2013) Mesic temperate deciduous forest phenology. In: Schwartz MD (ed) Phenology: an integrative environmental science, 2nd edn. Springer, New York

Hayden BP (1998) Ecosystem feedbacks on climate at the landscape scale. Philos Trans R Soc Lond B 353:5–18. doi:10.1098/rstb 1998.0186

Henebry GM & Su H (1995) Observing spatial structure in the Flint Hills using AVHRR maximum biweekly NDVI composites. Proceedings of 14th North American Prairie Conference. Kansas State University Press, Manhattan, KS. pp. 143-151

Henebry GM & de Beurs KM (2013) Remote Sensing of Land Surface Phenology: A Prospectus. In: Schwartz MD (ed) Phenology: an integrative environmental science, 2nd edn. Springer, New York

Henricksen BL, Durkin JW (1986) Growing period and drought early warning in Africa using satellite data. Int J Remote Sens 7:1583–1608. doi:10.1080/01431168608948955

Herfindal I, Solberg EJ, Sæther B-E, Høgda KA, Andersen R (2006) Environmental phenology and geographical gradients in moose body mass. Oecologia 150:213–224. doi:10.1007/s00442-006-0519-8

Holben BN (1986) Characteristics of maximum-value composite images from temporal AVHRR data. Int J Remote Sens 7:1417–1434

Huemmrich KF, Black TA, Jarvis PG, McCaughey JH, Hall FG (1999) High temporal resolution NDVI phenology from micrometeorological radiation sensors. J Geophys Res Atmos 104:27935–27944. doi:10.1029/1999JD900164

Huete AR (1988) A soil-adjusted vegetation index (SAVI). Remote Sens Environ 25:295–309. doi:10.1016/0034-4257(88)90106-X

Huete AR, Liu HQ (1994) An error and sensitivity analysis of the atmospheric-and soil-correcting variants of the NDVI for the MODIS-EOS. IEEE T Geosci Remote 32:897–905. doi:10.1109/36.298018

Huete A, Justice C, van Leeuwen W (1999) MODIS vegetation index (MOD 13) algorithm theoretical basis document. Version 3. http://modis.gsfc.nasa.gov/data/atbd/atbd_mod13.pdf. Accessed 8 Aug 2012

Huete A, Didan K, Miura T, Rodriguez EP, Gao X, Ferreira LG (2002) Overview of the radiometric and biophysical performance of the MODIS vegetation indices. Remote Sens Environ 83:195–213. doi:10.1016/S0034-4257(02)00096-2

Hufkens K, Friedl M, Sonnentag O, Braswell BH, Milliman T, Richardson AD (2012) Linking near-surface and satellite remote sensing measurements of deciduous broadleaf forest phenology. Remote Sens Environ 117:307–321. doi:10.1016/j.rse.2011.10.006

Ivits E, Cherlet M, Tóth G, Sommer S, Mehl W, Vogt J, Micale F (2012) Combining satellite derived phenology with climate data for climate change impact assessment. Global Planet Change 88–89:85–97. doi:10.1016/j.gloplacha.2012.03.010

James ME & Kalluri SNV (1994) The Pathfinder AVHRR land data set: An improved coarse resolution data set for terrestrial monitoring. Remote Sensing of Environment, 15(17):3347–3363. doi:10.1080/01431169408954335

Jönsson P, Eklundh L (2004) TIMESAT—a program for analyzing time-series of satellite sensor data. Comput Geosci 30:833–845. doi:10.1016/j.cageo.2004.05.006

Ju JC, Roy DP, Shuai YM, Schaaf C (2010) Development of an approach for generation of temporally complete daily nadir MODIS reflectance time series. Remote Sens of Environ 114:1–20. doi:10.1016/j.rse.2009.05.022

Justice CO, Holben BN, Gwynne MD (1986) Monitoring East African vegetation using AVHRR data. Int J Remote Sens 7:1453–1474

Justice CO, Vermote E, Townshend JRG, Defries R, Roy DP, Hall DK, Salomonson VV, Privette JL, Riggs G & Strahler A (1998) The Moderate resolution imaging spectroradiometer

(MODIS): land remote sensing for global change research. IEEE Trans Geosci Remote Sens 36:1228–1249

Justice CO (1986) Monitoring the Grasslands of Semiarid Africa Using NOAA AVHRR Data - Editorial. Int J Remote Sens 7:1385–1390

Kang S, Running SW, Lim J-H, Zhao M, Park C-R, Loehman R (2003) A regional phenology model for detecting onset of greenness in temperate mixed forests, Korea: an application of MODIS leaf area index. Remote Sens Environ 86:232–242. doi:10.1016/S0034-4257(03)00103-2

Kaufman YJ, Tanre D (1992) Atmospherically resistant vegetation index (ARVI) for EOS-MODIS. IEEE T Geosci Remote 30:261–270. doi:10.1109/36.134076

Knapp AK, Carter GA (1998) Variability in leaf optical properties among 26 species from a broad range of habitats. Am J Bot 85:940–946

Knipling EB (1970) Physical and physiological basis for the reflectance of visible and near-infrared radiation from vegetation. Remote Sens Environ 1:155–159. doi:10.1016/S0034-4257(70)80021-9

Kovalskyy V, Roy DP, Zhang XY, Ju J (2012) The suitability of multi-temporal web-enabled Landsat data NDVI for phenological monitoring – a comparison with flux tower and MODIS NDVI. Remote Sens Lett 3:325–334. doi:10.1080/01431161.2011.593581

Lee DW, O'Keefe J, Holbrook NM, Feild TS (2003) Pigment dynamics and autumn leaf senescence in a New England deciduous forest, Eastern USA. Ecol Res 18:677–694. doi:10.1111/j.1440-1703.2003.00588.x

Liang L, Schwartz MD (2009) Landscape phenology: an integrative approach to seasonal vegetation dynamics. Landscape Ecol 24:465–472. doi:10.1007/s10980-009-9328-x

Liang L, Schwartz MD, Fei S (2011) Validating satellite phenology through intensive ground observation and landscape scaling in a mixed seasonal forest. Remote Sens Environ 115:143–157. doi:10.1016/j.rse.2010.08.013

Lloyd D (1990) A phenological classification of terrestrial vegetation cover using shortwave vegetation index imagery. Int J Remote Sens 11:2269–2279

Loveland TR, Merchant JW, Ohlen DO, Brown JF (1991) Development of a land-cover characteristics database for the conterminous U.S. Photogram Eng Rem S 57:1453–1463

Morisette JT (2010) Toward a standard nomenclature for imagery spatial resolution. Int J Remote Sens 31:2347–2349. doi:10.1080/01431160902994457

Morisette JT, Richardson AD, Knapp AK, Fisher JI, Graham EA, Abatzoglou J, Wilson BE, Breshears DD, Henebry GM, Hanes JM, Liang L (2009) Tracking the rhythm of the seasons in the face of global change: phenological research in the 21st century. Front Ecol Environ 7:253–260. doi:10.1890/070217

Myneni RB, Keeling CD, Tucker CJ, Asrar G, Nemani RR (1997) Increased plant growth in the northern high latitudes from 1981 to 1991. Nature 386:698–702. doi:10.1038/386698a0

Myneni RB, Hoffman S, Knyazikhin Y, Privette JL, Glassy J, Tian Y, Wang Y, Song X, Zhang Y, Smith GR, Lotsch A, Friedl M, Morisette JT, Votava P, Nemani RR, Running SW (2002) Global products of vegetation leaf area and fraction absorbed PAR from year one of MODIS data. Remote Sens Environ 83:214–231

Ollinger SV (2011) Sources of variability in canopy reflectance and the convergent properties of plants. New Phytol 189:375–394. doi:10.1111/j.1469-8137.2010.03536.x

Park K-A, Bayarsaikhan U, Kim K-R (2012) Effects of El Niño on spring phenology of the highest mountain in North-East Asia. Int J Remote Sens 33:5268–5288. doi:10.1080/01431161.2012.657362

Peñuelas J, Filella I (1998) Visible and near-infrared reflectance techniques for diagnosing plant physiological status. Trends Plant Sci 3:151–156. doi:10.1016/S1360-1385(98)01213-8

Pouliot D, Latifovic R, Fernandes R, Olthof I (2011) Evaluation of compositing period and AVHRR and MERIS combination for improvement of spring phenology detection in deciduous forests. Remote Sens Environ 115:158–166. doi:10.1016/j.rse.2010.08.014

Reed BC, Brown JF, VanderZee D, Loveland TR, Merchant JW, Ohlen DO (1994) Measuring phenological variability from satellite imagery. J Veg Sci 5:703–714. doi:10.2307/3235884

Reed BC, Schwartz MD, Xiao X (2009) Remote sensing phenology: status and the way forward. In: Noormets A (ed) Phenology of ecosystem processes: applications in global change research. Springer, Heidelberg

Richardson AD, Jenkins JP, Braswell BH, Hollinger DY, Ollinger SV, Smith M-L (2007) Use of digital webcam images to track spring green-up in a deciduous broadleaf forest. Oecologia 152:323–334. doi:10.1007/s00442-006-0657-z

Richardson AD, Braswell BH, Hollinger DY, Jenkins JP, Ollinger SV (2009a) Near-surface remote sensing of spatial and temporal variation in canopy phenology. Ecol Appl 19:1417–1428. doi:10.1890/08-2022.1

Richardson AD, Hollinger DY, Dail DB, Lee JT, Munger JW, O'Keefe J (2009b) Influence of spring phenology on seasonal and annual carbon balance in two contrasting New England forests. Tree Physiol 29:321–331. doi:10.1093/treephys/tpn040

Richardson AD, Anderson RS, Arain MA, Barr AG, Bohrer G, Chen G, Chen JM, Ciais P, Davis KJ, Desai AR, Dietze MC, Dragoni D, Garrity SR, Gough CM, Grant R, Hollinger DY, Margolis HA, McCaughey H, Migliavacca M, Monson RK, Munger JW, Poulter B, Raczka BM, Ricciuto DM, Sahoo AK, Schaefer K, Tian H, Vargas R, Verbeeck H, Xiao J, Xue Y (2012) Terrestrial biosphere models need better representation of vegetation phenology: results from the North American carbon program site synthesis. Glob Change Biol 18:566–584. doi:10.1111/j.1365-2486.2011.02562.x

Rosenzweig C, Casassa G, Karoly DJ, Imeson A, Liu C, Menzel A, Rawlins S, Root TL, Seguin B, Tryjanowski P (2007) Assessment of observed changes and responses in natural and managed systems. Climate change 2007: impacts, adaptation and vulnerability. In: Parry ML, Canziani OF, Palutikof JP, van der Linden PJ, Hanson CE (eds) Contribution of working group II to the fourth assessment report of the intergovernmental panel on climate change. Cambridge University Press, Cambridge

Rouse J-W, Haas R-H, Schell J-A, Deering D-W, Harlan J-C (1974) Monitoring the vernal advancements and retrogradation (Greenwave effect) of nature vegetation. NASA/GSFC final report, NASA, Greenbelt

Roy DP, Ju J, Kline K, Scaramuzza PL, Kovalskyy V, Hansen M, Loveland TR, Vermote R, Zhang C (2010) Web-enabled landsat data (WELD): landsat ETM + composited mosaics of the conterminous United States. Remote Sens Environ 114:35–49. doi:10.1016/j.rse.2009.08.011

Running SW, Nemani RR, Heinsch FA, Zhao M, Reeves M, Hashimoto H (2004) A continuous satellite-derived measure of global terrestrial primary production. Bioscience 54:547–560

Saleska SR, Didan K, Huete AR, da Rocha HR (2007) Amazon Forests Green-Up During 2005 Drought. Science 318(5850):612

Samanta A, Ganguly S, Hashimoto H, Devadiga S, Vrmote E, Knyazikhin Y, Nemani R, Myneni R (2010) Amazon forests did not green-up during the 2005 drought. Geophys Res Lett 37:L05401. doi:10.1029/2009GL042154

Samanta A, Ganguly S, Vermote E, Nemani RR, Myneni RB (2012) Why is remote sensing of Amazon forest greenness so challenging? Earth Int 16(2). Paper 7. doi:10.1175/2012EI440.1

Schwartz MD (1990) Detecting the onset of spring: a possible application of phenological models. Climate Res 1:23–29

Schwartz MD (1994) Monitoring global change with phenology: the case of the spring green wave. Int J Biometeorol 38:18–22. doi:10.1007/BF01241799

Schwartz MD (1996) Examining the spring discontinuity in daily temperature ranges. J Climate 9:803–808. doi:10.1175/1520-0442(1996)009<0803:ETSDID>2.0.CO;2

Schwartz MD (1997) Spring index models: an approach to connecting satellite and surface phenology. In: Lieth H, Schwartz MD (eds) Phenology of seasonal climates. Backhuys, Netherlands

Schwartz MD, Hanes JM (2010) Intercomparing multiple measures of the onset of spring in eastern North America. Int J Climatol 30:1614–1626. doi:10.1002/joc.2008

Schwartz MD, Reed BC (1999) Surface phenology and satellite sensor-derived onset of greenness: an initial comparison. Int J Remote Sens 20:3451–3457. doi:10.1080/014311699211499

Schwartz MD, Reed BC, White MA (2002) Assessing satellite-derived start-of-season measures in the conterminous USA. Int J Climatol 22:1793–1805. doi:10.1002/joc.819

Schwartz MD, Hanes JM, Liang L (2013) Comparing carbon flux and high-resolution spring phenological measurements in a northern mixed forest. Agr Forest Meteorol 169:136–147

Schneider SR, McGinnis SR & Gatlin JA (1981) Use of NOAA/AVHRR visible and near-infrared data for land remote sensing. NOAA Technical Report, NESS 84, USDC, Washington, D.C

Shellito BA (2012) Introduction to geospatial technologies. W.H. Freeman and Company, New York

Slaton MR, Hunt EMR Jr, Smith WK (2001) Estimating near-infrared leaf reflectance from leaf structural characteristics. Am J Bot 88:278–284

Sonnentag O, Hufkens K, Teshera-Sterne C, Young AM, Friedl M, Braswell BH, Milliman T, O'Keefe J, Richardson AD (2012) Digital repeat photography for phenological research in forest ecosystems. Agric For Meteorol 152:159–177

Stöckli R, Rutishauser T, Dragoni D, O'Keefe J, Thornton PE, Jolly M, Lu L, Denning AS (2008) Remote sensing data assimilation for a prognostic phenology model. J Geophys Res 113:G04021. doi:10.1029/2008JG000781

Stöckli R, Rutishauser T, Baker I, Liniger MA, Denning AS (2011) A global reanalysis of vegetation phenology. J Geophys Res 116:G03020. doi:10.1029/2010JG001545

Tan B, Morisette JT, Wolfe RE, Gao F, Ederer GA, Nightingale J, Pedelty JA (2008) Vegetation phenology metrics derived from temporally smoothed and gap-filled MODIS data. Proc IGARSS 3:593–596. doi:10.1109/IGARSS.2008.4779417

Tan B, Morisette JT, Wolfe RE, Gao F, Ederer GA, Nightingale J, Pedelty JA (2010) An enhanced TIMESAT algorithm for estimating vegetation phenology metrics from MODIS data. IEEE J Sel Top Appl 4:361–371. doi:10.1109/JSTARS.2010.2075916

Tarpley J (1991) The NOAA global vegetation index product—A review. Global and Planetary Change, 4:189–194

Thayn JB, Price KP (2008) Julian dates and introduced temporal error in remote sensing vegetation phenology studies. Int J Remote Sens 29:6045–6049. doi:10.1080/01431160802235829

Townshend JRG & Tucker CJ (1981) Utility of AVHRR of NOAA 6 and 7 for vegetation mapping. In Matching Remote Sensing Technologies and their Applications Proceedings (London: Remote Sensing Society), p. 97

Tucker CJ, Pinzon JE, Brown ME, Slayback DA, Pak EW, Mahoney R, Vermote EF, El Saleous N (2005) An extended AVHRR 8-km NDVI dataset compatible with MODIS and SPOT vegetation NDVI data. Int J Remote Sens 26:4485–4498. doi:10.1080/01431160500168686

Wang Q, Tenhunen J, Dinh NQ, Reichstein M, Otieno D, Granier A, Pilegarrd K (2005) Evaluation of seasonal variation of MODIS derived leaf area index at two European deciduous broadleaf forest sites. Remote Sens Environ 96:475–484. doi:10.1016/j.rse.2005.04.003

White MA, Thornton PE, Running SW (1997) A continental phenology model for monitoring vegetation responses to interannual climatic variability. Glob Biogeochem Cycles 11:217–234. doi:10.1029/97GB00330

White MA, Schwartz MD, Running SW (1999) Young students, satellites aid understanding of climate–biosphere link. EOS Trans 81(1):5. doi:10.1029/00EO00001

White MA, Nemani RR, Thornton PE, Running SW (2002) Satellite evidence of phenological differences between urbanized and rural areas of the Eastern United States deciduous broadleaf forest. Ecosystems 5:260–273. doi:10.1007/s10021-001-0070-8

White MA, Hoffman F, Hargrove WW, Nemani RR (2005) A global framework for monitoring phenological responses to climate change. Geophys Res Lett 32:L04705. doi:10.1029/2004GL021961

White MA, de Beurs KM, Didan K, Inouye DW, Richardson AD, Jensen OP, O' Keefe J, Zhang G, Nemani RR, van Leeuwen WJD, Brown JF, de Wit A, Schaepman M, Lin X, Dettinger M, Bailey AS, Kimball J, Schwartz MD, Baldocchi DD, Lee JT, Lauenroth WK (2009) Intercomparison, interpretation, and assessment of spring phenology in North America estimated from remote sensing for 1982–2006. Glob Change Biol 15:2335–2359. doi:10.1111/j.1365-2486.2009.01910.x

Wu J, Loucks OL (1995) From balance of nature to hierarchical patch dynamics: a paradigm shift in ecology. Q Rev Biol 70:439–466

Yang W, Huang D, Tan B, Stroeve JC, Shabanov NV, Knyazikhin Y, Nemani RR, Myneni RB (2006) Analysis of leaf area index and fraction of PAR absorbed by vegetation products from the terra MODIS sensor: 2000–2005. IEEE Trans Geosci Remote Sens 44:1829–1842. doi:10.1109/TGRS.2006.871214

Zhang X, Goldberg MD (2011) Monitoring fall foliage coloration dynamics using time-series satellite data. Remote Sens Environ 115:382–391. doi:10.1016/j.rse.2010.09.009

Zhang X, Hodges JCF, Schaaf CB, Friedl MA, Strahler AH, Gao F (2001) Global vegetation phenology from AVHRR and MODIS data. Proc IGARSS 5:2262–2264. doi:10.1109/IGARSS.2001.977969

Zhang X, Friedl MA, Schaaf CB, Strahler AH, Hodges JCF, Gao F, Reed BC, Huete A (2003) Monitoring vegetation phenology using MODIS. Remote Sens Environ 84:471–475. doi:10.1016/S0034-4257(02)00135-9

Zhang X, Friedl MA, Schaaf CB, Strahler AH, Schneider A (2004) The footprint of urban climates on vegetation phenology. Geophys Res Lett 31:L12209. doi:10.1029/2004GL020137

Chapter 5
Gross Primary Production of Terrestrial Vegetation

Xiangming Xiao, Cui Jin and Jinwei Dong

Abstract Gross primary production (GPP) of vegetation is the first and important flux of the terrestrial carbon cycle, and there is no direct measurement technique for GPP at ecosystem and landscape scales. A number of satellite-based Light Use Efficiency (LUE) models or Production Efficiency Models (PEM) have been developed to estimate GPP in the past few decades, and they are driven by satellite images with or without climate data. This chapter provides a brief review on some of these LUE models, and illustrates the Vegetation Photosynthesis Model (VPM) through its simulations of C3 crop (soybean) and C4 crop (maize) at the CO2 eddy flux tower site in Nebraska, USA.

5.1 Introduction

Gross primary production (GPP) and net primary production (NPP) are two important components of the carbon cycle. GPP is defined as the rate at which vegetation captures and stores carbon dioxide in a given length of time via a photosynthetic process. NPP is defined as the difference between GPP and autotrophic respiration (R_a), and is often measured as net production or accumulation of dry matter in vegetation during a year (Roxburgh et al. 2005). Plant photosynthesis at the chloroplast and leaf levels can be accurately measured through various instruments (Taiz and Zeiger 2002). However, GPP at the canopy, ecosystem, and landscape scales cannot be directly measured through instruments, yet. Therefore, how to scale up the estimates of GPP from individual leaves to the canopy, ecosystem and landscape scales is still a challenging scientific question. Currently, three research approaches are widely applied to estimate GPP at

X. Xiao (✉) · C. Jin · J. Dong
Department of Microbiology and Plant Biology, Center for Spatial Analysis, University of Oklahoma, Norman, OK, USA
e-mail: xiangming.xiao@ou.edu

J. M. Hanes (ed.), *Biophysical Applications of Satellite Remote Sensing*, Springer Remote Sensing/Photogrammetry, DOI: 10.1007/978-3-642-25047-7_5,

ecosystem and landscape scales: (1) CO_2 flux measurements by eddy covariance technique (Goulden et al. 2011; Moureaux et al. 2008; Verbeeck et al. 2008); (2) process-based biogeochemical models that incorporate a number of physiological processes and use climate data as inputs (Matsushita et al. 2004; Running 1993); and (3) Production Efficiency Models (PEM) that use the principle of radiation-use efficiency (RUE) or light-use efficiency (LUE) with the inputs of satellite images and climate data (Peng and Gitelson 2012; Potter et al. 1993; Prince and Goward 1995a, b; Running et al. 1999; Sims et al. 2008; Sims et al. 2006a; Xiao et al. 2005a, b).

The first year-long continuous measurements of net ecosystem CO_2 exchange (NEE) from the eddy covariance technique were conducted at the Harvard Forest site in Massachusetts in 1990 (Wofsy et al. 1993). The integrated CO_2 flux measurements available at CO_2 flux tower sites cover footprints with various sizes and shapes, which range from hundreds of meters to several kilometers, depending on tower heights, canopy physical characteristics, and wind velocity (Baldocchi et al. 1996). Continuous measurements of NEE between terrestrial ecosystems and the atmosphere from eddy flux towers at half-hour intervals allow for more detailed study of ecosystem respiration (R_e) and GPP at ecosystem and landscape scales (Wofsy et al. 1993). NEE data can be gap-filled and partitioned into R_e and GPP with different methods (Papale et al. 2006; Reichstein et al. 2005); however, there are still large uncertainties in estimating seasonal dynamics and spatial variation of R_e and GPP at the canopy and landscape scales due to spatial heterogeneity within the footprints of flux measurements in a flux tower.

Process-based biogeochemical models describe the energy conversion in the vegetation growth process, including photosynthesis and respiration. A number of process-based biogeochemical models have been developed, such as the Bio-Geochemical Cycles model (BIOME-BGC) (Running and Gower 1991), the Terrestrial Ecosystem Model (TEM) (McGuire et al. 1995), the CENTURY model (Parton et al. 1993), the Carbon Exchange in the Vegetation-Soil-Atmosphere model (CEVSA) (Cao and Woodward 1998a, b; Woodward et al. 1995), and the Atmosphere-Vegetation Interaction Model (AVIM) (Ji 1995). These models often have a number of state variables and a large number of parameters that describe the responses of various biogeochemical processes to climate, soils, and water. Model calibration is essential and is often done before these models are applied to simulate the carbon dynamics of terrestrial ecosystems at landscape and regional scales (Chen and Zhuang 2012; Chiesi et al. 2012).

The PEM was first proposed to estimate NPP of vegetation by Monteith (Monteith 1972; Monteith 1977), based on the theory of RUE or LUE. In simple terms, NPP is estimated as the product of absorbed photosynthetically active radiation (PAR) and RUE or LUE. Based on this concept, a number of PEMs have been developed to estimate gross and net primary productions with the use of satellite image data and climate data (Field et al. 1995; Potter et al. 1993; Prince and Goward 1995; Running et al. 1994, 2004; Xiao et al. 2004c), such as the Global Production Efficiency Model (GLO-PEM) (Prince and Goward 1995), the Carnegie-Ames-Stanford Approach model (CASA) (Potter 1999; Potter et al.

1993), the Vegetation Photosynthesis Model (VPM) (Xiao et al. 2004a), the Terrestrial Uptake and Release of Carbon model (TRUC) (Ruimy et al. 1996a), and the MODIS Daily Photosynthesis model (PSN) (Running et al. 2000). Several recent reviews have discussed existing PEMs from different perspectives (Hilker et al. 2008; McCallum 2009). There is still a need to compare PEMs in the context of model variables (e.g., light absorption) and model parameters (e.g., maximum light-use efficiency).

This book chapter is organized into five sections. In the first section we briefly review the theory of PEMs. The second section compares several well-developed PEMs in the contexts of model variables (e.g., light absorption) and model parameters (e.g., light-use efficiency). The third section presents the validation strategy using in situ data from eddy covariance technique. In the fourth section we illustrate the simulation and evaluation processes of PEMs with a case study that estimates GPP of maize (C_4 plant) and soybeans (C_3 plant) over years using the VPM model. We conclude with a series of recommendations for parameter estimation and improvements of validation exercises for PEMs.

5.2 Theoretical Basis

Plant photosynthesis occurs within the chloroplasts of plant leaves and is composed of two processes: (1) light absorption and (2) carbon fixation. Chlorophyll pigment absorbs incoming PAR (mostly in the spectrum of 400–700 nm) from sunlight, and the absorbed energy is then used to combine water and CO_2 to produce carbohydrates.

When incoming radiance reaches the plant canopy, we can measure the amounts of radiance that are reflected, transmitted, and absorbed. What fractions of PAR are absorbed by the vegetation canopy and by chlorophyll pigment, respectively? At the leaf level, individual green leaves have pigments (chlorophyll and other pigments) and nonphotosynthetic materials (e.g., cell walls, veins, etc.). At the canopy level, a plant canopy has chlorophyll pigments and nonphotosynthetic vegetation (NPV; e.g., nonphotosynthetic branches, stems, trunks, senescent leaves). Therefore, the fraction of PAR absorbed by the vegetation canopy ($FPAR_{canopy}$) should be partitioned into the fraction of PAR absorbed by chlorophyll ($FPAR_{chl}$) and the fraction of PAR absorbed by the nonphotosynthetic vegetation component ($FPAR_{NPV}$). The total amount of PAR absorbed by the vegetation canopy ($APAR_{canopy}$) is the sum of (1) the amount of PAR absorbed by chlorophyll ($APAR_{chl}$) and (2) the amount of PAR absorbed by NPV ($APAR_{NPV}$).

$$Canopy = chlorophyll + NPV \tag{5.1}$$

$$FPAR_{canopy} = FPAR_{chl} + FPAR_{NPV} \tag{5.2}$$

$$APAR_{canopy} = APAR_{chl} + APAR_{NPV} \tag{5.3}$$

$$APAR_{canopy} = FPAR_{canopy} \times PAR \tag{5.4}$$

$$APAR_{chl} = FPAR_{chl} \times PAR \tag{5.5}$$

$$APAR_{NPV} = FPAR_{NPV} \times PAR \tag{5.6}$$

The framework of PEMs was first proposed in the early 1970s as a function of APAR and LUE (Monteith 1972, 1977). Therefore, GPP and NPP can be estimated as a product of (1) the total amount of absorbed PAR, and (2) the radiation (light)-use efficiency (ε_g for GPP, and ε_n for NPP) with the following formulas:

$$GPP = \varepsilon_g \times APAR \tag{5.7}$$

$$NPP = \varepsilon_n \times APAR \tag{5.8}$$

Based on the above-mentioned conceptual partitioning between $FPAR_{chl}$ and $FPAR_{npv}$, the PEMs can be divided into two groups. One group of PEMs uses $FPAR_{canopy}$ to estimate GPP:

$$GPP = \varepsilon_g \times FPAR_{canopy} \times PAR \tag{5.9}$$

The other group of PEMs uses $FPAR_{chl}$ to estimate GPP:

$$GPP = \varepsilon_g \times FPAR_{chl} \times PAR \tag{5.10}$$

5.3 Methods

The development histories, key parameters, and variables of several well-established PEMs are summarized in Table 5.1. Variations among the different PEMs appear in the calculation of FPAR, the estimation of the maximum LUE parameter, and the use of scalars or downregulation factors.

Generally, $FPAR_{canopy}$ can be estimated with two methods by using (1) the leaf area index (LAI) from in situ measurements at the site scale, or (2) satellite-derived vegetation indices at the large scale. For large scale GPP modeling with PEMs, the Normalized Difference Vegetation Index (NDVI, Tucker et al. 1979) is often used to estimate $FPAR_{canopy}$ (Potter et al. 1993; Prince and Goward 1995; Ruimy et al. 1999; Running et al. 2004; Veroustraete et al. 2002; Yuan et al. 2007) with a simple empirical or physical function, as shown in Eqs. 5.11 and 5.12. About the estimation of $FPAR_{chl}$, Xiao et al. (2004a) first proposed using the Enhanced Vegetation Index (EVI) (Huete et al. 1997) to estimate $FPAR_{chl}$ (see Eqs. 5.13 and 5.14). By simulating $FPAR_{canopy}$ and $FPAR_{chl}$ using the radiative transfer model, it was reported that EVI time series data are closer to the dynamic of $FPAR_{chl}$ (Zhang et al. 2006). Recently, EVI and other chlorophyll vegetation indices have increasingly been adopted by new PEMs (Gitelson et al. 2006; Potter

Table 5.1 A comparison of major model variables among the 10 well-documented Production Efficiency Models (PEMs)

Model	FPAR	FPAR estimation	ε_g or ε_n (g C m^{-2} MJ^{-1} APAR)	E_0 (g C m^{-2} MJ^{-1} APAR)	Year and references
CASA	$FPAR_{canopy}$	NDVI	$\varepsilon_n = \varepsilon_0 \times T \times f$ (AET, PET)	0.55	Potter (1999), Potter et al. (1993)
CASA	$FPAR_{chl}$	EVI	$\varepsilon_n = \varepsilon_0 \times T \times f$ (AET, PET)	0.389	Potter (2012)
GLO-PEM	$FPAR_{canopy}$	NDVI	$\varepsilon_g = \varepsilon_0 \times T \times SM \times VPD$	55.2α[a], 2.76[b]	Prince (1995)
TURC	$FPAR_{canopy}$	NDVI	$\varepsilon_g = \varepsilon_0$	4.04	Ruimy et al. (1996a, b), (1994)
MODIS-PSN	$FPAR_{canopy}$	NDVI	$\varepsilon_g = \varepsilon_0 \times T \times VPD$	0.604-1.259[c]	Running et al. (2000)
C-Fix	$FPAR_{canopy}$	NDVI	$\varepsilon_g = \varepsilon_0 \times T \times CO_2$	1.1	Veroustraete et al. (2002)
VPM	$FPAR_{chl}$	EVI	$\varepsilon_g = \varepsilon_0 \times T \times W \times P$	2.208[d]; 2.484[e]	Xiao et al. (2005b)
GR	$FPAR_{chl}$	VI_{chl}	$\varepsilon_g = f(VI_{chl})$	–	Gitelson et al. (2006)
TG	$FPAR_{chl}$	EVI	$\varepsilon_g = f$(EVI, LST)	–	Sims et al. (2008), (2006a)
EC-LUE	$FPAR_{canopy}$	NDVI	$\varepsilon_g = \varepsilon_0 \times \min(T, EF)$	2.14	Yuan et al (2007), (2010)

T Air temperature scalar; *SM* soil moisture scalar; *VPD* water vapor pressure deficit scalar; *AET* Actual Evapotranspiration; *PET* Potential Evapotranspiration; CO_2 the normalized CO_2 fertilization factor; *EF* Evaporative Fraction; *LST* Land Surface Temperature

[a] For C3 vegetation, α is quantum yield

[b] For C4 vegetation

[c] For 11 standard global biome types

[d] For evergreen needle leaf forests

[e] For moist tropical evergreen forests

2012; Sims et al. 2006a; Xiao et al. 2005b), such as the updated version of the CASA model (Potter et al. 2012).

$$FPAR_{canopy} = f\,(NDVI) \tag{5.11}$$

where NDVI is calculated using surface reflectance from the red and near-infrared bands (Tucker 1979):

$$\mathrm{NDVI} = \frac{\rho_{\mathrm{NIR}} - \rho_{\mathrm{red}}}{\rho_{\mathrm{NIR}} + \rho_{\mathrm{red}}} \tag{5.12}$$

$$FPAR_{chl} = f\,(EVI) \tag{5.13}$$

where *EVI* directly adjusts the reflectance in the red band as a function of the reflectance in the blue band, accounting for residual atmospheric contamination (e.g., aerosols), variable soil, and canopy background reflectance (Huete et al. 1997):

$$\mathrm{EVI} = \frac{\mathrm{G}(\rho_{\mathrm{NIR}} - \rho_{\mathrm{red}})}{\rho_{\mathrm{NIR}} + (\mathrm{C}_1 \times \rho_{\mathrm{red}} - \mathrm{C}_2 \times \rho_{\mathrm{blue}}) + \mathrm{L}} \tag{5.14}$$

where $G = 2.5$, $C_1 = 6$, $C_2 = 7.5$, and $L = 1$, and ρ_{NIR}, ρ_{red}, and ρ_{blue} are the land surface reflectance of the NIR, red, and blue bands, respectively. EVI is more sensitive in medium-to-high biomass areas than NDVI (Huete et al. 1997). The following sections describe detailed calculation methods of *FPAR* in different PEMs.

LUE is the rate at which absorbed radiation is converted into dry matter. It can be estimated with various methods: a constant conversion efficiency or the product of a maximum (optimum) constant adjusted by environmental stress scalars (Ruimy et al. 1999). Various environmental stress scalars, such as air temperature and soil moisture, result in downregulation of the maximum LUE (McCallum I. 2009). The GR and TG models estimate the parameter ε_g using remote sensing vegetation indices (Table 5.1). The TURC model assumes maximum light-use efficiency for all biome types without considering the environmental stresses. The other six PEMs calculate the parameter ε_g by adjusting maximum light-use efficiency ε_0 with soil moisture, air temperature, or CO_2 concentration scalars. Moreover, the CASA, TURC, C-Fix, and EC-LUE models use the same ε_0 across all vegetation types. GLO-PEM, VPM, and PSN models assign specific ε_0 for different biome types. A brief description of the unique variable calculations of PEMs is listed below.

5.3.1 The Carnegie-Ames-Stanford Approach (CASA) Model

The CASA model is a simple and mechanical process model, and it describes the processes of carbon dynamics in terrestrial vegetation and soils (Potter et al. 1993). The CASA model directly estimates NPP, avoiding complicated calculation of autotrophic respiration.

In the earlier version of the CASA model, $FPAR_{canopy}$ is estimated with NDVI and biome type (Potter et al. 1993). The maximum value of $FPAR_{canopy}$ is 0.95. $FPAR_{canopy}$ is defined as below:

$$FPAR_{\text{canopy}} = \min\left[\frac{SR - SR_{\min}}{SR_{\max} - SR_{\min}}, 0.95\right] \tag{5.15}$$

$$SR = \frac{1 + NDVI}{1 - NDVI} \tag{5.16}$$

where SR_{min} is 1.08 for bare land surface, and SR_{max} is determined by biome type, ranging from 4.14 to 6.17.

The updated version of the CASA model uses EVI to estimate $FPAR_{chl}$ (Potter 2012), following the work suggested by Xiao et al. (2004a):

$$FPAR_{chl} = EVI \tag{5.17}$$

The CASA model defines the constant values of ε_0 as 0.55 g C m^{-2} MJ^{-1} APAR (Potter 1999; Potter et al. 1993) or 0.389 g C m^{-2} MJ^{-1} APAR (Potter et al. 2003; Potter 2012) for global biome types, and ε_n is determined by Eq. 5.18

$$\varepsilon_n = \varepsilon_0 \times T \times W \tag{5.18}$$

where T is the temperature stress scalar computed with reference to the derivation of the optimal temperature (T_{opt}) for production; and W refers to the monthly relative soil moisture deficit based on the difference between actual and potential evapotranspiration estimated by a soil/water balance model (Nayak et al. 2010; Potter and Klooster 1997; Potter et al. 1993, 1998).

5.3.2 The Global Production Efficiency Model (GLO-PEM)

The GLO-PEM model estimates both GPP and NPP based on the production efficiency concept. It includes the components that describe the processes of canopy radiation absorption, utilization, autotrophic respiration, and the regulations of these processes by environmental factors (Goetz et al. 2000; Prince and Goward 1995). The GLO-PEM model estimates $FPAR_{canopy}$ with NDVI. NDVI of bare soil is approximately 0.05, and NDVI of the closed, thick, and green vegetation canopy is usually 0.9 or higher (Goward and Huemmrich 1992).

$$FPAR_{canopy} = 1.08 \times NDVI - 0.08 \tag{5.19}$$

ε_g is estimated through a modeling approach based on plant physiological principles (Prince and Goward 1995). Plant photosynthesis depends on both the capacity of photosynthetic enzymes to assimilate CO_2 (Collatz et al. 1991; Farquhar et al. 1980) and the stomatal conductance of CO_2 from the atmosphere into intercellular spaces (Harley et al. 1992). These two processes are affected by environmental factors such as air temperature (T), water vapor pressure deficit (VPD), and soil moisture (SM).

$$\varepsilon_g = \varepsilon_0 \times T \times SM \times VPD \tag{5.20}$$

Detailed approaches for modeling ε_g are described in earlier publications (Collatz et al. 1991, 1992; Goetz and Prince 1998, 1999; Prince and Goward 1995).

5.3.3 The Terrestrial Uptake and Release of Carbon (TURC) Model

The TURC model calculates NPP as the difference between GPP and autotrophic respiration (Cramer et al. 1999; Lafont et al. 2002; Ruimy et al. 1996a, 1999). The linear relationship between $FPAR_{canopy}$ and NDVI is defined with Eq. 5.21:

$$FPAR_{canopy} = 2.186 \times NDVI - 0.1914 \quad (5.21)$$

The TURC model assumes one constant ε_g (4.04 g C m^{-2} MJ^{-1} APAR) across all ecosystem types (Lafont et al. 2002). Autotrophic respiration is calculated as the sum of maintenance and growth respiration. Maintenance respiration is a linear function of air temperature and biomass for leaves, fine roots, and wood. Growth respiration is taken as a constant fraction (0.28) of GPP minus maintenance respiration (Lafont et al. 2002).

5.3.4 The MODIS Daily Photosynthesis (PSN) Model

The PSN model was developed from a process-based ecosystem model BIOME-BGC, and it estimates both GPP and NPP (Running et al. 2004). The PSN model is driven by datasets, including land cover, FPAR/LAI, and daily meteorological data from the Global Modeling and Assimilation Office (GMAO), NASA. It produces 8-day and yearly GPP and NPP estimates as the standard MODIS GPP/NPP product (MOD17) (Running et al. 1994; Zhao et al. 2005).

$FPAR_{canopy}$ is estimated as a function of NDVI, derived from the MODIS standard land product (MOD15) (Running et al. 1999, 2000, 2004).

$$FPAR_{canopy} \approx NDVI \quad (5.22)$$

A set of ε_0 is predefined for 12 biome types and recorded in the Biome Properties Look-Up Table (BPLUT) (Running et al. 2000), and ε_g is expressed by Eq. 5.23:

$$\varepsilon_g = \varepsilon_0 \times T \times VPD \quad (5.23)$$

where T is the daily minimum temperature scalar, and VPD is the daylight average water vapor pressure deficit.

5.3.5 The C-Fix Model

The C-Fix model estimates daily GPP and NPP, and also calculates Net Ecosystem Production (NEP) by taking account of soil respiration flux (Veroustraete et al. 2002, 2004). The $FPAR_{canopy}$ of the C-Fix model is calculated as follows:

$$FPAR_{canopy} = 0.8642 \times NDVI - 0.0814 \quad (5.24)$$

ε_0 is predefined as 1.1 (g C m^{-2} MJ^{-1} APAR) for all kinds of biomes. Then it is adjusted by air temperature and CO_2 fertilization within the upper atmosphere (Veroustraete et al. 2002, 2004).

$$\varepsilon_g = \varepsilon_0 \times T \times CO_2 \quad (5.25)$$

5.3.6 The Vegetation Photosynthesis Model (VPM)

The VPM model estimates $FPAR_{chl}$ as a linear function of EVI and the coefficient a, which is currently set to be 1.0 (Xiao et al. 2004a, b, c, 2005b):

$$FPAR_{chl} = a \times EVI \tag{5.26}$$

ε_g is estimated by the theoretical ε_0 predefined for various vegetation types, air temperature (T), land surface water conditions (W), and vegetation phenology (P):

$$\varepsilon_g = \varepsilon_0 \times T \times W \times P \tag{5.27}$$

5.3.7 The Greenness and Radiance Model

In the GR model, both the absorbed radiation for photosynthesis and LUE, are driven by total chlorophyll content (Chl_{canopy}, defined as a product of LAI and leaf chlorophyll content) (Gitelson et al. 2006), and $FPAR_{chl}$ can be estimated as below (Peng and Gitelson 2012):

$$FPAR_{chl} = VI_{chl} \tag{5.28}$$

where VI_{chl} can be divided into two groups: (1) commonly used VIs, such as NDVI, TVI, MTVI, and WDRVI, to estimate the green leaf area index (LAI), which indirectly indicate total chlorophyll content; (2) Chlorophyll VIs, such as the MERIS Terrestrial Chlorophyll Index (MTCI), which are chlorophyll indices that directly represent the leaf chlorophyll content (CI_{green} and CI_{red} edge) (Peng and Gitelson 2012). The choices of VI_{chl} mainly depend on spectral characteristics of satellite sensors (Peng et al. 2011). The GR model was applied to estimate GPP of crops, including maize, soybeans (Peng and Gitelson 2012; Peng et al. 2011; Sakamoto et al. 2011), and wheat (Wu et al. 2009).

5.3.8 The Temperature and Greenness Model

The TG model is entirely driven by remote sensing data: EVI and Land Surface Temperature (LST) (Sims et al. 2006a, 2008).

$$GPP = (scaledEVI \times scaledLST) \times m \tag{5.29}$$

The m is a scalar with the unit of $mol\ C\ m^{-2}\ day^{-1}$. It is estimated for deciduous and evergreen vegetation, respectively.

$$m = 2.49 - 0.074 \times LST_{an}\ for\ deciduous\ sites \tag{5.30}$$

$$m = 2.1 - 0.065 \times LST_{an}\ for\ evergreen\ sites \tag{5.31}$$

The *scaledEVI* and *scaledLST* are calculated as below:

$$scaledEVI = EVI - 0.1 \tag{5.32}$$

$$scaledLST = min\left[(LST/30); (2.5 - (0.05 \times LST))\right] \tag{5.33}$$

where LST_{an} is the annual mean nighttime LST. Like the GR model, without predefining the ε_0, the TG model directly calculates ε_g using both scaled EVI and LST. LST measures the surface temperature instead of air temperature. LST is an effective measurement of the physiological activity of top canopy leaves. Moreover, LST has been proven to have a strong relationship with VPD and can be used as the measurement of drought stress (Sims et al. 2008).

5.3.9 The Eddy Covariance Light-Use Efficiency Model (EC-LUE)

The EC-LUE model is driven by four variables: NDVI, PAR, air temperature, and the Bowen ratio of sensible to latent heat flux (Yuan et al. 2007). The parameters in the EC-LUE model are independent across various land cover types. However, the accurate estimation of the Bowen ratio with remote sensing datasets restricts the application of the EC-LUE model. $FPAR_{canopy}$ is expressed as the linear function of NDVI:

$$FPAR_{canopy} = 1.24 \times NDVI - 0.186 \tag{5.34}$$

ε_g is estimated as the product of ε_0 (2.14 g C m^{-2} MJ $^{-1}$ APAR) and the downregulation factor of air temperature (T) or water stress (W):

$$\varepsilon_g = \varepsilon_0 \times min(T, EF) \tag{5.35}$$

EF (evaporative fraction) is defined as a proxy of water condition:

$$EF = \frac{LE}{LE + H} \tag{5.36}$$

where *LE* and *H* are latent heat flux and sensible heat flux (W m^{-2}) from eddy covariance measurements, respectively. Recently, *EF* has been estimated as the ratio of evapotranspiration (ET) to net radiation, and can be derived from the Remote Sensing-Penman–Monteith (RS-PM) model.

5.4 Validation Efforts Using In Situ Measurements

In-situ observations from eddy covariance flux towers are effective data sources for the validation of GPP estimations by PEMs. Around six hundred eddy covariance flux tower sites continuously measure CO_2, water, and energy fluxes in various types of terrestrial ecosystems across the world (Xiao et al. 2011).

Several data-processing steps are necessary to generate high-quality and continuous datasets of NEE, GPP, and ecosystem respiration. Firstly, half-hourly CO_2 flux data (NEE) are examined, based on wind speed (i. e. less than 0.5 m s^{-1}), presence of rain and snow, incomplete sample periods, and instrument malfunction. Nighttime CO_2 flux data are also checked if the friction velocity (u^*) is below a certain threshold (i. e. 0.25 m s^{-1}). Secondly, all NEE data with PAR values less than 5 umol $m^{-2}s^{-1}$ (NEE_{night}) are used to estimate nighttime respiration (R_{night}). NEE_{night} is regressed against air or soil temperature (Lloyd and Taylor 1994; Reichstein et al. 2005):

$$R_{(\text{night})}\left(NEE_{\text{night}}\right) = \gamma \times e^{kT} \tag{5.37}$$

where R_{night} is night ecosystem respiration; it equals nighttime NEE (NEE_{night}). γ and k are regression coefficients determined by nonlinear optimization. And R_{night} is used to extrapolate daytime ecosystem respiration (R_{day}). Thirdly, NEE_{day} is gap-filled with the Michaelis-Menten equation:

$$NEE_{\text{day}} = \frac{\propto \times PPFD \times GPP_{\max}}{\propto \times PPFD + GPP_{\max}} - R_{\text{day}} \tag{5.38}$$

where α is the apparent quantum yield as PPFD approaches 0. Finally, gap-filled NEE_{day} and R_{day} data are used to estimate GPP (here simply called GPP_{EC}.):

$$GPP_{EC} = R_{day} - NEE_{day} \tag{5.39}$$

The resultant half-hourly GPP, NEE, and R_h data are aggregated to daily, weekly, and monthly intervals. Daily, weekly, and monthly GPP_{EC} estimated by the eddy covariance technique as ground truth data are used to evaluate GPP estimates from PEMs (GPP_{PEM}). Generally, seasonal dynamics and interannual variations of both GPP_{PEM} and GPP_{EC} during the vegetation growing season are analyzed. Correlation analysis is conducted to evaluate the relationship between GPP_{PEM} and GPP_{EC}, in addition to the calculation of the root mean squared error (RMSE) between GPP_{PEM} and GPP_{EC} within the vegetation growing season. The seasonal sums of GPP_{PEM} and GPP_{EC} within the vegetation growing season are also computed and compared for measuring their discrepancies at the seasonal scale.

5.5 Major Findings

The VPM has been extensively verified for various types of terrestrial ecosystems, including temperate, boreal, moist tropical evergreen forests (Xiao et al. 2004c, 2005b), temperate and plateau grassland (Li et al. 2007; Wu et al. 2008), and agricultural ecosystems (Kalfas et al. 2011; Wang et al. 2010) across American and Asian continents. Here, we presented a case study of maize (C_4) and soybean

(C_3) rotation cropland with the VPM model to illustrate the PEM simulation and validation processes.

Our study site is the Mead site at the University of Nebraska Agricultural Research and Development Center, near Mead, Nebraska, U.S.A. The site is at the western edge of the favorably rain-fed corn belt, and it has a deep, silty clay-loam soil texture and a temperate continental climate. The plant growing season starts in May and ends in October. It covers 524 000 m^2 and rotates between maize and soybean cultivation via a center-pivot irrigation system. The maize canopy height is up to 2.9 m. The eddy covariance flux measurement height is 3 m when the canopy height is less than 1 m, and is adjusted to 6 m after the canopy height is greater than 1 m until the harvest period (Verma et al. 2005). During the study period of 2001–2005, maize was cultivated in 2001, 2003, and 2005, and soybeans were cultivated in 2002 and 2004.

Figure 5.1 shows the seasonal dynamic of PAR, air temperature, and precipitation. The annual average temperature is around 10.5 °C. Fifty-five percent of annual precipitation occurs during the cultivation period, and 45 % occurs during late winter and early spring.

In this case study, the MODIS eight-day Land Surface Reflectance (MOD09A1) time-series dataset for the flux tower site was obtained from the MODIS data portal at the Earth Observation and Modeling Facility (EMOF), University of Oklahoma (http://www.eomf.ou.edu/visualization/manual/). MOD09A1 provides an estimation of land surface reflectance after the atmosphere correction. It contains Bands 1–7 at 500 m spatial resolution in eight-day intervals: 620–670 nm (red), 841–876 nm (NIR1), 459–479 nm (blue), 545–565 nm (green), 1230–1250 nm (NIR2), 1628–1652 nm (SWIR1), and 2105–2155 nm (SWIR2), respectively. With the reflectance values of blue, red, NIR1, and SWIR1, three satellite vegetation indices (NDVI, EVI, and LSWI) were calculated. The seasonal dynamics and interannual variation of three vegetation indices are shown in Fig. 5.2. The flux tower's footprint (less than a 250 m radius) is approximately comparable to one MODIS pixel (500 × 500 m) (Kalfas et al. 2011). Thus, the time-series vegetation indices during 2001–2005 from the MODIS pixel covering the eddy covariance flux tower site were applied for the VPM simulation.

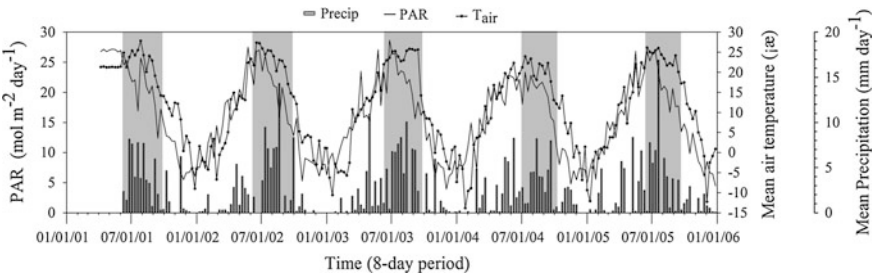

Fig. 5.1 Seasonal dynamics and interannual variations of the mean air temperature, photosynthetically active radiation (PAR), and precipitation during 2001–2005 at the Mead site, Nebraska, U.S.A. The *gray* area represents the crop growing season

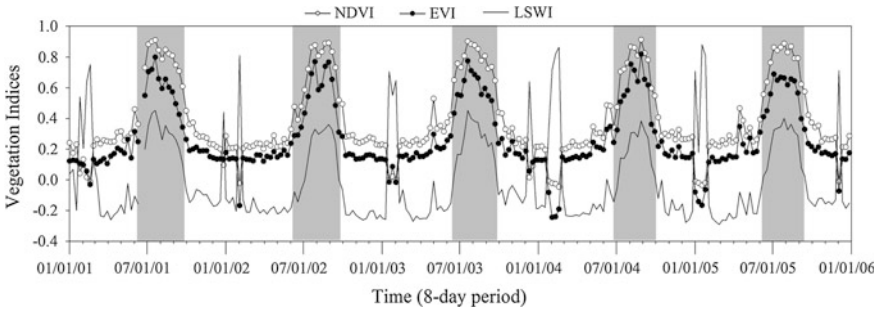

Fig. 5.2 Seasonal dynamics and interannual variations of Normalized Difference Vegetation Index (NDVI), Enhanced Vegetation Index (EVI) and Land Surface Water Index (LSWI) during 2001–2005 at the Mead site, Nebraska, USA

All meteorological and CO_2 flux datasets used in this case study were downloaded from the AmeriFlux data portal (http://public.ornl.gov/ameriflux/). The AmeriFlux network is a part of FLUXNET (http://daac.ornl.gov/FLUXNET), which aims to continuously observe CO_2, water, and energy fluxes at ecosystem and landscape levels. It provides meteorological and CO_2 flux datasets at daily, weekly, and monthly intervals. The weekly gap-filled and CO_2 flux-partitioned datasets of Level 4 products during 2001–2005 were chosen for this study, as this time scale matches the MODIS eight-day composite products used here.

The seasonal dynamics of GPP_{VPM} predicted by the VPM were compared with GPP_{EC} (Fig. 5.3). Both GPP_{VPM} and GPP_{EC} rose rapidly in June, and reached seasonal peaks in July–August for maize and soybeans. GPP_{VPM} decreased to zero in September and remained near zero until harvest, which agreed well with GPP_{EC} dynamics.

The scatterplots between GPP_{VPM} and GPP_{EC} of maize over the crop-growth period for an individual year and all years (Fig. 5.4) show that GPP_{VPM} is strongly correlated with GPP_{EC}, the correlation coefficient (R^2) is 0.92 across multiple

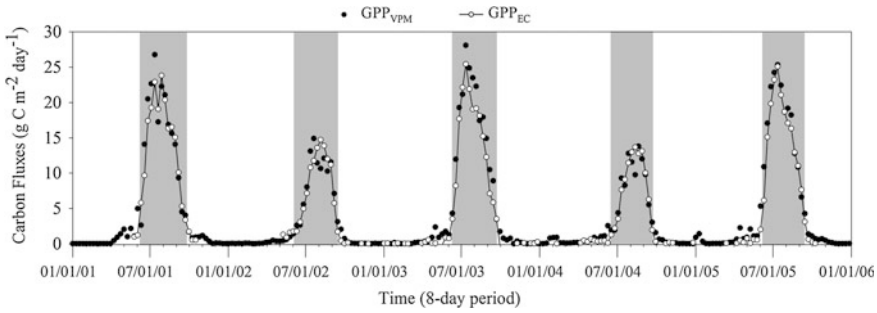

Fig. 5.3 Seasonal dynamics and interannual variations of the VPM-predicted gross primary production (GPP_{VPM}, g C m^{-2} day^{-1}) and the estimated GPP from the CO_2 eddy flux tower data (GPP_{EC}) during 2001–2005 at the Mead site, Nebraska, USA

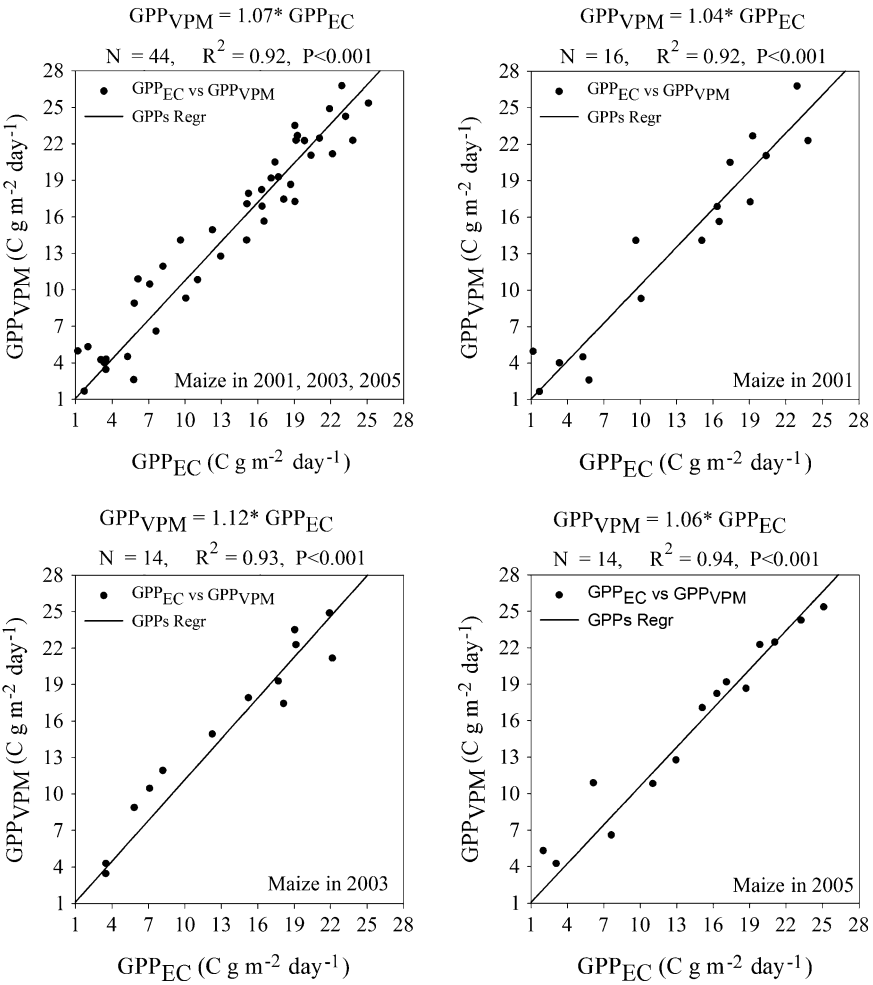

Fig. 5.4 Scatterplots between GPP_{EC} and GPP_{VPM} of maize in individual and multiple years

years, and R^2 values are 0.92, 0.93, and 0.94 for 2001, 2003, and 2005, respectively. As shown in Table 5.2, the root mean square deviation (RMSD) values of maize are less than 3 g C m^{-2} d^{-1} (2.4, 2.7, and 2.0 g C m^{-2} d^{-1} for 2001, 2003, and 2005, respectively). The seasonal sums of GPP over the crop-growth period between GPP_{VPM} and GPP_{EC} are also compared in Table 5.2. The relative error (%RE) ranged from 14.8 to 5.0 %.

Figure 5.5 shows the scatterplots between GPP_{VPM} and GPP_{EC} of soybeans over the crop-growth period across individual years and all years. The correlation between GPP_{VPM} and GPP_{EC} for soybeans is less strong than the relationship for maize. However, the R^2 is still relatively high, with the value of 0.85 across multiple years, and R^2 values are 0.82 and 0.88 for 2002 and 2004, respectively.

Table 5.2 Seasonal sums and statistics of gross primary production (GPP) at the Mead site, Nebraska, USA

Year	Crop Type	GPP_{EC}	GPP_{VPM}	GPP %RE	RMSD
2001	Maize	1662.32	1745.81	5.02	2.37
2003	Maize	1592.72	1828.19	14.78	2.66
2005	Maize	1593.92	1744.45	9.44	2.01
2002	Soybean	910.24	913.66	0.38	1.87
2004	Soybean	845.68	830.30	−1.82	1.46

RMSD Root Mean Squared Deviation
GPP_{EC} seasonal sum of GPP estimated from eddy covariance flux tower observations in g C m^{-2} yr^{-1}
GPP_{VPM} seasonal sum of GPP predicted by the VPM in g C m^{-2} yr^{-1}
GPP %RE: relative error in GPP sums calculated as $[(GPP_{EC}\text{-}GPP_{VPM})/GPP_{EC}] \times 100$

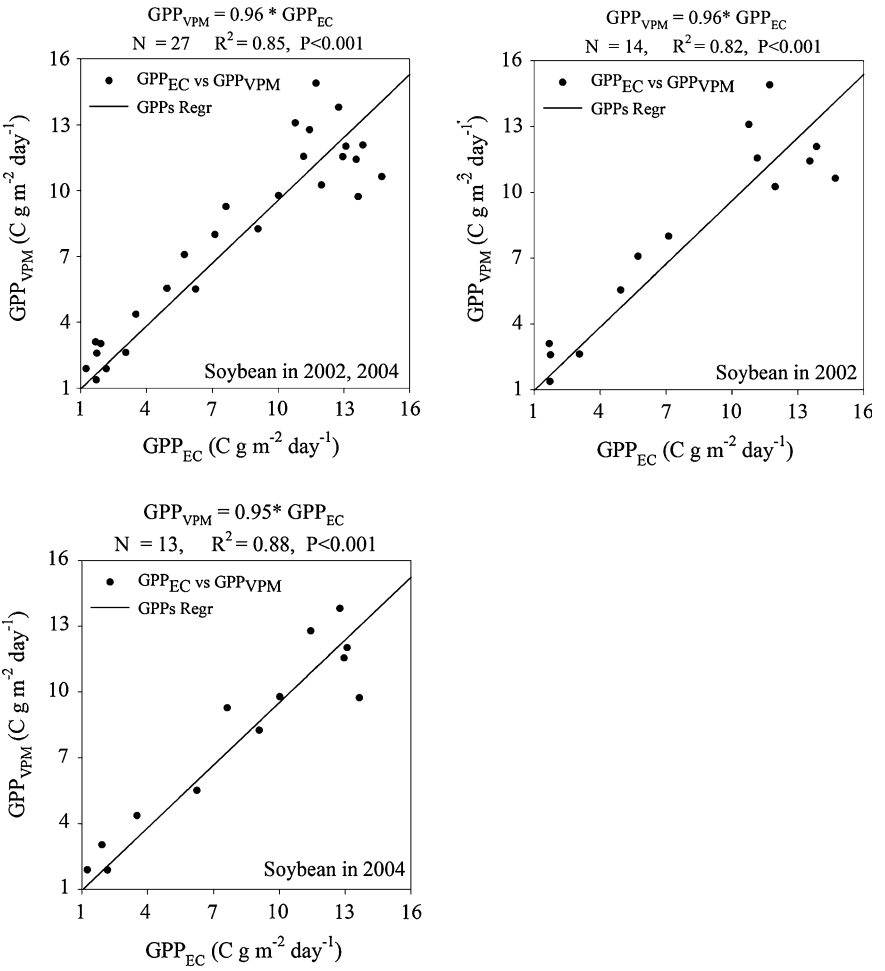

Fig. 5.5 Scatterplots between GPP_{EC} and GPP_{VPM} of soybean in individual and multiple years

As shown in Table 5.2, the RMSD values of soybeans were lower than 2 g C m^{-2} d^{-1} across multiple years (1.9 and 1.5 g C m^{-2} d^{-1} for 2002 and 2004, respectively). The relative error (%RE) values between the seasonal sums of GPP_{VPM} and GPP_{EC} were 0.4 and −1.8 % in 2002 and 2004, respectively.

The above simulation results show that the VPM, based on the concept of light absorption by chlorophyll, had great potential to estimate the seasonal dynamics and interannual variation of GPP for soybean (C_3) and maize (C_4) cropland rotation in different years. Another earlier study (Yan et al. 2009) used the VPM model to estimate GPP of winter wheat (C_3) and maize (C_4) rotation within a year in the North China Plain, China, and also reported good agreement between GPP_{VPM} and GPP_{EC} in the cropland site (Yan et al. 2009).

5.6 Future Research Directions

Remotely sensed data and PEMs have been widely used to estimate GPP and NPP over the last few decades, as several coarse and moderate resolution sensors (e.g., AVHRR, SPOT-VEGETATION, MODIS, and MERIS) provide images for the globe every day. However, further development and implementation of satellite-based PEMs still face three major challenges for more accurate estimation of GPP and NPP.

First, the uncertainty concerning the scaling-up of light absorption from chlorophyll and leaf levels to canopy, ecosystem and landscape levels is still significant, and how to accurately estimate the amount of light absorbed by chlorophyll is a challenging task from the perspectives of both field measurements and radiative transfer models (Zhang et al. 2005, 2006, 2009). The concept of FPAR at the canopy level ($FPAR_{canopy}$) has been widely adopted by the remote sensing and ecosystem modeling communities, and $FPAR_{canopy}$ is often calculated as a semi-empirical linear function of NDVI and leaf area index (LAI). It is noted that only light absorbed by chlorophyll pigments is used for photosynthesis, and the concept of $FPAR_{chl}$ is more meaningful for GPP estimation. Simulation results from a coupled leaf-canopy radiative transfer model have suggested that $FPAR_{canopy}$ is much higher than $FPAR_{leaf}$ or $FPAR_{chl}$ (Zhang et al. 2006). Recently, $FPAR_{chl}$ has been used for the development of several new PEMs and updated versions of existing PEMs (Potter 2012; Sims et al. 2006b, 2008 Wu et al. 2012; Xiao et al. 2005b; Yan et al. 2009). In these PEMs, $FPAR_{chl}$ is often estimated as the linear function of EVI or other chlorophyll-related vegetation indices, which have proved more consistent with the light absorption for photosynthesis at the chlorophyll level. Nevertheless, difficulties still exist in accurately quantifying leaf chlorophyll content and $FPAR_{chl}$. The empirical and semiempirical relationships between vegetation indices and $FPAR_{chl}$, (for example, FPARchl = a × EVI), need to be evaluated across various biome types with accurate in situ measurement, better implementation of radiative transfer models (both model variables and parameters), and selection of satellite images from various sensors (e.g., MODIS, MERIS and RapidEye). It is necessary to regularly measure both biochemical (chlorophyll

and $FPAR_{chl}$) and structural (LAI and $FPAR_{canopy}$) variables across leaf, canopy, and landscape levels and develope novel algorithms of chlorophyll content over terrestrial ecosystems. Since a large portion of leaf nitrogen is contained within leaf chloroplasts, more attention should also be paid to develop quantitative relationships among chlorophyll, $FPAR_{chl}$, and nitrogen content.

Secondly, the uncertainty concerning the scaling-up of light-use efficiency from chloroplast and leaf levels to canopy, ecosystem, and landscape levels is also still significant. The estimation methods and values of maximum light-use efficiency for various types of terrestrial ecosystems differ substantially and need more integrative studies across various levels: chloroplast, leaf, plant, canopy, ecosystem and landscape. LUE is the primary controlling parameter of satellite-based PEMs. For most PEMs, a species- or biome-specific maximum LUE value is predefined, and it is then down-regulated by the scalars representing various environmental stresses. Different definitions and choices of maximum LUE and environmental scalars are the main sources of uncertainty about PEMs. Daily NEE and PAR data are used to examine the continuous short-time changes of LUE. Recently, increasing effort has been reported for estimating LUE with remote sensing techniques (Garbulsky et al. 2011). Remote sensing can indirectly estimate LUE by adjusting maximum LUE values through environmental factors, including soil water content, temperature, nitrogen content, and so forth. Remote sensing can also directly estimate LUE by detecting the photoprotective mechanism from the leaf spectral reflectance change due to the epoxidation of xanthophyll cycle pigments (Barton and North 2001). The PRI (Photochemical Reflectance Index), which demonstrates the characteristics of spectrum absorption around 505 nm and 531 nm (Gamon et al. 1992), is found to have a strong correlation with LUE (Garbulsky et al. 2011; Hilker et al. 2009, 2010, 2012; Wu et al. 2010). Even though the temporal, spatial, and spectral resolutions of remote sensing, and the semiempirical feature of this approach, limit its application, the PRI can represent the integral effect of various environmental factors, and it has great potential to estimate LUE on regional and global scales in the future (Drolet et al. 2008). Considerations of the temporal and spatial dynamics of LUE will greatly improve the simulation accuracy of PEMs (Garbulsky et al. 2011).

Thirdly, there is still a great deal of uncertainty in delineating vegetation growing seasons (starting date, ending date, and the length of the vegetation growing season) from remote sensing data, which substantially affects the estimates of total GPP over the vegetation growing season (Falge et al. 2002; Richardson et al. 2010). There is a need for better understanding and quantification of vegetation phenology through analyses of both remote sensing data and CO_2 flux data (ecosystem physiology approach). Vegetation phenology varies over years, driven by interannual climate variability and climate change (e.g., temperature and precipitation) (Piao et al. 2006, 2011), and is also affected by topography (Doktor et al. 2009; Hwang et al. 2011; Piao et al. 2011). In addition, there are also significant differences among various algorithms that use remotely sensed data to retrieve vegetation phenology (Cong et al. 2012). Therefore, it is very important to continue evaluation and development of satellite-based algorithms to retrieve

vegetation phenology over time, with the assistance of in situ carbon and water flux data from the flux towers.

Data from eddy covariance flux tower sites have been widely used to evaluate the PEMs at ecosystem and landscape levels. Long-term efforts are required to validate satellite-based PEMs with the data from ground-based CO_2 eddy covariance technique. Currently, six hundred CO_2 eddy flux towers are operated across various biome types, with different land management and stages of disturbance and recovery. Abundant NEE data have been accumulated and are freely available to scientific users. Through a community-based effort, many researchers have partitioned the half-hourly NEE into GPP and ecosystem respiration, and made the data available to users, such as the Ameriflux and Asiaflux websites. Collaboration between the remote sensing community and the CO_2 flux tower community will certainly help evaluate and improve satellite-based PEMs.

Acknowledgments This study was supported by research grants from the NASA Data Analysis Program (NNX09AC39G, NNX11AJ35G), and the NSF EPSCoR program (NSF-0919466). The site-specific climate and CO_2 flux tower data from the Mead flux tower site in Nebraska were provided by the AmeriFlux network (http://public.ornl.gov/ameriflux/). We thank Drs. Shashi B. Verma and Andrew E. Suyker for their effort in collecting field data at the Mead flux tower site in Nebraska.

References

Baldocchi D, Valentini R, Running S, Oechel W, Dahlman R (1996) Strategies for measuring and modelling carbon dioxide and water vapour fluxes over terrestrial ecosystems. Glob Change Biol 2(3):159–168

Barton C, North P (2001) Remote sensing of canopy light use efficiency using the photochemical reflectance index—model and sensitivity analysis. Remote Sens Environ 78:264–273

Cao MK, Woodward FI (1998a) Dynamic responses of terrestrial ecosystem carbon cycling to global climate change. Nature 393(6682):249–252

Cao MK, Woodward FI (1998b) Net primary and ecosystem production and carbon stocks of terrestrial ecosystems and their responses to climate change. Glob Change Biol 4(2):185–198

Chen M, Zhuang Q (2012) Spatially explicit parameterization of a terrestrial ecosystem model and its application to the quantification of carbon dynamics of forest ecosystems in the conterminous United States. Earth Interact 16(5):1–22

Chiesi M et al (2012) Use of BIOME-BGC to simulate water and carbon fluxes within Mediterranean macchia. iForest-Biogeosci For 5(1): 38–43

Collatz GJ, Ball JT, Grivet C, Berry JA (1991) Physiological and environmental regulation of stomatal conductance, photosynthesis and transpiration: a model that includes a laminar boundary layer. Agr For Meteorol 54:107–136

Collatz GJ, Ribas-Carbon M, Ball JA (1992) Coupled photosynthesis-stomatal conductance model for leaves of C_4 plants. Aust J Plant Physiol 19:519–538

Cong N et al (2012) Spring vegetation green-up date in China inferred from SPOT NDVI data: a multiple model analysis. Agr For Meteorol 165:104–113

Cramer W et al (1999) Comparing global models of terrestrial net primary productivity (NPP): overview and key results. Glob Chang Biol 5:1–15

Doktor D, Bondeau A, Koslowski D, Badeck FW (2009) Influence of heterogeneous landscapes on computed green-up dates based on daily AVHRR NDVI observations. Remote Sens Environ 113(12):2618–2632

Drolet GG et al (2008) Regional mapping of gross light-use efficiency using MODIS spectral indices. Remote Sens Environ 112(6):3064–3078

Falge E et al (2002) Seasonality of ecosystem respiration and gross primary production as derived from FLUXNET measurements. Agr For Meteorol 113(1–4):53–74

Farquhar G, von Caemmerer S, Berry JA (1980) A biochemical model of photosynthetic CO_2 assimilation in leaves of C_3 species. Planta 149:78–90

Field CB, Randerson JT, Malmstrom CM (1995) Global net primary production—combining ecology and remote-sensing. Remote Sens Environ 51(1):74–88

Gamon JA, Penuelas J, Field CB (1992) A narrow-waveband spectral index that tracks diurnal changes in photosynthetic efficiency. Remote Sens Environ 41(1):35–44

Garbulsky MF, Penuelas J, Gamon J, Inoue Y, Filella I (2011) The photochemical reflectance index (PRI) and the remote sensing of leaf, canopy and ecosystem radiation use efficiencies. A review and meta-analysis. Remote Sens Environ 115(2): 281–297

Gitelson AA et al (2006) Relationship between gross primary production and chlorophyll content in crops: implications for the synoptic monitoring of vegetation productivity. J Geophys Res Atmos 111(D8):D08S11

Goetz SJ, Prince SD (1998) Variability in carbon exchange and light utilization among boreal forest stands: implications for remote sensing of net primary production. Can J For Res 28(3):375–389

Goetz SJ, Prince SD (1999) Modelling terrestrial carbon exchange and storage: evidence and implications of functional convergence in light-use efficiency. Adv Ecol Res 28:57–92

Goetz SJ, Prince SD, Small J, Gleason ACR (2000) Interannual variability of global terrestrial primary production: results of a model driven with satellite observations. J Geophys Res Atmos 105(D15):20077–20091

Goulden ML et al (2011) Patterns of NPP, GPP, respiration, and NEP during boreal forest succession. Glob Change Biol 17(2):855–871

Goward SN, Huemmrich KF (1992) Vegetation canopy PAR absorptance and the normalized difference vegetation index—an assessment using the SAIL model. Remote Sens Environ 39(2):119–140

Harley PC, Loreto F, Dimarco G, Sharkey TD (1992) Theoretical considerations when estimating the Mesophyll conductance to Co2 flux by analysis of the response of photosynthesis to Co2. Plant Physiol 98(4):1429–1436

Hilker T, Coops NC, Wulder MA, Black TA, Guy RD (2008) The use of remote sensing in light use efficiency based models of gross primary production: a review of current status and future requirements. Sci Total Environ 404(2–3):411–423

Hilker T et al (2010) Remote sensing of photosynthetic light-use efficiency across two forested biomes: spatial scaling. Remote Sens Environ 114(12):2863–2874

Hilker T et al (2012) Data assimilation of photosynthetic light-use efficiency using multi-angular satellite data: II model implementation and validation. Remote Sens Environ 121:287–300

Hilker T et al (2009) An assessment of photosynthetic light use efficiency from space: modeling the atmospheric and directional impacts on PRI reflectance. Remote Sens Environ 113(11):2463–2475

Huete AR, Liu HQ, Batchily K, vanLeeuwen W (1997) A comparison of vegetation indices over a global set of TM images for EOS-MODIS. Remote Sens Environ 59(3):440–451

Hwang T, Song CH, Vose JM, Band LE (2011) Topography-mediated controls on local vegetation phenology estimated from MODIS vegetation index. Landscape Ecol 26(4):541–556

Ji JJ (1995) A climate-vegetation interaction model: simulating physical and biological processes at the surface. J Biogeogr 22(2–3):445–451

Kalfas JL, Xiao XM, Vanegas DX, Verma SB, Suyker AE (2011) Modeling gross primary production of irrigated and rain-fed maize using MODIS imagery and CO(2) flux tower data. Agr For Meteorol 151(12):1514–1528

Lafont S et al (2002) Spatial and temporal variability of land CO2 fluxes estimated with remote sensing and analysis data over Western Eurasia. Tellus B 54(5):820–833

Li ZQ et al (2007) Modeling gross primary production of alpine ecosystems in the Tibetan Plateau using MODIS images and climate data. Remote Sens Environ 107(3):510–519

Lloyd J, Taylor JA (1994) On the temperature-dependence of soil respiration. Funct Ecol 8(3):315–323

Matsushita B, Xu M, Chen J, Kameyama S, Tamura M (2004) Estimation of regional net primary productivity (NPP) using a process-based ecosystem model: how important is the accuracy of climate data? Ecol Model 178(3–4):371–388

McCallum IWW, Schmullius C, Shvidenko A, Obersteiner M, Fritz S, Nilsson S (2009) Satellite-based terrestrial production efficiency modeling. Carbon Balance Manage. doi:10.1186/1750-0680-4-8

McGuire AD, Melillo JM, Kicklighter DW, Joyce LA (1995) Equilibrium responses of soil carbon to climate change: empirical and process-based estimates. J Biogeogr 22(4–5):785–796

Monteith JL (1972) Solar radiation and productivity in tropical ecosystems. J Appl Ecol 9:747–766

Monteith JL (1977) Climate and efficiency of crop production in Britain. Philos Trans Roy Soc Lond Series B Biol Sci 281(980):277–294

Moureaux C et al (2008) Carbon balance assessment of a Belgian winter wheat crop (Triticum aestivum L.). Global Change Biol 14(6):1353–1366

Nayak RK, Patel NR, Dadhwal VK (2010) Estimation and analysis of terrestrial net primary productivity over India by remote-sensing-driven terrestrial biosphere model. Environ Monit Assess 170(1–4):195–213

Papale D et al (2006) Towards a standardized processing of net ecosystem exchange measured with eddy covariance technique: algorithms and uncertainty estimation. Biogeosciences 3(4):571–583

Parton WJ et al (1993) Observations and modeling of biomass and soil organic-matter dynamics for the grassland biome worldwide. Glob Biogeochem Cycles 7(4):785–809

Peng Y, Gitelson AA (2012) Remote estimation of gross primary productivity in soybean and maize based on total crop chlorophyll content. Remote Sens Environ 117:440–448

Peng Y, Gitelson AA, Keydan G, Rundquist DC, Moses W (2011) Remote estimation of gross primary production in maize and support for a new paradigm based on total crop chlorophyll content. Remote Sens Environ 115(4):978–989

Piao S et al (2011) Altitude and temperature dependence of change in the spring vegetation green-up date from 1982 to 2006 in the Qinghai-Xizang Plateau. Agr For Meteorol 151(12):1599–1608

Piao SL, Friedlingstein P, Ciais P, Zhou LM, Chen AP (2006) Effect of climate and CO_2 changes on the greening of the Northern Hemisphere over the past two decades. Geophys Res Lett 33(23):L13802

Potter C et al (2003) Continental-scale comparisons of terrestrial carbon sinks estimated from satellite data and ecosystem modeling 1982–1998. Glob Planet Change 39(3–4):201–213

Potter C, Klooster S, Genovese V, Hiatt C, Boriah S, Kumar V, Mithal V, Garg A (2012) Terrestrial ecosystem carbon fluxes predicted from MODIS satellite data and large-scale disturbance modeling. Int J Geosci. doi:10.4236/ijg.2012

Potter CS (1999) Terrestrial biomass and the effects of deforestation on the global carbon cycle—results from a model of primary production using satellite observations. Bioscience 49(10):769–778

Potter CS et al (1998) Regional application of an ecosystem production model for studies of biogeochemistry in Brazilian Amazonia. Glob Change Biol 4(3):315–333

Potter CS, Klooster SA (1997) Global model estimates of carbon and nitrogen storage in litter and soil pools: response to changes in vegetation quality and biomass allocation. Tellus B 49(1):1–17

Potter CS et al (1993) Terrestrial ecosystem production—a process model-based on global satellite and surface data. Glob Biogeochem Cycles 7(4):811–841

Prince SD, Goward SN (1995a) Global primary production: a remote sensing approach. J Biogeogr 22(4–5):815–835

Prince SD, Goward SN (1995) Global primary production: a remote sensing approach. J Biogeogr 22:316–336

Reichstein M et al (2005) On the separation of net ecosystem exchange into assimilation and ecosystem respiration: review and improved algorithm. Glob Change Biol 11(9):1424–1439

Richardson AD et al (2010) Influence of spring and autumn phenological transitions on forest ecosystem productivity. Philos T Roy Soc B 365(1555):3227–3246

Roxburgh SH, Berry SL, Buckley TN, Barnes B, Roderick ML (2005) What is NPP? Inconsistent accounting of respiratory fluxes in the definition of net primary production. Funct Ecol 19(3):378–382

Ruimy A, Dedieu G, Saugier B (1996a) TURC: a diagnostic model of continental gross primary productivity and net primary productivity. Glob Biogeochem Cycles 10(2):269–285

Ruimy A, Kergoat L, Bondeau A, Intercomparison PPNM (1999) Comparing global models of terrestrial net primary productivity (NPP): analysis of differences in light absorption and light-use efficiency. Glob Change Biol 5:56–64

Ruimy A, Kergoat L, Field CB, Saugier B (1996b) The use of CO_2 flux measurements in models of the global terrestrial carbon budget. Glob Change Biol 2(3):287–296

Ruimy A, Saugier B, Dedieu G (1994) Methodology for the estimation of terrestrial net primary production from remotely sensed data. J Geophys Res Atmos 99(D3):5263–5283

Running SW, Gower ST (1991) Forest-BGC, a general-model of forest ecosystem processes for regional applications. 2. Dynamic carbon allocation and Nitrogen budgets. Tree Physiol 9(1–2):147–160

Running SW, Hunt Jr ER (1993) Generalization of a forest ecosystem process model for other biomes, BIOME-BCG, and an application for global-scale models. Academic Press, Inc, San Diego

Running SW et al (1994) Terrestrial remote-sensing science and algorithms planned for Eos Modis. Int J Remote Sens 15(17):3587–3620

Running SW, Nemani R, Glassy JM, Thornton P (1999) MODIS daily photosynthesis (PSN) and annual net primary production (NPP) product (MOD17), algorithm theoretical basis document, version 3.0, April 29 1999. http://modis.gsfc.nasa.gov/

Running SW et al (2004) A continuous satellite-derived measure of global terrestrial primary production. Bioscience 54(6):547–560

Running SW, Thornton PE, Nemani R, Glassy JM (2000) Global terrestrial gross and net primary productivity from the Earth Observing System. In: Sala OE, Jackson RB, Mooney HA, Howarth RW (eds) Methods in ecosystem science. Springer, New York, pp 44–57

Sakamoto T, Gitelson AA, Wardlow BD, Verma SB, Suyker AE (2011) Estimating daily gross primary production of maize based only on MODIS WDRVI and shortwave radiation data. Remote Sens Environ 115(12):3091–3101

Sims DA et al (2008) A new model of gross primary productivity for North American ecosystems based solely on the enhanced vegetation index and land surface temperature from MODIS. Remote Sens Environ 112(4):1633–1646

Sims DA et al (2006a) On the use of MODIS EVI to assess gross primary productivity of North American ecosystems. J Geophys Res Biogeo 111(G4):G04015

Sims DA et al (2006b) On the use of MODIS EVI to assess gross primary productivity of North American ecosystems. J Geophys Res Biogeo 111(G4)

Taiz L, Zeiger E (2002) Plant physiology. Sinauer Associates Inc., Sunderland 690p

Tucker CJ (1979) Red and photographic infrared linear combinations for monitoring vegetation. Remote Sens Environ 8(2):127–150

Verbeeck H, Samson R, Granier A, Montpied P, Lemeur R (2008) Multi-year model analysis of GPP in a temperate beech forest in France. Ecol Model 210(1–2):85–103
Verma SB et al (2005) Annual carbon dioxide exchange in irrigated and rainfed maize-based agroecosystems. Agric For Meteorol 131(1–2):77–96
Veroustraete F, Sabbe H, Eerens H (2002) Estimation of carbon mass fluxes over Europe using the C-Fix model and Euroflux data. Remote Sens Environ 83(3):376–399
Veroustraete F, Sabbe H, Rasse DP, Bertels L (2004) Carbon mass fluxes of forests in Belgium determined with low resolution optical sensors. Int J Remote Sens 25(4):769–792
Wang Z, Xiao XM, Yan XD (2010) Modeling gross primary production of maize cropland and degraded grassland in northeastern China. Agr For Meteorol 150(9):1160–1167
Wofsy SC et al (1993) Net exchange of CO_2 in a mid-latitude forest. Science 260(5112):1314–1317
Woodward FI, Smith TM, Emanuel WR (1995) A global land primary productivity and phytogeography model. Glob Biogeochem Cycles 9(4):471–490
Wu CY, Niu Z, Gao S (2012) The potential of the satellite derived green chlorophyll index for estimating midday light use efficiency in maize, coniferous forest and grassland. Ecol Indic 14(1):66–73
Wu CY et al (2009) Remote estimation of gross primary production in wheat using chlorophyll-related vegetation indices. Agr For Meteorol 149(6–7):1015–1021
Wu CY, Niu Z, Tang QA, Huang WJ (2010) Revised photochemical reflectance index (PRI) for predicting light use efficiency of wheat in a growth cycle: validation and comparison. Int J Remote Sens 31(11):2911–2924
Wu WX et al (2008) Modeling gross primary production of a temperate grassland ecosystem in inner Mongolia, China, using MODIS imagery and climate data. Sci China Series D Earth Sci 51(10):1501–1512
Xiao X et al (2004a) Satellite-based modeling of gross primary production in an evergreen needle leaf forest. Remote Sens Environ 89(4):519–534
Xiao X et al (2004b) Modeling gross primary production of a deciduous broadleaf forest using satellite images and climate data. Remote Sens Environ 91(2):256–270
Xiao XM, Yan HM, Kalfas JL, Zhang QY (2011) Satellite-based modeling of Gross Primary Production of terrestrial ecosystems. In: Wang QH (ed) advances in environmental remote sensing: sensors, algorithms, and application. Taylor & Francis Group, Boca Raton, pp 367–397
Xiao XM et al (2004c) Modeling gross primary production of temperate deciduous broadleaf forest using satellite images and climate data. Remote Sens Environ 91(2):256–270
Xiao XM, Zhang QY, Hollinger D, Aber J, Moore B (2005a) Modeling gross primary production of an evergreen needleleaf forest using modis and climate data. Ecol Appl 15(3):954–969
Xiao XM et al (2005b) Satellite-based modeling of gross primary production in a seasonally moist tropical evergreen forest. Remote Sens Environ 94(1):105–122
Yan HM et al (2009) Modeling gross primary productivity for winter wheat-maize double cropping system using MODIS time series and CO_2 eddy flux tower data. Agric Ecosyst Environ 129(4):391–400
Yuan WP et al (2007) Deriving a light use efficiency model from eddy covariance flux data for predicting daily gross primary production across biomes. Agr For Meteorol 143(3–4):189–207
Yuan WP et al (2010) Global estimates of evapotranspiration and gross primary production based on MODIS and global meteorology data. Remote Sens Environ 114(7):1416–1431
Zhang QY et al (2009) Can a satellite-derived estimate of the fraction of PAR absorbed by chlorophyll (FAPAR(chl)) improve predictions of light-use efficiency and ecosystem photosynthesis for a boreal aspen forest? Remote Sens Environ 113(4):880–888
Zhang QY et al (2005) Estimating light absorption by chlorophyll, leaf and canopy in a deciduous broadleaf forest using MODIS data and a radiative transfer model. Remote Sens Environ 99(3):357–371
Zhang QY et al (2006) Characterization of seasonal variation of forest canopy in a temperate deciduous broadleaf forest, using daily MODIS data. Remote Sens Environ 105(3):189–203
Zhao MS, Heinsch FA, Nemani RR, Running SW (2005) Improvements of the MODIS terrestrial gross and net primary production global data set. Remote Sens Environ 95(2):164–176

Chapter 6
Assessing Net Ecosystem Exchange of Carbon Dioxide Between the Terrestrial Biosphere and the Atmosphere Using Fluxnet Observations and Remote Sensing

Jingfeng Xiao

Abstract The quantification of net ecosystem exchange (NEE) of carbon dioxide over regions, continents, or the globe is essential for understanding the feedbacks between the terrestrial biosphere and the atmosphere in the context of global climate change. The eddy covariance technique provides continuous NEE measurements for a variety of ecosystem and climate types. These measurements, however, only represent the fluxes at the scale of the tower footprint. Here a data-driven approach and satellite remote sensing are used to upscale NEE observations from eddy covariance flux towers to the continental scale and to produce gridded flux estimates for the conterminous U.S. over the period 2000–2009. The resulting 10-year gridded flux estimates (EC-MOD) have 1 km spatial resolution and 8-day time step, and provide independent and alternative NEE estimates compared to traditional approaches. These flux estimates are used to examine the spatial and temporal dynamics of NEE at seasonal, annual, and interannual scales. On average, the annual NEE of U.S. natural ecosystems is -0.54 Pg C year^{-1}. The EC-MOD estimate of the U.S. carbon sink agrees with recent estimates from the literature. The dominant sources of the interannual variability in NEE of the U.S. include drought and disturbances. EC-MOD is also valuable for evaluating simulations from ecosystem models and atmospheric inversions.

6.1 Introduction

The quantification of net ecosystem exchange (NEE) of carbon dioxide (CO_2) over regions, continents, or the globe is essential for understanding the feedbacks between the terrestrial biosphere and the atmosphere in the context of global

J. Xiao (✉)
Earth Systems Research Center, Institute for the Study of Earth, Oceans, and Space, University of New Hampshire, Durham, NH, USA
e-mail: j.xiao@unh.edu

J. M. Hanes (ed.), *Biophysical Applications of Satellite Remote Sensing*, Springer Remote Sensing/Photogrammetry, DOI: 10.1007/978-3-642-25047-7_6,

climate change. Several methods including inventory approaches (e.g., Pacala et al. 2001; Goodale et al. 2002; SOCCR 2007), ecosystem modeling (e.g., Potter et al. 1993; Running and Hunt 1993; Xiao et al. 2009), and atmospheric inversions (e.g., Tans et al. 1990; Deng et al. 2007) have been widely used to estimate NEE over broad regions. The resulting flux estimates, however, exhibit large differences in both patterns and magnitude (e.g., Huntzinger et al. 2012) despite the general agreement that the terrestrial ecosystems in the northern hemisphere provide a large carbon sink (e.g., Pacala et al. 2001; Goodale et al. 2002; Deng et al. 2007; Pan et al. 2011a).

The eddy covariance technique provides an alternative approach for estimating NEE. Eddy covariance flux towers have been providing continuous measurements of ecosystem-level exchange of carbon, water, and energy spanning diurnal, synoptic, seasonal, and interannual time scales since the early 1990s (Wofsy et al. 1993; Baldocchi et al. 2001). These flux towers provides probably the best estimates of ecosystem-level carbon fluxes. These NEE measurements are routinely partitioned into its two major components: gross primary productivity (GPP) and ecosystem respiration (R_e) (Reichstein et al. 2005; Desai et al. 2008).

At present, over 500 eddy covariance flux towers are operating on a long-term and continuous basis around the world (FLUXNET, http://daac.ornl.gov/FLUXNET). This global network encompasses a large range of climate and biome types (Baldocchi et al. 2001). AmeriFlux is the regional network that coordinates analyses of observations from flux towers within the U.S. Despite the larger number of flux towers, the flux observations only represent fluxes at the scale of the tower footprint with longitudinal dimensions ranging between a hundred meters and several kilometers depending on homogeneous vegetation and fetch (Schmid 1994; Göckede et al. 2008). To quantify the net exchange of CO_2 between the terrestrial biosphere and the atmosphere over regions, continents, or the globe, significant efforts are needed to upscale flux observations from towers to these broad regions (Xiao et al. 2008).

Considerable advances have been made in the upscaling of flux observations during recent years (e.g., Xiao et al. 2008, 2010, 2011a; Jung et al. 2009; Sun et al. 2011; Zhang et al. 2011). For instance, a data-driven approach has been used to upscale carbon fluxes from the AmeriFlux network to the continental scale and to produce gridded fields of GPP and NEE with high spatial (1 km) and temporal (8-day) resolutions for the conterminous U.S. over the period 2000–2006 (Xiao et al. 2008, 2010, 2011a). The GPP and NEE fields were derived from eddy covariance (EC) flux measurements and MODIS data, and are referred to as EC-MOD. The continuous EC-MOD flux fields were used to assess the magnitude, distribution, and interannual variability of recent U.S. ecosystem carbon exchange (Xiao et al. 2010, 2011a). One of the main innovations in the EC-MOD estimates compared to traditional approaches is the use of daily NEE measurements from flux towers. These measurements represent direct samples of net CO_2 exchange from sites encompassing a wide variety of U.S. biomes and climate types, which have not been previously utilized in U.S. carbon budget studies (e.g., Houghton et al. 1999; Caspersen et al. 2000; Schimel et al. 2000; Pacala et al. 2001; SOCCR 2007).

The analysis based on EC-MOD flux estimates provides an alternative, independent, and novel perspective on recent U.S. ecosystem carbon exchange (Xiao et al. 2010, 2011a).

The gridded flux estimates are also valuable for evaluating simulations of ecosystem models and atmospheric inversions. EC-MOD fluxes have been used to evaluate GPP and NEE (Sun et al. 2011). The North American Carbon Program (NACP) regional interim synthesis also compared EC-MOD fluxes with simulations from a number of ecosystem models for temperate North America (Huntzinger et al. 2012). EC-MOD fluxes have also been used to evaluate the flux estimates derived from a boundary layer model at regional scales (Dang et al. 2011) and inversions for North America derived from a nested inversion model at the continental scale (Deng et al. 2013).

A number of upscaling studies have been reported at recent professional meetings and journals, following the early work by Xiao et al. (2008). The advances in the upscaling of flux observations were summarized in plenary talks at the 2nd North American Carbon Program (NACP) All-Investigators Meeting in San Diego, California (February 2009) and the AmeriFlux Science Meeting and 3rd NACP All-Investigators Meeting in New Orleans, Louisiana (January 31–February 4, 2011). A recent special issue in *Journal of Geophysical Research—Biogeosciences* is devoted to the upscaling of flux observations. This special issue consists of seven research articles on different topics of upscaling science and reflects the most recent advances in the upscaling of flux observations (Xiao et al. 2012).

Here I use a data-driven approach (Xiao et al. 2008) and satellite remote sensing to extend the NEE estimates of EC-MOD for the conterminous U.S. (2000–2006) (Xiao et al. 2011a) to the 10-year period from 2000 to 2009. Flux observations from the AmeriFlux network and various satellite data streams are combined to develop a predictive model for NEE, and the predictive model is then used to produce gridded NEE estimates with 1 km spatial resolution and 8-day time step for the 10-year period. The extended gridded flux estimates (EC-MOD) are then used to examine the spatial and temporal dynamics of NEE for U.S. terrestrial ecosystems at seasonal, annual, and interannual scales.

6.2 Theoretical Basis

NEE is the difference between GPP and ecosystem respiration (R_e). NEE is influenced by a variety of meteorological, physiological, atmospheric, hydrologic, and edaphic variables (Xiao et al. 2008). GPP is the amount of carbon fixed by vegetation through photosynthesis, and is influenced by incoming solar radiation, air temperature, vapor pressure deficit, soil moisture, and nitrogen availability (Clark et al. 1999, 2004). GPP is also regulated by leaf area index (LAI) and canopy phenology at the ecosystem level (Richardson et al. 2010). Ecosystem respiration (R_e) includes autotrophic (R_a) and heterotrophic respiration (R_h). The controlling

factors of R_a include air temperature, tissue carbon (foliage, stem, roots), and nitrogen content in vegetation compartments (Ryan 1991), whereas R_h is often modeled as a function of substrate availability, soil temperature and soil moisture (Ryan and Law 2005). All these factors influence NEE by regulating GPP and/or R_e. NEE is also affected by disturbances from fire and harvest (Amiro et al. 2010; Liu et al. 2011).

Satellite remote sensing can be used to account for many of these factors influencing NEE (Xiao et al. 2008). For instance, surface reflectance of vegetation depends on not only wavelength region and sun-object-sensor geometry but also on biophysical properties (e.g., biomass, leaf area, and stand age) and soil moisture (Ranson et al. 1985; Penuelas et al. 1993). Vegetation indices and biophysical parameters derived from surface reflectance can also account for factors influencing NEE, such as the enhanced vegetation index (EVI), the land surface temperature (LST), the normalized difference water index (NDWI), the fraction of photosynthetically active radiation absorbed by vegetation canopies (fPAR), and LAI.

Vegetation indices such as the normalized difference vegetation index (NDVI) capture the contrast between the visible-red and near-infrared reflectance of vegetation canopies, and are closely correlated to fPAR (Asrar et al. 1984). These vegetation indices are also related to vegetation biomass (Myneni et al. 2001), photosynthetic activity (Zhou et al. 2001; Xiao and Moody 2004), and fractional vegetation cover (Xiao and Moody 2005). However, NDVI has several limitations, including saturation in a multilayer closed canopy and sensitivity to both atmospheric aerosols and soil background (Huete et al. 2002; Xiao and Moody 2005). To account for these limitations of NDVI, Huete et al. (1997) developed the improved vegetation index—EVI:

$$EVI = 2.5\frac{\rho_{nir} - \rho_{red}}{\rho_{nir} + (6\rho_{red} - 7.5\rho_{blue}) + 1} \tag{6.1}$$

where ρ_{nir}, ρ_{red}, and ρ_{blue} are the spectral reflectance at the near-infrared, red, and blue wavelengths, respectively.

The LST derived from MODIS is a measure of the soil temperature at the surface. The MODIS LST agreed with in situ measured LST within 1 K in the range 263–322 K (Wan et al. 2002). LST is likely a good indicator of R_e as both R_a and R_H are significantly affected by air/surface temperature. For instance, Rahman et al. (2005) showed that satellite-derived LST was strongly correlated with R_e.

A combination of NIR and shortwave infrared (SWIR) bands has been used to derive water-sensitive vegetation indices (Ceccato et al. 2002) because of the sensitivity of SWIR to vegetation water content and soil moisture. For instance, Gao (1996) developed the NDWI from satellite data to measure vegetation liquid water:

$$NDWI = \frac{\rho_{nir} - \rho_{swir}}{\rho_{nir} + \rho_{swir}} \tag{6.2}$$

where ρ_{swir} is the reflectance at the shortwave infrared (SWIR) spectral band. The capability of NDWI for estimating canopy water stress status that affects photosynthesis is limited by its sensitivity to the relatively small changes in relative water content observed in natural vegetation and inability to discern changes in canopy biomass from changes in canopy moisture status (Hunt and Rock 1989; Gao 1996). Some studies, however, have shown that the NDWI is strongly correlated with leaf water content (equivalent water thickness) (Jackson et al. 2004) and soil moisture (Fensholt and Sandholt 2003) over time. NDWI has been used to derive a water scalar in a light use efficiency model (Xiao et al. 2005).

Satellite remote sensing has also been used to quantify LAI and fPAR (e.g., Myneni et al. 2002). These two variables characterize vegetation canopy functioning and energy absorption capacity (Myneni et al. 2002), and are key parameters in most ecosystem productivity and biogeochemical models due to their high correlation with GPP (Sellers et al. 1997).

The explanatory variables used in the data-driven approach include land cover, EVI, LST, NDWI, fPAR, LAI, and photosynthetically active radiation (PAR), and these variables can account for factors influencing NEE. The explanatory variables used here are slightly different from those used previously (Xiao et al. 2008) in that surface reflectance is not used here. All these variables can be obtained from MODIS data products, which also avoid the complications and difficulties to merge disparate data sources.

6.3 Methods

A data-driven approach (Xiao et al. 2008) is used to develop a predictive model for NEE using flux observations from AmeriFlux and MODIS data streams. The predictive model is then used to produce continuous NEE estimates for the conterminous U.S. over the period 2000–2009.

6.3.1 AmeriFlux Data

The AmeriFlux network consists of a number of active and inactive flux towers across the U.S. (Fig. 6.1). The Level 4 NEE data were obtained for AmeriFlux sites over the period 2000–2006 (Xiao et al. 2008). These sites are distributed across the conterminous U.S. The Level 4 product consists of NEE data with four different time steps, including half-hourly, daily, 8-day, and monthly. NEE was calculated using the storage obtained from the discrete approach or using a vertical CO_2 profile system, and was gap-filled using artificial neural network. The 8-day NEE data (g C m^{-2} day^{-1}) were used to match the compositing intervals of MODIS data.

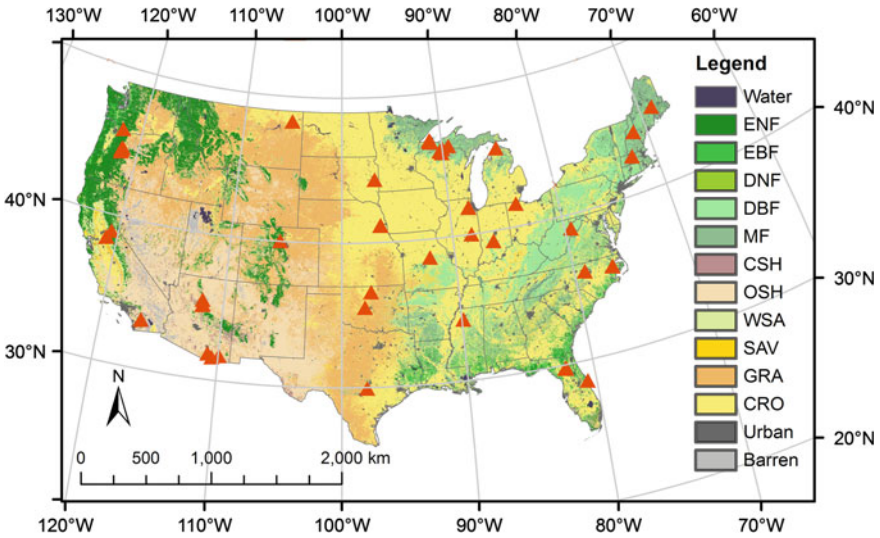

Fig. 6.1 The location and distribution of AmeriFlux sites in the conterminous U.S. Symbols stand for flux sites. The base map is the MODIS land cover map, and its land cover classes include: evergreen needleleaf forests (ENF), evergreen broadleaf forests (EBF), deciduous needleleaf forests (DNF), deciduous broadleaf forests (DBF), mixed forests (MF), closed shrublands (CSH), open shrublands (OSH), woody savannas (WSA), savannas (SAV), grasslands (GRA), croplands (CRO), urban areas (Urban), barren or sparsely vegetated (Barren), and water

NEE is the difference of two large carbon fluxes—photosynthesis (GPP) and ecosystem respiration (R_e), and the errors of these two fluxes compensate each other. For instance, underestimated GPP and underestimated R_e may lead to an accurate NEE estimate. A small error in GPP or R_e can also translate to a large error in NEE as the magnitude of GPP or R_e is typically much larger than NEE. To avoid compensating errors the basic processes underlying ecosystem carbon uptake and release should both be modeled well (Richardson et al. 2007). Unlike most modeling approaches, the data-driven approach directly estimates NEE, which avoids the compensating errors.

6.3.2 MODIS Data

MODIS ASCII (American Standard Code for Information Interchange) subsets (Collection 5) were obtained for each AmeriFlux site from the Oak Ridge National Laboratory's Distributed Active Archive Center (ORNL DAAC). These subsets consist of 7×7 km regions centered on the flux tower, including surface

reflectance, daytime and nighttime LST, EVI, LAI, and fPAR over the period 2000–2006. The processing of these subsets has been described in detail by Xiao et al. (2008). Average values were extracted for the central 3 × 3 km area within the 7 × 7 km cutouts to better represent the flux tower footprint (Rahman et al. 2005; Xiao et al. 2008). For each variable, the quality of the value of each pixel within the area was determined using the quality assurance (QA) flags included in the product. Each 16-day EVI value was used for the two 8-day intervals corresponding with the compositing interval of other MODIS data products. NDWI was calculated from band 2 and band 6 of the surface reflectance product.

Wall-to-wall MODIS data (Collection 5) including surface reflectance, daytime and nighttime LST, LAI, and EVI with 1 km spatial resolution were used for the estimation of NEE at the continental scale. These data were obtained from NASA's Warehouse Inventory Search Tool (WIST) for the period from March 2000 to December 2009. Similarly, for each variable, the quality of the value of each pixel was determined using the QA flags and replaced the bad-quality value using a linear interpolation approach (Zhao et al. 2005). The NDWI was calculated from band 2 (near-infrared, 841–876 nm) and band 6 (shortwave infrared, 1628–1652 nm) of the surface reflectance product (MOD09A1). Each 16-day EVI composite was used for two 8-day intervals corresponding to the compositing interval of other MODIS products.

The 1 km MODIS land cover map (Friedl et al. 2002; Fig. 6.1) is used to specify the vegetation type of each cell across the conterminous U.S. The land cover map is based on the University of Maryland (UMD) classification scheme. The vegetation classes of the land cover map are reclassified to seven broad classes: evergreen forests, deciduous forests, mixed forests, shrublands, savannas, grasslands, and croplands.

6.3.3 PAR Data

Gridded PAR data were obtained from the Modern Era Retrospective-Analysis for Research and Applications (MERRA) reanalysis data set. The MERRA time period covers the modern era of remotely sensed data from 1979 through the present. MERRA makes use of observations from NASA's Earth Observing System satellites and reduce the uncertainty in precipitation and interannual variability by improving the representation of the water cycle in reanalyses (Rienecker et al. 2011). MERRA data were obtained from the Global Modeling and Assimilation Office (GMAO; http://gmao.gsfc.nasa.gov/). This data set has a spatial resolution of 0.5° × 0.667°. The PAR data were resampled to 1 km spatial resolution to match the resolution of other explanatory variables.

6.3.4 Data-Driven Approach

A data-driven approach is used to upscale fluxes from the tower footprint to the continental scale. This approach has been fully described elsewhere (Xiao et al. 2008), and is briefly summarized here. The data-driven method is essentially an ensemble of regression models. This approach relies on rule-based models, each of which is a set of conditions associated with a multivariate linear submodel. These rule-based, piecewise regression models allow both numerical (e.g., carbon fluxes, temperature, vegetation index) and categorical variables (e.g., land cover type) as input variables, and account for possible nonlinear relationships between predictive and target variables.

In this approach, the predictive accuracy of a rule-based model can be improved by combining it with an instance-based/nearest-neighbor model that predicts the target value of a new case using the average predicted values of the n most similar cases (RuleQuest 2008). The use of the composite model can improve the predictive accuracy relative to the rule-based model alone. This approach can also generate committee models made up of several rule-based models, and each member of the committee model predicts the target value for a case (RuleQuest 2008). The member's predictions are averaged to give a final prediction.

A predictive NEE model was constructed using AmeriFlux and MODIS data. The predictive variables include a variety of MODIS data streams, such as vegetation type, EVI, LST, NDWI, and PAR. Three statistical measures are used to evaluate the quality of the constructed predictive model, including mean absolute error (MAE), relative error (RE), and product-moment correlation coefficient (Yang et al. 2003; Xiao et al. 2008). MAE is calculated as:

$$MAE = \frac{1}{N}\sum_{i=1}^{N}|y_i - \hat{y}_i| \tag{6.3}$$

where N is the number of samples used to establish the predictive model, and y_i and $\hat{y}_i$ are the actual and predicted values of the response variable, respectively. RE is calculated as:

$$RE = \frac{MAE_T}{MAE_\mu} \tag{6.4}$$

where MAE_T is the MAE of the constructed model, and MAE_μ is the MAE that would result from always predicting the mean value.

For forest sites, the MAE and RE are 0.48 g C m^{-2} day^{-1} and 0.37, respectively for the predictive model. For non-forest sites, the MAE and RE are 0.73 g C m^{-2} day^{-1} and 0.61, respectively. The performance of the model is slightly better for forest sites than for non-forest sites. Given the diversity in ecosystem types, age structures, fire and insect disturbances, and management practices, the performance of these models is encouraging (Xiao et al. 2008).

6.4 Validation

Cross-validation can provide an estimate of the predictive accuracy of the predictive model. The *k*-fold cross-validation, in which the cases are divided into *k* blocks of roughly the same size and target value distribution, is used here. For each block, a predictive model is constructed from the cases in the remaining blocks, while the cases in the hold-out block is then used to test the performance of the model (RuleQuest 2008). The cross-validation shows that the predictive models estimate NEE fairly well (Fig. 6.2). The performance of the model is slightly better for forest sites ($y = 0.87x - 0.08$, $R^2 = 0.87$, $p < 0.0001$) than for non-forest sites ($y = 0.85x - 0.08$, $R^2 = 0.85$, $p < 0.0001$). The Root Mean Squared Error (RMSE) of the model for forest sites is 34.0 % lower than that of the model for non-forest sites.

6.5 Major Findings

With validation, the predictive model is used to estimate NEE for each 1 × 1 km cell within the conterminous U.S. and for each 8-day interval from March 2000 to December 2009 to produce continuous NEE estimates with high spatial (1 km) and temporal (8-day) resolutions. EC-MOD provides alternative, independent gridded flux estimates for the U.S. compared to traditional methods including inventory

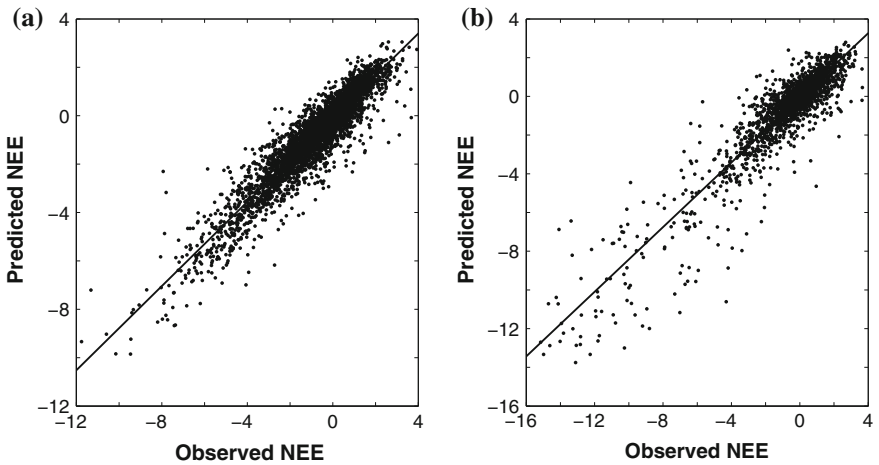

Fig. 6.2 Observed NEE versus predicted NEE based on 10-fold cross validation: **a** forest sites ($y = 0.87x - 0.08$, $R^2 = 0.87$, $p < 0.0001$; RMSE = 0.62 g C m^{-2} day^{-1}); **b** non-forest sites ($y = 0.85x - 0.08$, $R^2 = 0.85$, $p < 0.0001$; RMSE = 0.94 g C m^2 day^{-1}). The units are g C m^{-2} day^{-1}

approaches, ecosystem modeling, and atmospheric inversions. The extended EC-MOD flux estimates are used to examine the spatial and temporal dynamics of NEE at seasonal, annual, and interannual scales.

6.5.1 Monthly NEE and Seasonality

Figure 6.3 shows monthly NEE from January to December in 2009. The monthly NEE was aggregated from the 8-day NEE estimates. The results show that the data-driven model generally captures the spatial and temporal patterns of NEE. NEE varies substantially from month to month and from season to season. For each month/season, the flux also varies substantially over space. In the winter

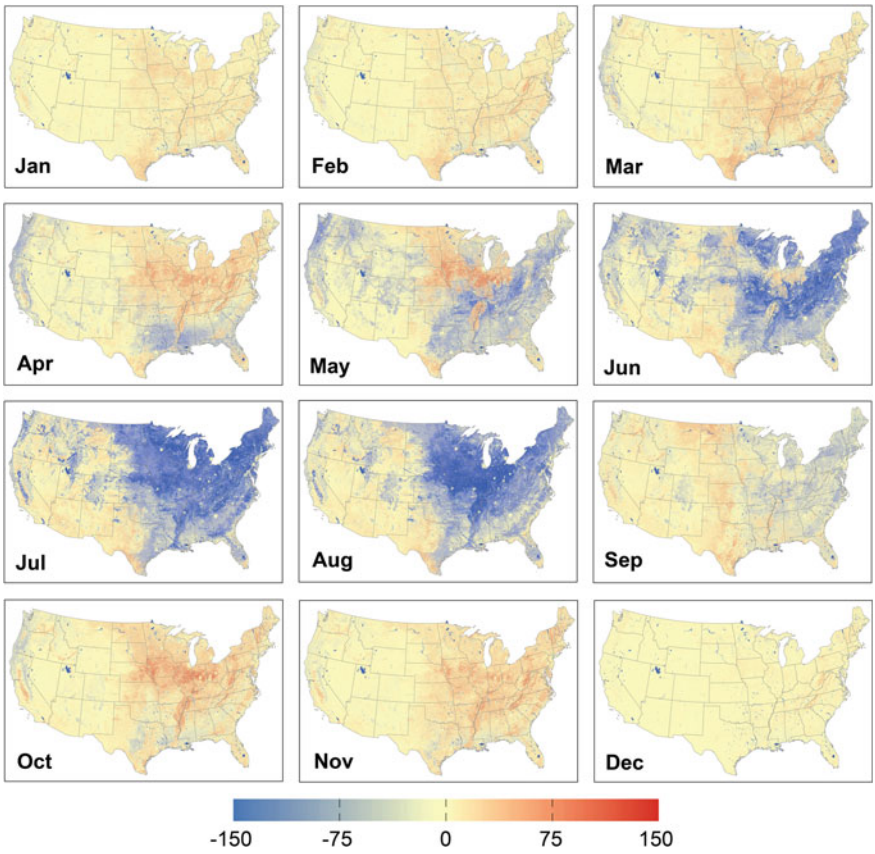

Fig. 6.3 Monthly NEE for the conterminous U.S. from January through December in 2009. The units are g C m^{-2} mo^{-1}. *Negative values* indicate carbon uptake, and *positive values* indicate carbon release. *Gray lines* indicate state boundaries

(December–March), the majority of the U.S. terrestrial ecosystems is nearly carbon neutral or slightly releases carbon. This is because the canopies of the terrestrial ecosystems are largely dormant in the winter with photosynthesis approaching 0 and ecosystem respiration exceeding photosynthesis.

In the spring (March–May), the onset of the growing season starts in the Gulf Coast region, and then progresses to north. In March, ecosystems in some areas, including the Gulf Coast, coastal Pacific Northwest, and California, slightly absorb carbon from the atmosphere because of the dominance of evergreen forests and mild temperatures in these areas (Waring and Franklin 1979; Anthoni et al. 2002). In May, the majority of eastern U.S. and many regions in the West assimilate carbon. The Midwestern region including the Upper Great Lakes region and the northern Great Plains still releases carbon. This region is dominated by croplands with most crops planted between April and June (Shroyer et al. 1996), and crops are sparse in the beginning of the growing season and ecosystem respiration exceeds GPP.

In the summer, the entire eastern U.S. assimilates carbon from the atmosphere. Croplands in the Midwest generally exhibit higher net carbon uptake than eastern forests. The majority of the West except the coastal Pacific Northwest and central California is nearly carbon neutral. Some areas in the west release carbon. The fall months (September–November) are the transition from the summer to the winter. Most ecosystems absorb less carbon in the fall than in the summer months as vegetation begins to the senesce and days become shorter.

The trajectory of the monthly NEE averaged over the U.S. depends on vegetation type (Fig. 6.4). Deciduous forests and croplands have large intra-annual variability in NEE, while evergreen forests, grasslands, and savannas have much less variability. During the peak of the growing season (June–August), deciduous forests and croplands have the largest net carbon uptake; mixed forests, savannas, and evergreen forests have intermediate carbon uptake; grasslands have the lowest carbon uptake. Shrublands release carbon from June to October due to high temperatures and large water deficits. Deciduous forests and croplands release carbon from late fall to early spring.

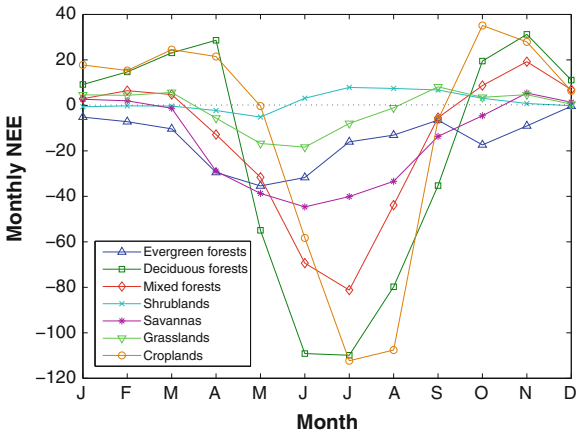

Fig. 6.4 Monthly NEE averaged across the conterminous U.S. for each broad vegetation type in 2009. The units are g C m^{-2} mo^{-1}

6.5.2 Annual NEE

The 8-day NEE estimates were aggregated to the annual scale for each year from 2001 to 2009, and mean annual NEE was then calculated for the 9-year period (Fig. 6.5). The net flux here represents the terrestrial part of the carbon cycle without fire emissions and immediate carbon loss caused by the removal and burning of biomass. The mean annual NEE map shows that the eastern U.S. sequesters CO_2 from the atmosphere and thus provides a carbon sink. The coastal Pacific Northwest, the Rocky Mountains, and a part of California also provide carbon sinks. Many other areas in the western U.S. including the Great Basin, the Colorado Plateau, and the western Great Plains, however, do not significantly sequester CO_2 from the atmosphere or release carbon and are thus nearly carbon neutral likely due to sparse vegetation and water stress. Some regions in the West, particularly southwestern states including Nevada, Arizona, New Mexico, and western Texas, provide minor carbon sources.

Figure 6.6 shows the mean annual NEE integrated over the U.S. and for each broad vegetation type. On average, the total annual NEE of the U.S. terrestrial ecosystems is -0.97 Pg C year^{-1} (1 Pg $= 10^{15}$ g). The annual NEE of natural ecosystems and croplands is -0.54 and -0.43 Pg C year^{-1}, respectively. These estimates are slightly lower than the previous EC-MOD estimates in absolute magnitude for the period 2001–2006 (-0.63 and -0.58 Pg C year^{-1} for natural ecosystems and croplands, respectively; Xiao et al. 2011a). Among natural ecosystems, forests and savannas provide the largest net carbon uptake, followed by savannas; grasslands provide the least carbon sink. Shrublands provide a minor carbon source.

The annual NEE estimates are not annual net biome productivity (NBP) as they do not explicitly include the fire emissions and immediate carbon loss caused by the removal and burning of biomass. The estimate from EC-MOD (0.54 Pg C year^{-1})

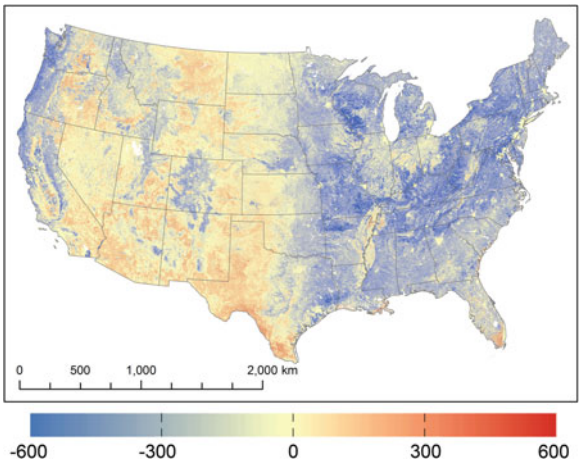

Fig. 6.5 Mean annual NEE for the conterminous U.S. over the period 2001–2009. Units are g C m^{-2} year^{-1}. *Negative values* indicate carbon uptake, and *positive values* indicate carbon release. *Gray lines* indicate state boundaries

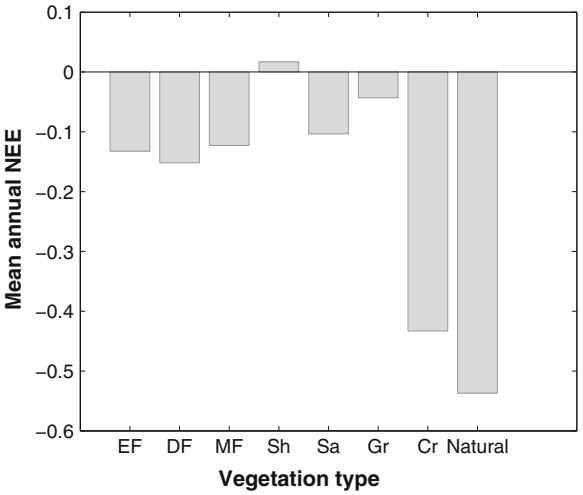

Fig. 6.6 Mean annual NEE for each broad vegetation type within the conterminous U.S. over the period 2001–2009: evergreen forests (EF), deciduous forests (DF), mixed forests (MF), shrublands (Sh), savannas (Sa), grasslands (Gr), and croplands (Cr). Natural ecosystems (Natural) consist of all these broad vegetation types except croplands. The units are Pg C year^{-1}

likely overestimates the magnitude of the U.S. carbon sink. Wiedinmyer and Neff (2007) estimated that wildfire in the U.S. released 0.06 Pg C year^{-1}. With fire emissions deducted, the EC-MOD estimate for the magnitude of the U.S. carbon sink is 0.48 Pg C year^{-1} over the period 2001–2009. This estimate is within the range (0.30–0.58 g C year^{-1}) estimated by Pacala et al. (2001) and almost identical with the estimate (0.49 Pg C year^{-1}) by the first North American State of the Carbon Cycle Report (SOCCR 2007).

6.5.3 Interannual Variability of NEE

The anomalies of annual NEE were calculated for each year relative to the 9-year mean (2001–2009) to examine the interannual variability of NEE. The NEE of terrestrial ecosystems exhibits large interannual variability over the 9-year period. Figure 6.7 shows the anomalies of annual NEE for 2002. The sign and magnitude of the anomalies vary over space. The Great Plains and some regions in the Midwest exhibit large positive anomalies, indicating reduced carbon uptake or net carbon release. Some regions in the eastern U.S., including Minnesota, Kentucky, and Tennessee, exhibit large negative anomalies, indicating increased net carbon uptake. The remaining regions large exhibit small anomalies.

The annual NEE of U.S. terrestrial ecosystems varies from year to year (Fig. 6.8). The annual NEE of the U.S. terrestrial ecosystems varies between −0.77 and −1.09 Pg C year^{-1} over the period 2001–2009. During the 9 years, 2009 had the lowest net carbon uptake (−0.77 Pg C year^{-1}), followed by 2002 and 2006 (−0.90 and −0.89 Pg C year^{-1}, respectively). The annual NEE in 2009 was 20.6 % lower than the 9-year mean (−0.97 Pg C year^{-1}) and 29.4 % lower than

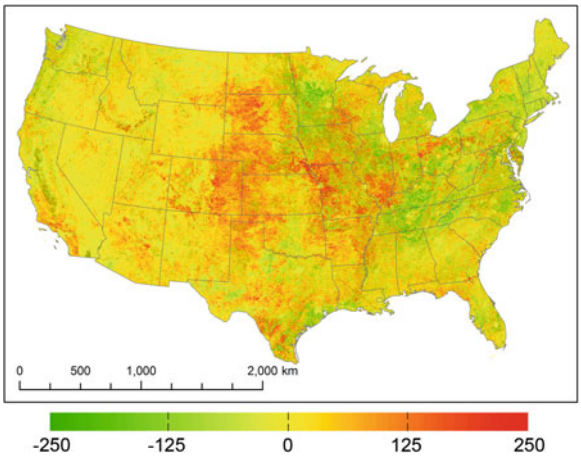

Fig. 6.7 Anomaly of annual NEE in 2002 relative to the 2001–2009 mean. The units are g C m^{-2} $year^{-1}$. *Negatives values* indicate increased carbon uptake, and *positive values* indicate reduced carbon uptake or net carbon release

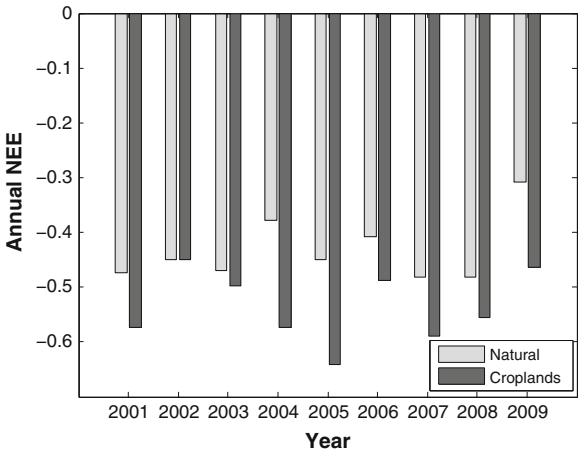

Fig. 6.8 Annual NEE of natural ecosystems and croplands for the conterminous U.S. over the period 2001–2009. The units are Pg C $year^{-1}$. *Negative values* indicate carbon uptake, and *positive values* indicate carbon release

2005 with the highest net carbon uptake (-1.09 Pg C $year^{-1}$). The reduction of annual NEE is mainly caused by the decrease in NEE for natural ecosystems. The annual NEE of croplands is less variable than that of natural ecosystems because irrigation can effectively reduce water stress for crops.

The dominant sources of the interannual variability in annual NEE of the U.S. include severe extended drought and disturbances (e.g., fires, hurricanes, and insect outbreaks) (Xiao et al. 2011a). Major forest disturbances include fire, hurricanes, harvesting, and insect outbreaks, each of which can have substantial impacts on carbon stocks and fluxes via their effects on forest structure and function (Amiro et al. 2010). Disturbances affect carbon dynamics in two major ways (Liu et al. 2011). First, disturbance transfer carbon among pools (e.g., from live boles to dead coarse woody debris, or from live biomass pool and surface soil

pool to atmosphere). Second, disturbances modify soil physical and chemical factors and microclimate, creating ecological legacies that affect carbon dynamics over ensuing decades or even centuries. The low net carbon uptake in 2002, 2006, and 2009 are likely mainly caused by severe extended droughts and wild fires.

6.5.4 Sources of Uncertainty

Despite the encouraging performance of the data-driven model, the resulting gridded flux estimates for the U.S. exhibit significant uncertainties. There are several sources of uncertainty associated with the NEE estimates, including uncertainty in flux observations from towers, uncertainty in other input data (e.g., land cover), model structural uncertainty, and uncertainty resulting from the representativeness of the AmeriFlux network (Xiao et al. 2011a).

The uncertainty of input data can propagate through model simulations and lead to biases in the flux estimates. The NEE measurements from eddy covariance flux towers contain significant uncertainty largely due to random measurement error (Hollinger and Richardson 2005). The potential uncertainties associated with the eddy covariance technique include systematic errors from insensitivity to high-frequency turbulence, random errors from inadequate sample size associated with averaging period, vertical and horizontal advection, u^* filtering, and gap-filling methods (e.g., Hollinger and Richardson 2005; Loescher et al. 2006). Other input data, particularly the land cover map, also contain significant uncertainty. Land-cover maps are typically derived from satellite remote sensing, and their uncertainty is associated with the limited accuracy of image classification. The sub-grid heterogeneity in land cover, topography, and climate can also influence the accuracy of the gridded flux estimates.

There is also significant uncertainty associated with the algorithm of the data-driven approach. As mentioned earlier, a variety of variables derived from satellite remote sensing including EVI, LST, NDWI, and LAI are used as explanatory variables for the prediction of NEE. Although these variables can partly account for the climatic, physiological, and hydrological factors controlling NEE, some important factors influencing NEE such as soil organic carbon pools and disturbances are not represented. In addition, it is debatable whether NDWI provides a sufficient measure of ecosystem water stress, although it is strongly related to leaf water content (Jackson et al. 2004) and soil moisture (Fensholt and Sandholt 2003). Microwave sensors including AMSR-E provide global estimates of soil moisture that can be potentially used in upscaling efforts. These estimates, however, are not available for densely vegetated areas that are important for terrestrial carbon cycling. For a given cell, the data-driven approach can also introduce biases to the flux estimates if the values of the explanatory variables are beyond the range of the training data.

The representativeness of the AmeriFlux network also leads to uncertainty in the gridded flux estimates. Although the AmeriFlux sites are fairly representative

of the major U.S. ecosystem and climate types (Hargrove et al. 2003; Xiao et al. 2011a), some geographical regions and vegetation types are still underrepresented. For example, there are very few sites in the Great Basin, the Rocky Mountain, and the western Great Plains regions. There are also very limited sites for open shrublands and savannas. The temporal representativeness of the AmeirFlux data may also influence the flux estimates. Multiple years of data (2000–2004) were used to train the models here to account for the interannual variability of fluxes. A 5-year period of time, however, is perhaps still limited for capturing some extreme events.

6.6 Future Research Directions

Satellite remote sensing provides valuable information for upscaling flux observations from the tower footprint to regional and continental scales. The resulting gridded flux estimates generally capture the spatial and temporal patterns of NEE. These flux estimates can be used to examine the magnitude, distribution, and interannual variability of net carbon uptake/release over broad regions.

In future work, the upscaling of flux observations should explicitly incorporate the impacts of disturbance on ecosystem carbon exchange (e.g., Amiro et al. 2010; Liu et al. 2011). Satellite remote sensing can be used to produce spatially-explicit information on aboveground biomass (Zhang and Kondragunta 2006), disturbance (Goward et al. 2008; Huang et al. 2010), and stand age (Pan et al. 2011b), which is potentially useful for accounting for the state and stages of forest ecosystems and the impacts of disturbances. Future upscaling work is also expected to advance towards quantifying uncertainties associated with gridded flux estimates by considering various sources of uncertainty (Xiao et al. 2011b, 2012). Future upscaling efforts will benefit from the intercomparison of multiple upscaling methods including data-driven (e.g., Xiao et al. 2008, 2010, 2011a; Jung et al. 2009; Zhang et al. 2011) and data assimilation (e.g., Xiao et al. 2011b) approaches and the resulting flux fields. The intercomparison of flux estimates resulting from different upscaling approaches as well as comparison of these approaches to other methods such as atmospheric inversions, biomass inventories, and ecosystem models can provide complementary information for the diagnostics of net carbon exchange between the terrestrial biosphere and the atmosphere and valuable information for future improvement of these approaches (Xiao et al. 2012).

Acknowledgments This work is supported by National Science Foundation (NSF) through Macrosystems Biology program under award 1065777, National Aeronautics and Space Administration (NASA) through Carbon Monitoring System (CMS) under grant NNX11AL32G, and Department of Energy (DOE) through National Institute for Climatic Change Research (NICCR) under grant 14U776. I thank the research/technical personnel of the AmeriFlux towers, MODIS data products, and MERRA data products for making the flux observations, MODIS data streams, and MERRA data available, respectively. I also thank the two anonymous reviewers for their constructive comments on the manuscript.

References

Amiro BD, Barr AG, Barr JG, Black TA, Brach R, Brown M, Chen J, Clark KL, Davis KJ, Desai AR, Dore S, Engel V, Fuentes JD, Goldstein AH, Goulden ML, Kolb TE, Lavigne MB, Law BE, Margolis HA, Martin T, McCaughey JH, Misson L, Montes-Helu M, Noormets A, Randerson JT, Starr G, Xiao J (2010) Ecosystem carbon dioxide fluxes after disturbance in forests of North America. J Geophys Res Biogeosci 115:G00K02. doi:10.1029/2010JG001390

Anthoni PM, Unsworth MH, Law BE, Irvine J, Baldocchi DD, Tuyl SV, Moore D (2002) Seasonal differences in carbon and water vapor exchange in young and old-growth ponderosa pine ecosystems. Agri For Meteorol 111:203–222

Asrar G, Fuchs M, Kanemasu ET, Hatfield JL (1984) Estimating of absorbed photosynthesis radiation and leaf area index from spectral reflectance in wheat. Agron J 6:300–306

Baldocchi D, Falge E, Gu L, Olson R, Hollinger D, Running S, Anthoni P, Bernhofer C, Davis K, Evans R, Fuentes J, Goldstein A, Katul G, Law B, Lee X, Malhi Y, Meyers T, Munger W, Oechel W, Paw UKT, Pilegaard K, Schmid HP, Valentini R, Verma S, Vesala T, Wilson K, Wofsy S (2001) FLUXNET: a new tool to study the temporal and spatial variability of ecosystem-scale carbon dioxide, water vapor, and energy flux densities. Bull Am Meteorol Soc 82:2415–2434

Caspersen JP, Pacala SW, Jenkins JC, Hurtt GC, Moorcroft PR, Birdsey RA (2000) Contributions of land-use history to carbon accumulation in U.S. forests. Science 290:1148–1151

Ceccato P, Gobron N, Flasse S, Pinty B, Tarantola S (2002) Designing a spectral index to estimate vegetation water content from remote sensing data: part 1—theoretical approach. Remote Sen Environ 82:188–197

Clark KL, Gholz HL, Moncrieff JB, Cropley F, Loescher HW (1999) Environmental controls over net carbon dioxide from contrasting Florida ecosystems. Ecol Appl 9:936–948

Clark KL, Gholz HL, Castro MS (2004) Carbon dynamics along a chronosequence of slash pine plantations in N. Florida. Ecol Appl 4:1154–1171

Dang X, Lai C-T, Hollinger D, Schauer A, Xiao J, Munger W, Owensby C, Ehleringer JR (2011) Combining tower mixing ratio and community model data to estimate regional-scale net ecosystem carbon exchange by boundary layer inversion over 4 flux towers in the USA. J Geophys Res Biogeosci 116:G03036. doi:10.1029/2010JG001554

Desai AR, Richardson AD, Moffat AM, Kattge J, Hollinger DY, Barr A, Falge E, Noormets A, Papale D, Reichstein M, Stauch, VJ (2008) Cross-site evaluation of eddy covariance GPP and RE decomposition techniques. Agric For Meteorol 148:821–838

Deng F, Chen JM, Ishizawa M, Yuen C-W, Mo G, Higuchi K, Chan D, Maksyutov S (2007) Global monthly CO_2 flux inversion with a focus over North America. Tellus 59B:179–190

Deng F, Chen JM, Pan Y, Peters W, Birdsey R, McCullough K, Xiao J (2013) The use of forest stand age information in an atmospheric CO2 inversion applied to North America. Biogeosciences 10:5335–5348

Fensholt R, Sandholt I (2003) Derivation of a shortwave infrared water stress index from MODIS near- and shortwave infrared data in a semiarid environment. Remote Sens Environ 87:111–121

Friedl MA, McIver DK, Hodges JCF, Zhang XY, Muchoney D, Strahler AH, Woodcock CE, Gopal S, Schneider A, Cooper A, Baccini A, Gao F, Schaaf C (2002) Global land cover mapping from MODIS: algorithms and early results. Remote Sens Environ 83:287–302

Gao BC (1996) NDWI—a normalized difference water index for remote sensing of vegetation liquid water from space. Remote Sens Environ 58:257–266

Göckede M, Foken T, Aubinet M, Aurela M, Banza J, Bernhofer C, Bonnefond JM, Brunet Y, Carrara A, Clement R, Dellwik E, Elbers J, Eugster W, Fuhrer J, Granier A, Grünwald T, Heinesch B, Janssens IA, Knohl A, Koeble R, Laurila T, Longdoz B, Manca G, Marek M, Markkanen T, Mateus J, Matteucci G, Mauder M, Migliavacca M, Minerbi S, Moncrieff J, Montagnani L, Moors E, Ourcival J-M, Papale D, Pereira J, Pilegaard K, Pita G, Rambal S,

Rebmann C, Rodrigues A, Rotenberg E, Sanz MJ, Sedlak P, Seufert G, Siebicke L, Soussana JF, Valentini R, Vesala T, Verbeeck H, Yakir D (2008) Quality control of CarboEurope flux data—part 1: coupling footprint analyses with flux data quality assessment to evaluate sites in forest ecosystems. Biogeosciences 5:433–450

Goodale CL, Apps MJ, Birdsey RA, Field CB, Heath LS, Houghton RA, Jenkins JC, Kohlmaier GH, Kurz WA, Liu S, Nabuurs G-J, Nilsson S, Shvidenko AZ (2002) Forest carbon sinks in the Northern Hemisphere. Ecol Appl 12:891–899

Goward SN, Masek JG, Cohen W, Moisen G, Collatz GJ, Healey S, Houghton R, Huang C, Kennedy R, Law B, Turner D, Powell S, Wulder M (2008) Forest disturbance and North American carbon flux. EOS Trans Am Geophys Union 89:105–106

Hargrove WW, Hoffman FM, Law BE (2003) New analysis reveals representativeness of the AmeriFlux network. EOS Trans 84:529–544

Hollinger DY, Richardson AD (2005) Uncertainty in eddy covariance measurements and its application to physiological models. Tree Physiol 25:873–885

Houghton RA, Hackler JL, Lawrence KT (1999) The U.S. carbon budget: contributions from land-use change. Science 285:574–578

Huang C, Goward SN, Masek JG, Thomas N, Zhu Z, Vogelmann JE (2010) An automated approach for reconstructing recent forest disturbance history using dense Landsat time series stacks. Remote Sens Environ 114:183–198

Huete AR, Liu HQ, Batchily K, van Leeuwen OW (1997) A comparison of vegetation indices global set of TM images for EOS-MODIS. Remote Sens Environ 59:440–451

Huete A, Didan K, Miura T, Rodriguez EP, Gao X, Ferreira LG (2002) Overview of the radiometric and biophysical performance of the MODIS vegetation indices. Remote Sens Environ 83:195–213

Hunt ER, Rock BN (1989) Detection of changes in leaf water content using near and middle-infrared reflectances. Remote Sens Environ 30:43–54

Huntzinger DN, Post WM, Wei Y, Michalak AM, West TO, Jacobson AR, Baker IT, Chen JM, Davis KJ, Hayes DJ, Hoffman FM, Jain AK, Liu S, McGuire AD, Neilson RP, Potter C, Poulter B, Price D, Raczka BM, Tian HQ, Thornton P, Tomelleri E, Viovy N, Xiao J, Yuan W, Zeng N, Zhao M, Cook R (2012) North American carbon program (NACP) regional interim synthesis: terrestrial biosphere model intercomparison. Ecol Model 232:144–157. doi:10.1016/j.ecolmodel.2012.02.004

Jackson TJ, Chen D, Cosh M, Li F, Anderson M, Walthall C, Doriaswamy P, Hunt ER (2004) Vegetation water content mapping using Landsat data derived normalized difference water index fro corn and soybeans. Remote Sens Environ 92:475–482

Jung M, Reichstein M, Bondeau A (2009) Towards global empirical upscaling of FLUXNET eddy covariance observations: validation of a model tree ensemble approach using a biosphere model. Biogeosciences 6:2001–2013

Liu S, Bond-Lamberty B, Hicke JA, Vargas R, Zhao S, Chen J, Edburg SL, Hu Y, Liu J, McGuire AD, Xiao J, Keane R, Yuan W, Tang J, Luo Y, Potter C, Oeding J (2011) Simulating the impacts of disturbances on forest carbon cycling in North America: processes, data, models, and challenges. J Geophys Res Biogeosci 116:G00K08. doi:10.1029/2010JG001585

Loescher HW, Law BE, Mahrt L, Hollinger DY, Campbell J, Wofsy SC (2006) Uncertainties in, and interpretation of, carbon flux estimates using the eddy covariance technique. J Geophys Res 111: D21S90. doi:10.1029/2005JD006932

Myneni RB, Dong J, Tucker CJ, Kaufmann RK, Kauppi PE, Liski J, Zhou L, Alexeyev V, Hughes MK (2001) A large carbon sink in the woody biomass of northern forests. PNAS 98:14784–14789

Myneni RB, Hoffman S, Knyazikhin Y, Privette JL, Glassy J, Tian Y, Wang Y, Song X, Zhang Y, Smith GR, Lotsch A, Friedl M, Morisette JT, Votava P, Nemani RR, Running SW (2002) Global products of vegetation leaf area and fraction absorbed PAR from year one of MODIS data. Remote Sens Environ 83:214–231

Pacala SW, Hurtt GC, Baker D, Peylin P, Houghton RA, Birdsey RA, Heath L, Sundquist ET, Stallard RF, Ciais P, Moorcroft P, Caspersen JP, Shevliakova E, Moore B, Kohlmaier G,

Holland E, Gloor M, Harmon ME, Fan S-M, Sarmiento JL, Goodale CL, Schimel D, Field CB (2001) Consistent land- and atmosphere-based U.S. carbon sink estimates. Science 292:2316–2320

Pan Y et al (2011a) A large and persistent carbon sink in the world's forests. Science 333:988–993

Pan Y, Chen JM, Birdsey R, McCullough K, He L, Deng F (2011b) Age structure and disturbance legacy of North American forests. Biogeosciences 8(715–732):979–1020

Penuelas J, Gamon JA, Griffin KL, Field CB (1993) Assessing community type, plant biomass, pigment composition, and photosynthetic efficiency of aquatic vegetation from spectral reflectance. Remote Sens Environ 46:110–118

Potter CS, Randerson JT, Field CB, Matson PA, Vitousek PM, Mooney HA, Klosster SA (1993) Terrestrial ecosystem production—a process model based on global satellite and surface data. Glob Biogeochem Cycles 7:811–841

Rahman AF, Sims DA, Cordova VD, El-Masri BZ (2005) Potential of MODIS EVI and surface temperature for directly estimating per-pixel ecosystem C fluxes. Geophy Res Lett 32:L19404. doi:10.1029/2005GL024127

Ranson KJ, Daughtry CST, Biehl LL, Bauer ME (1985) Sun-view angle effects on reflectance factors of corn canopies. Remote Sens Environ 18:47–161

Reichstein M, Falge E, Baldocchi D, Papale D, Aubinet M, Berbigier P, Bernhofer C, Buchmann N, Gilmanov T, Granier A, Grunwald T, Havrankova K, Ilvesniemi H, Janous D, Knohl A, Laurila T, Lohila A, Loustau D, Matteucci G, Meyers T, Miglietta F, Ourcival JM, Pumpanen J, Rambal S, Rotenberg E, Sanz M, Tenhunen J, Seufert G, Vaccari F, Vesala T, Yakir D, Valentini R (2005) On the separation of net ecosystem exchange into assimilation and ecosystem respiration: review and improved algorithm. Glob Change Biol 11:1424–1439

Richardson AD, Hollinger DY, Aber JD, Qllinger SV, Braswell BH (2007) Environmental variation is directly responsible for short- but not long-term variation in forest-atmosphere carbon exchange. Glob Change Biol 13:788–803

Richardson AD, Black TA, Ciais P, Delbart N, Friedl MA, Gobron N, Hollinger DY, Kutsch WL, Longdoz B, Luyssaert S, Migliavacca M, Montagnani L, Munger JW, Moors E, Piao S, Rebmann C, Reichstein M, Saigusa N, Tomelleri E, Vargas R, Varlagin A (2010) Influence of spring and autumn phenological transition on forest ecosystem productivity. Philos Trans R Soc B 365:3227–3246

Rienecker MM, Suarez MJ, Gelaro R, Todling R, Bacmeister J, Liu E et al (2011) MERRA—NASA's modern-era retrospective analysis for research and applications. J Clim 24:3624–3648. doi:10.1175/JCLI-D-11-00015.1

RuleQuest (2008) http://www.rulequest.com. Accessed 18 Oct 2007

Running SW, Hunt ER (1993) Generalization of a forest ecosystem process model for other biomes, Biome-BGC, and an application for global-scale models. Scaling processes between leaf and landscape levels. In: Ehleringer JR, Field CB (eds) Scaling physiological processes: leaf to globe. Academic Press, San Diego, pp 141–158

Ryan MG (1991) Effects of climate change on plant respiration. Ecol Appl 1:157–167

Ryan MG, Law BE (2005) Interpreting, measuring, and modeling soil respiration. Biogeochemistry 73:3–27

Schimel D, Melillo J, Tian H, McGuire AD, Kicklighter D, Kittel T, Rosenbloom N, Running S, Thornton P, Ojima D, Parton W, Kelly R, Sykes M, Neilson R, Rizzo B (2000) Contribution of increasing CO_2 and climate to carbon storage by ecosystems in the United States. Science 287:2004–2006

Schmid HP (1994) Source areas for scalars and scalar fluxes. Bound Layer Meteorol 67:293–318

Sellers PJ, Randall DA, Betts AK, Hall FG, Berry JA, Collatz GJ, Denning AS, Mooney HA, Nobre CA, Sato N, Field CB, Henderson-sellers A (1997) Modeling the exchanges of energy, water, and carbon between continents and the atmosphere. Science 275:502–509

Shroyer JP, Thompson C, Brown R, Ohlenbach PD, Fjell DL, Staggenborg S, Duncan S, Kilgore GL (1996) Kansas crop planting guide, vol L-818. Kansas State University, Manhattan, pp 2

SOCCR (2007) King AW et al (eds) The First state of the carbon cycle report (SOCCR): the North American carbon budget and implications for the global carbon cycle. US Climate Change Science Program, Washington, p 19

Sun G, Caldwell P, Noormets A, McNulty SG, Cohen E, Moore Myers J, Domec J-C, Treasure E, Mu Q, Xiao J, John R, Chen J (2011) Upscaling key ecosystem functions across the conterminous United States by a water-centric ecosystem model. J Geophys Res Biogeosci 116:G00J05. doi:10.1029/2010JG001573

Tans PP, Fung IY, Takahashi T (1990) Observational constraints on the global atmospheric CO_2 budget. Science 247:1431–1438

Wan Z, Zhang Y, Zhang Q, Li Z-L (2002) Validation of the land-surface temperature products retrieved from Terra Moderate Resolution Imaging Spectroradiometer data. Remote Sens Environ 83:163–180

Waring RH, Franklin JF (1979) Evergreen coniferous forests of the Pacific Northwest. Science 204:1380–1386

Wiedinmyer C, Neff JC (2007) Estimates of CO_2 from fires in the United States: implications for carbon management. Carbon Balance Manag 2. doi:10.1186/1750-0680-2-10

Wofsy SC, Goulden ML, Munger JW, Fan S-M, Bakwin PS, Daube BC, Bassow SL, Bazzaz FA (1993) Net exchange of CO_2 in a mid-latitude forest. Science 260:1314–1317

Xiao J, Moody A (2004) Photosynthetic activity of US biomes: responses to the spatial variability and seasonality of precipitation and temperature. Glob Change Biol 10:437–451

Xiao J, Moody A (2005) A comparison of methods for estimating fractional green vegetation cover within a dsert-to-upland transition zone in central New Mexico, USA. Remote Sens Environ 98:237–250

Xiao J, Zhuang Q, Liang E, McGuire AD, Moody A, Kicklighter DW, Melillo JM (2009) Twentieth century droughts and their impacts on terrestrial carbon cycling in China. Earth Interact 13(010):1–31. doi:10.1175/2009EI275.1

Xiao J, Zhuang Q, Baldocchi DD, Law BE, Richardson AD, Chen J, Oren R, Starr G, Noormets A, Ma S, Verma SB, Wharton S, Wofsy SC, Bolstad PV, Burns SP, Cook DR, Curtis PS, Drake BG, Falk M, Fischer ML, Foster DR, Gu L, Hadley JL, Hollinger DY, Katul GG, Litvak M, Martin TA, Matamala R, McNulty S, Meyers TP, Monson RK, Munger JW, Oechel WC, Paw UKT, Schmid HP, Scott RL, Sun G, Suyker AE, Torn MS (2008) Estimation of net ecosystem carbon exchange for the conterminous United States by combining MODIS and AmeriFlux data. Agric For Meteorol 148:1827–1847. doi:10.1016/j.agrformet.2008.06.015

Xiao J, Zhuang Q, Law BE, Chen J, Baldocchi DD, Cook DR, Oren R, Richardson AD, Wharton S, Ma S, Martin TA, Verma SB, Suyker AE, Scott RL, Monson RK, Litvak M, Hollinger DY, Sun G, Davis KJ, Bolstad PV, Burns SP, Curtis PS, Drake BG, Falk M, Fischer ML, Foster DR, Gu L, Hadley JL, Katul GG, Matamala R, McNulty S, Meyers TP, Munger JW, Noormets A, Oechel WC, Paw UKT, Schmid HP, Starr G, Torn MS, Wofsy SC (2010) A continuous measure of gross primary production for the conterminous U.S. derived from MODIS and AmeriFlux data. Remote Sens Environ 114:576–591. doi:10.1016/j.rse.2009.10.013

Xiao J, Zhuang Q, Law BE, Baldocchi DD, Chen J, Richardson AD, Melillo JM, Davis KJ, Hollinger DY, Wharton S, Oren R, Noormets A, Fischer ML, Verma SB, Cook DR, Sun G, McNulty S, Wofsy SC, Bolstad PV, Burns SP, Curtis PS, Drake BG, Falk M, Foster DR, Gu L, Hadley JL, Katul GG, Litvak M, Ma S, Martin TA, Matamala R, Meyers TP, Monson RK, Munger JW, Oechel WC, Paw UKT, Schmid HP, Scott RL, Starr G, Suyker AE, Torn MS (2011a) Assessing Net ecosystem carbon exchange of U.S. terrestrial ecosystems by integrating eddy covariance flux measurements and satellite observations. Agric For Meteorol 151:60–69. doi:10.1016/j.agrformet.2010.09.002

Xiao J, Davis KJ, Urban NM, Keller K, Saliendra NZ (2011b) Upscaling carbon fluxes from towers to the regional scale: influence of parameter variability and land cover representation on regional flux estimates. J Geophys Res 116:G00J06. doi:10.1029/2010JG001568

Xiao J, Chen J, Davis KJ, Reichstein M (2012) Advances in upscaling of eddy covariance measurements of carbon and water fluxes. J Geophys Res Biogeosci 117:G00J01. doi:10.1029/2011JG001889

Xiao X, Zhang Q, Saleska S, Hutyra L, Camargo PD et al (2005) Satellite-based modeling of gross primary production in a seasonally moist tropical evergreen forest. Remote Sens Environ 94:105–122

Yang L, Huang C, Homer C, Wylie BK, Coan MJ (2003) An approach for mapping large-area impervious surfaces: synergistic use of Landsat-7 ETM + and high spatial resolution imagery. Can J Remote Sens 29:230–240

Zhang L, Wylie BK, Ji L, Gilmanov TG, Tieszen LL, Howard DM (2011) Upscaling carbon fluxes over the great plains grasslands: sinks and sources. J Geophys Res 116:G00J03. doi:10.1029/2010JG001504

Zhang X, Kondragunta S (2006) Estimating forest biomass in the USA using generalized allometric models and MODIS land products. Geophys Res Lett 33:L09402. doi:10.1029/2006GL025879

Zhao M, Heinsch FA, Nemani RR, Running SW (2005) Improvements of the MODIS terrestrial gross and net primary production global data set. Remote Sens Environ 95:164–175

Zhou L, Tucker CJ, Kaufmann RK, Slayback D, Shabanov NV, Myneni RB (2001) Variations in northern vegetation activity inferred from satellite data of vegetation index during 1981 to 1999. J Geophys Res 106:20069–20083

Chapter 7
Oceanic Chlorophyll-*a* Content

Chuanmin Hu and Janet Campbell

Abstract Ever since the first Earth-observing satellite was launched, it became the dream of oceanographers to measure ocean chlorophyll *a* from space. Through more than a decade of dedicated theoretical, laboratory, and field research, the Coastal Zone Color Scanner was launched onboard NASA's Nimbus-7 satellite in 1978. Originally intended as a proof-of-concept mission, the CZCS endured well beyond its two-year design life (1978–1986), and provided oceanographers with clear evidence that ocean chlorophyll *a* could be observed from space. Continued community effort led to the successor missions of the Sea-viewing Wide Field-of-view Sensor (SeaWiFS, 1997–2010), Moderate Resolution Imaging Spectroradiometer (MODIS, 1999—present for Terra and 2002—present for Aqua), Medium Resolution Imaging Spectrometer (MERIS, 2002–2012), and other modern satellite instruments. This chapter provides a brief review of how oceanic chlorophyll *a* is "measured", validated, and used in various research studies and applications including the ocean's response to climate variability and the assessment of coastal ocean changes to help resource management. Particular emphasis is given to atmospheric correction, bio-optical inversion, and algorithm validation. Finally, future satellite ocean color missions and research directions to support these missions are briefly discussed.

C. Hu (✉)
College of Marine Science, University of South Florida, St. Petersburg, FL, USA
e-mail: huc@usf.edu

J. Campbell
Institute for the Study of Earth, Oceans, and Space, University of New Hampshire, Durham, NH, USA

J. M. Hanes (ed.), *Biophysical Applications of Satellite Remote Sensing*,
Springer Remote Sensing/Photogrammetry, DOI: 10.1007/978-3-642-25047-7_7,

7.1 Introduction

Soon after the first satellite images of the Earth became available in the 1960s, biological oceanographers started to wonder whether it was possible to measure the ocean's phytoplankton biomass from space. Yentsch (1965) first discussed the distribution of chlorophyll and phaeophytin in the ocean and described how their varying patterns might appear in satellite images. In 1967, the debut of the first airborne spectroradiometer on the C-47 aircraft of the Woods Hole Oceanographic Institute represented the birth of biological ocean remote sensing (Clarke et al. 1970). In the 1970s, several research institutions and research groups pioneered instrument and radiative transfer theory development that provided the basis for a proof-of-concept satellite mission. These included, for example, the Scripps VisLab's development of various spectroradiometers, the NOAA R/V Discoverer's optical survey of the Peru coastal upwelling, and theoretical work of Preisendorfer, Morel, Gordon, Zaneveld, and their coworkers (e.g., Preisendorfer 1976; Morel and Prieur 1977; Zaneveld 1982; Gordon and Morel 1983). After more than a decade of effort, in 1978, the Coastal Zone Color Scanner (CZCS) was launched onboard the Nimbus-7 satellite and, until 1986, provided unprecedented data to study the ocean's biology (Hovis et al. 1980). Initial results showed moderate success in estimating the surface chlorophyll concentration (Gordon et al. 1980; Smith and Baker 1982), and numerous studies of the ocean's primary productivity, biogeochemistry, and response to climate perturbations followed thereafter. These were summarized in a special volume of the Journal of Geophysical Research (Mitchell 1994).

There was a 10 year gap between 1986 and 1996 before the next ocean color sensor, the short-lived Ocean Color and Temperature Sensor (OCTS, Nov 1996–June 1997), was carried aboard the Japanese Midori satellite. Soon thereafter, the Sea-viewing Wide Field-of-view Sensor (SeaWiFS, August 1997–December 2010) was launched onboard the Orbview-2 satellite, ushering in the modern era of continuous space-based ocean color observations (Hooker et al. 1992; McClain 2009). Since then, many follow-on ocean color sensors have been launched into space by the U.S. NASA, the European Space Agency (ESA), and other international agencies. These include the Moderate Resolution Imaging Spectroradiometer (MODIS, 1999–present for Terra and 2002–present for Aqua, NASA), the Medium Resolution Imaging Spectrometer (MERIS, 2002–2012, ESA), the Ocean Color Monitor (OCM-1, 1999–present; OCM-2, 2009–present, India), and more recently, the Geostationary Ocean Color Imager (GOCI, 2010–present, South Korea) and the Visible Infrared Imager Radiometer Suite (VIIRS, 2011–present, NASA and NOAA). For a reference, Table 7.1 lists the characteristics of several ocean color sensors commonly used by the scientific community. After proper calibration and validation, the frequent and synoptic observations of the global and regional oceans from these large-swath satellite observations have been used in a variety of research and applications well beyond the original scope of mapping ocean chlorophyll. For example, ocean color observations have been used to study the ocean's biogeochemistry and primary production, to trace ocean circulation

Table 7.1 Characteristics of several popular ocean color sensors

Sensor	Res. (km)	Swath (km)	Revisit (day)	Bands (nm)	Source	Duration
CZCS (8)	0.8	1556	1–3	4, 443–670	NASA	1978–1986
SeaWiFS (10)	1.1	2801	1–2	8, 412–865	NASA	1997–2010
MODISA (12)	1.1	2330	1–2	9, 412–869	NASA	2002–now
MERIS (12)	1.2	1150	1–3	12, 413–865	ESA	2002–2012

Only ocean bands are included here. Numbers in the parentheses are digitization bits. Signal-to-noise ratios (SNRs) determined from measurements over homogeneous ocean targets under typical radiance inputs are presented in Hu et al. (2012a)

and upwelling, to monitor harmful algal blooms (HABs) and pollution events such as oil spills, to document coastal water quality changes, to assess ocean fishery and other resources, and to help make management decisions. Yet, to date, the single most-often used parameter from these satellite missions is the surface ocean chlorophyll-*a* concentration (Chl in mg m^{-3}), which has often been used interchangeably with the term "ocean color."

Here, based on the most recent research findings from the ocean color community, a brief review is provided on how Chl is derived from satellite measurements and how Chl maps help to understand global ocean biology and biogeochemistry, regional oceanography, and coastal water quality changes. This chapter is not meant to present a comprehensive list of all possible topics enabled by satellite-based Chl observations, but rather its focus is on the methods of Chl retrievals with several examples showing major findings. Interested readers may read the refereed literature and technical reports compiled by the International Ocean Colour Coordinating Group (http://www.ioccg.org) to get a full breadth and depth of knowledge in the various aspects of ocean color remote sensing.

7.2 Theoretical Basis

The theory of ocean optics and optical remote sensing has been described in numerous textbooks and articles (e.g., Gordon and Morel 1983; Mobley 1994; Morel and Maritorena 2001). Conceptually, the dominant material affecting ocean color is the water itself, which scatters blue light and absorbs red light. Variability in ocean color is determined by the light absorption and scattering properties of the materials suspended and dissolved in the upper ocean. Over most of the ocean, the only suspended materials are microscopic algae, known as phytoplankton, and organic matter produced by the algae. The ubiquitous green pigment chlorophyll *a* is found in all phytoplankton, as in other photosynthetic plants, and its concentration has traditionally been used as a measure of phytoplankton biomass. In the simplest terms, waters low in Chl are blue whereas waters with higher Chl are green. This basic concept led to the premise that remote sensing measurements of blue and green reflectance could be used to quantify Chl in the surface ocean.

More precisely, the spectral reflectance ($R(\lambda)$) of the ocean is determined by the inherent optical properties (IOPs) of the water molecules and constituents dissolved or suspended in the surface waters. Optically significant constituents (OSCs) in the ocean include phytoplankton, colored dissolved organic matter (CDOM), and non-algal particles. Non-algal particles include both phytoplankton degradation products (organic detrital particles) and inorganic particles (e.g., resuspended sediments generally found in coastal waters). In shallow waters the bottom may also influence the color of the ocean, and under windy conditions, the OSCs also include bubbles (Zhang et al. 1998). The two fundamental IOPs are the spectral absorption coefficient ($a(\lambda)$, m^{-1}) and volume scattering coefficient ($\beta(\lambda)$, m^{-1} sr^{-1}). In remote sensing, an often used IOP is the backscattering coefficient, $b_b(\lambda)$ (m^{-1}), which is derived as $b_b(\lambda) = \int \beta(\lambda)\, d\Theta$, where integration is over the backward hemisphere.

From radiative transfer equations, early efforts in the 1970s showed the following simple relationship (Prieur 1976):

$$R(\lambda) = 0.33\,(b_b(\lambda)/a(\lambda))(1+\Delta), \tag{7.1}$$

where R is the irradiance reflectance just below the water surface and Δ, typically small (a few percent) and often omitted, is related to the radiance distribution which depends on the solar zenith angle. The simple relationship in Eq. 7.1 has evolved continuously with improvements in predicting $R(\lambda)$ under various scenarios (Gordon et al. 1975, 1988; Kirk 1984; Morel and Gentili 1991).

For modeling the remotely sensed radiance, irradiance reflectance is normally replaced by the remote-sensing reflectance (R_{rs}, sr^{-1}) defined as the ratio of upwelling radiance to downwelling irradiance, which is considered more appropriate since the sensor actually measures spectral radiance. A simplified equation for R_{rs}, similar to Eq. 7.1, that has often been used is:

$$R_{rs} = G\big(b_{bw} + b_{bp}\big)/\big(a + b_{bw} + b_{bp}\big). \tag{7.2}$$

where for simplicity the dependence on λ is omitted, and G *is* a parameter related to the solar and sensor viewing geometry. Justification for this simplified expression has been explained using radiative transfer theory by Zaneveld (1995) and Zaneveld et al. (2005).

In these equations, the total absorption coefficient, a, is a mathematical sum of the individual absorption coefficients of water (a_w) and the various OSCs, namely phytoplankton pigments (a_{ph}), CDOM (a_g), and detrital particles (a_d). Thus, the color (reflectance) of the ocean is:

$$R_{rs} = G\big(b_{bw} + b_{bp}\big)/\big(a_w + a_{ph} + a_g + a_d + b_{bw} + b_{bp}\big). \tag{7.3}$$

Equation 7.3 shows that for optically deep waters (i.e., where bottom contribution to surface reflectance is negligible), deriving $R_{rs}(\lambda)$ is straightforward once the individual IOPs are known. In this equation, a_w and b_{bw} are known from laboratory measurements (Pope and Fry 1997, Fig 7.1a) and can be treated as

constants except at extreme salinity (Sullivan et al. 2006; Zhang et al. 2009). In practice, a_g and a_d are often combined (a_{dg}) because of the similarity in their spectral shapes, and the IOPs can be expressed as (IOCCG 2006):

$$\begin{aligned} a_{ph}(\lambda) &= a_{ph}(443)\, a_{ph}^{+}(\lambda) \\ a_{dg}(\lambda) &= a_{dg}(443)\, e^{-S(\lambda-443)} \\ b_{\mathrm{bp}}(\lambda) &= b_{\mathrm{bp}}(443) \left(\frac{443}{\lambda}\right)^{\eta} \end{aligned} \tag{7.4}$$

where each IOP is expressed as the product of its value at a reference wavelength (443 nm) and a spectral shape function. The wavelength 443 nm is commonly chosen because it is the location of a chlorophyll absorption peak, and thus is the center of a blue band used by all ocean color sensors since the CZCS.

In the open ocean, so-called Case I waters (Morel and Prieur 1977)[1] where optical properties are dominated by phytoplankton, the terms in Eq. 7.4 tend to covary with Chl. Thus, both $a_{ph}(\lambda)$ and $a_{ph}^{+}(\lambda)$, have been modeled as functions of Chl (Bricaud et al. 1995, 2004; IOCCG 2006). For example, $a_{ph}(\lambda)$, can be modeled as:

$$a_{ph}(\lambda) = A(\lambda)\mathrm{Chl}^{B(\lambda)}, \tag{7.5}$$

where $A(\lambda)$ and $B(\lambda)$ are empirical regression coefficients determined from measurements. Bricaud et al. (2004) reported typical values of $A(\lambda)$ and $B(\lambda)$ while recognizing that they do change with phytoplankton community composition. Similarly, for phytoplankton-dominated waters $b_{\mathrm{bp}}(\lambda)$ has also been modeled as a function of Chl (Morel 1988; Gordon 1992) although it has been noted that phytoplankton cannot fully account for the backscattering variability even in the open ocean (Morel and Ahn, 1990; Antoine et al. 2011). The spectral slope parameter for a_{dg}, S, varies only slightly with typical values of 0.015–0.018 nm^{-1}, and the spectral slope parameter for b_{bp}, η, varies inversely with Chl, owing to a relationship between particle size distributions and the trophic state as indicated by Chl. Figure 7.1b, c show typical modeled IOP spectra (Eq. 7.4), while Fig. 7.1d shows how R_{rs} varies with Chl (Eq. 7.3).

While several optical models have been developed to derive R_{rs} using Chl and other IOPs (e.g., Sathyendranath et al. 1989; Maritorena et al. 2002; IOCCG 2006; also see Mobley 1994 and references therein), their fundamental principles are the same and the mathematical expressions are similar to the above. Likewise, inversion

[1] The concept of Case I and Case II waters introduced by Morel and Prieur (1977) has been used extensively by the ocean color community. Case I refers to waters with optical properties dominated by phytoplankton and their degradation products, whereas Case II waters include all other water types in which optical properties are influenced by CDOM, inorganic particles, or the shallow ocean bottom. The concept has been recently revisited by Mobley et al. (2004) and Lee and Hu (2006), who found that water types can be better described by their different IOPs. Nevertheless, the terminology of Case I and Case II follows the convention in this context.

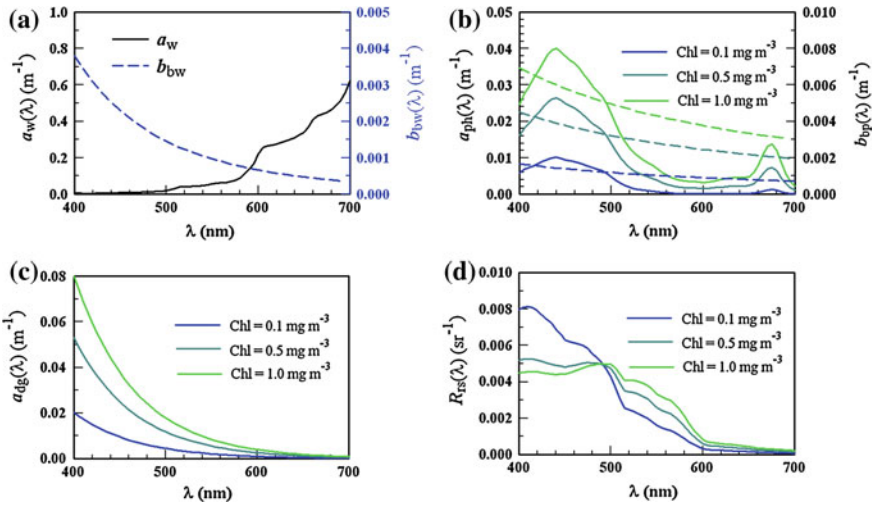

Fig 7.1 An example showing effects of Chl on inherent optical properties (IOPs) and remote-sensing reflectance (R_{rs}). **a** Absorption and backscattering coefficients of water molecules (Pope and Fry 1997). **b** Phytoplankton pigment absorption coefficients (*solid lines*) and particulate backscattering coefficients (*dashed lines*) for three Chl concentrations. **c** CDOM and detrital particle absorption coefficients for three Chl concentrations. **d** R_{rs} spectra corresponding to the IOPs in a–c, as derived from Eqs. 7.3–7.5. Note that chlorophyll-a fluorescence was not included in the model

models have been developed to derive Chl and IOPs using R_{rs} (e.g., Sathyendranath et al. 1989; Maritorena et al. 2002; IOCCG 2006; Brewin et al. 2013).

Figure 7.2 is a schematic diagram showing how the color of the ocean ($R_{rs}(\lambda)$) is determined (and therefore can be modeled) by the various OSCs and in particular by Chl, when $R_{rs}(\lambda)$ is measured in the field, for example from a ship. As shown in Fig. 7.1d, the magnitude and spectral shape of $R_{rs}(\lambda)$ are functions of Chl, hence the latter can be derived from the former using inversion algorithms (See Methods).

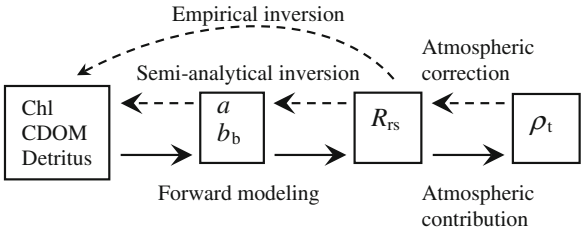

Fig 7.2 Schematic diagram showing how Chl and other OSCs determine the IOPs (a and b_b), remote-sensing reflectance (R_{rs}), and together with the atmosphere determine the satellite signal (ρ_t). To derive Chl from satellite measurements, the whole process is reversed through atmospheric correction and bio-optical inversion (either empirically or semi-analytically)

When measured by a satellite above the atmosphere, R_{rs} is modulated by the atmospheric diffuse transmission (t), while the atmosphere itself contributes a significant (often dominant) portion of the satellite signal (Gordon 1997). This is expressed as:

$$\rho_t(\lambda) = \rho_r(\lambda) + \rho_{ar}(\lambda) + t(\lambda)\rho_{wc}(\lambda) + T(\lambda)\rho_g(\lambda) + \pi t(\lambda)t_0(\lambda)R_{rs}(\lambda), \quad (7.6)$$

where $\rho_t(\lambda)$ is the satellite measured total reflectance after accounting for gaseous absorption, ρ_r is the atmosphere reflectance due to Rayleigh scattering, ρ_{ar} is that due to aerosol scattering and aerosol-Rayleigh interactions, ρ_{wc} is the whitecap reflectance, ρ_g is the sun glint reflectance, T and t are the direct and diffuse transmittance from the ocean to the satellite, and t_0 is the diffuse transmittance from the sun to the ocean. Note that this notation assumes that the ocean signal (R_{rs}) is sufficiently small so that it can be de-coupled from the atmosphere signal. Similar to modeling of R_{rs} using OSCs, the various reflectance and transmittance terms in Eq. 7.6 can be modeled as functions of the atmospheric surface pressure, aerosol optical thickness and type, water vapor, and wind speed through radiative transfer theory (Gordon 1997; IOCCG 2010, and references therein).

Thus, the satellite signal (ρ_t) is a function of Chl and other in-water OSCs as well as atmospheric properties through forward radiative transfer modeling, as depicted in Fig 7.2. The inverse process of deriving Chl from ρ_t through atmospheric correction and bio-optical algorithms is described in the next section.

7.3 Methods

For most open ocean waters, $R_{rs}(\lambda)$ contributes only a small portion (<10 %) to the total satellite signal, and thus estimation of the various reflectance and transmittance terms in Eq. 7.6 requires a sophisticated atmospheric correction scheme to derive $R_{rs}(\lambda)$ from $\rho_t(\lambda)$. The scheme was first detailed in works prepared for CZCS (Gordon and Morel 1983; Gordon 1994), and recently updated for modern sensors (Gordon and Wang 1994a; Gordon 1997; Ahmad et al. 2010; Bailey et al. 2010). A thorough review is given by IOCCG (2010).

7.3.1 Atmospheric Correction

The first step is to calibrate the sensor-received signal (usually a digitized voltage) radiometrically to obtain radiance (L_{t}) in mW cm^{-2} $\mu\mathrm{m}^{-1}$ sr^{-1}. This involves a series of corrections of the sensor's response to temperature, out-of-band stray light, polarization, temporal stability, and vicarious calibration (e.g., Franz et al. 2007). The calibration requires reliable measurements under optimal conditions which are currently provided by the Marine Optical Buoy (MOBY) (Clark et al.

1997) or the Bouée pour l'acquisition de Séries Optiques â Long Terme (BOUSOULLE) mooring (Antoine et al. 2008). Then from L_t, the calibrated total reflectance ($\rho_t = \pi L_t/(F_o \cos\theta_o)$) is calculated where F_o is the time-dependent solar irradiance and θ_o is the solar zenith angle. After adjustment for gaseous absorption, $\rho_t(\lambda)$ is used in Eq. 7.6 to derive $R_{rs}(\lambda)$ through atmospheric correction.

Whitecap (ρ_{wc}) and sun glint (ρ_g) contributions to ρ_t are first estimated using surface wind and solar/viewing geometry (Gordon and Wang 1994b; Frouin et al. 1996; Wang and Bailey 2001), and then removed from ρ_t. For a known solar/viewing geometry at a given location (satellite image pixel) and surface pressure (obtained from ancillary data), ρ_r is estimated accurately using an exact computation (Gordon 1993) and subtracted from ρ_t, resulting in

$$\rho_t'(\lambda) = \rho_{ar}(\lambda) + \pi t(\lambda) t_0(\lambda) R_{rs}(\lambda), \tag{7.7}$$

where $\rho_t'(\lambda)$ is $\rho_t(\lambda)$ after correction for whitecaps, sun glint, and Rayleigh scattering contributions.

The remaining step in the atmospheric correction, also the most challenging one, is to estimate and remove the effects of aerosols (represented by $\rho_{ar}(\lambda)$ as well as the transmittances). At certain wavelengths (λ_r) in the red and near IR, it can be assumed that R_{rs} is negligible (i.e., <1 digital count) due to strong water absorption (Fig. 7.1a) so that $\rho_t'(\lambda_r) = \rho_{ar}(\lambda_r)$. Because $\rho_{ar}(\lambda)$ is only a function of aerosol type and optical thickness, this dependence can be computed using radiative transfer simulations and stored in look-up tables. Then, a pair of satellite-derived $\rho_{ar}(\lambda_r)$ at two wavelengths is used to search the look-up tables to determine the corresponding aerosol type and thickness, and to determine the spectral ρ_{ar}, t, and t_0 for all wavelengths. $R_{rs}(\lambda)$ is then derived from $\rho_t'(\lambda)$ using Eq. 7.7. For most scenarios, simulation results have shown $R_{rs}(443)$ retrieval uncertainties to within $\pm$ 0.0006 sr^{-1} (Gordon and Wang 1994a; Gordon 1997), corresponding to about 5 % of the clear-water $R_{rs}(443)$.

For modern sensors, such as SeaWiFS, MODIS, and MERIS, the bands used for λ_r are in the NIR because for most ocean waters $R_{rs}(\lambda_r)$ is indeed negligible. However, for turbid coastal waters, this "dark pixel" assumption often fails due to significant amounts of scattering by particulate matter (either phytoplankton or non-algal particles). In these cases, several alternative approaches have been proposed (Arnone et al. 1998; Hu et al. 2000; Ruddick et al. 2000; Siegel et al. 2000; Chomko and Gordon 2001; Chomko et al. 2003; Stumpf et al. 2003a; Lavender et al. 2005; Bailey et al. 2010). More recently, λ_r were chosen at longer wavelengths in the shortwave IR (Wang 2007; Wang and Shi 2007), for example at 1240, 1640, or 2130 nm. Because of the significantly increased water absorption at those bands, $R_{rs}(\lambda_r)$ in the shortwave IR is negligible for nearly all turbid waters, so that the Gordon and Wang (1994a) "dark pixel" scheme can be extended.

7.3.2 Bio-Optical Inversion

Once $R_{rs}(\lambda)$ is derived from $\rho_t(\lambda)$ through atmospheric correction, the next step is to derive Chl from $R_{rs}(\lambda)$ through bio-optical inversion (Fig. 7.2). Two general approaches have been developed and applied to satellite data for the inversion: empirical regression and semi-analytical modeling.

The earliest empirical inversion used a blue/green band ratio (Clarke et al. 1970; Morel and Prieur 1977), that was later applied to CZCS data by Gordon and Clark (1980), Smith and Baker (1982), and others. The approach took the following form:

$$\text{Chl} = AR^B, \tag{7.8}$$

where A and B are regression coefficients (constants) and R is the ratio of reflectance or radiance at 443 or 520 to that at 550 nm. The rationale for using a blue/green band ratio to derive Chl was simple: as the green pigment, Chl, is increased, its strong absorption in the blue shifts the reflectance from blue toward green wavelengths. The CZCS algorithm switched from 443 to 520 as radiance in the 443 band diminished due to strong Chl absorption. The band at 550 nm was chosen because it is located in a stable spectral region minimally affected by Chl. Furthermore, by using a ratio of bands, extraneous effects (e.g. the G factor in Eq. 7.3) tend to cancel one another. This rationale has also been used for modern sensors, with an algorithm fitted to data from a large (n > 3,000) in situ dataset (Fig. 7.3). These algorithms use the following form (O'Reilly et al. 2000):

$$\begin{aligned} \text{Chl} &= 10^y \\ y &= a_0 + a_1 \cdot \chi + a_2 \cdot \chi^2 + a_3 \cdot \chi^3 + a_4 \cdot \chi^4 \\ \chi &= \log_{10}(MBR), \end{aligned} \tag{7.9}$$

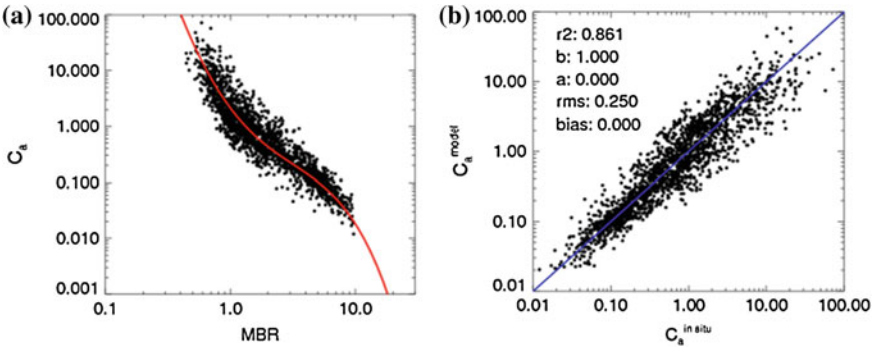

Fig 7.3 Empirical Chl algorithm for SeaWiFS (OC4V6). **a** Algorithm curve (*red line*, Eq. 7.9) fitted to in situ measurements of surface Chl versus the maximal band ratio (MBR), defined as $\max(R_{rs}(\lambda_b))/R_{rs}(555)$ for $\lambda_b = 443, 490, 510$ nm; **b** Algorithm-derived Chl versus measured Chl. Figure adapted from NASA Ocean Biology Processing Group after version 6 of algorithm coefficient tuning (http://oceancolor.gsfc.nasa.gov/REPROCESSING/R2009/ocv6/)

where a_0–a_4 are the empirical regression coefficients, and *MBR* is the maximum blue/green band ratio selected as follows:

$$MBR = \max[R_{rs}(443), R_{rs}(490), R_{rs}(510)]/R_{rs}(555) \text{ for SeaWiFS}$$
$$MBR = \max[R_{rs}(443), R_{rs}(488)]/R_{rs}(547) \text{ for MODIS}$$
$$MBR = \max[R_{rs}(443), R_{rs}(490), R_{rs}(510)]/R_{rs}(560) \text{ for MERIS}$$

The most recent SeaWiFS Chl algorithm (version 6) uses the regression coefficient values a_0–a_4 = 0.3272, −2.9940, 2.7218, −1.2259, −0.5683, respectively (http://oceancolor.gsfc.nasa.gov/REPROCESSING/R2009/ocv6/). Coefficients for MODIS and MERIS are different to adapt for the different band centers. These algorithms are currently used as the default Chl algorithms in the NASA data processing software package (SeaWiFS Data Processing System or SeaDAS), and they are often termed as OCxVy, where "x" stands for the number of bands and "y" is the algorithm version. Figure 7.3 shows the OC4V6 regression algorithm for SeaWiFS, and Fig. 7.4 illustrates the results after each step of SeaWiFS data processing as it generates the different data products, from ρ_t (4a), to R_{rs} (4b), to Chl (4c) using the OC4V6 algorithm, and the result of averaging Chl over 4 years between 1997 and 2001 (4d).

Several other forms of empirical inversion algorithms have also been proposed in the past. Campbell and Esaias (1983) proposed to use a curvature algorithm in the form of $S_j^2/(S_iS_k)$ to derive Chl, where S_j represents the measured signal in one band and S_i and S_k represent the signals from the two neighboring bands. Frouin (1997) combined the band ratios of 443/555 and 490/555 for the POLarization and Directionality of the Earth's Reflectances (POLDER) instrument (Mukai et al. 2000). Early efforts for algorithm development also proposed blue-green band-difference algorithms (Viollier et al. 1978; Viollier et al. 1980; Tassan 1981). More recently, a 3-band difference color index algorithm (CI) was proposed for clear waters (Chl ≤ 0.25 mg m^{-3}) in order to increase algorithm tolerance to atmospheric correction errors (Hu et al. 2012b). For SeaWiFS, the algorithm takes the form:

$$\mathrm{CI} = \mathrm{R_{rs}}(555) - [\mathrm{R_{rs}}(443) + (555 - 443)/(670 - 443) * (R_{rs}(670) - R_{rs}(443))]$$
$$\mathrm{Chl} = 10^{-0.4909+191.6590*\mathrm{CI}} \qquad [\mathrm{CI} \leq -0.0005] \tag{7.10}$$

The algorithm appears to have better performance over band-ratio algorithms in both accuracy and image quality for low Chl (≤0.25 mg m^{-3}) waters (Hu et al. 2012b), because the algorithm is nearly immune to the spectrally related atmospheric correction errors that are amplified when extrapolated to blue wavelengths. For intermediate Chl waters (between 0.25 and 0.3), a blending scheme was used to transition to the standard band-ratio algorithm when Chl is >0.3 mg m^{-3}.

A recent round-robin effort compared the performance of several Chl algorithms and many other IOP inversion algorithms (Brewin et al. 2013), where the pros and

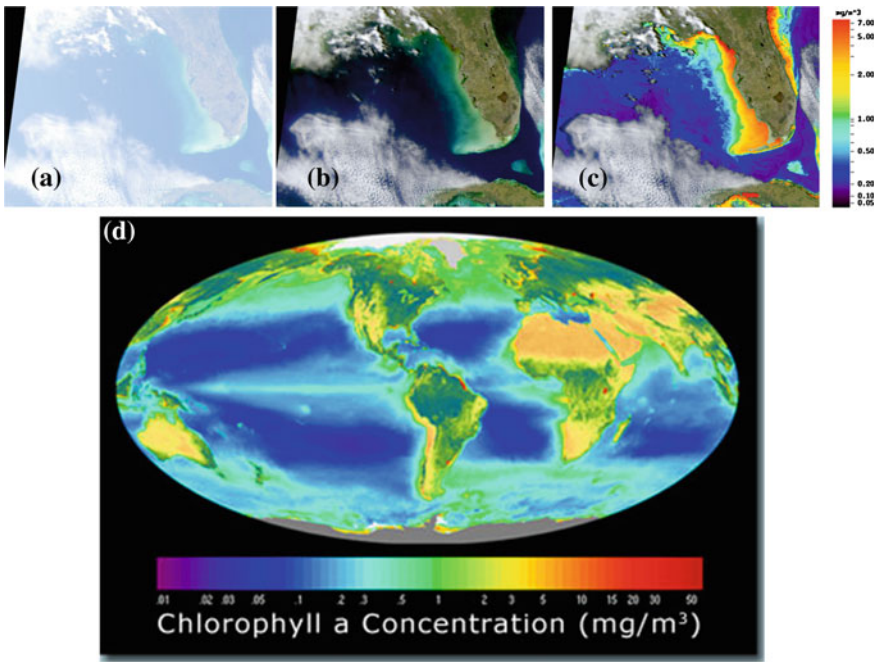

Fig. 7.4 Illustration of the general steps in deriving the surface ocean Chl from SeaWiFS measurements over the eastern Gulf of Mexico. **a** Composite image using $\rho_t(670)$ (*red*), $\rho_t(555)$ (*green*), and $\rho_t(443)$ (*blue*). Most of the signal over the ocean comes from the atmosphere. **b** RGB composite using $R_{rs}(670)$, $R_{rs}(555)$, and $R_{rs}(443)$ after atmospheric correction. **c** Chl image derived from $R_{rs}(\lambda)$ using the OC4V6 empirical band-ratio algorithm (Eq. 7.9). **d** Average Chl from SeaWiFS measurements between 1997 and 2001 over the global ocean, together with normalized difference vegetation index (NDVI) over land (image courtesy of NASA Goddard Space Flight Center)

cons of the algorithms have been discussed. The pros and cons of empirical band-ratio Chl algorithms have also been discussed in Dierssen (2010). The algorithms are based on the assumption that optical properties are dominated by phytoplankton and their degradation products (i.e., Case I waters). The impact of other OSCs is implicitly included in the algorithm coefficients. For global applications, the algorithm coefficients are tuned to minimize uncertainty from the global datasets. However, different ocean regions are known to have different OSC compositions (i.e., relative contributions of CDOM and detrital particles to total a and b_b), and the same amount of Chl can result in different a_{ph} depending on community composition. Szeto et al. (2011) found systematic biases in the global algorithms among the major oceans, and concluded that these are related to differences in the relative proportion of the OSCs and their optical properties. Likewise, Sauer et al. (2012) reported on the influence of varying IOPs on the empirical algorithm. To improve algorithm performance, the coefficients may be tuned for regional applications (e.g., Kahru and Mitchell 1999; McKee et al. 2007a; Mitchell and Kahru 2009).

Similarly, other empirical approaches, such as neural networks (e.g., Schiller and Doerffer 1999; Dzwonkowski and Yan 2005; Schroeder et al. 2007) that require algorithm tuning often use regional data, and are thus applicable to regions with similar optical properties. On the other hand, empirical algorithms are relatively easy to implement, and the resulting satellite images have smooth transitions between different regions when the same algorithm coefficients are used. More importantly, some of the residual errors from atmospheric correction, often spectrally related, are partially removed in the band-ratio OCx algorithms and nearly completely removed in the band-subtraction CI algorithm.

Empirical algorithms do not separate Chl from other OSCs, but treat all OSCs as a whole. In contrast, semi-analytical algorithms derive all OSCs (including Chl) simultaneously, or derive a_{ph} first and then use a pre-defined Chl-a_{ph} relationship to derive Chl (e.g., Sathyendranath et al. 1989; Roesler and Perry 1995; Hoge and Lyon 1996; Carder et al. 1991, 1999; Lee et al. 1999, 2002; Maritorena et al. 2002). In these approaches, the absorption spectral shapes of CDOM, detritus, and phytoplankton pigments are often derived from global datasets and assumed time- and space-independent. Therefore, in waters (especially coastal waters) where these absorption shapes differ significantly from the global mean, algorithm retuning is required. Because the emphasis of this chapter is on empirical algorithms, interested readers are referred to the published literature to get more in-depth knowledge on semi-analytical algorithms.

Coastal waters, especially river plumes and estuaries, often have a significant amount of CDOM from terrestrial discharge that dominates the light absorption in the blue, resulting in a poor relationship between blue/green band ratios and Chl (e.g., Odriozola et al. 2007). Figure 7.5a shows an example of the poor performance of blue/green band ratio algorithms (OC3 and OC4) in deriving Chl for a moderately turbid estuary, Tampa Bay (Le et al. 2013). Under these circumstances, spectral bands in the red and NIR, which are less affected by CDOM than in the blue, can be used to avoid this problem. MODIS and MERIS are equipped with bands specifically designed to quantify solar-stimulated phytoplankton fluorescence in the red, and band-subtraction algorithms have been developed to derive fluorescence line height (FLH, Letilier et al. 1996) and maximum chlorophyll index (MCI, Gower et al. 2005) as proxies for Chl. Application of the MODIS FLH over the global open ocean, after adjustments for non-photochemical quenching and phytoplankton packaging effects, showed excellent agreement with the band-ratio-derived Chl for a large dynamic range (Behrenfeld et al. 2009). Application in SW Florida coastal waters also showed tight correlation with in situ Chl in CDOM-rich waters (Hu et al. 2005). Moreover, radiative transfer simulations showed that FLH is insensitive to CDOM changes, such that a 10-fold increase in CDOM only resulted in a 50 % decrease in FLH (McKee et al. 2007b). However, for sediment-rich waters, FLH is positively biased due to the unequal contribution of the sediments to the reflectance in the FLH bands (Gilerson et al. 2007), resulting in a poor relationship between FLH and Chl.

Other forms of empirical algorithms using various band combinations in the red and NIR have been proposed to avoid the CDOM contamination problems and to

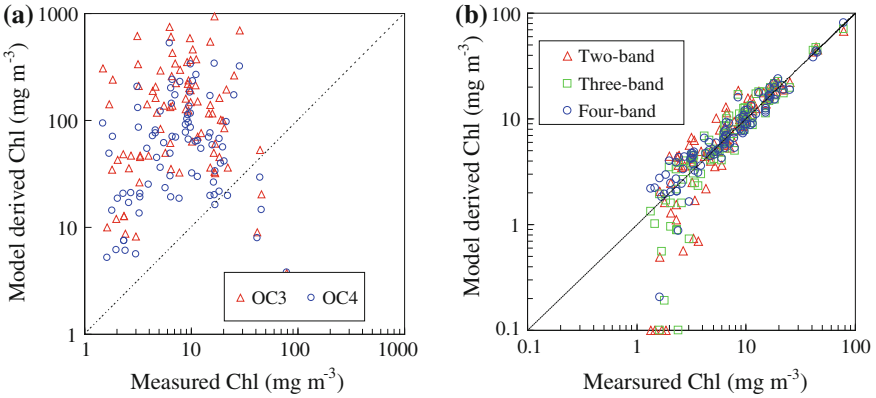

Fig. 7.5 **a** Chl derived from the OC3 and OC4 *blue-green* R_{rs} ratio algorithms shows poor correlation with measured Chl in Tampa Bay, Florida; **b** In contrast, algorithms using R_{rs} in the *red* and NIR show much improved performance for Chl > 2 mg m^{-3}. Figure adapted from Le et al. (2013). Reprinted from Remote Sensing of Environment, 129, C. Le, C. Hu, J. Cannizzaro, D. English, F. Muller-Karger, and Z. Lee, Evaluation of chlorophyll-a remote sensing algorithms for an optically complex estuary, 75–89, Copyright (2013), with permission from Elsevier

account for sediment resuspension. Among these are the 2-band ratio algorithms (Ruddick et al. 2001; Jiao et al. 2006; Dall'Olmo et al. 2005; Gitelson et al. 2008; Pierson and Sträombäack 2000; Thiemann and Kaufman, 2000), 3-band algorithms (Dall'Olmo et al. 2005; Gitelson et al. 2008), and 4-band algorithms (Tassan and Ferrari 2003; Tzortziou et al. 2006; Le et al. 2009). Applications of these algorithms often require regional tuning of the algorithm coefficients to account for the specific optical variability in coastal waters. Figure 7.5b shows that after algorithm tuning, all 2-, 3-, and 4-band algorithms performed reasonably well for Chl > 2 mg m^{-3} in Tampa Bay (Le et al. 2013). Alternatively, all spectral bands may be used in a neural-network approach (Keiner and Brown 1999) or empirical orthogonal function (EOF) analysis (Craig et al. 2012) in order to derive empirical Chl using locally tuned algorithm coefficients.

The globally tuned OCx algorithms have been implemented in various satellite data processing software such as SeaDAS (http://seadas.gsfc.nasa.gov/) and BEAM (http://envisat.esa.int/beam). SeaDAS was originally developed by NASA to process SeaWiFS data, but it has evolved over the past decade to process CZCS, MODIS, MERIS, and OCTS. Sensor calibration, atmospheric correction, and bio-optical inversion have all been updated periodically to incorporate the most recent research results. Likewise, the BEAM software was originally developed to facilitate the use of ENVISAT data, but now can be used to analyze data from several other satellite sensors including MODIS. Briefly, to derive the Chl data products, one would start from Level-0 or Level-1A data (un-calibrated digital counts) and process to Level-1B (calibrated radiance). Then, vicarious calibration and atmospheric correction are applied to process from Level-1B to Level-2, where spectral $R_{rs}(\lambda)$ are derived and fed into bio-optical algorithms to derive Chl.

Currently the default algorithms used by SeaDAS are the OC4 (SeaWiFS) and OC3 (MODIS) band-ratio algorithms (O'Reilly et al. 2000; Eq. 7.9 for version 6) while the Carder et al. (1999) and Maritorena et al. (2002) semi-analytical algorithms as well as the most recent CI algorithm (Hu et al. 2012b) are options within the software. Based on the Level-2 $R_{rs}(\lambda)$ data one can also implement regional empirical or semi-analytical algorithms. Finally, the Level-2 Chl data products are map-projected or binned to produce geo-referenced Chl data products at regional or global scales. Figure 7.4a–c show examples of map-projected products for the eastern Gulf of Mexico, while Fig. 7.4d shows an example of the globally map-projected Chl product (after binning) from SeaWiFS multi-year measurements. All data products are stored in HDF or NetCDF computer files. Most of these data products can be obtained from the U.S. NASA Goddard Space Flight Center (http://oceancolor.gsfc.nasa.gov). Likewise, MERIS data products can be obtained from the European Space Agency.

7.4 Validation Efforts Using in Situ Measurements

As with algorithm development, in situ Chl must be determined and quality controlled in order to validate the algorithm performance. Starting in 1997, the Sensor Intercomparison and Merger for Biological and Interdisciplinary Oceanic Studies (SIMBIOS, Fargion et al. 2004) program initiated by NASA has funded numerous researchers to collect bio-optical data in the global oceans, most of which have been archived in the SeaWiFS Bio-optical Archive and Storage System (SeaBASS, http://seabass.gsfc.nasa.gov, Hooker et al. 1994) and are available for both algorithm development and validation. Also available is a subset of SeaBASS, the NOMAD dataset (Werdell and Bailey 2005), that was specifically compiled for bio-optical algorithm development, as it contains coincident measurements of Chl, $R_{rs}(\lambda)$, and other data collected simultaneously in the global oceans. In addition to data available in SeaBASS, researchers working on individual projects have collected regional bio-optical data, which can also be used for algorithm development and validation.

Most of the Chl data collected from field and laboratory measurements and available in SeaBASS were determined using fluorometric methods. Other Chl data have been determined via HPLC (Hooker and Heukelem 2011), most of which show excellent agreement with fluorometric Chl (Fig. 7.6 of Werdell and Bailey 2005). However, for low concentrations Chl determined from fluorometric methods sometimes suffers from contaminations by chlorophyll *b* and chlorophyll *c* (Marrari et al. 2006; Dierssen 2010). Nevertheless, because of its wide availability, fluorometric Chl is often used to validate the satellite observations of Chl.

Chl data products derived from the various ocean color sensors have been evaluated and validated extensively by the research community. To perform the evaluation, caution must be taken to address the inherent difference in both time and space between satellite and in situ measurements. Spatial and temporal

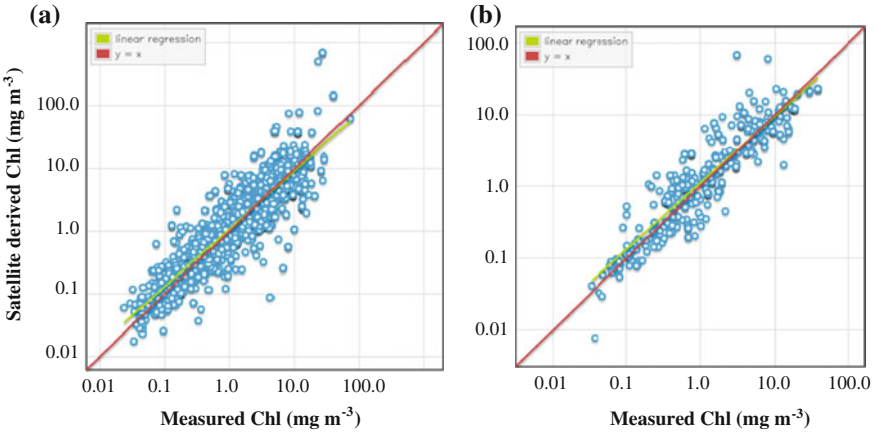

Fig. 7.6 Global Chl validation results using data from the SeaBASS data archive and online query (http://seabass.gsfc.nasa.gov/seabasscgi/validation_search.cgi). **a** SeaWiFS (1997–2010); **b** MODIS/Aqua (MODISA, 2002–2011). The default validation criteria have been applied (Werdell et al. 2005). Validation statistics are listed in Table 7.2

constraints are required to obtain a satellite-in situ "matching" pair. For example, a common practice is to restrict the time difference to ±3 h and the 3 × 3 pixel coefficient of variation <0.15 (Bailey et al. 2000). The latter constraint is to ensure that the ocean is relatively homogeneous so a satellite pixel (usually ~1 km^2) can be represented by a point measurement in the field. Further, to avoid cloud-edge pixels and other such problems, additional constraints such as wind speed, solar zenith angle, and satellite viewing angle are also used to find the matching pairs. Lastly, because $R_{rs}(\lambda)$ is a weighted measure of OSCs within the upper optical depth with the weighting factor decreasing exponentially with increasing depth (Zaneveld 1982; Gordon 1992), Chl collected at multiple depths, whenever available, should be used to calculate a depth-weighted Chl in order to validate the satellite observations (e.g., Cannizzaro et al. 2013).

Global validation efforts of the SeaWiFS Chl data product showed that for most open ocean waters, the algorithm performed well, with RMS differences between SeaWiFS and in situ Chl (after logarithmic transformation) of 0.2–0.3 without significant bias (Gregg and Casey 2004; McClain et al. 2004; Bailey and Werdel 2006). This translates to about 50–60 % RMS relative difference. Global validation of the semi-analytical Chl (Maritorena et al. 2002, 2010) using merged data from SeaWiFS, MODISA, and MERIS showed slightly worse performance for Chl between 0.02 and 10.0 mg^{-3}, possibly due to residual inconsistencies between sensors.

Online validation tools have been provided by NASA through the SeaBASS online query (http://seabass.gsfc.nasa.gov/seabasscgi/validation_search.cgi) and by ESA through the MERis Matchup In-situ Database (MERMAID, http://hermes.acri.fr/mermaid/matchup/matchup.php), where the area of interest, temporal window, and validation criteria can all be specified. Figure 7.6 and Table 7.2

Table 7.2 Global validation results of SeaWiFS (1997–2010) and MODISA (2002–2011) determined from the NASA SeaBASS archive

Sensor	N	Slope	Intercept	R^2	Median ratio	Abs % Diff	RMSE
SeaWiFS	2009	0.9213	0.03539	0.82	1.03	35.1	0.29
MODISA	527	0.9269	0.0501	0.84	1.03	33.2	0.26

Median ratio and percentage difference were derived from the original data, while other statistical measures were derived from log-transformed Chl (Fig. 7.6), because Chl distributions in nature tend to be log normal (Campbell 1995)

show the SeaWiFS and MODIS/Aqua validation results obtained from SeaBASS data collected prior to April 2012. In general, satellite-based Chl agrees well with in situ measurements, with $R^2 > 0.82$ and median ratio between satellite and in situ Chl approaching 1.0 for >2 orders of magnitude. However, there is substantial data scatter for each Chl range, and the results varied among different ocean basins because the same algorithm coefficients, determined from the global dataset optimization, were applied universally while the proportions of CDOM absorption and particulate backscattering (relative to Chl) may vary substantially in different ocean basins (Gregg and Casey 2004; Dierssen et al. 2010; Szeto et al. 2011; Sauer et al. 2012). The variable performance of the global algorithm, when applied to local waters, has been demonstrated in several regional studies (Stumpf et al. 2000; D'Ortenzio et al. 2002; D'Sa et al. 2003; Hu et al. 2003; Melin et al. 2003; Darecki and Stramski 2004; Zhang et al. 2006; Antoine et al. 2008; Zibordi et al. 2006, 2009; Hyde et al. 2007; Werdell et al. 2009), where algorithm tuning may be required to account for different water types (e.g., Kahru and Mitchell 1999; McKee et al. 2007a; Mitchell and Kahru, 2009).

An example of algorithm performance for a local region, namely the west Florida Shelf (WFS), is presented in Fig 7.7. Details of the methodology can be found in Cannizzaro et al. (2013). For this shallow shelf, SeaWiFS Chl, based on the OC4V6 algorithm, is very accurate (RMS difference $\sim$0.1 in log-transformed Chl, equivalent to 25.9 %) for <0.5 mg m^{-3}. For higher concentrations, SeaWiFS Chl is biased high due to three effects: bottom reflectance (e.g., Cannizzaro and Carder 2006), CDOM contamination (Hu et al. 2005), and suspended sediments (Wynne et al. 2006). If all data are included for the range of 0.1 to 10 mg m^{-3} (N = 289), RMS difference is 0.274 in log-transformed Chl, equivalent to 87.9 %, comparable to those found for global oceans (Gregg and Casey 2004). However, algorithm performance in estuarine waters is generally worse because of significant contributions of OSCs other than phytoplankton (e.g., Fig. 7.5a). Algorithms avoiding the blue wavelengths show better performance than blue-green band ratio algorithms (e.g., Fig. 7.5b), thus may be preferred for estuaries.

In short, the operational Chl product may be regarded as valid or at least temporally consistent for most global ocean open waters. This is especially true for waters where optical properties are either dominated by phytoplankton or co-varying among the OSCs (the Case I water scenario). Consequently, the standard Chl product can be used to address the global or regional ocean changes as a whole. Known problems remain in coastal waters due to the optical complexity of

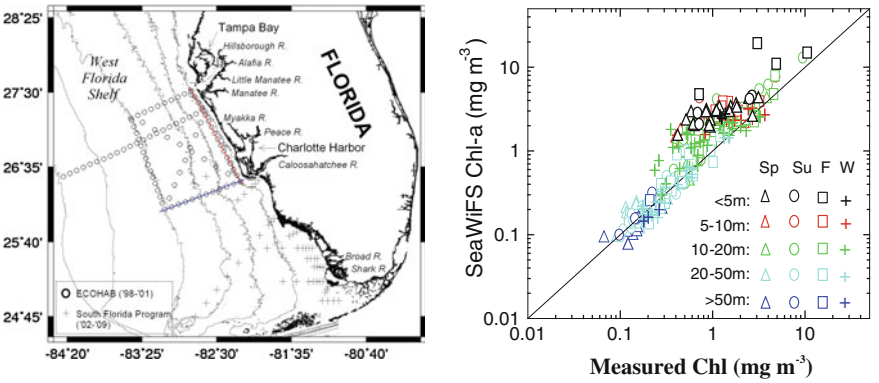

Fig. 7.7 Comparison between near-concurrent (±3 h) SeaWiFS and in situ Chl for the west Florida Shelf (1998–2009). SeaWiFS Chl was derived from the OC4V6 algorithm. In situ Chl were collected from rigorously quality controlled bio-optical measurements. **a** Cruise stations; **b** Data were partitioned into four seasons (Spring–March 21 to June 20; Summer–June 21 to September 22; Fall–September 23 to December 20; Winter–December 21 to March 20) and color coded for different *bottom* depths. Figure adapted from Cannizzaro et al. (2013). Reprinted from the Journal of Coastal Research, Cannizzaro, J. P., C. Hu, K. L. Carder, C. R. Kelble, N. Melo, E. M. Johns, G. A. Vargo, and C. A. Heil, On the accuracy of SeaWiFS ocean color data products on the West Florida Shelf, Copyright (2013), with permission from The Coastal Education and Research Foundation, Inc

various OSCs typically found in coastal regions. For these waters, algorithm tuning using local data or alternative algorithms may need to be developed to address specific needs.

7.5 Major Findings

The validated Chl data products over the global ocean from the late 1990s to the 2010s led to numerous research findings on ocean changes over various temporal and spatial scales. Such findings would have been impossible with traditional field sampling efforts due to insufficient spatial and temporal coverage. Several review articles (Yoder and Kennelly 2006; McClain et al. 2009), special volumes of journals (Siegel et al. 2004a, b), and technical reports published by the International Ocean Colour Coordinating Group (IOCCG 2008, 2009) have provided excellent summaries and references for major findings using satellite-based Chl data products. Some of these findings as well as those from more recent studies are briefly introduced here.

A major topic in Earth Science is the ocean's response to climate variability, where satellite ocean color observations play a key role in documenting ocean changes at both global and regional scales. One example is the ocean's response to the El Niño–Southern Oscillation (ENSO) between 1997 and 2000. Behrenfeld

et al. (2001) used SeaWiFS data to show significant differences in the monthly mean Chl over the global ocean between the El Niño and the subsequent La Niña year due to altered ocean nutrient distributions. Low Chl levels during the El Niño were followed by a 10 % increase between September 1997 and December 1998. Moreover, such changes were not restricted to the equatorial Pacific but rather spread in the global ocean. During the subsequent La Niña period of January 1999–August 2000, global mean Chl continued to increase but at a slower annual rate of 2.2 %, and such increases primarily occurred in the Pacific Ocean.

The global ocean Chl response to ENSO was further detailed in Yoder and Kennelly (2003), and the biological response to the 1997–1998 El Niño in the equatorial Pacific Ocean was studied with SeaWiFS Chl (Chavez et al. 1999). The surface ocean showed the lowest Chl biomass in 1997, followed by a dramatic increase in mid-1998 corresponding to the recovery from El Niño. The spatial extent of the phytoplankton bloom reached a record high for the equatorial Pacific. Such responses to El Niño were linked to changes in the upwelling of nutrient-enriched waters, and coincided with sea-surface height anomalies observed by the U.S.–French TOPEX/Poseidon satellite (NRC 2008, Fig. 7.8).

More recent satellite observations have extended the above results (Fig. 7.9), where the inter-annual changes in the global mean Chl are highly correlated with the Multivariate ENSO Index (MEI). The global mean Chl showed clear seasonality, with minima occurring between November and March and maxima occurring between May and September. This is because phytoplankton blooms during summer in the Northern Hemisphere exceeded those in the Southern Hemisphere summer. Inter-annual changes at magnitudes similar to the 1997–2000 ENSO also occurred, for example, between 2001–2003 and 2004–2006, for the same reasons of altered nutrient distributions. In longer terms, decadal oscillations in phytoplankton biomass of major ocean basins, derived from combined CZCS and

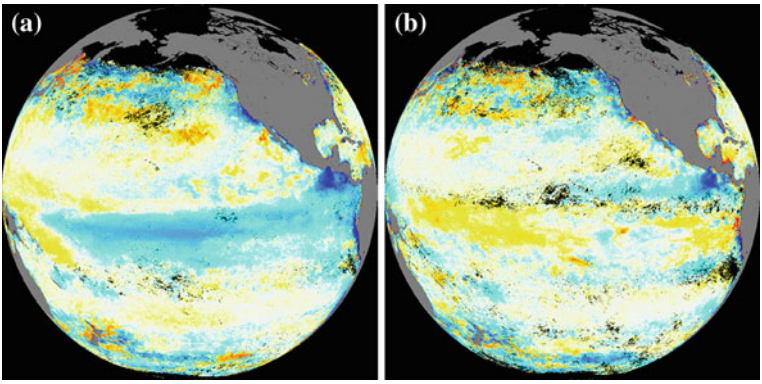

Fig. 7.8 Chl anomaly in the Equatorial Pacific derived from SeaWiFS. **a** El Niño year (1997) **b** La Niña year (1998). *Blue* shades indicate lower than normal Chl while *yellow* shades indicate higher than normal Chl. Figure reprinted with permission from NRC (2008) by the National Academy of Sciences, Courtesy of the National Academies Press, Washington, D.C

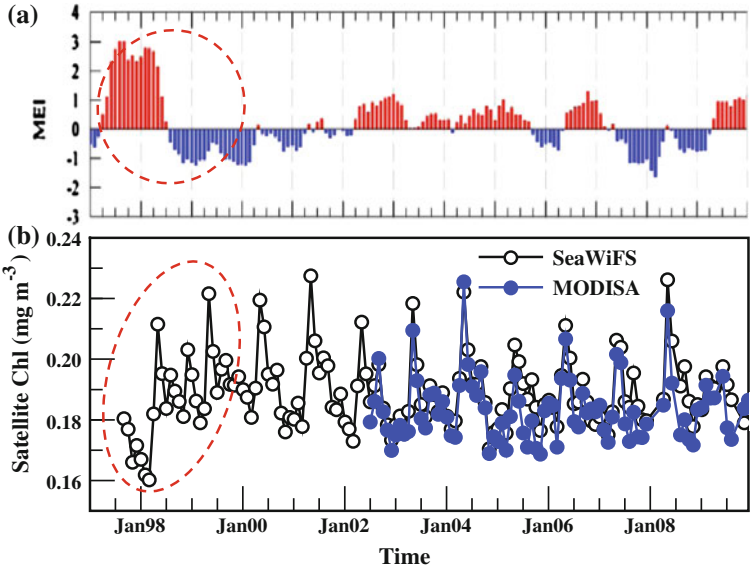

Fig. 7.9 **a** Multivariate ENSO Index (MEI) between 1997 and 2009 obtained from NOAA (www.esrl.noaa.gov/psd/enso/mei/mei.html), with red for EI Niño phase and blue for La Niña phase; **b** Monthly mean Chl derived from SeaWiFS and MODISA over the global open ocean (bottom depth >200 m) using the most recent calibration and algorithm updates in SeaDAS6.2 (reprocessing 2010.10). Note the significant increase between late 1997 and 1999 during the transition from EI Niño to La Niña (Behrenfeld et al. 2001)

SeaWiFS data, were found to be highly correlated with large-scale and long-term climate variability (Martinez et al. 2009). Similarly, the correlations between Chl and climate fluctuations have been reported by Behrenfeld et al. (2008) through paired Chl and sea surface temperature (SST) observations.

Other physical variables such as wind and sea surface height have also been used to study the global biological variability in the context of physical dynamics (Wilson and Adamec 2002; Doney et al. 2003; Uz and Yoder 2004; Wilson and Coles 2005). In particular, several studies documented the Rossby wave signatures in the global Chl patterns (Cipollini et al. 2001; Uz et al. 2001; Charria et al. 2003; Dandonneau et al. 2003; Killworth et al. 2004), although there has been some debate on the exact mechanism leading to such patterns, either through upwelling-induced biomass enhancement or wave-induced surface accumulation (Dandonneau et al. 2004; Killworth 2004). In a broader context, physical mechanisms shaping Chl patterns associated with meso-scale eddies (both cyclonic and anti-cyclonic) have been addressed using satellite and other observations (Brown et al. 1985; McGillicuddy et al. 2001, 2007). Increased Chl is found in cyclonic eddies, a result of uplifts of the isopycnals and the nutricline. Further, McGillicuddy et al. (2007) demonstrated that interactions between wind and eddies can retard upwelling in cyclonic eddies.

Chl is only a measure of phytoplankton biomass. When combined with other ocean variables such as chlorophyll fluorescence, CDOM, and particulate matter distributions, wind, temperature, photosynthetic available radiation, nutrients, and mixed layer depth, details can be revealed on ocean primary productivity (e.g., Behrenfeld et al. 2001, 2006), phytoplankton physiology (Behrenfeld et al. 2005, 2009), inter-relationship between various OSCs (Siegel et al. 2005; Loisel et al. 2002; Hu et al. 2006), and regional processes that lead to phytoplankton blooms (e.g., the Sverdrup's critical depth hypothesis, Siegel et al. 2002).

Satellite Chl has also been used in studies of basin-scale or regional ocean changes. For example, using multi-year SeaWiFS Chl data, Polovina et al. (2008) showed that several major ocean gyres (defined by SeaWiFS Chl $\leq$ 0.07 mg m^{-3}) had expanded from 1998 to 2006, and gyre variability was revisited by Signorini et al. (2011). Arrigo et al. (2008) found significant impacts of shrinking Arctic ice cover on local primary productivity. Hamme et al. (2010) and Lin et al. (2011) showed how volcanic ashes fuel the Gulf of Alaska and the oligotrophic Pacific Ocean, respectively, and stimulate phytoplankton blooms. Likewise, numerous studies have shown enhanced Chl biomass after tropical cyclones due to either deeper ocean mixing or upwelling (e.g., Lin et al. 2003; Babin et al. 2004; Walker et al. 2005; Siswanto et al. 2007). On continental shelves where terrestrial runoff plays a significant role in modulating the ocean's nutrient budget and biogeochemistry, Chl tends to follow local precipitation and river runoff closely. The riverine influence of the Amazon River and Mississippi/Atchafalaya Rivers on the downstream oceans has been well documented by several studies (e.g., Salisbury et al. 2004, 2011). Figure 7.10 shows such an example, where SeaWiFS Chl in a coastal region immediately downstream of a local river appeared to be driven by river discharge. Similarly, coastal blooms off California were found to be related to agricultural irrigation (Beman et al. 2005).

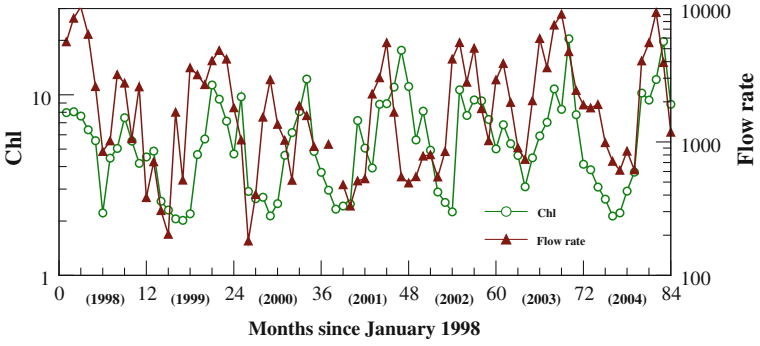

Fig. 7.10 SeaWiFS monthly mean Chl (mg m^{-3}) for a shallow area (depth <10 m) south of Charlotte Harbor over the West Florida Shelf (Fig. 7.7a). Also plotted is the mean monthly river flow rate (ft^3 s^{-1}) of a local river discharging into Charlotte Harbor between 1998 and 2004. The two datasets showed a correlation coefficient of 0.45, which increased to 0.56 when the river flow data were shifted 1 month forward (corresponding to a 1 month lag in a biological response to the discharge)

In addition to scientific research on global or regional biogeochemistry, satellite Chl has been used widely for a variety of applications, from fishery and other resource assessment to management decision support. For example, Polovina et al. (2001) used SeaWiFS Chl in the North Pacific to define a critical habitat for fish and turtles in the transition frontal zone at the boundary between the low Chl subtropical gyres and high Chl subarctic gyres. Platt et al. (2003) found that the timing of the spring algal bloom in the North Atlantic, as gauged by SeaWiFS Chl, was closely related to larval fish survival. Soto et al. (2009) applied a 9 year SeaWiFS Chl time series to establish a connectivity matrix for the Meso-American Barrier Reef System. Kahru and Mitchell (2008) used global time-series data and found statistically significant increasing trend in the annual maximal Chl in several coastal regions between 1997 and 2007. Schaeffer et al. (2012) applied multi-year SeaWiFS and MODIS/A Chl data over pre-defined coastal zones off Florida to help monitor coastal bloom conditions in order to implement nutrient management plans. Stumpf et al. (2003b) used Chl anomaly imagery to delineate potential harmful algal blooms of *Karenia brevis* off Florida, where large uncertainties in satellite Chl due to shallow bottom, CDOM, and suspended sediments are partially compensated by the anomaly subtraction.

Due to the space limit, the scientific findings and applications enabled by satellite Chl have only been mentioned briefly with the selected examples. Indeed, a recent query of Web of Science using the keyword "ocean color" showed a continuously increasing number of publications every year since the 1990s. The review articles by Yoder and Kennelly (2006) and by McClain (2009) provide excellent references for ocean color research. More recently, IOCCG published two technical reports summarizing a variety of research and application topics using remotely sensed Chl. These include a dedicated monograph on societal benefits of using ocean color data (IOCCG 2008), and a volume focused on marine fisheries, ecosystem and resource management (IOCCG 2009). With more ocean color missions currently being planned and with the recommendations by the U.S. National Research Council (2004) that Chl be considered a key environmental and climate data record, one can foresee that the use of remotely sensed Chl to address Earth Science questions will continue to increase in the future.

7.6 Future Research Directions

The biological and ecological response of the ocean to climate variability can only been addressed through long-term and consistent ocean color observations, where Chl plays a key role in assessing the standing stocks of algal biomass as well as primary productivity and other biogeochemical and ecological processes. The potential uses of validated satellite Chl data products have been well demonstrated in the above examples and in the published literature. However, most satellite missions have a 5 years designed mission life. Even though the majority of them have functioned well beyond this planned duration (e.g., SeaWiFS lasted

for >13 years, MERIS for 10 years, and MODISA for >10 years), data quality may not be as robust during the extended mission as in the early years. Of these sensors, only MODIS (both Terra and Aqua) is operational, with data quality showing some degradation. Thus, it is critical to plan continuity missions for the future to establish seamless time-series observations.

NASA, ESA, and several other international agencies have been actively planning for future ocean color missions, among which are two identical Sentinel-3 ESA satellites as part of the Global Monitoring for Environment and Security (GMES) programme and three NASA missions recommended by the Decadal Survey for Earth Science (NRC 2007). The OLCI (Ocean Land Colour Imager) instrument on board Sentinel-3, to be launched in late 2014, will serve as a continuity mission of MERIS with enhanced performance in spectral resolution and revisit frequency. The three recommended NASA missions are: (1) Aerosol-Clouds-Ecosystems (ACE); (2) Geostationary Coastal and Air Pollution Events (GEO-CAPE, Fishman et al. 2012); and (3) Hyperspectral Infrared Imager (HyspIRI). Each of these NASA missions has ocean color capability and a unique set of science goals (NRC 2007). In particular, the hyperspectral sensors on these missions will enable improved Chl retrievals in coastal waters (e.g., Hoogenboom et al. 1998; Brando and Dekker 2003). Currently, the missions are under development, with launch dates tentatively scheduled for 2020 and beyond. Under the auspices of the climate initiative, NASA is also planning a Pre-ACE (PACE) mission for a 2019 launch (NASA 2010). These ocean color continuity missions require continued efforts in calibration and algorithm development to ensure cross-sensor consistency. Such a consistency is extremely critical when studying decadal-scale ocean changes, as demonstrated by two independent studies using CZCS and SeaWiFS to study Chl changes between the 1970–1980s and 1990–2000s (Antoine et al. 2005; Gregg et al. 2005). More recently, multi-decadal oscillations of phytoplankton abundance in the global ocean from the two ocean color missions were found to be driven by climate variability (Martinez et al. 2009), even after allowing for different calibrations and algorithms used for the two sensors. SeaWiFS and MODIS/A operated simultaneously for a period of years (2002–2010), and though both were managed by NASA, there are discrepancies between the Chl records. Recently, the CI algorithm has been shown to yield more consistent Chl data records for the open ocean (Fig. 7.11, Hu et al. 2012b), where discrepancy between SeaWiFS and MODIS/A Chl records was reduced by at least 50 % for most of the time period for global clear waters. Such an improvement is expected to lead to reduced uncertainties in the globally merged data products from multiple sensors (e.g., Maritorena et al. 2010).

While all sensor characterization and calibration procedures as well as algorithm development are mature for the open ocean, future emphasis will be on Chl algorithm improvement for coastal waters. The effects of shallow bottom, CDOM, and suspended sediments must be resolved either implicitly through empirical regression or explicitly through semi-analytical inversion. Currently, there are several approaches to use the red-NIR wavelengths to avoid the effect of CDOM, and a preliminary approach to remove sediment effects empirically (Wynne et al.

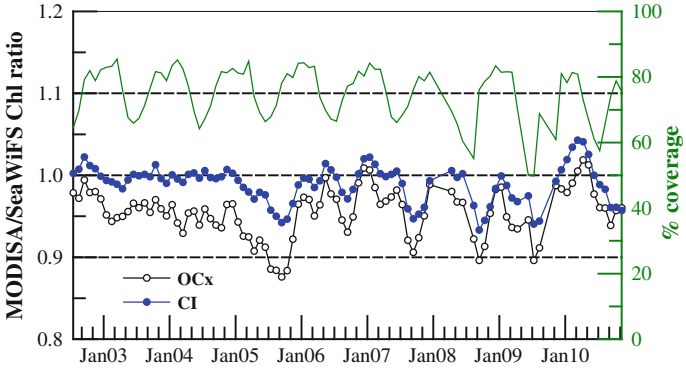

Fig. 7.11 MODISA/SeaWiFS Chl ratio for the global open ocean (Chl $\leq$ 0.25 mg m^{-3}). Empty circles are from the operational (OCx) band-ratio algorithms, and filled circles are from the CI band-subtraction algorithm (Hu et al. 2012b). Also shown is the percentage coverage of the monthly measurements, referenced against a SeaWiFS mission climatology. Note that the statistics were pulled from identical pixels between sensors and between algorithms

2006). These approaches need refinement with more field data to account for the optical variability of all OSCs, and they also need regional tuning for the different mixtures of OSCs found in coastal waters. In particular, there has been the lack of a general approach to remove the bottom signal in optically shallow waters (Cannizzaro and Carder 2006), and, in particular, this problem needs to be addressed around coral reefs.

One difficulty in the past has been the lack of reliable in situ Chl data with sufficient spatial and temporal coverage to validate satellite Chl under all possible circumstances. Despite more than a decade of SIMBIOS effort, most ocean waters are still under-sampled. This lack of data inherently hinders any effort for algorithm coefficient tuning of both empirical and semi-analytical algorithms. Systematic measurements of Chl using autonomous platforms such as gliders, drifters, or marine buoys, may help overcome this difficulty and eventually lead to improved algorithms and better data products.

The benefits of ocean color measurements extend beyond Chl. Recent efforts have used multi-band R_{rs} or optical models to classify major phytoplankton functional types (PFTs) in the global ocean (Subramaniam et al. 1999; Alvain et al. 2005; Westberry and Siegel 2006; Nair et al. 2008; Mouw and Yoder 2010). This is possible, in theory at least, because different PFTs have different pigment composition, resulting in distinguishable pigment absorption and R_{rs} spectral shapes. On regional scales, Sathyendranath et al. (2004) developed an optical inversion model to separate diatom blooms from other blooms in the North Atlantic. Cannizzaro et al. (2008) used backscattering/Chl ratios (or backscattering efficiency) and Tomlinson et al. (2009) used R_{rs} spectral curvatures in the blue-green to distinguish *K. brevis* blooms from other blooms on the West Florida Shelf. Further efforts are required to characterize the optical properties (absorption

and scattering) of various PFTs, accompanied with HPLC pigment analysis or microscopic taxonomy, so that PFTs can be better estimated from satellite imagery not only in the open ocean, but also in coastal waters.

At the time of this writing, VIIRS has been in orbit since late 2011, and preliminary data products are available online to the science community. Once validated, the VIIRS Chl data product is expected to continue the SeaWiFS/MODISA/MERIS observations of the global ocean and extend the legacy of these missions to further strengthen our understanding of ocean carbon cycles, the ocean response to climate variability and anthropogenic influence, and to help establish a multi-decadal Chl Climate Data Record to address both science and management needs.

Acknowledgments This review chapter reflects the collective community effort on all aspects of ocean color research from sensor development, calibration, in situ measurement, algorithm development, data archiving and sharing, to scientific research and applications. The authors are particularly grateful to NASA for both financial and data support. Due to space limitations, the authors could only briefly present some examples from a wealth of literature while many other studies that were not covered here can be accessed through the cited references. We are indebted to an anonymous reviewer who provided very detailed comments and suggestions on this manuscript.

References

Ahmad Z, Franz BA, Charles CR, Kwiatkowska EJ, Werdell J, Shettle EP, Holben BN (2010) New aerosol models for the retrieval of aerosol optical thickness and normalized water-leaving radiances from the SeaWiFS and MODIS sensors over coastal regions and open oceans. Appl Opt 49:5545–5560

Alvain S, Moulin C, Dandonneau Y, Breon FM (2005) Remote sensing of phytoplankton groups in case 1 waters from global SeaWiFS imagery. Deep Sea Res Part I 52:1989–2004

Antoine D, Morel A, Gordon HR, Banzon VF, Evans RH (2005) Bridging ocean color observations of the 1980s and 2000s in search of long-term trends. J Geophys Res. doi:10.1029/2004JC002620

Antoine D, d'Ortenzio F, Hooker SB, Bécu G, Gentili B, Tailliez D, Scott AJ (2008) Assessment of uncertainty in the ocean reflectance determined by three satellite ocean color sensors (MERIS, SeaWiFS and MODIS-A) at an offshore site in the Mediterranean Sea (BOUSSOLE project). J Geophys Res 113. doi:10.1029/2007JC004472

Antoine D, Siegel DA, Kostadinov T, Maritorena S, Nelson NB, Gentili B, Vellucci V, Guillocheau N (2011) Variability in optical particle backscattering in contrasting bio-optical oceanic regimes. Limnol Oceanogr 56:955–973

Arnone RA, Martinolich P, Gould RW Jr, Stumpf R, Ladner S (1998) Coastal optical properties using SeaWiFS.SPIE. In: Ackleson S, Campbell, J (eds) Proceedings of Ocean Optics XIV, Office of Naval Research, Washington, DC, 1998

Arrigo KR, van Dijken GL, Pabi S (2008) The impact of a shrinking Arctic ice cover on marine primary production. Geophy Res Lett 35:L19603. doi:10.1029/2008GL035028

Babin SM, Carton JA, Dickey TD, Wiggert JD (2004) Satellite evidence of hurricane-induced phytoplankton blooms in an oceanic desert. J Geophys Res 109:C03043. doi:10.1029/2003JC001938

Bailey SW, McCLain CR, Werdell PJ, Schieber BD (2000) Normalized water-leaving radiance and chlorophyll a match-up analyses. In: Hooker SB, Firestone ER (eds), NASA Technical Memorandum 2000-206892SeaWiFS postlaunch calibration and validation analyses, NASA Goddard Space Flight Centerm, Part 2, vol 10. Greenbelt, Maryland, pp 45–52

Bailey SW, Werdell PJ (2006) A multi-sensor approach for the on-orbit validation of ocean color satellite data products. Remote Sens Environ 102:12–23

Bailey SW, Franz BA, Werdell PJ (2010) Estimation of near-infrared water-leaving reflectance for satellite ocean color data processing. Opt Express 18:7521–7527

Behrenfeld MJ, Randerson JT, McClain CR et al (2001) Biospheric primary production during an ENSO transition. Science 291:2594–2597

Behrenfeld MJ, Boss E, Siegel DA, Shea DM (2005) Global remote sensing of phytoplankton physiology. Global Biogeochem Cycles 19:GB1006. doi:10.1029/2004GB002299

Behrenfeld MJ, Siegel DA, O'Malley RT (2008) Global ocean phytoplankton and productivity. BAMS 89(7):S56–S61

Behrenfeld M, O'Malley R, Siegel DA, McClain CR, Sarmiento J, Feldman G, Falkowski P, Boss E, Milligan A (2006) Climate-driven trends in contemporary ocean productivity. Nature 444:752–755

Behrenfeld MJ, Westberry TK, Boss ES, O'Malley RT, Siegel DA, Wiggert JD, Franz BA, McClain CR, Feldman GC, Doney SC, Moore JK, Dall'Olmo G, Milligan AJ, Lima I, Mahowald N (2009) Satellite-detected fluorescence reveals global physiology of ocean phytoplankton. Biogeosciences 6:779–794

Beman JM, Arrigo KR, Matson PA (2005) Agricultural runoff fuels large phytoplankton blooms in vulnerable areas of the ocean. Nature 434:211–214

Brando VE, Dekker AG (2003) Satellite hyperspectral remote sensing for estimating estuarine and coastal water quality. IEEE Trans Geosci Remote Sens 41:1378–1387

Brewin RJW, Sathyendranath S, Mueller D et al (2013). The ocean colour climate change initiative: a round-robin comparison on in-water bio-optical algorithms. Remote Sens Environ (in press)

Bricaud A, Babin M, Morel A, Claustre H (1995) Variability in the chlorophyll-specific absorption coefficients of natural phytoplankton: analysis and parameterization. J Geophys Res 100:13321–13332

Bricaud A, Claustre H, Ras J, Oubelkheir K (2004) Natural variability of phytoplanktonic absorption in oceanic waters: influence of the size structure of algal populations. J Geophys Res 109:C11010

Brown O, Evans RH, Brown JW, Gordon HR, Smith RC et al (1985) Phytoplankton blooming of the U.S. east coast: a satellite description. Science 229:163–167

Campbell JW, Esaias WE (1983) Basis for spectral curvature algorithms in remote sensing of chlorophyll. Appl Opt 22:1084–1093

Campbell JW (1995) The lognormal distribution as a model for bio-optical variability in the sea. J Geophys Rex 100(C7):13237–13254

Cannizzaro JP, Carder KL (2006) Estimating chlorophyll *a* concentrations from remote-sensing reflectance data in optically shallow waters. Remote Sens Environ 101:13–24

Cannizzaro JP, Carder KL, Chen FR, Heil CA, Vargo GA (2008) A novel technique for detection of the toxic dinoflagellate, *Karenia brevis*, in the Gulf of Mexico from remotely sensed ocean color data. Cont Shelf Res 28:137–158

Cannizzaro JP, Hu C, Carder KL, Kelble CR, Melo N, Johns EM, Vargo GA, Heil CA (2013) On the accuracy of SeaWiFS ocean color data products on the West Florida Shelf. J Coastal Res. doi:10.2112/JCOASTRES-D-12-00223.1

Carder KL, Hawes SK, Baker KA, Smith RC, Steward RG, Mitchell BG (1991) Reflectance model for quantifying chlorophyll a in the presence of productivity degradation products. J Geophys Res 96:20599–20611

Carder KL, Chen FR, Lee ZP, Hawes SK, Kamykowski D (1999) Semianalytic moderate-resolution imaging spectrometer algorithms for chlorophyll a and absorption with bio-optical domains based on nitrate-depletion temperatures. J Geophys Res 104:5403–5421

Charria G, Mélin F, Dadou I, Radenac M-H, Garçon V (2003) Rossby wave and ocean color: The cells uplifting hypothesis in the South Atlantic Subtropical Convergence Zone. Geophys Res Lett 30(3):1125. doi:10.1029/2002GL016390

Chavez FP, Strutton PG, Friederich CE et al (1999) Biological and chemical response of the equatorial Pacific Ocean to the 1997–1998 El Nino. Science 286:2126–2131

Chomko RM, Gordon HR (2001) Atmospheric correction of ocean color imagery: test of the spectral optimization algorithm with the sea-viewing wide field-of-view sensor. Appl Opt 40:2973–2984

Chomko RM, Gordon HR, Maritorena S, Siegel DA (2003) Simultaneous retrieval of oceanic and atmospheric parameters for ocean color imagery by spectral optimization: a validation. Remote Sens Environ 84:208–220

Cipollini P, Cromwell D, Challenor PG, Raffaglio S (2001) Rossby waves detected in global ocean colour data. Geophys Res Lett 28:323–326

Clarke GK, Ewing GC, Lorenzen CJ (1970) Spectra of backscattered light from the sea obtained from aircraft as a measure of chlorophyll concentration. Science 167:1119–1121

Clark DK, Gordon HR, Voss KJ, Ge Y, Broenkow W et al (1997) Validation of atmospheric correction over the ocean. J Geophys Res 102:17209–17217

Craig S, Jones CT, Li WKW, Lazin G, Horne E, Caverhill C, Cullen JJ (2012) Deriving optical metrics of coastal phytoplankton biomass from ocean colour. Remote Sens Envion 119:72–83

Dall'Olmo G, Gitelson AA, Rundquist DC, Leavitt B, Barrow T, Holz JC (2005) Assessing the potential of SeaWiFS and MODIS for estimating chlorophyll concentration in turbid productive waters using red and near-infrared bands. Remote Sens Environ 96(2):176–187

Dandonneau Y, Vega A, Loisel H, du Penhoat Y, Menkes C (2003) Oceanic Rossby waves acting as a "hayrake" for ecosystem floating by-products. Science 302:1548–1551

Dandonneau Y, Menkes C, Gorgues T, Madec G (2004) Reponse to comment on "Oceanic Rossby waves acting as a 'hay rake' for ecosystem floating by-products". Science 304:390c

Darecki M, Stramski D (2004) An evaluation of MODIS and SeaWiFS bio-optical algorithms in the Baltic Sea. Remote Sens Environ 89:326–350

Dierssen HM (2010) Perspectives on empirical approaches for ocean color remote sensing of chlorophyll in a changing climate. Proc Nat Acad Sci 107:17073–17078

Doney SC, Glover DM, McCue SJ, Fuentes M (2003). Mesoscale variability of sea-viewing wide field-of-view sensor (SeaWiFS) satellite ocean color: Global patterns and spatial scales. J Geophys Res 108(C2):3024. doi:10.1029/2001JC000843

D'Ortenzio F, Marullo S, Ragni M, d'Alcala MR, Santoleri R (2002) Validation of empirical SeaWiFS algorithms for chlorophyll-*a* retrieval in the Mediterranean Sea: a case study of oligotrophic seas. Remote Sens Environ 82:79–84

D'Sa EJ, Miller RL (2003) Bio-optical properties in waters influenced by the Mississippi River during low flow conditions. Remote Sens Environ 84:538–549

Dzwonkowski B, Yan X (2005) Development and application of a neural network based ocean colour algorithm in coastal waters. Int J Remote Sens 26:1175–1200

Fargion GS, Franz BA, Kwiatkowska EJ, Pietras CM, Bailey SW, Gales J, et al (2004) SIMBIOS program in support of ocean color missions: 1997–2003. In: Frouin RJ, Gilbert GD, Pan D (eds) Ocean remote sensing and imaging: II. Proceedings SPIE, vol 5155.The Society of Photo-Optical Instrumentation Engineers, pp 49–60

Fishman J, Al-Saadi J, Bontempi P et al (2012). Fulfilling the Mandate and Meeting the Challenges of the Nation's Next Generation of Atmospheric Composition and Coastal Ecosystem Measurements: NASA's Geostationary Coastal and Air Pollution Events (GEO-CAPE) Mission. Bull Am Meteorol Soc 93:1457–1566

Franz BA, Bailey SW, Werdell PJ, McClain CR (2007) Sensor-independent approach to the vicarious calibration of satellite ocean color radiometry. Appl Opt 46:5068–5082

Frouin R, Schwindling M, Deschamps P.-Y (1996). Spectral reflectance of sea foam in the visible and near-infrared: In situ measurements and remote sensing implications. J Geophys Res 101:14361–14371

Frouin R (1997) NDPI for satellite ocean color applications, In: Proceedings of the Fourth IPSWT, Boussens, France, 1997

Gilerson A, Zhou J, Hlaing S, Ioannou I, Schalles J, Gross B, Moshary F, Ahmed S (2007) Fluorescence component in the reflectance spectra from coastal waters. Dependence on water composition. Opt Express 15:15702–15721

Gitelson AA, Dall'Olmo G, Moses WM, Rundquist DC, Barrow T, Fisher TR, Gurlin D, Holz J (2008) A simple semi-analytical model for remote estimation of chlorophyll-a in turbid waters: validation. Remote Sens Environ 112(9):3582–3593

Gordon HR, Brown OB, Jacobs MM (1975) Computed relationships between the Inherent and Apparent Optical Properties. Appl Opt 14:417–427

Gordon HR, Clark DK (1980) Atmospheric effects in the remote sensing of phytoplankton pigments. Bound Layer Meteorol 18:299–313

Gordon HR, Clark DK, Muller JL, Hovis WA (1980) Phytoplankton pigments from the Nimbus-7 Coastal zone color scanner–comparisons with surface measurements. Science 210:63–66

Gordon HR, Morel AY (1983) Remote assessment of ocean color for interpretation of satellite visible imagery. A review. Springer, New York p 114

Gordon HR, Brown OB, Evans RH, Brown JW, Smith RC, Baker KS, Clark DK (1988) A semianalytical radiance model of ocean color. J Geophys Res 93:10909–10924

Gordon HR (1992) Diffuse reflectance of the ocean: influence of nonuniform phytoplankton pigment profile. Appl Opt 31:2116–2129

Gordon HR (1993) Radiative transfer in the atmosphere for correction of ocean color remote sensors. In: Barale V, Schlittenhardt PM (eds) Ocean colour: theory and applications in a decade of CZCS experience, 1993 ECSC, EEC, EAEC, Brussels and Luxembourg, pp 33–77

Gordon HR, Wang M (1994a) Retrieval of water-leaving radiance and aerosol optical thickness over the oceans with SeaWiFS: a preliminary algorithm. Appl Opt 33:443–452

Gordon HR, Wang M (1994b) Influence of oceanic whitecaps on atmospheric correction of SeaWiFS. Appl Opt 33:7754–7763

Gordon HR (1997) Atmospheric correction of ocean color imagery in the earth observing system era. J Geophys Res 102:17081–17106

Gower J, King S, Borstad G, Brown L (2005) Detection of intense plankton blooms using the 709 nm band of the MERIS imaging spectrometer. Int J Remote Sens 26:2005–2012

Gregg WW, Casey NW (2004) Global and regional evaluation of the SeaWiFS chlorophyll dataset. Remote Sens Environ 93:463–479

Gregg WW, Casey NW, McClain CR (2005) Recent trends in global ocean chlorophyll. Geophys Res Lett 32:L03606. doi:10.1029/2004GL021808

Hamme RC, Webbey PW, Crawford WR et al (2010) Volcanic ash fuels anomalous plankton bloom in subarctic northeast Pacific. Geophys Res Lett 37:L19604. doi:10.1029/2010GL044629

Hoge FE, Lyon PE (1996) Satellite retrieval of inherent optical properties by linear matrix inversion of oceanic radiance models: an analysis of model and radiance measurement errors. J Geophys Res 101:16631–16648

Hoogenboom HJ, Dekker AG, Althuis IA (1998) Simulation of AVIRIS sensitivity for detecting chlorophyll over coastal and inland waters. Remote Sens Environ 65:333–340

Hooker SB, Esaias WE, Feldman GC, Gregg WW, McClain CR (1992) An overview of SeaWiFS and ocean color. NASA Technical Memorandum. National Aeronautics and Space Administration, Goddard Space Flight Center, vol 104566. Greenbelt, MD

Hooker SB, McClain CR, Firestone JK, Westphal TL, Yeh E-N, Ge.Y (1994) The SeaWiFS bio-optical archive and storage system (SeaBASS): Part 1. NASA Technical Memorandum. National Aeronautics and Space Administration, Goddard Space Flight Center, vol 104566. Greenbelt, MD

Hooker SB, Heukelem LV (2011) An investigation into HPLC data quality problems. NASA Technical Memorandum. National Aeronautics and Space Administration, Goddard Space Flight Center, vol 215867. Greenbelt, MD

Hovis WA, Clark DK, Anderson F et al (1980) Nimbus-7 coastal zone color scanner–system description and initial imagery. Science 210:60–63

Hu C, Carder KL, Muller-Karger FE (2000) Atmospheric correction of SeaWiFS imagery over turbid coastal waters: a practical method. Remote Sens Environ 74:195–206

Hu C, Müller-Karger FE, Biggs DC, Carder KL, Nababan B, Nadeau D, Vanderbloemen J (2003) Comparison of ship and satellite bio-optical measurements on the continental margin of the NE Gulf of Mexico. Int J Remote Sens 24:2597–2612

Hu C, Müller-Karger FE, Taylor C, Carder KL, Kelble C, Johns E, Heil CA (2005) Red tide detection and tracing using MODIS fluorescence data: an example in SW Florida coastal waters. Remote Sens Environ 97:311–321

Hu C, Lee Z, Muller-Karger FE, Carder KL, Walsh JJ (2006) Ocean color reveals phase shift between marine plants and yellow substance. IEEE Geosci Remote Sens Lett 3:262–266

Hu C, Feng L, Lee Z, Davis CO, Mannino A, McClain CR, Franz BA (2012a) Dynamic range and sensitivity requirements of satellite ocean color sensors: learning from the past. Appl Opt 51:6045–6062

Hu C, Lee Z, Franz B (2012b) Chlorophyll-*a* algorithms for oligotrophic oceans: a novel approach based on three-band reflectance difference. J Geophys Res 117:C01011. doi:10.1029/2011JC007395

IOCCG (2006) Remote sensing of inherent optical properties: fundamentals, tests of algorithms, and applications. In: Lee Z-P (ed) Reports of the international ocean-colour coordinating group, No. 5, Dartmouth, Canada

IOCCG (2008). Why Ocean Colour? The Societal Benefits of Ocean-Colour Technology. Platt T, Hoepffner N, Stuart V, Brown C (eds) Reports of the International Ocean-Colour Coordinating Group, No. 7, IOCCG, Dartmouth, Canada

IOCCG (2009).Remote Sensing in Fisheries and Aquaculture. Forget M-H, Stuart V, Platt T (eds) Reports of the International Ocean-Colour Coordinating Group, No. 8, IOCCG, Dartmouth, Canada

IOCCG (2010). Atmospheric Correction for Remotely-Sensed Ocean-Colour Products. Wang, M. (ed) Reports of the International Ocean-Colour Coordinating Group, No. 10, IOCCG, Dartmouth, Canada

Jiao HB, Zha Y, Gao J, Li YM, Wei YC, Huang JZ (2006) Estimation of chlorophyll-a concentration in Lake Tai, China using in situ hyperspectral data. Int J Remote Sens 27:4267–4276

Kahru M, Mitchell BG (1999) Empirical chlorophyll algorithm and preliminary SeaWiFS validation for the California Current. Int J Remote Sens 20(17):3423–3429

Kahru M, Mitchell BG (2008) Ocean color reveals increased blooms in various parts of the World. EOS, Trans AGU 89(18):170

Keiner LE, Brown CW (1999) Estimating oceanic chlorophyll concentrations with neural networks. Int J Remote Sens 20:189–194

Killworth PD (2004) Comment on Oceanic Rossby waves acting as a 'Hay Rake' for ecosystem floating by-products. Science 304:390b

Killworth PD, Cipollini P, Uz BM, Blundell JR (2004) Physical and biological mechanisms for planetary waves observed in satellite-derived chlorophyll. J Geophys Res 109:C07002. doi:10.1029/2003JC001768

Kirk JTO (1984) Dependence of relationship between inherent and apparentoptical properties of water on solar altitude. Limnol Oceanogr 29:350–356

Lavender SJ, Pinkerton MH, Moore GF, Aiken J, Blondeau-Patissier D (2005) Modification to the atmospheric correction of SeaWiFS ocean colour images over turbid waters. Cont Shelf Res 25:539–555

Le C, Li YM, Zha Y, Sun DY, Huang CC, Lu H (2009) A four-band semi-analytical model for estimating chlorophyll a in highly turbid lakes: the case of Taihu Lake. China Remote Sens Environ 113:1175–1182

Le C, Hu C, Cannizzaro J, English D, Muller-Karger F, Lee Z (2013) Evaluation of chlorophyll-a remote sensing algorithms for an optically complex estuary. Remote Sens Environ 129:75–89

Lee ZP, Carder KL, Mobley CD, Steward RG, Patch JS (1999) Hyperspectral remote sensing for shallow waters: 2. Deriving bottom depths and water properties by optimization. Appl Opt 38:3831–3843

Lee ZP, Carder KL, Arnone RA (2002) Deriving inherent optical properties from water color: a multi-band quasi-analytical algorithm for optically deep waters. Appl Opt 41:5755–5772

Lee Z, Hu C (2006) Global distribution of Case-1 waters: an analysis from SeaWiFS measurements. Remote Sens Environ 101:270–276

Letelier RM, Abott MR (1996) An analysis of chlorophyll fluorescence algorithms for the Moderate Resolution Imaging Spectrometer (MODIS). Remote Sens Environ 58:215–223

Lin I–I, Liu WT, Wu C–C, Wong GTF, Hu C, Chen Z, Liang W-D, Yang Y, Liu K–K (2003). New evidence for enhanced ocean primary production triggered by tropical cyclone. Geophys Res Lett 30(13). doi:10.1029/2003GL017141

Lin I–I, Hu C, Li Y-H, Ho T-Y, Fischer T, Wong GTF, Wu J, Huang C-W, Chu DA, Ko D-S, Chen J-P (2011) Fertilization potential of volcanic dust in the low-nutrient low-chlorophyll western North 35 Pacific subtropical gyre: Satellite evidence and laboratory study. Global Biogeochem Cycles 25:GB1006. doi:10.1029/2009GB003758

Loisel H, Nicolas J-M, Deschamps P-Y, Frouin R (2002) Seasonal and inter-annual variability of particulate organic matter in the global ocean. Geophys Res Lett 29(24):2196. doi: 10.1029/2002GL015948

Maritorena S, Siegel DA, Peterson A (2002) Optimization of a semi-analytical ocean color model for global scale applications. Appl Opt 41:2705–2714

Maritorena S, D'Andon OHF, Mangin A, Siegel DA (2010) Merged satellite ocean color data products using a bio-optical model: Characteristics, benefits and issues. Remote Sens Environ 114(8):1791-1804

Marrari M, Hu C, Daly K (2006) Validation of SeaWiFS chlorophyll-a concentrations in the Southern Ocean: A revisit. Remote Sens Environ 105:367–375

Martinez E, Antoine D, D'Ortenzio F, Gentili B (2009) Climate-driven basin-scale decadal oscillations of oceanic phytoplankton. Science 326:1253–1256

McClain CR, Feldman GC, Hooker SB (2004) An overview of the SeaWiFS project and strategies for producing a climate research quality global ocean bio-optical time series. Deep-Sea Res II 51:5–42

McClain CR (2009) A decade of satellite ocean color observations. Annu Rev Mar Sci 1:19–42

McGillicuddy DJ Jr, Kosnyrev VK, Ryan JP, Yoder JA (2001) Covariation of mesoscale ocean color and sea-surface temperature patterns in the Sargasso Sea. Deep-Sea Res II 48:1823–1836

McGillicuddy DJ Jr, Anderson LA, Bates NR, Biddy T, Buesseler KO et al (2007) Eddy/wind interactions stimulate extraordinary mid-ocean plankton blooms. Science 316:1021–1026

McKee D, Cunningham A, Dudek A (2007a) Optical water type discrimination and tuning remote sensing band-ratio algorithms: Application to retrieval of chlorophyll and $K_d(490)$ in the Irish and Celtic Seas. Estuar Coast Shelf Sci 73:827–834

McKee D, Cunningham A, Wright D, Hay L (2007b) Potential impacts of nonalgal materials on water-leaving Sun induced chlorophyll fluorescence signals in coastal waters. Appl Opt 46:7720–7729

Mélin F, Zibordi G, Berthon J-F (2003) Assessment of SeaWiFS atmospheric and marine products for the Adriatic Sea. IEEE Trans Geosci Remote Sens 41:548–558

Mitchell BG (1994) Coastal zone color scanner retrospective. J Geophys Res 99(C4):7291–7292

Mitchell BG, Kahru M (2009) Bio-optical algorithms for ADEOS-2 GLI. J Remote Sens Soc Jpn 29:80–85

Mobley CD (1994) Light and Water: radiative transfer in natural waters. Academic Press, New York

Mobley CD, Stramski D, Bissett WP, Boss E (2004) Optical modeling of ocean waters: is the Case 1–Case 2 classification still useful? Oceanography 17:60–67

Morel A, Prieur L (1977) Analysis of variations in ocean color. Limnol Oceanogr 22:709–722

Morel A (1988) Optical modeling of the upper ocean in relation to its biogenous matter content (Case I Waters). J Geophys Res 49:177–202
Morel A, Ahn YH (1990) Optical efficiency factors of free-living marine bacteria: Influence of bacterioplankton upon the optical properties and particulate organic carbon in oceanic waters. J Mar Res 48:145–175
Morel A, Gentili B (1991) Diffuse reflectance of oceanic waters: its dependence on sun angle as influenced by molecular scattering contribution. Appl Opt 30:4427–4438
Morel A, Maritorena S (2001) Bio-optical properties of oceanic waters: A reappraisal. J Geophys Res 106:7163–7180
Mouw CB, Yoder JA (2010) Optical determination of phytoplankton size composition from global SeaWiFS imagery. J Geophys Res 115:C12018. doi:10.1029/2010JC006337
Mukai S, Sano I, Okada Y (2000) Inverse problems in the atmosphere–ocean system: estimation of aerosol characteristics and phytoplankton distribution. Appl Math Comput 116:93–101. doi:10.1016/S0096-3003(99)00197-6
Nair A, Sathyendranath S, Platt T, Morales J, Stuart V, Forget M, Devred E, Bouman H (2008) Remote sensing of phytoplankton functional types. Remote Sens Environ 112:3366–3375
National Aeronautics and Space Administration (2010) Responding to the challenge of climate and environmental change: NASA's plan for a climate-centric architecture for earth observations and applications from space. p 48 (http://science.nasa.gov/earth-science/)
National Research Council (2004) Climate data records from environmental satellites: interim report. committee on climate data records from NOAA operational satellites. ISBN: 0-309-09168-3, p 150
National Research Council (2007) Earth science and applications from space: national imperatives for the next decade and beyond. Committee on earth science and applications from space: a community assessment and strategy for the future, National Research Council. ISBN: 0-309-66714-3, p 456. (http://www.nap.edu/catalog/11820.html)
National Research Council (2008). Earth observations from space: the first 50 years of scientific accomplishments. National Academies Press, Washington, D.C
Odriozola AL, Varela R, Hu C, Astor Y, Lorenzoni L, Muller-Karger FE (2007) On the absorption of light in the Orinoco River plume. Cont Shelf Res 27:1447–1464
O'Reilly JE et al (2000) SeaWiFS Postlaunch Calibration and Validation Analyses, Part 3. NASA Technical Memorandum 2000-206892, Hooker SB, Firestone ER, (eds.) (NASA Goddard Space Flight Center), Vol 11, p 49
Pierson D, Sträombäack N (2000) A modeling approach to evaluate preliminary remote sensing algorithms: use of water quality data from Swedish great lakes. Geophysical 36:177–202
Platt T, Fuentes-Yaco C, Frank KT (2003) Marine ecology: spring algal bloom and larval fish survival. Nature 423:398–399
Polovina JJ, Howell EA, Kobayashi DR et al (2001) The transition zone chlorophyll front, a dynamic global feature defining migration and forage habitat for marine resources. Prog Oceanogr 49:469–483
Polovina JJ, Howell EA, Abecassis M (2008) Ocean's least productive waters are expanding. Geophys Rev Lett 35:L03618. doi:10.1029/2007GL031745
Pope R, Fry E (1997) Absorption spectrum (380–700 nm) of pure waters: II. Integrating cavity measurements. Appl Opt 36:8710–8723
Prieur L (1976) Transfert radiatif dans les eaux de mer. Application a la determination de parametres optiques caracteris ant leur teneur en substances dissoutes et leur contenu en particules. D. Sci. Thesis, Univ. Pierre et Marie Curie, p 243
Preisendorfer RW (1976) Hydrologic optics, vol 1: Introduction. Springfield: National Technical Information Service. Also available on CD, Office of Naval Research
Roesler CS, Perry MJ (1995) In situ phytoplankton absorption, fluorescence emission, and particulate backscattering spectra determined from reflectance. J Geophys Res 100:13279–13294
Ruddick KG, Ovidio f, Rijkeboer M (2000) Atmospheric correction of SeaWiFS imagery for turbid coastal and inland waters. Appl Opt 39:897–912

Ruddick KG, Gons HJ, Rijkeboer M, Tilston G (2001) Optical remote sensing of chlorophyll a in case 2 waters by use of an adaptive two-band algorithm with optimal error properties. Appl Opt 40:3575–3585

Salisbury JE, Campbell JW, Linder E, Meeker LD, Muller-Karger FE, Vorosmarty CJ (2004) On the seasonal correlation of surface particle fields with wind stress and Mississippi discharge in the northern Gulf of Mexico. Deep Sea Res II 51:1187–1203

Salisbury J, Vandemark D, Campbell J, Hunt C, Wisser D, Reul N, Chapron B (2011) Spatial and temporal coherence between Amazon River discharge, salinity, and light absorption by colored organic carbon in western tropical Atlantic surface waters. J Geophys Res 116:C00H02, doi:10.1029/2011JC006989

Sathyendranath S, Prieur L, More A (1989) A three component model of ocean colour and its application to remote sensing of phytoplankton pigments in coastal waters. Int J Remote Sens 10:1373–1394

Sathyendranath S, Watts L, Devred E, Platt T, Caverhill C, Maass H (2004) Discrimination of diatoms from other phytoplankton using ocean colour data. Mar Ecol Prog Ser 272:59–68

Sauer MJ, Roesler CS, Werdell PJ, Barnard A (2012) Under the hood of satellite empirical chlorophyll a algorithms: revealing the dependencies of maximum band ratio algorithms on inherent optical properties. Opt Express 20:20920–20933

Schaeffer BA, Hagy JD, Conmy RN, Lehrter JC, Stumpf RP (2012) An approach to developing numeric water quality criteria for coastal waters using the SeaWiFS satellite data record. Environmental Sci Tech 46:916–922

Schiller H, Doerffer R (1999) Neural Network for emulation of an inverse model — Operational derivation of Case II water properties from MERIS data. Int J Remote Sens 20(9):1735–1746

Schroeder T, Behnert I, Schaale M, Fischer J, Doerffer R (2007) Atmospheric correction algorithm for MERIS above case-2 waters. Int J Remote Sens 28:1469–1486

Siegel DA, Wang M, Maritorena S, Robinson W (2000) Atmospheric correction of satellite ocean color imagery: The black pixel assumption. Appl Opt 39:3582–3591

Siegel DA, Doney SC, Yoder JA (2002) The North Atlantic spring phytoplankton bloom and Sverdrup's critical depth hypothesis. Science 296:730–733

Siegel DA, Thomas AC, Marra eds. J (2004a) Special issue: views of ocean processes from the Sea-viewingWide Field-of-view Sensor (SeaWiFS) mission: Vol 1. Deep-Sea Res II 51:1–3

Siegel DA, Thomas AC, Marra eds. J (2004b) Special issue: views of ocean processes from the SeaviewingWide Field-of-view Sensor (SeaWiFS) mission: Vol 2. Deep-Sea Res II 51:10–11

Siegel DA, Maritorena S, Nelson NB, Behrenfeld MJ (2005) Independence and interdependencies among global ocean color properties: reassessing the bio-optical assumption. J Geophys Res 110:C07011. doi:10.1029/2004JC002527

Signorini S, McClain CR (2011) Subtropical gyre variability as seen from satellites. Remote Sens Lett 3:471–479

Siswanto E, Ishizaka J, Yokouchi K, Tanabe K, Tan CK (2007) Estimation of interannual and interdecadal variations of typhoon-induced primary production: a case study for the outer shelf of the East China Sea. Geophys Res Lett 34:L03604

Smith RC, Baker KS (1982) Oceanic chlorophyll concentrations as determined by satellite (Nimbus-7 Coastal Zone Color Scanner). Mar Biol 66:269–279

Soto I, Andrefouet S, Hu C, Muller-Karger FE, Wall CC, Sheng J, Hatcher BG (2009) Physical connectivity in the Mesoamerican Barrier Reef System inferred from 9 years of ocean color observations. Coral Reefs. doi:10.1007/s00338-009-0465-0

Stumpf RP, Arnone RA, Gould RW, Martinolich P, Ransibrahmanakul V, Tester P.A, Steward R.G, Subramaniam A, Culver ME, Pennoc, JR (2000) SeaWiFS ocean color data for US Southeast coastal waters. In: Proceedings of the Sixth International Conference on Remote Sensing for Marine and Coastal Environments. Ann Arbor, MI: Veridian ERIM Intl, pp 25–27

Stumpf RP, Arnone RA, Gould Jr RW, Martinolich PM, Ransibrahmanakul V (2003a) A partially coupled ocean-atmosphere model for retrieval of water-leaving radiance from SeaWiFS in coastal waters. In: Hooker SB, Firestone ER (eds) SeaWiFS postlaunch technical report series, vol 22: Algorithm updates for the fourth SeaWiFS data processing, p 51–59

Stumpf RP, Culver ME, Tester PA et al (2003b) Monitoring *Karenia brevis* blooms in the Gulf of Mexico using satellite ocean color imagery and other data. Harmful Algae 2:147–160

Szeto M, Werdell PJ, Moore TS, Campbell JW (2011) Are the world's oceans optically different? J Geophys Res 116:C00H04, doi:10.1029/2011 JC007230

Subramaniam A, Carpenter EJ, Falkowski PG (1999) Bio-optical properties of the marine diazotrophic cyanobacteria Trichodesmium spp. II. A reflectance model for remote sensing. Limnol Oceanogr 44(3):618–627

Sullivan JM, Twardowski MS, Zaneveld JRV, Moore CM, Barnard AH, Donaghay PL, Rhoades B (2006) Hyperspectral temperature and salt dependencies of absorption by water and heavy water in the 400–750 nm spectral range. Appl Opt 45:5294–5309

Tassan S (1981) A global sensitivity analysis for the retrieval of chlorophyll concentrations from remote sensed radiances–the influence of wind. In: Gower JRF (ed) Oceanography from Space. Plenum Press, New York, pp 371–376

Tassan S, Ferrari GM (2003) Variability of light absorption by aquatic particles in the near-infrared spectral region. Appl Opt 42(24):4802–4810

Thiemann S, Kaufman H (2000) Determination of chlorophyll contentand tropic state of lakes using field spectrometer and IRS-IC satellite data in the Mecklenburg Lake Distract, Germany. Remote Sens Environ 73:227–235

Tomlinson MC, Wynne TT, Stumpf RP (2009) An evaluation of remote sensing techniques for enhanced detection of the toxic dinoflagellate Karenia brevis. Remote Sens Environ 113:598–609

Tzortziou M, Herman JR, Gallegos CL, Neale PJ, Subramaniam A, Harding LW Jr, Ahmad Z (2006) Bio-optics of the Chesapeake Bay from measurements and radiative transfer closure. Estuar Coast Shelf Sci 68:348–362

Uz BM, Yoder JA, Osychny V (2001) Pumping of nutrients to ocean surface waters by the action of propagating planetary waves. Nature 409:597–600

Uz M, Yoder JA (2004) High frequency and mesoscale variability in SeaWiFS chlorophyll imagery and its relation to other remotely sensed oceanographic variables. Deep-Sea Res II 51:1001–1017

Viollier M, Deschamps PY, Lecomte P (1978) Airborne remote sensing of chlorophyll content under cloudy sky as applied to the tropical waters in the Gulf of Guinea. Remote Sens Environ 7:235–248

Viollier M, Tanre D, Deschamps PY (1980) An algorithm for remote sensing of water color from space. Bound Layer Meteorol 18:247–267

Walker ND, Leben RR, Balasubramanian S (2005) Hurricane-forced upwelling and chlorophyll *a* enhancement within cold-core cyclones in the Gulf of Mexico. Geophys Res Lett 32:L18610. doi:10.1029/2005GL023716

Wang M, Bailey SW (2001) Correction of sun glint contamination on the SeaWiFS ocean and atmosphere products. Appl Opt 40:4790–4798

Wang M (2007) Remote sensing of the ocean contributions from ultraviolet the near-infrared using the shortwave infrared bands: simulations. Appl Opt 46:1535–1547

Wang M, Shi W (2007) The NIR-SWIR combined atmospheric correction approach for MODIS ocean color data processing. Opt Express 15:15722–15733

Werdell PJ, Bailey SW (2005) An improved in situ bio-optical data set for ocean color algorithm development and satellite data product validation. Remote Sens Environ 98:122–140

Werdell PJ, Bailey SW, Franz BA, Harding LW Jr, Feldman GC, McClain CR (2009) Regional and seasonal variability of chlorophyll-a in Chesapeake Bay as observed by SeaWiFS and MODIS-Aqua. Remote Sens Environ 113:1319–1330

Westberry TK, Siegel DA (2006) Spatial and temporal distribution of trichodesmium blooms in the world's oceans. Global Biogeochem. Cycles 20:GB4016

Wilson C, Adamec D (2002) A global view of bio-physical coupling from SeaWiFS and TOPEX satellite data, 1997–2001. Geophys Res Lett 29(8):1257. doi:10.1029/2001GL014063

Wilson C, Coles VJ (2005) Global climatological relationships between satellite biological and physical observations and upper ocean properties. J Geophys Res 110:C10001. doi:10.1029/2004JC002724

Wynne TT, Stumpf RP, Richardson AG (2006) Discerning resuspended chlorophyll concentrations from ocean color satellite imagery. Cont Shelf Res 26:2583–2597

Yentsch CS (1965) Distribution of chlorophyll and phaeophytin in the open ocean. Deep Sea Res. 12:653–666

Yoder JA, Kennelly MA (2003) Seasonal and ENSO variability in global ocean phytoplankton chlorophyll derived from 4 years of SeaWiFS measurements. Global Biogeochem Cycles 17:1112. doi:1110.1029/2002GB001942

Yoder JA, Kennelly MA (2006) What have we learned about ocean variability from satellite ocean color imagers? Oceanography 19:152–171

Zaneveld JRV (1982) Remote sensed reflectance and its dependence on vertical structure: a theoretical derivation. Appl Opt 21:4146–4150

Zaneveld JRV (1995) A theoretical derivation of the dependence of the remotely sensed reflectance of the ocean on the inherent optical properties. J Geophys Res 100:13135–13142

Zaneveld JRV, Barnard AH, Boss E (2005) Theoretical derivation of the depth average of remotely sensed optical parameters. Opt Express 13:9052–9061

Zhang C, Hu C, Shang S, Muller-Karger FE, Li Y, Dai M, Huang B, Ning X, Hong H (2006) Bridging between SeaWiFS and MODIS for continuity of chlorophyll-*a* assessments off Southeastern China. Remote Sens Environ 102:250–263

Zhang X, Lewis M, Johnson B (1998) Influence of bubbles on scattering of light in the ocean. Appl Opt 37:6525–6536. doi:10.1364/AO.37.006525

Zhang X, Hu L, He M-X (2009) Scattering by pure seawater: effect of salinity. Opt Express 17:5698–5710

Zibordi G, Melin F, Berthon JF (2006) Comparison of SeaWiFS, MODIS, and MERIS radiometric products at a coastal site. Geophys Res Lett 33:L06617. doi:10.1029/2006GL025778

Zibordi G, Berthon J-F, Mélin F, D'Alimonte D, Kaitala S (2009) Validation of satellite ocean color primary products at optically complex coastal sites: northern adriatic sea, northern baltic proper and Gulf of Finland. Remote Sens Environ 113:2574–2591

Chapter 8
Oceanic Net Primary Production

Toby K. Westberry and Michael J. Behrenfeld

Abstract Production of organic matter in the ocean is a fundamental process for biogeochemical cycling of elements (carbon, nitrogen, etc.) as well as for providing the foundation of nearly all marine food webs. Satellite remote sensing provides the only means of estimating this rate at basin and global scales. A variety of satellite-based models for estimation of net primary production exist spanning a wide range of complexity. Results from applying these models to the satellite record have yielded valuable insight on the ocean's role in the earth climate system and the coupling of physics and biology. A vision for the next generation of NPP models aimed at utilizing existing tools and anticipated improvements in future satellite ocean color missions is also given.

8.1 Introduction

Nearly one third of annual anthropogenic CO_2 introduced to the atmosphere each year ends up in the ocean, with much of it mediated by biological uptake initiated by photosynthetic conversion of CO_2 to organic matter. Quantification of marine photosynthesis has been the subject of study since prior to the twentieth century (see review by Barber and Hilting 2002 on the history of plankton productivity studies in the ocean). Photosynthetic primary production in the ocean relies on a diverse community of planktonic algae (phytoplankton) distributed across a wide range of oceanic habitats. The standing stock of phytoplankton at any time is small ($\leq$1 Pg C), yet amazingly their cumulative rates of annual net primary production (NPP) equal or even exceed those of terrestrial plants (Field et al. 1998; Behrenfeld et al. 2001). NPP is defined as the fraction of total photosynthetic carbon fixation

T. K. Westberry (✉) · M. J. Behrenfeld
Department of Botany and Plant Pathology, Oregon State University,
Corvallis, OR 97330-2902, USA
e-mail: westbert@science.oregonstate.edu

J. M. Hanes (ed.), *Biophysical Applications of Satellite Remote Sensing*,
Springer Remote Sensing/Photogrammetry, DOI: 10.1007/978-3-642-25047-7_8,

available for phytoplankton growth or consumption by the heterotrophic community and is a rate (generally expressed in units of carbon production per unit time). Variability in basin-scale marine NPP is clearly associated with climate fluctuations that are expressed as interannual changes in the environment, periodic phenomena such as El Niño/La Niña cycles, and glacial-interglacial transitions. However, ocean NPP is not simply forced by climate, but also participates in complex feedbacks governing climate (e.g., Falkowski et al. 1998a). Understanding the distribution of NPP and its environmental dependencies is thus critical for evaluating ocean biogeochemical cycles and climate change. In addition, NPP is the foundation of nearly all marine food webs. Organic matter produced through photosynthesis supports grazing by zooplankton and other herbivorous organisms and ultimately all carnivorous invertebrates and vertebrate fish and mammals. Although quantitative links between NPP and higher trophic levels have been difficult to establish (Friedland et al. 2012), NPP is a critical input variable for many types of fisheries models and is used as a constraint when evaluating harvestable catches (Sherman et al. 2009; Chassot et al. 2010; Pauly and Christensen 1995).

Assessment of NPP rates has relied primarily on traditional shipboard sampling which is costly, laborious, and provides coarse spatial and temporal resolution. The only viable approach for basin or global scale assessments has been through the use of airborne or satellite platforms. Radiometric measurements from early aircraft efforts provided the seed for remotely detecting phytoplankton, with an initial focus on assessing pigment (chlorophyll) concentration (Clarke et al. 1970). A first-order correlation exists between chlorophyll concentration and NPP, implying that successful remote sensing retrieval of the former property could yield estimates of the latter rate. In 1978, the Coastal Zone Color Scanner (CZCS) was launched and represented the first dedicated satellite ocean color sensor for estimating pigment concentrations, and subsequently NPP (Gordon et al. 1980; Hovis et al. 1980). The CZCS effort was very successful and its data are still used in contemporary investigations for multi-decadal studies of ocean color (e.g., Martinez et al. 2009; Antoine et al. 2005). Linking a fundamental radiometric quantity (satellite radiance) to a high-level rate process (NPP) has remained a key justification for modern ocean color satellite missions (e.g., SeaWiFS, MODIS). Pre-launch documents for these missions have explicitly identified NPP as a Level 4 product calculable from a combination of lower level products (Falkowski et al. 1998b; Esaias 1996). Even today, NPP remains a key ocean biological rate process targeted by all active satellite ocean color missions.

Accurate assessment of global ocean NPP is a daunting task. Much of the phytoplankton community contributing to production lies ‘hidden’ below the shallow surface layer detected by satellite sensors. The conversion of detected standing stocks to a rate processes remains a major challenge and is complicated by a variety of phytoplankton physiological attributes. Nevertheless, significant progress has been made since the launch of the CZCS with respect to evaluating ocean NPP and detecting its dependency on climate forcings. In this review, we begin with a general overview of the theoretical basis for remote sensing NPP algorithms, describe contemporary approaches, and discuss the validation of

derived products. We then review some of the major findings regarding global ocean NPP and its variability and conclude with a discussion of new directions for improving our retrieval and understanding of this critical ecosystem property.

8.2 Theoretical Basis

Field measurements of ocean primary production were made throughout the twentieth century, but the modern measurement of NPP using radiolabeled carbon (^{14}C) can be traced to Steeman-Nielsen (1952). Following its introduction, application of the ^{14}C technique proliferated in oceanographic field studies, owing to its ease of use, high sensitivity, and ability to yield production estimates following a relatively short sample incubation period. Early ^{14}C studies provided fundamental insights that were soon incorporated into NPP modeling efforts. Simple empirical relationships between NPP and Chl or ambient light (PAR) emerged as some of the first predictive expressions for aquatic NPP (Ryther and Yentsch 1957; Talling 1957; Vollenweider 1966). Subsequent modeling efforts have focused on a variety of additional factors, including detailed descriptions of the underwater light field (Morel 1991; Smyth et al. 2005), improved characterization of physiology (Armstrong 2006; Westberry et al. 2008), and definition of regionally-specific properties (Longhurst et al. 1995; Arrigo et al. 2008b). Unfortunately, the increasing complexity of NPP models has often not translated into improved predictive ability (see Sect. 8.4) and even the most complex satellite NPP models remain necessarily crude representations of the photosynthetic variability revealed by genetic, biochemical, and physiological laboratory studies.

While remote sensing retrieval of NPP is challenging, its fundamental relationship is straight forward. By definition, NPP in a given water parcel is the product of the extant phytoplankton biomass (expressed in the same currency as NPP, carbon) and its specific growth rate (μ),

$$NPP = C_{phyto} \, X \, \mu \tag{8.1}$$

The two quantities, C_{phyto} x μ, encapsulate dependencies on several aspects of the phytoplankton growth environment. For example, biomass (C_{phyto}) reflects a balance between growth and loss processes, such as grazing by zooplankton. By contrast, μ is largely a function of light and nutrient availability.

Equation 8.1 represents the fundamental relationship for NPP, but it is not the basis for most remote sensing NPP algorithms because both C_{phtyo} and μ are grossly undersampled in the ocean, largely due to methodological difficulties. In practice, chlorophyll concentration (Chl) has served as the central metric of phytoplankton standing stock. Conversion of Chl into NPP thus requires a characterization of assimilation efficiency (i.e., net primary production per unit chlorophyll; P^b). Much of the current error in NPP estimates results from unconstrained variability in this 'photosynthetic efficiency' term (Milutinovic and Bertino 2011;

Behrenfeld and Falkowski 1997a). P^b is a function of incident photosynthetically available radiation (PAR) and thus varies with time of day, depth in the water column, season, and cloudiness. Fully resolved NPP models attempt to characterize this variability in the dynamic underwater light field. However, many simpler NPP algorithms employ time- and depth-integrated parameters and calculate productivity as a function of incident daily PAR and a maximum daily assimilation efficiency for the water column $\left(P^b_{opt}\right)$. Behrenfeld and Falkowski (1997a) summarize and compare the various classes of models, distinguishing between approaches by time, depth, and wavelength resolution.

A key derived property for many ecological applications is daily water-column–integrated NPP ($\sum$PP). In addition to subsurface light availability described above, assessment of $\sum$PP requires assumptions regarding other depth-dependent properties. In particular, surface mixed layer depth and vertically-varying nutrient loads, grazing pressures, and light conditions give rise to variations in biomass and phytoplankton physiological state (photoacclimation and growth rate). Numerous approaches have been developed to account for these effects. Depth-integrated models generally assume the water column is composed of two layers, one light saturated and the other light limited. An empirical function then relates the fraction of the water column that is light saturated to the incident irradiance. Behrenfeld and Falkowski (1997a) demonstrate that this approach is sufficient to capture >80 % of the variance in observed $\sum$PP when evaluated over a wide range of trophic conditions. Depth-resolved NPP models may take many forms. In some cases, vertical structure is prescribed using empirical relationships with surface properties (e.g., characterizing the profile of chlorophyll from surface chlorophyll concentration). More complex approaches incorporate information on mixing depths to assign an upper layer of uniform biomass and physiology, and then below this depth iteratively adjust chlorophyll stocks and physiological state based on models of photoacclimation, attenuation, and a prescribed shift from nutrient limitation to light limitation at depth (e.g., Westberry et al. 2008). As our knowledge of vertical variability improves, it will be these depth-resolved models that will provide the appropriate model scaffolding to incorporate this information to achieve improved NPP assessments.

All chlorophyll-based models of NPP, from simple depth-integrated algorithms to fully resolved time- and depth-dependent models, require a characterization of assimilation efficiencies (P^b, P^b_{opt}, etc.). In most cases, this aspect of NPP models is least mature. The most common approach is to relate assimilation efficiency to sea surface temperature (SST), with a somewhat bewildering array of SST-dependent models proposed (see Fig. 8.4 in Behrenfeld and Falkowski 1997a). One of the most commonly employed functions expresses assimilation efficiency as an increasing exponential function of temperature. The Q_{10} for this exponent was based on a compilation of laboratory phytoplankton growth rates, where an exponential relationship was fit to the maximum observed growth rates over a wide range of temperatures (after Eppley 1972). There is no a *priori* reason to assume that this growth-rate-based function has any direct physiological relevance to the

calculation of mean assimilation efficiencies. Behrenfeld and Falkowski (1997b) introduced an alternative temperature-dependent function that has also been widely applied. In their relationship, assimilation efficiency increases approximately exponentially up to 20 °C and then decreases, with a Q_{10} for the lower temperature range being similar to that of the 'Eppley curve'. The Behrenfeld and Falkowski relationship was empirically derived from field ^{14}C data and the downturn in efficiencies at >20 °C was interpreted to reflect effects of nutrient stress. It is now recognized that nutrient stress, in and of itself, is not synonymous with a reduction in photosynthetic efficiency (Halsey et al. 2010; Parkhill et al. 2001). Thus, there is also no clear physiological basis for the temperature-dependent function of Behrenfeld and Falkowski (1997b).

Development of new approaches for characterizing spatial-temporal variability in phytoplankton assimilation efficiencies is essential to advancing global ocean NPP estimates if surface chlorophyll concentration continues to be the remotely detected property of choice for phytoplankton biomass. Clearly, these advances must be based on a fundamental understanding of physiological responses to environmental growth conditions, rather than empirical relationships with SST. Nevertheless, employment of simple SST functions has yielded NPP estimates that exhibit reasonable relationships with field measured values. So, what is the basis of this success? The most likely explanation is that SST can, at times, function as a surrogate for an environmental factor directly governing variability in assimilation efficiency: light. Phytoplankton acclimate to changes in light conditions on time scales of days to a week or more. A decrease in incident light or an increase in mixing depth results in an increase in cellular chlorophyll. This light-driven

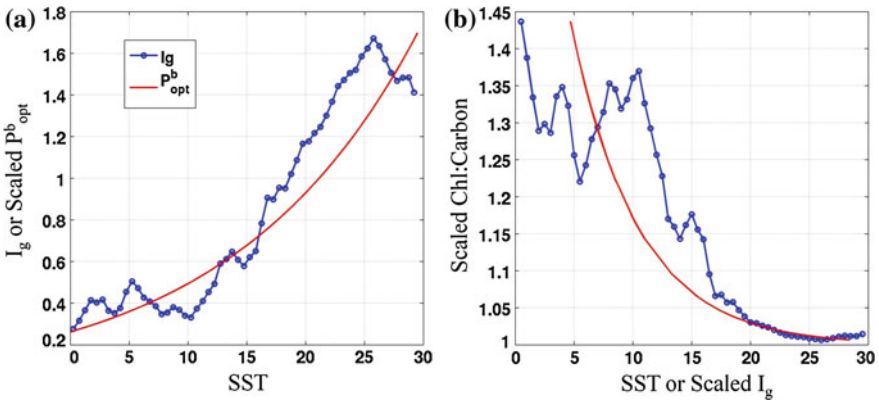

Fig. 8.1 Demonstration of covariance between mixed layer growth irradiance (I_g) and sea surface temperature (SST). **a** Panel on left shows classical relationship between SST and P^b_{opt} (red line) derived from Eppley (1972). Also shown is the median I_g (blue line) within discrete SST bins, calculated following Westberry et al. (2008). **b** Panel on right shows an idealized photoacclimation response (Chl:C, red line), where the dependent variable, I_g, has been scaled to match the range of SST. Blue line shows the same Chl:C as a function of SST. In both cases, Chl:C is expressed relative to a high light value of 1 (units not important)

increase in chlorophyll is not paralleled by an increase in carbon fixing capacity and thus results in a lower apparent assimilation efficiency (i.e., NPP/Chl decreases). In nature, regions of low incident light and/or deep mixing also tend to have lower SST. Thus, lower SST is broadly associated with low growth irradiance (I_g) and, thus, lower assimilation efficiencies. This tendency is illustrated in Fig. 8.1a where mean mixed layer light levels (I_g) exhibit roughly an exponential positive relationship with SST when evaluated over the global open ocean. The increase in I_g with SST drives a physiological acclimation that yields increasing assimilation efficiency with increasing SST. As a result, the implied change in cellular chlorophyll content viewed as a function of SST exhibits a pattern remarkably similar to expected changes as a function of I_g (Fig. 8.1b).

8.3 Methods

Satellite sensors provide a range of geophysical products relevant to NPP calculations, with three central properties being chlorophyll concentration, cloudiness-corrected PAR, and sea surface temperature (SST). These 3 variables are sufficient to initiate many NPP models (e.g., Behrenfeld and Falkowski 1997b), while other models require additional inputs. For example, some models require information on mixed layer depths (Howard and Yoder 1997; Westberry et al. 2008) or employ precalculated lookup tables (Antoine et al. 1996; others). Some recent NPP models have been developed that are based on inherent optical properties derived from ocean color inversion algorithms, including phytoplankton absorption coefficients (Lee et al. 1996) and/or particulate backscattering coefficients (b_{bp}) (Westberry et al. 2008). In many cases, NPP models can be viewed as modular in construct, in the sense that alternative formulations can be readily substituted. For example, the Vertically Generalized Production Model (VGPM) of Behrenfeld and Falkowski (1997b) is often executed with different temperature functions for P^b_{opt}, most often with exponential Eppley-type dependence.

While most global-scale NPP algorithms are based on chlorophyll as the index of standing stock, a notable exception is the model of Westberry et al. (2008). In their approach, phytoplankton carbon concentration is inferred from satellite b_{bp} data and used as the core biomass index. Simultaneous satellite retrievals of chlorophyll and carbon concentrations are then used to directly infer information on physiological status of phytoplankton within the surface mixed layer using understanding of Chl:C variability from laboratory studies. The Westberry et al. model is both depth and wavelength resolved, but is also unique in that it operates iteratively through the water column. Specifically, the model assumes biomass and physiological uniformity within the mixed layer, and then iteratively calculates spectral irradiance at each subsequent depth horizon as a function of integrated changes in biomass, pigment, and attenuation directly above. The resulting light field, in turn, defines the photoacclimation state (i.e., cellular pigmentation) of the

phytoplankton within the current depth horizon and their growth rate. Finally, in regions of surface macronutrient depletion, the model allows for a switch from nutrient-limitation to light-limitation at depths below the mixed layer. While additional work is needed to validate various aspects of this 'carbon-based approach', it does provide an excellent framework for incorporating more sophisticated descriptions of physiological variability (see Sect. 8.6).

8.4 Validation Efforts

Validation of satellite-based NPP estimates has largely been limited to matchup comparisons with field ^{14}C uptake measurements. While considerable ambiguity remains regarding exactly what the ^{14}C method measures, it is generally accepted that reasonably long (i.e., >12 h) incubations yield carbon fixation rates that approximate *net* primary production. The 'ambiguity' of the measurement includes unconstrained artifacts of sample confinement in bottles, unnatural light conditions during incubation (either on deck of the ship or *in situ*), and an incomplete understanding of how respiratory and other metabolic pathways impact lifetimes of newly formed carbon products. Alternative measures of photosynthetic primary production (e.g., *gross* primary production) are less frequently used for validation of satellite-based estimates. Both, $^{18}O_2$ incubations and the more recently developed triple-oxygen isotope method ($^{17}\Delta O_2$) provide a measure of gross primary production. Importantly, the latter method does not require sample incubations (Luz and Barkan 2009). However, empirical conversions are required to equate the different oxygen and carbon measurements and to characterize losses between gross and net photosynthetic production. Hence, we limit the following discussion to comparisons with measurements of ^{14}C uptake.

A series of blind, round-robin exercises were initiated by NASA in the mid-1990's in order to evaluate the performance of a wide variety of satellite NPP models. This Primary Productivity Algorithm Round Robin (PPARR) exercise has since evolved in its scope and expanded in the range of model types, numbers, and field measurements represented (Campbell et al. 2002; Carr et al. 2006; Friedrichs et al. 2009; Saba et al. 2010, 2011). Key findings of the PPARR activities have been: (1) increasing model complexity does not equate to improved predictive skill, (2) model skill varies regionally, and (3) reducing uncertainty in input parameters to NPP models (e.g., PAR, Chl) can reduce average RMS errors by >50 %. The first point above has been made on several occasions (Siegel et al. 2001; Behrenfeld and Falkowski 1997a), but is perhaps best demonstrated by Carr et al. (2006). In their report, a cluster analysis was performed on the correlation between NPP estimates for >30 models, spanning a wide range of complexity. The analysis revealed that correlations between model NPP estimates were not grouped according to model complexity, such that the simplest and most complex models often showed the highest correlation. Instead, correlations between models were largely determined by the underlying expression used to describe variability in

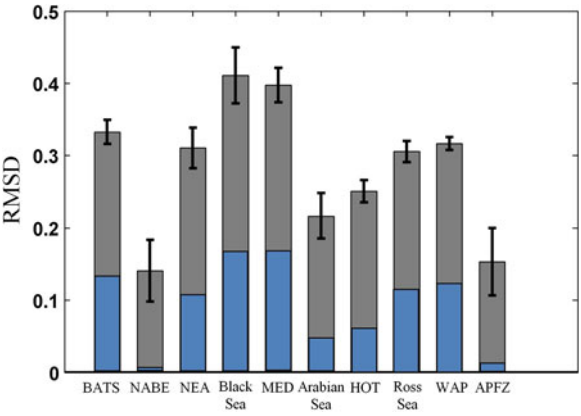

Fig. 8.2 Average root mean square difference (RMSD) of 21 satellite NPP models evaluated against field 14C measurements for several different locations. Error bars represent 2x standard error. Blue portions of each bar represent maximum potential reduction in RMSD if uncertainties in model input and field measurements are accounted for. For details regarding specific models and field dataset used, see Saba et al. (2011)

assimilation efficiencies (e.g., models that used an 'Eppley-type' formulation clustered together). The most comprehensive study demonstrating the second point was made by Saba et al. (2011). Output from 21 satellite-based ocean color models were analyzed against >1000 *in situ* ^{14}C measurements from diverse ocean regions spanning the Black Sea, Southern Ocean, high latitude North Atlantic, and subtropical Pacific and Atlantic. Some of the results are reproduced in Fig. 8.2 which show the ensemble average root mean square error (RMSE) in each region. Lower RMSE results from better predictive ability of NPP models (no distinction between models is made here).

The last finding listed above from the PPARR exercises underscores that a model's ability to accurately predict NPP is highly dependent upon the uncertainties inherent in the input data (Fig. 8.2) (Saba et al. 2011). While this may seem obvious, it is often difficult to propagate errors through complex analytical formulations resulting in model NPP estimates being reported with no accompanying error estimates. Saba et al. (2010) found that the majority of models were unable to accurately reproduce the observed trends in NPP at open ocean sites in the North Pacific (Station ALOHA near Hawaii) and the Atlantic (BATS near Bermuda). However, holding all other properties the same, but employing *in situ* estimates of Chl in the NPP models allowed many of the models to match the sign, and to a lesser extent, the magnitude of the observed trends in NPP. Siegel et al. (2001) also demonstrated the influence of using time-varying or site-averaged photosynthetic parameters in NPP models at BATS and found the predictive ability dropped significantly ($r^2 = 0.80$ to $r^2 = 0.27$) when mean values were used.

8.5 Major Findings

One of the fundamental realizations provided by remote sensing estimates of marine NPP is that the ocean contribution to biospheric annual NPP is roughly equivalent to that from terrestrial sources. Field et al. (1998) first synthesized

global estimates of marine NPP from the VGPM and terrestrial NPP from the CASA model (Potter et al. 1993). Although state-of-the-art at the time, the averaging periods for land and oceans were significantly different, the spatial resolutions were coarse, and quality for the ocean color data was well below today's standards. Nevertheless, the global picture that emerged indicated a marine NPP contribution of ~49 Pg C of the combined 105 Pg C for the biosphere. Compilation of historical estimates of oceanic NPP based on ^{14}C measurements yields a mean value similar to the Field et al. (1998) satellite-based estimate, but uncertainty in the field-based assessment is large enough to render the estimate meaningless (see Barber and Hilting 2002 for a chronology of global NPP estimates).

Recalculation of biospheric NPP using more recent data than employed by Field et al. (1998) yields values for a typical year (2004) of 54 and 50 Pg C year^{-1} for the oceans and land, respectively. Figure 8.3 shows the spatial distribution of combined land and ocean NPP, where both estimates are based on MODIS remote sensing data (Zhao et al. 2005; Behrenfeld and Falkowski 1997b). While maximum values of areal NPP rates can be substantially higher on land than in the ocean, the much greater spatial extent of ocean area mitigates this difference in zonally integrated values (Fig. 8.3). From the zonal profiles we find that tropical NPP on land is approximately twice that of equatorial marine primary production. Northern boreal forests (between 40°N and 60°N) are also a factor of 2× higher than oceanic totals across the same latitude domain. Marine NPP dominates southern hemisphere NPP south of 25°S.

Many of the major findings which remote sensing of NPP has enabled are related to improving our understanding of the links between physical forcing (e.g., climate) and biological response in the ocean. For example, the El Niño-Southern Oscillation (ENSO) phenomenon is a periodic climate perturbation that elicits significant changes in a wide array of marine ecosystem properties. The first modern era ocean color satellite (SeaWiFS) was launched during one of the largest ENSO events on

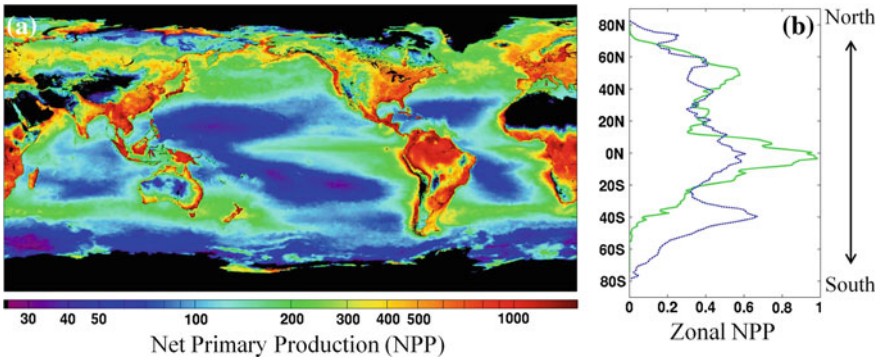

Fig. 8.3 **a** Average annual satellite NPP (gC m^{-2} yr^{-1}) from a combination of terrestrial and oceanic sources. **b** Right-hand panel shows zonally integrated NPP (Pg C yr^{-1}) for land (green line) and ocean (blue line) areas

record. The first 3 years of the mission captured the peak of the El Niño event and the following transition to an equally large La Niña (Behrenfeld et al. 2001). The peak to peak change in ocean NPP across this transition ($\sim$6 Pg C) exceeds any other anomaly since observed in the satellite ocean color record (Arndt et al. 2010; Blunden et al. 2011). El Niño is accompanied by higher than normal SST throughout much of the tropical Pacific Ocean and interrupts the normal upwelling pattern which supports significantly elevated NPP in the eastern tropical Pacific. Field studies have estimated reductions in nutrient supply and NPP of $\sim$80 % during El Niño (Barber and Chavez 1983; Chavez et al. 2002). A similar relationship was reported by Behrenfeld et al. (2006a) over the entire stratified surface ocean ($\sim$40°N to 40°S) based on remote sensing estimates of NPP.

A central objective underlying the development of a long-term, climate-quality satellite ocean color data record is to improve understanding of climate-ocean ecology interactions. It has been estimated that 50 or more years of continuous satellite observations will be necessary in many ocean regions to clearly detect the signature of anthropogenic impacts from natural variability (Henson et al. 2009). Clearly, this is far too long to wait. However, over much shorter time scales, natural forms of climate variation can provide critical insights on NPP and phytoplankton biomass variability. To this end, Behrenfeld et al. (2006a) showed that over the first 10 years of SeaWiFS observations, anomalies in water column integrated chlorophyll and modeled NPP (VGPM and CbPM) integrated over the permanently stratified oceans (i.e., annual average SST >15 °C) were highly correlated with variations in SST and surface mixing depths. Furthermore, the spatial distribution of NPP anomalies mirrored those of SST anomalies.

The Behrenfeld et al. (2006a) study has been followed by a series of similar analyses. In Behrenfeld et al. (2008), the strong correlation between chlorophyll and SST anomalies was also shown to occur at higher northern latitudes, but no significant trends were found for the Southern Ocean. This latter conclusion was repeated by Arrigo et al. (2008b) who reported no significant trend in Southern Ocean NPP between 1998 and 2006. Annual totals for the domain south of 50°S were $\sim 2 \pm 0.07$ Pg C year^{-1}, nearly half of previous remote sensing based estimates for this region. Martinez et al. (2009) significantly expanded the time period of evaluation by combining SeaWiFS data with the earlier CZCS record. Their study again reported significant inverse relationships between global ocean SST and chlorophyll anomalies, both in regionally integrated data and spatially-resolved fields. With this expanded data set, these authors were also able to clearly identify impacts of the longer time-scale climate fluctuations associated with ocean basin decadal oscillations. Additional analyses of temporal ocean color data employing both SeaWiFS and MODIS measurements were provided in reports by (Arndt et al. 2010; Blunden et al. 2011). Interestingly, several recent studies addressing temporal changes using in situ measured NPP have reported conflicting results from those found using satellite data (Dave and Lozier 2010; Lozier et al. 2011; Saba et al. 2010; Chavez et al. 2011). These differences highlight the difficulty in comparing quantities and trends derived from singular locations representing small spatial scales to integrated signals over entire ocean basins.

An important question arising from the aforementioned studies was what the underlying basis is for the inverse relationship between chlorophyll and SST anomalies. The magnitude of the SST anomalies is far too small to be directly responsible for the observed chlorophyll responses. Instead, and as suggested by Behrenfeld et al. (2006a), changes in SST are likely functioning as a proxy for altered surface mixing depths, where shallower mixing is accompanied by decreasing chlorophyll. Two mechanisms likely contribute to the link between surface chlorophyll concentrations to mixing depth: an impact on vertical nutrient transport from depth and changes in the average light level experienced by surface phytoplankton. To distinguish which of these two factors dominate, Behrenfeld et al. (2008) separated chlorophyll variability in permanently stratified ocean into that due to biomass changes and that due to intracellular chlorophyll (Chl:carbon) changes. Their study showed that, over most of the SeaWiFS record, chlorophyll variability was largely due to physiological changes in Chl:carbon and that most of this variability was attributable to changes in the upper ocean light environment, not nutrients. These findings imply that significant variations in chlorophyll detected in the satellite record are likely not linked to parallel changes in NPP. However, most contemporary NPP models are not equipped to make this distinction (see Sect. 8.6.1). More recently, Siegel et al. (2013) extended the analysis of physiological variability to all global ocean regions and additionally showed that apparent anomalies in chlorophyll may be, in part, traceable instead to variations in colored dissolved organic material. Taken together, these studies once again emphasize that careful attention must be given to physiological attributes if global ocean NPP and its temporal variability are to be accurate evaluated.

As global, synoptic estimates of NPP have advanced, opportunities have arisen for investigating relationships between NPP and more derived, yet critical, carbon cycle parameters. For example, the fraction of NPP delivered from the surface ocean to depth is a critical quantity of interest when addressing the ocean's role in carbon sequestration. This *export* production is traditionally measured in the field using sediment traps that collect and preserve sinking material, but these measurements have longstanding caveats (Buesseler et al. 2007 and references therein) and are extremely sparse in both space and time. Satellite observations of NPP, when combined with ecosystem model results and field measurements have provided simple, yet powerful empirical parameterizations that allow globally resolved fields of export production (Laws et al. 2000; Dunne et al. 2005). Current estimates of export production are ~ 10 Pg C year^{-1} globally and its spatial distribution gives us insight into ecosystem functioning. For example, Laws et al. (2000) showed that the Atlantic and Pacific Oceans contribute equally to total export (~ 4.3 Pg year^{-1} each), despite their two-fold differences in size ($\sim 75 \times 10^6$ km^2 and $\sim 160 \times 10^6$ km^2, respectively). Recently, Westberry et al. (2012) applied satellite NPP estimates to field-derived photosynthesis-respiration relationships to characterize global ocean respiration rates and net *community* production. These net community production rates set an upper constraint on export production for comparison with alternative approaches. Validation of these advanced, satellite-based carbon cycle parameters has yet to be carried out and should be an active research area in the future (see following section).

8.6 Future Research Directions

As detailed herein, significant progress has been made in quantifying NPP from global satellite data and applying these estimates to ecological questions, yet opportunities abound for making major improvements. Such improvements may take a variety of forms, including greater accuracy of NPP retrievals when compared to field measurements, development of new field metrics for validation, exploitation of advances in future satellite design capabilities, and more sophisticated physiological formulations in NPP models. Some of these improvements are relatively straightforward and may entail advances in engineering (e.g., higher spectral/spatial resolution on future ocean color sensors), while others will be more challenging (treatment of phytoplankton physiology). In this final section, we attempt a forward-looking view at potential avenues for refining global NPP assessments, particularly with respect to advancing characterization of physiological attributes.

8.6.1 Photoacclimation

Global surface ocean chlorophyll concentrations vary by roughly 3 orders of magnitude. Physiological changes in intracellular chlorophyll from varying light and nutrient conditions can span over 1.5 orders of magnitude, with the light effect alone (i.e., photoacclimation) contributing up to a factor of 10 variability (Falkowski and Laroche 1991). While variability in chlorophyll concentration due to changes in biomass or nutrient availability is positively correlated with changes in NPP, changes in chlorophyll due to photoacclimation are inversely correlated with NPP. In other words, all else being constant, an increase in daily light exposure results in a decrease in chlorophyll and an increase in assimilation efficiency. Given the magnitude of the photoacclimation response, it is somewhat surprising therefore that this physiological property is routinely ignored in all but a few marine NPP models. Even an imperfect assessment of photoacclimation could significantly improve NPP predictions and does not require a highly sophisticated model to effectuate. For example, the simple wavelength- and depth-integrated VGPM could be applied to satellite chlorophyll fields that are first corrected for photoacclimation. For this approach, global data on incident PAR, diffuse attenuation (K_d), and mixed layer depths (MLD) are needed to calculate I_g. Next, a laboratory-based relationship between I_g and cellular chlorophyll content can be employed to normalize satellite chlorophyll data to a uniform photoacclimation state and then these data applied in the VGPM with a constant value for P^b_{opt}. In essence, this strategy is equivalent to the approach of the Carbon-based Production Model (CbPM) of Westberry et al. (2008). The CbPM distinguishes Chl variability into that due to biomass changes and intracellular pigmentation. The latter property is then divided into light- and nutrient-dependent terms, where the

photoacclimation effect is determined from PAR, K_d, and MLD. The residual Chl:C variability is due to nutrient effects and is linearly proportional to NPP variability.

An important aspect of characterizing photoacclimation in the mixed layer (i.e., the portion of the water column sampled from space) is identifying the light level to which a natural phytoplankton community is acclimated. The uppermost reaches of the surface ocean are a turbulent, well mixed environment where a given phytoplankton population may circulate through a typical mixed layer of 50 m thickness >10 times per day (D'Asaro 2003). Laboratory studies indicate that the light-dependent signal for chlorophyll synthesis is keyed to the redox state of the plastoquinone (PQ) pool between photosystem II and photosystem I (Escoubas et al. 1995). An oxidized PQ pool signals for chlorophyll synthesis, while a reduced pool indicates that adequate chlorophyll (i.e., light harvesting capacity) exists. PQ pool reduction occurs at all saturating light levels, thus regulation of pigment synthesis is essentially an on–off switch (i.e., once light exceeds saturation, the signal for chlorophyll synthesis is off and further increases have no additional impact). Acclimation in such a system is thus best characterized as a function of the median light level within the mixed layer, rather than the average light level with is impacted by light levels in excess of saturation. The remaining issue is spatially- and temporally characterizing global MLD. Unfortunately, MLD is not a property directly retrieved by remote sensing. Consequently, we currently must rely on model or model-data assimilation schemes to generate the necessary MLD fields (e.g., Clancy and Sadler 1992). Notably, significant uncertainty remains in these MLD products, particularly at high latitudes (e.g., Southern Ocean), reducing this uncertainty will make a significant contribution toward advancing NPP assessments.

An additional issue regarding characterization of phytoplankton photoacclimation is distinction between the 'physiological' mixed layer depth from 'physical' mixed layer depth calculated from water column density or temperature properties. For much of the year and many parts of the ocean, there may be little difference between the 'physiological' and 'physical' mixed layers, but under certain, important conditions significant differences may exist. For example, the onset of winter-spring stratification in temperate and high-latitude seas can be rapid and non-monotonic. During this period, photoacclimation of the phytoplankton community will be responding to changes in the mixed layer light environment on timescales of order $\sim$1–2 weeks. Photoacclimation timescales are also dependent on the direction the light changes, taking longer when I_g is decreasing than when it is increasing. At timescales significantly <1 week, it is likely that passage of brief mixing events (associated with meteorological fronts) will not be registered by the phytoplankton, whereas the physical mixed layer depth may be significantly perturbed for a day or so, then return to its previous position. A practical approach to estimate a physiological MLD may exist through the use of dissolved O_2 profiles. Castro-Morales and Kaiser (2012) demonstrated the utility of this approach over a limited geographic region and found significant differences from traditional hydrographically determined mixed layers.

8.6.2 Nutrient Effects

Short-term perturbations in macronutrient availability can result in a brief period of unbalanced growth where phytoplankton assimilation efficiencies are reduced. However, under the steady state conditions found across most of the ocean, phytoplankton are well acclimated to their nutrient environment. Under such conditions, cellular chlorophyll levels are adjusted in direct proportion to nutrient availability and apparent assimilation efficiencies can be as high as under nutrient replete growth. Thus, the long-held assumption that nutrient stress is associated with inefficient photosynthesis is largely incorrect. This conclusion is supported by laboratory work demonstrating highly tuned photosynthetic light harvesting capacities optimized to macronutrient-defined growth rates (Laws and Bannister 1980).

While the aforementioned considerations suggest that assessing nutrient status may not be as critical once thought for assessing global ocean NPP, this conclusion may not be valid for conditions of iron stress. Iron concentrations are vanishingly low over much of the open ocean, and phytoplankton have evolved a variety of strategies for optimizing iron economy (Behrenfeld and Milligan 2013). These adjustments, however, can have a significant impact on apparent assimilation efficiencies, particularly under conditions where macronutrients are replete. Greater than one-third of the ocean surface area has conditions of low iron and high macronutrients (the so-called High-Nutrient, Low-Chlorophyll (HNLC) regions). Ironically, recent studies have shown that phytoplankton under HNLC conditions actually over-express chlorophyll synthesis relative to growth (Behrenfeld and Milligan 2013; Schrader et al. 2011; Behrenfeld et al. 2006b). This excess Chl does not contribute to photosynthesis (it is functionally "decoupled" from the photosystems), but is registered in satellite Chl retrievals. The pool of 'dysfunctional' Chl may account for >40 % of the total Chl in HNLC waters (Behrenfeld et al. 2006b; Schrader et al. 2011) and must be accounted for when assessing assimilation efficiencies. Behrenfeld et al. (2006b) estimated the magnitude of error in satellite NPP introduced by this bias in Chl over the Equatorial Pacific Ocean. The authors exploited field measurements of fluorescence signatures linked to functional and dysfunctional Chl and concluded that annual NPP for the region (using the VGPM and CbPM) may need to be revised downward by $\sim$15 %.

Recent advances in our understanding of solar-stimulated chlorophyll fluorescence measured from satellite (i.e., MODIS, MERIS) may provide an avenue for correcting satellite Chl and NPP fields for Fe-stress effects globally. Similar to the field diagnostics of Fe-stress employed by Behrenfeld et al. (2006b), satellite Chl fluorescence registers the imprint of Fe-stress (Behrenfeld et al. 2009; Westberry et al. 2013). Due to the pool of dysfunctional Chl described above and to shifts in photosystem stoichiometry occurring under iron stress (Behrenfeld and Milligan 2013), higher intrinsic fluorescence yields are observed in iron-stressed ocean region under the high light conditions of satellite fluorescence measurements. As a demonstration of this link between Fe-stress and satellite Chl fluorescence, Westberry et al. (2013) showed that purposeful addition of Fe to natural phytoplankton

communities resulted in a marked decrease in satellite-based chlorophyll fluorescence efficiency. Further evidence was given by Behrenfeld et al. (2009) who highlighted the tight correspondence between regions of elevated MODIS fluorescence quantum yields and modeled regions of Fe-limitation and low dust deposition (the primary mechanism for Fe input to the open ocean). These findings imply that satellite-detected regions of elevated Chl fluorescence yields may provide an avenue for time-resolved assessments of phytoplankton assimilation efficiencies that can account for the unique physiological consequences iron stress. Furthermore, such an approach could account for the highly dynamic nature of iron supply, which can be linked to episodic upwelling or atmospheric deposition events.

8.6.3 Phytoplankton Community Composition

It has long been recognized that ocean NPP exhibits strong regional variability and that some of this variability is tied to community taxonomic structure. Regionally specific NPP algorithms have been employed to indirectly account for taxonomic variability. For example, several studies have partitioned the ocean into distinct 'biogeographical provinces' that are empirically assigned unique photosynthetic parameters (Longhurst et al. 1995; Sathyendranath et al. 1995). This approach draws upon extensive field data sets of ^{14}C uptake data and avoids any necessity for explicit predictive relationships. Alternatively, empirical predictive relationships may be derived for specific broad ocean regions, such as the Arctic or Southern Ocean (Arrigo et al. 2008a, b).

In addition to influencing regional variability, taxonomic contributions to NPP have relevance to understanding ecosystem carbon flow, export efficiency, and fisheries production (Ryther 1969), for example. A variety of satellite ocean-color based studies have aimed to directly decompose bulk emergent bio-optical signals into contributions from different phytoplankton groups. While few models have been successful at resolving species-level differences in satellite ocean color data (Westberry and Siegel 2006; Balch et al. 2005; Alvain et al. 2008; Bracher et al. 2009), algorithms do exist for identifying broad phytoplankton size classes (Ciotti et al. 2002; Devred et al. 2006; Uitz et al. 2006; Hirata et al. 2008). These techniques rely on the first order relationship between cell size and ecosystem function (after Sieburth et al. 1978). However, the end-point of most of these studies has been to assess different phytoplankton size-class contributions to pigment biomass (Chl) only, rather than their contributions to NPP. For example, Uitz et al. (2006) used a large in situ dataset of Chl and other diagnostic pigment markers to generate empirical parameterizations between surface [satellite] Chl and relative dominance of three size classes of phytoplankton; pico-, nano-, and micro-phytoplankton. The link between size-fractionated Chl estimates and NPP was made in subsequent work by Uitz and co-workers who associated class-specific photophysiological variables with pigment-based size classes in field datasets (Uitz et al. 2008), then applied these relationships to satellite data (Uitz et al. 2010).

The approaches described above all suffer from their reliance on satellite Chl as an indicator of biomass. As a result, they interpret higher Chl as more biomass, and by inference, a greater contribution from larger size classes of phytoplankton. One solution to this problem in the context of remote sensing is to build on the body of work which employs satellite estimates of particulate backscattering (b_{bp}) to quantify phytoplankton carbon directly (Behrenfeld et al. 2005; Westberry et al. 2008; Kostadinov et al. 2009). The global relationship of Westberry et al. (2008) relating particulate backscattering to C_{phyto} can be improved through (1) routine field measurements of C_{phyto} (currently there are none) to better constrain the relationship, (2) improvements in bio-optical inversion schemes that estimate b_{bp} from satellite radiance, and (3) algorithm development that accounts for anomalous sources of b_{bp} biasing estimates of C_{phyto} (e.g., coccolithophores). Kostadinov et al. (2009, 2010) recently introduced a remote sensing method for characterizing particle size distributions (PSD) based on spectral b_{bp} retrievals. Resultant PSDs can be expressed as a continuous function of size and related to specific phytoplankton size ranges, such as pico-, nano-, and micro-phytoplankton. Given biovolume-specific carbon concentrations, which are available from laboratory studies, this method could yield class-specific carbon biomass explicitly. Perhaps an even more compelling avenue would be to combine the approaches of Uitz et al. (2006) and Kostadinov et al. (2009) to partition both Chl and C_{phyto} individually to characterize size-class specific Chl:C_{phyto} ratios. Any existing NPP model that accounts for Chl:C_{phyto} variability would surely benefit from this added information.

Another means of incorporating taxonomic information is through the use of phytoplankton absorption, a_{ph}, rather than Chl concentration. NPP models employing Chl implicitly assume a fixed Chl-specific absorption capacity, a^*_{ph}, despite order of magnitude variability that exists in a^*_{ph} (Bricaud et al. 1995, 1998). Much of this variability can be related to the size distribution of extant phytoplankton and presumably taxonomic composition (Bricaud et al. 2004). Lee et al. (1996) provide a NPP model amenable to remote sensing which is cast in terms of a_{ph}, rather than Chl. For the dataset these authors investigated, a_{ph}-based NPP models were far superior to Chl-based analogs. In addition to the conceptual advantages of using a_{ph} over Chl for estimating NPP, retrieval of a_{ph} from satellite reflectance has also been suggested to be preferable to direct estimation of biogeochemical quantities such as Chl (Lee et al. 2002).

8.6.4 New Tools

The various avenues discussed above for improving global assessments of ocean NPP are largely focused on advances that can be made with currently available observational and model-derived data sets. Major future advancements, however, may also be realized through engineering developments, both in the ocean and in space. Autonomously collected data by free-drifting and profiling floats and gliders

is already returning unprecedented measurements of physical, optical, nutrient, and oxygen properties. Already, these data have been used to track the seasonal evolution of phytoplankton blooms (Boss and Behrenfeld 2010) and constrain the upwelling supply of nutrients available for photosynthesis (Johnson et al. 2010), to name just a few applications. Following the success of the Argo program (Roemmich and Owens 2000), the Bio-Argo program strongly supports development and deployment of floats equipped with sensors for measuring key biogeochemical properties, such as Chl fluorescence and particulate backscattering. Similar efforts are in place to make routine O_2 measurements on profiling float platforms (Gruber et al. 2007). Inclusion of these capabilities represents the first precursors to NPP-enabled floats. Indeed, prototype floats capable of the aforementioned measurements and more (e.g., radiometers) already exist and should enable a single platform to yield a complete suite of data suitable for initial NPP calculations.

Another exciting yet unexploited tool for ocean ecological studies is space-based lidar (Light Dectection And Ranging) systems. Lidar technology is widely used in terrestrial and atmospheric disciplines, but ocean applications have been limited to targeted near-shore and coastal studies using aircraft or ship-based systems (e.g., Churnside and Wilson 2001). Nevertheless, space-borne LIDAR assets are available for investigating their application to subsurface ocean retrievals. For example, the CALIOP lidar on the CALIPSO satellite conducts routine vertical profiling measurements at 532 and 1064 nm. The latter wavelength is too long to penetrate the ocean surface, but the former should effectively sample near surface plankton populations. CALIPSO's stated science objectives are aimed atmospheric aerosol and cloud science applications. Nevertheless, preliminary analyses suggest subsurface scattering signals can be detected from the ocean surface. CALIOP was not designed for ocean applications, but these early results suggest that a more capable ocean-penetrating space lidar could provide critical independent constraints on ocean particle pools and perhaps even assessments of vertical structure in plankton distributions with links to mixed layer depths.

Significant opportunities also exist for realizing major advances in ocean ecosystem characterization from upcoming passive ocean color sensors designed with capabilities far exceeding those of our heritage sensors. Technological developments since the conception of CZCS, SeaWiFS, and MODIS now enable major improvements in spatial, temporal, and spectral resolution, although not necessarily all within a single instrument. Increased spectral resolution and expansion into the near-ultraviolet wavebands (350–400 nm) will allow further discrimination of different phytoplankton groups and separation of phytoplankton from other optical constituents (sediments, detritus, dissolved organics). Improved atmospheric corrections may also be realized by flying an advanced ocean color sensor with a profiling lidar and multi-angle spectral polarimeter. A satellite constellation of this sort will not only improve atmospheric corrections for more accurate water leaving radiance retrievals, but would also provide simultaneous lidar subsurface retrievals described above and a capacity for discriminating organic and inorganic particles through the polarimeter measurements (Loisel et al. 2008).

8.6.5 Vision for Future Remote Sensing of NPP

The preceding subsections outlined various avenues for advancing space-based NPP models. Here, an example is given which employs some of these pieces and allows a glimpse of how the distribution of NPP and our understanding may differ when taken into consideration. This new approach is termed the Carbon, Absorption, and Fluorescence Euphotic-resolving (CAFE) NPP model. For this exercise, the VGPM is used as a prototypical satellite NPP model, and its annual average NPP rate is shown in Fig. 8.4. In contrast, the CAFE NPP model assimilates new satellite-derived information into its estimation of NPP rates. First, the model employs satellite-derived estimates of particulate backscattering that are used to estimate phytoplankton carbon biomass (C) directly. This parameter also allows estimation of Chl:C which provides physiological information (i.e., photoacclimation) and a link to the phytoplankton growth rate, μ (Laws and Bannister 1980). Thus, we can estimate NPP directly using Eq. 8.1. Using this approach, the model is able to distinguish physiological changes in cellular pigmentation from changes in biomass. The result is that many high Chl regions (i.e., North Atlantic) have reduced NPP as some fraction of the bulk Chl is attributed to photoacclimation. In contrast, many low Chl regions (i.e., North Pacific Subtropical Gyre) exhibit increased NPP relative to the VGPM as their biomass (and Chl) may be low, but their growth rates can still be high. Second, chlorophyll fluorescence from satellite has been shown to register the unique imprint of iron stress over much of the ocean (Behrenfeld et al. 2009; Westberry et al. 2013). The reason for this, in part, results from chlorophyll present in phytoplankton and reflected in satellite-based Chl retrievals, but which is dissociated from photosynthetic electron transport (Behrenfeld and Milligan 2013). Therefore, NPP models which employ Chl as a biomass indicator will tend to overestimate NPP where phytoplankton are iron stressed. Satellite estimates of chlorophyll fluorescence efficiency (φ_f, Behrenfeld et al. 2009) can be used to correct for this effect (Fig. 8.4). Here, a simple linear correction is applied that assumes the strength of iron limitation is directly proportional to φ_f above some threshold value that marks the onset of iron limitation. The effects are largely irrelevant outside the equatorial oceans, but can reduce NPP by up to 40 % in some places. This is consistent with the observation that up to 40 % of the total Chl content in iron stressed cells can be in a 'dissociated' state (Moseley et al. 2002). In the example given, this correction alone decreases global annual, marine NPP by >3 Pg year^{-1}, nearly all of which is in the tropics between 20°N and 20°S. Third, the CbPM can be recast in terms of phytoplankton absorption (a_{ph}) per unit carbon rather than Chl:C. This approach has the benefit of accounting for all accessory pigments which can play an important role in light absorption and photosynthesis. Absorption-based NPP modeling has shown superior predictive ability in some field datasets (Lee et al. 1996). In addition, this approach should also reduce uncertainties arising from empirical retrievals of Chl, as phytoplankton absorption is more closely tied to the fundamental satellite measurements of radiance.

Taking another step forward, CAFE NPP can be partitioned amongst various phytoplankton groups. This step can be achieved in many ways (e.g., Uitz et al. 2010). Here, the model of Kostadinov et al. (2009, 2010) has been used which links satellite-derived particulate backscattering to the particle size distribution. In this example, the fraction of total particle biovolume in each of three size-based phytoplankton groups (pico-, nano-, micro-) has been estimated and directly assigned to the fraction of NPP in each group. Ideally, this partitioning of particle volume (a proxy for biomass) would occur first and NPP would then be calculated in parallel for each group. Further, Chl could be partitioned in a similar manner (e.g., Uitz et al. 2006) and allow group specific Chl:C for use in the CAFE model. Nevertheless, this proof of concept allows us to visualize the contribution to total NPP from different phytoplankton groups (Fig. 8.4). The patterns largely confirm many years' worth of expeditionary field measurements and demonstrate the predominance of small phytoplankton in the open ocean and the overwhelming contribution of large phytoplankton in nutrient rich areas. This annual composite likely masks many seasonal and small scale bloom features. Last, the newly

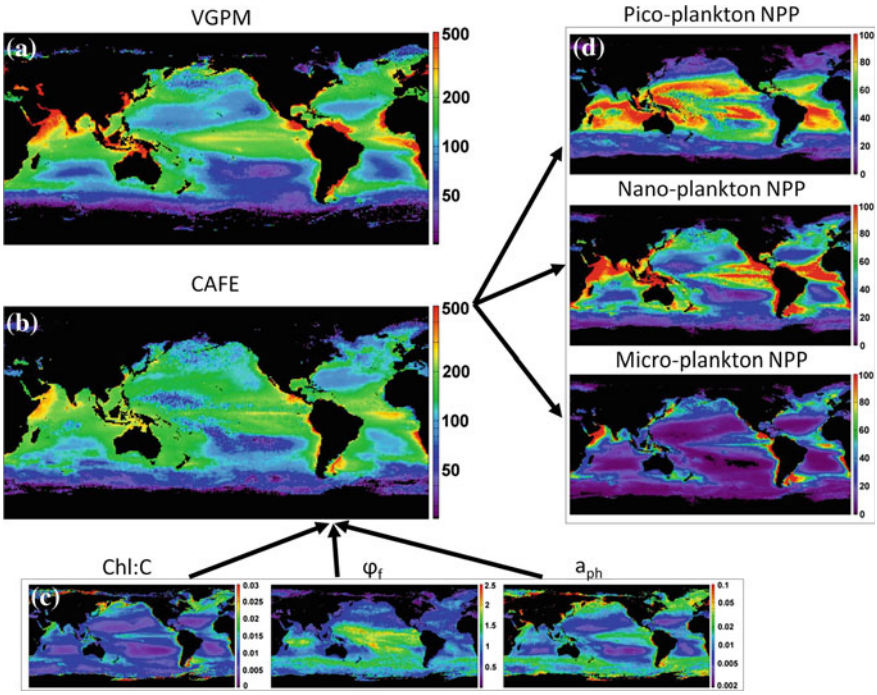

Fig. 8.4 Illustration of current and next generation satellite-based marine NPP models. **a** VGPM represents prototypical current NPP model. **b** New CAFE NPP model for same time period. **c** Additional satellite-derived inputs to CAFE characterizing photoacclimation (Chl:C), iron stress (φ_f), and phytoplankton absorption (a_{ph}). **d** Further, NPP can be resolved into coarse, size-based taxonomic groups (pico, nano, micro), yielding group-specific NPP

revised CAFE NPP rates can be used in conjunction with recent laboratory findings that show remarkable consistency between rates of *gross* primary production (GPP) and its use by phytoplankton for cellular growth and maintenance. Halsey et al. (2010) showed that constant fractions of Chl-normalized GPP were allocated to light-dependent respiration (15 %), nitrogen and sulfur reduction (10 %), synthesis of short-lived carbon products not reflected in NPP measurements (45 %), and NPP (30 %). These relationships were valid across the entire range of growth rates experienced by the phytoplankton (from 0.1 to 1.2 d^{-1}). Thus, oceanic estimates of GPP may be in the range 150–170 Pg C $year^{-1}$, of which ~70 Pg is fixed carbon, but which is not measured or estimated as NPP. These realizations, if true at the global scale, require careful reconsideration of energy and matter flow through marine ecosystems.

8.6.6 Beyond NPP

While NPP is an essential attribute of all surface ocean ecosystems, fully understanding ocean ecological interactions, biogeochemistry, and change necessitates assessments of many additional properties. Gross primary production, autotrophic and community respiration, net community production, export production and other intermediate rate measurements each convey different information about an ecosystem. Currently, it is unclear what governs the relationships between these rates or whether universal relationships exist between properties. Halsey et al. (2010) recently reported remarkable stability in the ratio of Chl-specific gross and net primary production rates. Similar results are not generally observed in the field, although the contribution of field methodological issues to this observed variability is not well constrained. The comparable global values of NPP reported for ocean and terrestrial systems (e.g., Field et al. 1998; Behrenfeld et al. 2001; Friend et al. 2009) certainly do not exist at the level of GPP, as terrestrial plants have a much lower ratio of photosynthetic to respiratory tissue. However, the extent of this difference will not be clear until ocean GPP assessments can be made. Currently, a wide range of ratios between gross and net primary production have been reported in the literature (Luz and Barkan 2009; Quay et al. 2010; Marra 2009).

Additional work is also needed in understanding ecosystem balances between phytoplankton growth and loss rates. In this case, satellite data may be extremely useful. Currently approaches allow for the calculation of phytoplankton NPP and assessment of C_{phyto}. As indicated by equation (8.1), the ratio of NPP: C_{phyto} yields an estimate of μ. Continuous time series of C_{phyto} also allow direct assessment of net population growth rates (r) through calculation of the rate of change in C_{phyto} between any two observational time points. As $r = \mu - l$, it is now possible to investigate regional relationships between phytoplankton growth and loss dynamics and relate these interactions to environmental forcings. An example of this type of analysis is provided by Behrenfeld (2010), where controls on North Atlantic vernal phytoplankton blooms were investigated and related to mixed layer

dynamics. Application of this approach to other major ocean systems will inevitably result in significant new insights ecosystem dynamics. This satellite-based assessment of phytoplankton loss rates (l), unfortunately does not distinguish grazing losses from other losses, such as carbon export. For processes such as export that are multiple levels removed from remotely sensed properties, we have to continue relying heavily on the integration of satellite data with mechanistic ocean ecosystems models.

References

Alvain S, Moulin C, Dandonneau Y, Loisel H (2008) Seasonal distribution and succession of dominant phytoplankton groups in the global ocean: a satellite view. Glob Biogeochem Cycles 22(3). doi:10.1029/2007gb003154

Antoine D, Morel A (1996) Oceanic primary production, 1, Adaptation of a spectral light-photosynthesis model in view of application to satellite chlorophyll observations. Glob Biogeochem Cycles 10:43–55

Antoine D, Morel A, Gordon HR, Banzon VF, Evans RH (2005) Bridging ocean color observations of the 1980s and 2000s in search of long-term trends. J Geophys Res 110(C6). doi:10.1029/2004jc002620

Armstrong RA (2006) Optimality-based modeling of nitrogen allocation and photo acclimation in photosynthesis. Deep-Sea Res Part II-Topical Stud Oceanogr 53(5–7):513–531. doi:10.1016/j.dsr2.2006.01.020

Arndt DS, Baringer MO, Johnson MR (2010) State of the climate in 2009. Bull Am Meteorol Soc 91(7):s1-s222. doi:10.1175/BAMS-91-7-StateoftheClimate

Arrigo KR, van Dijken G, Pabi S (2008a) Impact of a shrinking arctic ice cover on marine primary production. Geophys Res Lett 35(19):L19603

Arrigo KR, van Dijken GL, Bushinsky S (2008b) Primary production in the southern ocean, 1997–2006. J Geophys Res 113(C8):C08004

Balch WM, Gordon HR, Bowler BC, Drapeau DT, Booth ES (2005) Calcium carbonate measurements in the surface global ocean based on moderate-resolution imaging spectroradiometer data. J Geophys Res 110(C7):C07001

Barber RT, Chavez FP (1983) Biological consequences of el-nino. Science 222(4629): 1203–1210. doi:10.1126/science.222.4629.1203

Barber RT, Hilting AK (2002) History of the study of plankton productivity. In: Williams PJlB, Thomas DN, Reynolds CS (eds) Phytoplankton productivity. Blackwell Science Ltd, pp 16–43. doi:10.1002/9780470995204.ch2

Behrenfeld MJ (2010) Abandoning sverdrup critical depth hypothesis on phytoplankton blooms. Ecology 91(4):977–989. doi:10.1890/09-1207.1

Behrenfeld MJ, Boss E, Siegel DA, Shea DM (2005) Carbon-based ocean productivity and phytoplankton physiology from space. Glob Biogeochem Cycles 19(1):1–14. doi:10.1029/2004GB002299

Behrenfeld MJ, Falkowski PG (1997a) A consumer'' guide to phytoplankton primary productivity models. Limnol Oceanogr 42(7):1479–1491

Behrenfeld MJ, Falkowski PG (1997b) Photosynthetic rates derived from satellite-based chlorophyll concentration. Limnol Oceanogr 42(1):1–20

Behrenfeld MJ, Halsey KH, Milligan AJ (2008) Evolved physiological responses of phytoplankton to their integrated growth environment. Philos Trans R Soc Lond B 363:2687–2703

Behrenfeld MJ, Milligan AJ (2013) Photophysiological Expressions of Iron Stress in Phytoplankton. Annu Rev Mar Sci 5:217–246

Behrenfeld MJ, O''alley RT, Siegel DA, McClain CR, Sarmiento JL, Feldman GC, Milligan AJ, Falkowski PG, Letelier RM, Boss ES (2006a) Climate-driven trends in contemporary ocean productivity. Nature 444(7120):752–755

Behrenfeld MJ, Randerson JT, McClain CR, Feldman GC, Los SO, Tucker CJ, Falkowski PG, Field CB, Frouin R, Esaias WE, Kolber DD, Pollack NH (2001) Biospheric primary production during an enso transition. Science 291(5513):2594–2597

Behrenfeld MJ, Westberry TK, Boss ES, O''alley RT, Siegel DA, Wiggert JD, Franz BA, McClain CR, Feldman GC, Doney SC, Moore JK, Dall''lmo G, Milligan AJ, Lima I, Mahowald N (2009) Satellite-detected fluorescence reveals global physiology of ocean phytoplankton. Biogeosciences 6:779–794

Behrenfeld MJ, Worthington K, Sherrell RM, Chavez FP, Strutton P, McPhaden M, Shea DM (2006b) Controls on tropical Pacific ocean productivity revealed through nutrient stress diagnostics. Nature 442(7106):1025–1028

Blunden J, Arndt DS, Baringer MO (2011) State of the climate in 2010. Bull Am Meteorol Soc 92(6):S1-S236. doi:10.1175/1520-0477-92.6.s1

Boss E, Behrenfeld M (2010) In situ evaluation of the initiation of the North Atlantic phytoplankton bloom. Geophys Res Lett 37. doi:10.1029/2010gl044174

Bracher A, Vountas M, Dinter T, Burrows JP, Rottgers R, Peeken I (2009) Quantitative observation of cyanobacteria and diatoms from space using phytodoas on sciamachy data. Biogeosciences 6(5):751–764

Bricaud A, Babin M, Morel A, Claustre H (1995) Variability in the chlorophyll-specific absorption coefficients for natural phytoplankton: Analysis and parameterization. J Geophys Res 100:13,321–13,332

Bricaud A, Claustre H, Ras J, Oubelkheir K (2004) Natural variability of phytoplanktonic absorption in oceanic waters: Influence of the size structure of algal populations. J Geophys Res 109. doi: 10.1029/2004JC002419

Bricaud A, Morel A, Babin M, Allalli K, Claustre H (1998) Variations of light absorption by suspended particles with chlorophyll a concentration in oceanic (case 1) waters: Analysis and implications for bio-optical models. J Geophys Res 103:31,033–31,044

Buesseler KO, Antia AN, Chen M, Fowler SW, Gardner WD, Gustafsson O, Harada K, Michaels AF, van der Loeff'' MR, Sarin M, Steinberg DK, Trull T (2007) An assessment of the use of sediment traps for estimating upper ocean particle fluxes. J Mar Res 65(3):345–416

Campbell J, Antoine D, Armstrong R, Arrigo K, Balch W, Barber R, Behrenfeld M, Bidigare R, Bishop J, Carr ME, Esaias W, Falkowski P, Hoepffner N, Iverson R, Kiefer D, Lohrenz S, Marra J, Morel A, Ryan J, Vedernikov V, Waters K, Yentsch C, Yoder J (2002) Comparison of algorithms for estimating ocean primary production from surface chlorophyll, temperature, and irradiance. Glob Biogeochem Cycles 16(3):1035

Carr ME, Friedrichs MAM, Schmeltz M, Aita MN, Antoine D, Arrigo KR, Asanuma I, Aumont O, Barber R, Behrenfeld M, Bidigare R, Buitenhuis ET, Campbell J, Ciotti A, Dierssen H, Dowell M, Dunne J, Esaias W, Gentili B, Gregg W, Groom S, Hoepffner N, Ishizaka J, Kameda T, Le Quere C, Lohrenz S, Marra J, Melin F, Moore K, Morel A, Reddy TE, Ryan J, Scardi M, Smyth T, Turpie K, Tilstone G, Waters K, Yamanaka Y (2006) A comparison of global estimates of marine primary production from ocean color. Deep-Sea Res Part II-Topical Stud Oceanogr 53(5–7):741–770

Castro-Morales K, Kaiser J (2012) Using dissolved oxygen concentrations to determine mixed layer depths in the bellingshausen sea. Ocean Sci 8(1):1–10. doi:10.5194/os-8-1-2012

Chassot E, Bonhommeau S, Dulvy NK, Melin F, Watson R, Gascuel D, Le Pape O (2010) Global marine primary production constrains fisheries catches. Ecol Lett 13:495–505. doi:10.1111/j.1461-0248.2010.01443.x

Chavez FP, Messie M, Pennington JT (2011) Marine primary production in relation to climate variability and change. In: Carlson CA, Giovannoni SJ (eds) Annu Rev Mar Sci 3:227–260. doi:10.1146/annurev.marine.010908.163917

Chavez FP, Pennington JT, Castro CG, Ryan JP, Michisaki RP, Schlining B, Walz P, Buck KR, McFadyen A, Collins CA (2002) Biological and chemical consequences of the 1997–1998 el

nino in central california waters. Prog Oceanogr 54(1–4):205–232. doi:10.1016/s0079-6611(02)00050-2
Churnside JH, Wilson JJ (2001) Airborne lidar for fisheries applications. Opt Eng 40(3):406–414. doi:10.1117/1.1348000
Ciotti AM, Lewis MR, Cullen JJ (2002) Assessment of the relationships between dominant cell size in natural phytoplankton communities and the spectral shape of the absorption coefficient. Limnol Oceanogr 47(2):404–417
Clancy RM, Sadler WD (1992) The fleet numerical oceanography center suite of oceanographic models and products. Weather Forecast 7(2):307–327
Clarke GL, Ewing GC, Lorenzen CJ (1970) Spectra of backscattered light from the sea obtained from aircraft as a measure of chlorophyll concentration. Science 167(3921):1119–1121
D''saro EA (2003) Performance of autonomous lagrangian floats. J Atmos Ocean Technol 20(6):896–911
Dave AC, Lozier MS (2010) Local stratification control of marine productivity in the subtropical north pacific. J Geophys Res 115. doi:10.1029/2010jc006507
Devred E, Sathyendranath S, Stuart V, Maass H, Ulloa O, Platt T (2006) A two-component model of phytoplankton absorption in the open ocean: Theory and applications. J Geophys Res 111(C3). doi:C03011 10.1029/2005jc002880
Dunne JP, Armstrong RA, Gnanadesikan A, Sarmiento JL (2005) Empirical and mechanistic models for the particle export ratio. Glob Biogeochem Cycles 19(4). doi:10.1029/2004gb002390
Eppley RW (1972) Temperature and phytoplankton growth in the sea. Fish Bull 70(4):1063–1085
Esaias WE (1996) Algorithm theoretical basis document for modis product mod-27 ocean primary productivity. Goddard Space Flight Center
Escoubas JM, Lomas M, LaRoche J, Falkowski PG (1995) Light intensity regulation of cab gene transcription is signaled by the redox state of the plastoquinone pool. Proc Natl Acad Sci USA 92(22):10237–10241
Falkowski PG, Barber RT, Smetacek V (1998a) Biogeochemical controls and feedbacks on ocean primary production. Science 281(5374):200–206
Falkowski PG, Behrenfeld MJ, Esaias WE, Balch WM, Campbell JW, Iverson RL, Kiefer DA, Morel A, Yoder JA (1998b) Satellite primary productivity data and algorithm development: A science plan for mission to planet earth. NASA Technical Memo 1998-104566, vol 42. NASA Goddard Space Flight Center, Greenbelt, Maryland
Falkowski PG, Laroche J (1991) Acclimation to spectral irradiance in algae. J Phycol 27(1):8–14. doi:10.1111/j.0022-3646.1991.00008.x
Field CB, Behrenfeld MJ, Randerson JT, Falkowski P (1998) Primary production of the biosphere: integrating terrestrial and oceanic components. Science 281(5374):237–240
Friedland KD, Stock C, Drinkwater KF, Link JS, Leaf RT, Shank BV, Rose JM, Pilskaln CH, Fogarty MJ (2012) Pathways between primary production and fisheries yields of large marine ecosystems. Plos One 7(1). doi:10.1371/journal.pone.0028945
Friedrichs MAM, Carr ME, Barber RT, Scardi M, Antoine D, Armstrong RA, Asanuma I, Behrenfeld MJ, Buitenhuis ET, Chai F, Christian JR, Ciotti AM, Doney SC, Dowell M, Dunne J, Gentili B, Gregg W, Hoepffner N, Ishizaka J, Kameda T, Lima I, Marra J, Melin F, Moore JK, Morel A, O''alley RT, O''eilly J, Saba VS, Schmeltz M, Smyth TJ, Tjiputra J, Waters K, Westberry TK, Winguth A (2009) Assessing the uncertainties of model estimates of primary productivity in the tropical Pacific Ocean. J Mar Syst 76(1–2):113–133. doi:10.1016/j.jmarsys.2008.05.010
Friend AD, Geider RJ, Behrenfeld MJ, Still CJ (2009) Photosynthesis in global-scale models. In: Laisk A, Nedbal L, Govindjee G (eds) Advances in photosynthesis and respiration vol 29. Springer, The Netherlands, pp 465–497. doi:10.1007/978-1-4020-9237-4_20
Gordon HR, Clark DK, Mueller JL, Hovis WA (1980) Phytoplankton pigments from the nimbus-7 coastal zone color scanner: comparisons with surface measurements. Science 210(4465):63–66

Gruber N, Doney SC, Emerson SR, Gilbert D, Kobayashi T, Kortzinger A, Johnson GC, Johnson KJ, Riser SC, Ulloa O (2007) The argo-oxygen program. Argo Steering Committee

Halsey KH, Milligan AJ, Behrenfeld MJ (2010) Physiological optimization underlies growth rate-independent chlorophyll-specific gross and net primary production. Photosynth Res 103(2):125–137

Henson SA, Raitsos D, Dunne JP, McQuatters-Gollop A (2009) Decadal variability in biogeochemical models: Comparison with a 50-year ocean colour dataset. Geophys Res Lett 36. doi:10.1029/2009gl040874

Hirata T, Aiken J, Hardman-Mountford N, Smyth TJ, Barlow RG (2008) An absorption model to determine phytoplankton size classes from satellite ocean colour. Remote Sens Environ 112(6):3153–3159. doi:10.1016/j.rse.2008.03.011

Hovis WA, Clark DK, Anderson F, Austin RW, Wilson WH, Baker ET, Ball D, Gordon HR, Mueller JL, El-Sayed SZ, Sturm B, Wrigley RC, Yentsch CS (1980) Nimbus-7 coastal zone color scanner—system description and initial imagery. Science 210(4465):60–63

Howard KL, Yoder JA (1997) Contribution of the sub-tropical oceans to global primary production. In: Liu C-T (ed) Proceedings of cospar colloquium on space remote sensing of subtropical oceans. New York, pp 157–168

Johnson KS, Riser SC, Karl DM (2010) Nitrate supply from deep to near-surface waters of the north pacific subtropical gyre. Nature 465(7301):1062–1065. doi:10.1038/nature09170

Kostadinov TS, Siegel DA, Maritorena S (2009) Retrieval of the particle size distribution from satellite ocean color observations. J Geophys Res 114. doi:10.1029/2009jc005303

Kostadinov TS, Siegel DA, Maritorena S (2010) Global variability of phytoplankton functional types from space: Assessment via the particle size distribution. Biogeosciences 7(10):3239–3257. doi:10.5194/bg-7-3239-2010

Laws EA, Bannister TT (1980) Nutrient-limited and light-limited growth of thalassiosira-fluviatilis in continuous culture, with implications for phytoplankton growth in the ocean. Limnol Oceanogr 25(3):457–473

Laws EA, Falkowski PG, Smith WO, Ducklow H, McCarthy JJ (2000) Temperature effects on export production in the open ocean. Glob Biogeochem Cycles 14(4):1231–1246

Lee ZP, Carder KL, Arnone RA (2002) Deriving inherent optical properties from water color: a multiband quasi-analytical algorithm for optically deep waters. Appl Opt 41(27):5755–5772

Lee ZP, Carder KL, Marra J, Steward RG, Perry MJ (1996) Estimating primary production at depth from remote sensing. Appl Optics 35(3):463–474

Loisel H, Duforet L, Dessailly D, Chami M, Dubuisson P (2008) Investigation of the variations in the water leaving polarized reflectance from the polder satellite data over two biogeochemical contrasted oceanic areas. Opt Express 16(17):12905–12918. doi:10.1364/oe.16.012905

Longhurst A, Sathyendranath S, Platt T, Caverhill C (1995) An estimate of global primary production in the ocean from satellite radiometer data. J Plankton Res 17:1245–1271

Lozier MS, Dave AC, Palter JB, Gerber LM, Barber RT (2011) On the relationship between stratification and primary productivity in the north atlantic. Geophys Res Lett 38. doi:10.1029/2011gl049414

Luz B, Barkan E (2009) Net and gross oxygen production from o-2/ar, o-17/o-16 and o-18/o-16 ratios. Aquat Microb Ecol 56(2–3):133–145. doi:10.3354/ame01296

Marra J (2009) Net and gross productivity: weighing in with (14)c. Aquat Microb Ecol 56(2–3):123–131. doi:10.3354/ame01306

Martinez E, Antoine D, D''rtenzio F, Gentili B (2009) Climate-driven basin-scale decadal oscillations of oceanic phytoplankton. Science 326(5957):1253–1256. doi:10.1126/science.1177012

Milutinovic S, Bertino L (2011) Assessment and propagation of uncertainties in input terms through an ocean-color-based model of primary productivity. Remote Sens Environ 115(8):1906–1917. doi:10.1016/j.rse.2011.03.013

Morel A (1991) Light and marine photosynthesis: a spectral model with geochemical and climatological implications 26:263–306

Moseley JL, Allinger T, Herzog S, Hoerth P, Wehinger E, Merchant S, Hippler M (2002) Adaptation to Fe-deficiency requires remodeling of the photosynthetic apparatus. Embo J 21(24):6709–6720

Parkhill JP, Maillet G, Cullen JJ (2001) Fluorescence-based maximal quantum yield for psii as a diagnostic of nutrient stress. J Phycol 37(4):517–529

Pauly D, Christensen V (1995) Primary production required to sustain global fisheries. Nature 374:255–257

Potter CS, Randerson JT, Field CB, Matson PA, Vitousek PM, Mooney HA, Klooster SA (1993) Terrestrial ecosystem production - a process model-based on global satellite and surface data. Glob Biogeochem Cycles 7(4):811–841. doi:10.1029/93gb02725

Quay PD, Peacock C, Bjorkman K, Karl DM (2010) Measuring primary production rates in the ocean: Enigmatic results between incubation and non-incubation methods at station aloha. Glob Biogeochem Cycles 24. doi:10.1029/2009gb003665

Roemmich D, Owens WB (2000) The Argo project: global ocean observations for understanding and prediction of climate variability. Oceanography 13(2):45–50

Ryther JH (1969) Photosynthesis and fish production in sea. Science 166(3901):72–000. doi:10.1126/science.166.3901.72

Ryther JH, Yentsch CS (1957) The estimation of phytoplankton production in the ocean from chlorophyll and light data. Limnol Oceanogr 2:281–286

Saba VS, Friedrichs MAM, Antoine D, Armstrong RA, Asanuma I, Behrenfeld MJ, Ciotti AM, Dowell M, Hoepffner N, Hyde KJW, Ishizaka J, Kameda T, Marra J, Melin F, Morel A, O''eilly J, Scardi M, Smith WO, Smyth TJ, Tang S, Uitz J, Waters K, Westberry TK (2011) An evaluation of ocean color model estimates of marine primary productivity in coastal and pelagic regions across the globe. Biogeosciences 8(2):489–503. doi:10.5194/bg-8-489-2011

Saba VS, Friedrichs MAM, Carr ME, Antoine D, Armstrong RA, Asanuma I, Aumont O, Bates NR, Behrenfeld MJ, Bennington V, Bopp L, Bruggeman J, Buitenhuis ET, Church MJ, Ciotti AM, Doney SC, Dowell M, Dunne J, Dutkiewicz S, Gregg W, Hoepffner N, Hyde KJW, Ishizaka J, Kameda T, Karl DM, Lima I, Lomas MW, Marra J, McKinley GA, Melin F, Moore JK, Morel A, O''eilly J, Salihoglu B, Scardi M, Smyth TJ, Tang SL, Tjiputra J, Uitz J, Vichi M, Waters K, Westberry TK, Yool A (2010) Challenges of modeling depth-integrated marine primary productivity over multiple decades: a case study at bats and hot. Glob Biogeochem Cycles 24. doi:10.1029/2009gb003655

Sathyendranath S, Longhurst A, Caverhill CM, Platt T (1995) Regionally and seasonally differentiated primary production in the North Atlantic. Deep-Sea Res Part I-Oceanogr Res Papers 42(10):1773–1802. doi:10.1016/0967-0637(95)00059-f

Schrader PS, Milligan AJ, Behrenfeld MJ (2011) Surplus photosynthetic antennae complexes underlie diagnostics of iron limitation in a cyanobacterium. PLoS ONE 6 (4). doi:e1875310.1371/journal.pone.0018753

Sherman K, Belkin IM, Friedland KD, O''eilly J, Hyde K (2009) Accelerated warming and emergent trends in fisheries biomass yields of the world'' large marine ecosystems. Ambio 38(4):215–224

Sieburth JM, Smetacek V, Lenz J (1978) Pelagic ecosystem structure—heterotrophic compartments of plankton and their relationship to plankton size fractions—comment. Limnol Oceanogr 23(6):1256–1263

Siegel DA, Behrenfeld MJ, Maritorena S, McClain CR, Antoine D, Bailey SW, Bontempi PS, Boss E, Dierssen HM, Doney SC, Eplee RE, Evans RH, Feldman GC, Fields E, Franz BA, Kuring NA, Mengalt C, Nelson NB, Patt FS, Robinson WS, Sarmiento JS, Swan CM, Werdell PJ, Westberry TK, Wilding JG, Yoder JA (2013) Regional to global assessments of phytoplankton dynamics from the SeaWiFS mission. Remote Sens Environ 135:77–91

Siegel DA, Westberry TK, O''rien MC, Nelson NB, Michaels AF, Morrison JR, Scott A, Caporelli EA, Sorensen JC, Maritorena S, Garver SA, Brody EA, Ubante J, Hammer MA (2001) Bio-optical modeling of primary production on regional scales: The Bermuda biooptics project. Deep-Sea Res Part II-Topical Stud Oceanogr 48(8–9):1865–1896

Smyth TJ, Tilstone GH, Groom SB (2005) Integration of radiative transfer into satellite models of ocean primary production. J Geophys Res 110(C10). doi:10.1029/2004jc002784

Steemann Nielsen E (1952) The use of radio-active carbon (c^{14}) for measuring organic production in the sea. J Cons Cons Int Explor Mer 18:117–140

Talling JF (1957) The phytoplankton population as a compound photosynthetic system. New Phytol 56(2):133–149

Uitz J, Claustre H, Gentili B, Stramski D (2010) Phytoplankton class-specific primary production in the world'' oceans: Seasonal and interannual variability from satellite observations. Glob Biogeochem Cycles 24. doi:10.1029/2009gb003680

Uitz J, Claustre H, Morel A, Hooker SB (2006) Vertical distribution of phytoplankton communities in open ocean: An assessment based on surface chlorophyll. J Geophys Res 111(C8). doi:10.1029/2005jc003207

Uitz J, Huot Y, Bruyant F, Babin M, Claustre H (2008) Relating phytoplankton photophysiological properties to community structure on large scales. Limnol Oceanogr 53(2):614–630

Vollenweider RA (1966) Calculation models of photosynthesis-depth curves and some implications regarding day rate estimates in primary production measurements. In: Goldman CR (ed) Primary productivity in aquatic environments. University of California Press, Berkeley. pp 455–472

Westberry T, Behrenfeld MJ, Siegel DA, Boss E (2008) Carbon-based primary productivity modeling with vertically resolved photoacclimation. Glob Biogeochem Cycles 22(2):GB2024

Westberry TK, Behrenfeld MJ, Milligan AJ, Doney SC (2013) Retrospective satellite ocean color analysis of purposeful and natural ocean iron fertilization. Deep-Sea Res Part I 73:1–16

Westberry TK, Siegel DA (2006) Spatial and temporal distribution of *Trichodesmium* blooms in the world's oceans. Glob Biogeochem Cycles 20(4). doi:10.1029/2005gb002673

Westberry TK, Williams PJ. Le B, Behrenfeld MJ (2012) Global net community production and the putative net heterotrophy of the Oligotrophic Oceans. Global Biogeochem Cycles 26. doi:10.1029/2011GB004094

Zhao MS, Heinsch FA, Nemani RR, Running SW (2005) Improvements of the modis terrestrial gross and net primary production global data set. Remote Sens Environ 95(2):164–176. doi:10.1016/j.rse.2004.12.011